Project No. 13-5365

Doubling the Life of Concrete Structures

Fuel Cycle Research and Development

Batric Pesic
University of Idaho

In collaboration with:
University of Colorado-Boulder

John Orchard, Federal POC
Ken Sorenson, Technical POC

NEUP Nuclear Energy University Programs
U.S. Department of Energy

Research Performance Final Report

Federal Agency and Organization Element	U.S. Department of Energy Office of Nuclear Research
Award Number	DE-NE0000659
Project Title	Doubling the Life of Concrete Structures
Principal Investigator	Batric Pesic Professor, Department of Chemical and Materials Engineering, University of Idaho Moscow ID 83844-3024 pesic@uidaho.edu; tel. 208.885.6569
Collaborators	Prof. Krishnan S. Raja (University of Idaho) Prof. Yunping Xi (University of Colorado-Boulder) Dr. Jiheon Jun (Oak Ridge National Laboratory)
Recipient Organization	University of Idaho Office of Sponsored Programs P.O. Box 443020 Moscow, ID 83844
DUNS Number	075746271
Distribution Notice	No limitation
Submission Date	July 20, 2017
Signature of Submitting Official	

Executive Summary

Overall objective of the project was to study the fundamental properties of concrete (with and without steel reinforcement) with respect to chemical and physical parameters that can influence its structural integrity. There were three distinct research teams. At University of Idaho, the research lead, the main focus was on electrochemical (corrosion) phenomena and the examination of effects of nanoviscosity modifiers on the moisture transport properties. The research at Colorado University-Boulder considered the simultaneous effects of moisture and temperature variations, the damage of concrete due to the ice formation at low temperatures, and the effects of admixtures (glycerol and fumed silica) on the moisture transport properties in concrete under freeze/thaw conditions. The collaboration with Oak Ridge National Laboratory started with Dr. Guang-Ling Song, who unfortunately left the laboratory early in this project. His final replacement was Dr. Jiheon Jun. Dr. Jun and Dr. Raja (University of Idaho) utilized the electrochemical impedance spectroscopy to study the moisture transport properties in concrete, the idea based on electrochemical models developed by Dr. Song.

What has been learned on this project, and what else should be studied?

The conceptual approach for increasing the integrity of concrete structures (doubling its life) was based on the reduction of moisture absorption and transfer. That could be achieved either by reducing the diffusivity of water, or by blocking the water pathways in the form of pores. It was found that glycerol addition to cement in the range of 0.5-2.0 wt% was an effective method for reduction of moisture transport. The explanation for this beneficiary effect of glycerol is found in Benz equation, which describes the correlation between the diffusivity and viscosity. Accordingly, glycerol was termed as nanoviscosity modifier. Among the pathway blockers to moisture (fumed silica, micro silica and colloidal silica), fumed silica proved to be very effective. This finding is in line with the results found in literature. Contrary to micro and colloidal silica, fumed silica poses no environmental and health hazards, an important property to state. The beneficial effects of glycerol and fumed silica were also confirmed by the collaborator at Colorado University-Boulder.

Perhaps most important finding is that corrosion of reinforcement steel in concrete can be studied in a classical corrosion method, consisting of working, counter and reference electrode. In the study previous to this project, the PI (Pesic) has shown that it is possible to embed a reference electrode into concrete and treat the system as a regular corrosion cell. That was demonstrated by using the so called mini Ag/AgCl leak free reference electrode. In the current NEUP project, it was discovered that a bare Ag wire embedded in concrete can also serve as the source of a very stable potential. The potential difference between a classical Ag/AgCl and Ag wire embedded in concrete is about 130 mV. What happens when silver wire is embedded in concrete is the surface oxidation of silver to Ag_2O. In essence, silver wire becomes a well-known Ag/Ag_2O reference electrode, which explains the difference of 130 mV with respect to Ag/AgCl. The reference potential stays stable indefinitely providing the pH does not change below 12. (pH in concrete pore solutions is between 12 and 12.5). It is envisaged that the future concrete structures will have methodically wrapped 50-100 micron diameter silver wires around reinforcement steel structures and use the potential difference (open circuit potential) between silver and steel structure as the *in-situ* information on the status of steel corrosion, and also on physico-chemical status of concrete. The potential difference can be measured with a regular voltmeter, with no

need for expensive equipment for corrosion studies. The idea of using silver wire as the source of stable reference potential in concrete is most likely patentable however the PI decided not pursue this effort.

The next finding of importance is that rebar corrosion in simulated cement solution is different from corrosion in actual cement saturated solution. In literature, all studies on corrosion in concrete were done with the use of NaOH to produce the simulated cement solution (pH 12.5). In this project, the saturated cement solution was produced by leaching actual Portland cement in excess to the amount of water to produce the actual saturated cements solution. When rebar corrosion studies were performed with these two types of solutions the results were different, clearly indicating that the literature results with simulated concrete pore solutions should be taken with reservation.

The future research. What needs to be examined in future is the role of interface between cement and aggregate with regard to the transport of moisture in concrete. Different aggregates (granite, basalt, limestone) provide different surface properties with respect to adhesion, wetting, etc. influencing the transport of moisture throughout concrete differently. No fundamental research was performed thus far with regard to this important fundamental property. These data should be compared to the transport properties of pure Portland cement phase. This information would provide critical information on the contribution of each (interface vs. cement phase) to the moisture transport.

Next, the implementation of silver wire as the source of standard potential in actual corrosion studies (field and laboratory), as described above, should definitely be studied further. The proposed research would be of great practical importance.

Project Summary

This is the final report to the NEUP regarding the "Doubling the life of concrete structures" project. This report describes the project activities conducted during the period February 13, 2014 through April 30, 2017. The report includes a brief statement of the project objectives and approach, followed by the details of the research activities and an outline of the ongoing and future work.

Administrative

From the administrative aspects, the following are the key dated events.

- ❑ Official contract between DOE and University of Idaho was signed on February 13, 2014. This was done after three contract modifications.

- ❑ The three year project was planned to terminate on December 5, 2016. However, the PI has asked NEUP for no cost extension, which was granted with the new termination date of May1, 2017. The objective for no cost extension was to run some additional tests on concrete permeability. The research with concrete is intrinsically slow, often out of control of those involved, therefore additional time was required.

- ❑ This contract has two subcontracts. One went directly to ORNL. Initially the recipient was Dr. Guang-Ling Song as the Co-PI, who after leaving ORNL has been replaced with Dr. Sergei Shipilov, then with Dr. Jiheon Jun. The other subcontract is with Colorado University, with Prof. Yunping Xi as the Co-PI.

- ❑ All reporting formalities have been fulfilled, including milestones, deliverables, quad charts, etc.

Research

From the research point of view, the major activities and accomplishments are:

University of Idaho

- At the University of Idaho, the corrosion of reinforcement steel (rebar) embedded in concrete (Task A, Task C, and Task D) has been completed as planned. The major parameter of study is the role of admixtures.

- *Dr. Pesic (PI)*, performed two additional studies. One of the studies was the corrosion of reinforcement steel with saturated concrete pores solution (Task A). The concrete pore solution was prepared by mixing the cement powder with water for several days under stirring conditions in order to achieve the saturation condition (pH). Solution was separated by pressure filtration and stored in jars for experimentation on corrosion of reinforcement steel as a function of admixtures (glycerol and silica). These data served as the control of the corrosion results for the steel embedded in concrete.

  The second study was the development of experimental procedure for direct measurement of concrete permeability. This method is termed as "Tube Method". The permeability was evaluated by measuring the concentration of chloride ions, with time, in the receiving compartment. Chloride ion was measured with ion chromatography. The purpose of this

experimentation was to compare the concrete permeability data, as a function of admixture, obtained by two different methods, (1) indirect measurements (corrosion), and (2) direct measurements (change of chloride concentration) by Tube Method.

- *The CoPI, Dr. Raja*, completed the research with the cured concrete samples, each with particular admixture, for his electrochemical impedance measurements (Task C), all as a function of immersion time. The complete data are reported here.

- In order to clarify the role of chlorides in the concrete and understand the effect of viscosity modifiers on the chloride induced corrosion, Dr. Raja followed an experimental matrix he developed. The main objective of this sub-task was to determine the threshold chloride content for passivity breakdown in cement solution as a function of pH, and viscosity modifier additions.

  Contrary to the previous results and expectations EIS is not strong enough technique to discriminate between the effect of admixtures, such as glycerol, fumed silica, and micro silica.

- Separately, Dr. Raja evaluated if admixtures such as glycerol and fumed silica act as corrosion inhibitors rather than diffusion controlling additives.

Colorado University-Boulder

- *The CoPI, Dr. Xi*, at Colorado University-Boulder, is evaluating the effect of temperature (Task B) and the moisture transfer under wind-driven rain (WDR) conditions (Task E) on the permeability of concrete.

<u>The conclusions for Task B, the effect of temperature on moisture transfer, are:</u>

- An experimental technique was established for understanding the temperature effect on moisture transfer in concrete. The technique was used for studying the moisture penetration into concrete with and without temperature gradient. The test data show that the elevated temperature without a temperature gradient does not have a significant effect on moisture transfer. Moreover, the effect of temperature gradient is significant and should be considered in the analysis of moisture transport in concrete under non-isothermal condition.

- An analysis method was developed based on the governing equations to calculate the coupling parameter D_{HT} (coefficient of the Soret effect). The results show that D_{HT} is not a constant but increases with temperature gradient increasing. A material model was developed for D_{HT} using the test data obtained in this study.

- For the effect of AEA on the thermal strain, it is evidenced from Figures 12, 13, and 14 that the addition of AEA can effectively decrease the variation of thermal strains during the cooling process, and thus decrease the dilation in the concrete. Similarly, from Fig. 15, 16, and 17 it is obvious that increasing w/c effectively decreases the variation of thermal strains during the cooling process. Both methods are increasing the internal porosity in the concrete: more internal space is available for the ice to deposit in the pores and thus the overall expansion is reduced.

- The theoretical model based on the Mori-Tanaka method successfully simulated the concrete from microscale to mesoscale. Figure 21 shows the calculating results for the specific concrete sample.

From the results one can see that as temperature decreasing, the Young's modulus increases at the beginning and then decreases. This agrees with the temperature dependent CTE test results.

- Freeze-thaw performance and chloride penetration were both improved when *glycerol* was added in the concrete. The sample with *glycerol* showed a better effect than the control sample. Thus, g*lycerol* indeed has the positive effect on improving the durability of concrete.

From the experimental results including the compressive strength, total porosity, chloride penetration, and temperature dependent CTE, one can see that the concrete sample with *fumed silica* has better performance characteristics than the control sample. Thus, *fumed silica* can improve both mechanical and durability properties of concrete.

<u>The conclusions for the Task E, the effect of admixtures on RILEM tube test method (to test wind driven rain effect) are:</u>

- The water head of concrete sample with the highest w/c and largest amount of AEA drops at the fastest rate among all groups. Thus, the water transport under WDR is strongly dependent on the concrete mix design and quantity of additive. Therefore, optimization of concrete mix design for resistance to WDR is very important.

- Adding *fumed silica* can decrease the penetration rate of water under the Wind-Driven Rain. Thus, the concrete sample can be protected from the WDR by adding a proper amount of *fumed silica*.

- A new variable P (pore pressure) was introduced in the moisture transfer model for WDR, which is an internal pressure in pores related to the water pressure in liquid water transfer process or the vapor pressure in water vapor transfer process. The boundary condition of the pressure P is the pressure induced by the wind-driven rain defined by the RILEM tube testing method.

- The theoretical solution of a 1D diffusion equation in an infinitely long bar can be used as a simplified theoretical model to predict the internal pore pressure P in concrete sample under the RILEM tube test.

- The moisture diffusivity in the simplified theoretical model was inversely determined using the RILEM tube test data. And the comparisons of the theoretical predictions and the test data agreed well.

Oak Ridge National Laboratory

The CoPI was Dr. Jiheon Jun, who assessed the effect of modifiers to retard O_2 and Cl^- transport in simple and aggregated concretes using EIS technique and equivalent circuit model. The effect of temperature was also estimated. The results can be summarized:

- The equivalent circuit applicable to the corroding steel in a solution-permeated concrete was suggested. This circuit consists of *R*-CPE and W_o-*R*-CPE in series connection where *R*-CPE and W_o-

R-CPE account for the impedance responses of the concrete layer and corroding steel under diffusion control, respectively.

- No satisfactory fitting was obtained between measured and modeled impedance spectra. The real impedance values at 0.1 Hz (the lower frequency limit) were used instead to compare the resistive and diffusion-related impedances associated with the transport of O_2 and Cl^-. The addition of fumed silica increased the real impedance of both simple and aggregated concretes indicating it is effective to slow down O_2 and Cl^-. Micro silica showed a significant effect in the simple concretes but not in aggregated concretes. Glycol had limited effect only in the simple concretes. Colloidal silica was least effective.

  The diffusion of O_2 and Cl^- in concrete is expected to increase by increasing temperature.

Products Developed

University of Idaho

- Respectively, Robert Blair (University of Idaho) and Batric Pesic (University of Idaho) had a poster and paper presentations at the TMS 2015 143rd Annual Meeting and Exhibition in Orlando, FL. Robert Blair applied for a grant for this trip, which he won. His poster "Doubling the Life of Concrete Structures" is uploaded in PICS. According to the notification provided by Journal of Metals (JOM, vol. 67, No. 6, 2015) our poster won the best poster award.

- Robert Blair also participated in the regional "paper night" competition organized by the local ASM Chapter. He won 3rd place. His presentation "Doubling the Life of Concrete Structures" has also been uploaded in PICS.

- At University of Idaho, Dr. Pesic (PI) travelled to Europe to present his papers at two conferences. In Paris, he presented a paper at the Global 2015 Conference. More important feature of this conference was the field trip to AREVA's nuclear fuel reprocessing plant at La Hague. This was once in a life time opportunity and Dr. Pesic is grateful to the NEUP management team for agreeing to approve this trip.

- The PI travelled to the TMS 2016 145th Annual Meeting and Exhibition in Nashville, TN, where he delivered the presentation "Transport of chloride ions through modulated concrete structures". The non-travelling co-authors were Dr. K.S. Raja, Robert Blair, Ian Ehrsam, and Jake Kline.

- The PI took all three of his students to the Materials Science & Technology 2016 Conference in Salt Lake City, UT. The students are Kline Jacob, Blair Robert, and Ehrsam Ian. They presented the papers at two symposia. Here are the titles:

  Kline, J., Pesic, B., Blair, R. and Ehrsam, I., Controlling the Permeability of Corrosion Inducing Ions in the Concrete by Nano-viscosity Modifiers: An EIS Study, Materials Science & Technology 2016, Materials Development for Nuclear Applications and Extreme Environments Symposium, Materials Science & Technology 2016, Salt Lake City, UT, October 23-27, 2016.

  Blair, R., Pesic, B., Raja, K., Ehrsam, I., Jacob Kline, Role of Admixtures in Concrete during Corrosion of Rebar: Effect of Glycerol and Silica Formulations, Materials Selection and Characterization for Corrosion Control Symposium, Materials Science & Technology 2016, Salt Lake City, UT, October 23-27, 2016.

- At the same MS&T 2016 Conference, Kline, J., Pesic, B., Raja, K., Blair, R. Ehrsam, I., had a poster presentation. The poster presenter was Jacob Kline, who won the 1st price for the best poster presentation. (A year ago Robert Blair won the best poster presentation at the TMS Conference in Orlando, Florida.) Title of the poster was "Doubling the life of concrete structures".
- In April 2016, Jacob Kline won the best paper presentation at the regional ASM Chapter. The title of the presentation was "Doubling the Life of Concrete Structures- Effect of Silica Admixtures".

- Dr. Pesic travelled to the 4th Annual International Conference on Chemistry, (July 18-21, 2016) that was held in Athens, Greece. The paper presentation was "Transport of chloride ions evaluation through modulated concrete microstructures".

- Blair, R., Pesic, B.*, Kline, J., Ehrsam, I., Raja, K., Threshold chloride concentrations and passivity breakdown of rebar steel in real concrete solution at different pH conditions with addition of glycerol, Acta Metallurgica Sinica, Springer, *(2017),* DOI 10.1007/s40195-017-0532-4 .

Colorado University-Boulder

- "Moisture transfer under Wind-Driven Rain (WDR): experimental study and theoretical model", Wang Y., and Xi Y. (2017), in preparation.

- "The effect of temperature on moisture transfer in concrete", Wang Y., and Xi Y. (2017), submitted to *Materials*.

- "Temperature dependent CTE of concrete under low temperatures", Wang Y., and Xi Y. (2017), in preparation.

- "Mori-Tanaka model for Young's modulus of concrete under low temperatures", Wang Y., and Xi Y. (2017), in preparation.

- "Experimental study on temperature dependent CTE of concrete with Nanoscale Viscosity Modifier", Wang Y., and Xi Y. (2017), in preparation.

PROJECT BACKGROUND

Objectives and Scope

The objectives of the proposed research are to:

1. Develop methods for doubling the service life of concrete structures. The *nanoscale viscosity modifiers* will be used to control transport phenomena in the conductive pathways. While viscosity modifiers will be responsible for transport properties of pore solution, another mechanism to be explored will be the reduction of pore volume. This will be achieved by addition of nano SiO2, a *nano-pozzolanic promoter* among particles of C-S-H gel2, resulting in decreased permeability.

2. Study the effect of temperature load and temperature cycling (freezing and thawing) on the conductive pathways by the proposed electrochemical methods.

3. Study the combined effect of temperature, moisture, and strong wind on the durability of concrete.

4. Exploit the DC, AC electrochemistry (EIS), and Scanning Probe Electrochemical Techniques in the methods for non-destructive evaluation of concrete performance, i.e., evaluation of concrete microstructure (conductive pathways) and hydration mechanisms.

Approach

The proposed research has been broken down into the following separate tasks.

Task A: This task is made of two distinct tasks, Task A1 and Task A2. (Dr. Pesic and Dr. Raja at UI)
In the Task A1, glycerol will be used as the nanoviscosity modifier. The expectation here is that glycerol will increase the viscosity of concrete by two fold, therefore reducing the permeability of concrete to moisture by two fold, i.e. doubling the life of concrete. The Task A2 will focus on the use of nanoscale SiO_2 as the filler of pores in concrete. The expectation is the same as with the use of glycerol- the reduction of permeability to moisture.

Task B: Effect of Temperature Differential Studies. (Dr. Y. Xi at CU-Boulder)
During cold winter conditions the ice formed on the outside wall of cylindrical concrete structure causes the outside wall expansion while the inner wall continues with its contraction.

The ensued stress causes the mechanical delamination of concrete structure. It is expected that the addition of appropriate admixtures, such as glycerol, or nanosilica, would preclude the concrete delation, i.e. the concrete wall should continuously shrink on both, the outside and the inside.

Task C: Equivalent Circuit Models for Electrochemical Impedance Spectroscopy of Concrete. (Dr. G.-L. Song at ORNL and Dr. K.S. Raja at UI).
AC electrochemical impedance spectroscopy (EIS) is a technique that can non-destructively evaluate the permeability/transport performance of concrete. EIS also directly measures the ion mobility in concrete that is responsible for the initiation of concrete degradation caused by the ingress of environmental aggressive species. Here, the EIS testing results will be fitted with the mathematical models corresponding to analog electronic circuits composed of resistors and capacitors. The value of resistors will reflect to resistance to moisture permeability via pores in present in particular concrete. The model would be able to simulate moisture transport via continuous pore path, discontinuous pore path, discontinuous point path and 'insulator' pore path. In essence, in this approach, the EIS testing and mathematical model are describing the microstructure of concrete.

Task D: Nondestructive Polarization Testing Methods of Concrete.
This task will utilize a unique approach used for the first time in the PI's laboratory. Here, the working electrode, reinforcement steel (rebar) and reference electrode are both embedded into the concrete. The counter electrode is coiled outside the cylindrical concrete specimen. By immersing the concrete specimen in water containing chloride ions the corrosion of rebar can be studied. The corrosion results provide two benefits- the corrosion performance of rebar in concrete and the permeability of concrete to moisture, i.e. chloride ion. Therefore, the corrosion method can be used to evaluate the effect of admixtures (glycerol and nanosilica) on permeability of concrete with respect to moisture.

Task E: Nondestructive Testing Methods of Permeability of Concrete.
Wind driven rain (WDR) can significantly increase the moisture content in concrete due to the high pressure of wind on the concrete surface. A freezing temperature after a WDR can turn the moisture into ice and thus damage the concrete. When RILEM tube is affixed to the concrete wall with water column 12 cm high then the water uptake by concrete simulates the category-2 hurricane. In this project, the water uptake will be studied by the RILEM tube method on the concrete prepared with the glycerol as the nanoviscosity modifier, and nanosilica concrete pore filler.

TABLE OF CONTENTS

DOUBLING THE LIFE OF CONCRETE STRUCTURES

PI: Dr. Batric Pesic, Students: Robert Blair, Ian Ehrsam and Jacob Kline

TASK A & D

Introduction

The final report discusses experimental methods, procedures and results of research on concrete permeability. Both AC and DC Electrochemical techniques were applied to study the concrete and steel environment. Observation of corrosion mechanisms and rates, allowed for better understanding of migration of moisture and ionic species through concrete. In principle, rebar corrosion is a function of moisture and corrosion inducing species (primarily chloride ion) concentration on its surface. If moisture and ions are not impeded (high permeability), they will travel through the concrete pore pathways to the steels surface and corrosion rates will be high. In contrast, if moisture and ions are impeded (low permeability) within the pore pathways the result will be later onset of corrosion and lower corrosion rates. In the second case, a steel reinforced concrete structures lifetime would be extended. Using electrochemical methods to correlate corrosion rate of rebar to concrete moisture permeability is a novel approach in that it is non-destructive to the concrete itself. In addition, more traditional destructive techniques were also applied, in which diffusion of moisture was measured by drilling into the concrete.

The research objective was reduction of concrete permeability by modulating concrete composition via selective additives. These additives included glycerol, micro silica, fumed silica and colloidal silica. Bentz et.al proposed that a concrete structure's lifetime could be doubled by increasing moisture viscosity within the porous pathways. [1] [2] This novel approach differs from more standard practices. Application of a viscosity modifier is unique since ionic ingress is reduced without physically changing pore diameter. In this study, glycerol served as a viscosity modifier to the pore solution. By increasing the viscosity of the pore solution, the migration of corrosion inducing species (Cl^-, CO_2, O_2, and H_2O) would be slowed.

Restricted permeability could also be achieved by modifying size and density of concrete pores, essentially adding a filling material to "plug" the pathways. For this second method, a range of silica additives was studied. Three species of silica were chosen, each with its own unique properties, micro silica, fumed silica and colloidal silica. These materials take part in C-S-H hydration reactions, effectively reducing pore volume and augmenting concrete density.[3][4] These silica particles could also remain within the pores after curing, "plugging" the pores and reducing available area for moisture migration. The research approach has been illustrated in Fig. A-1.

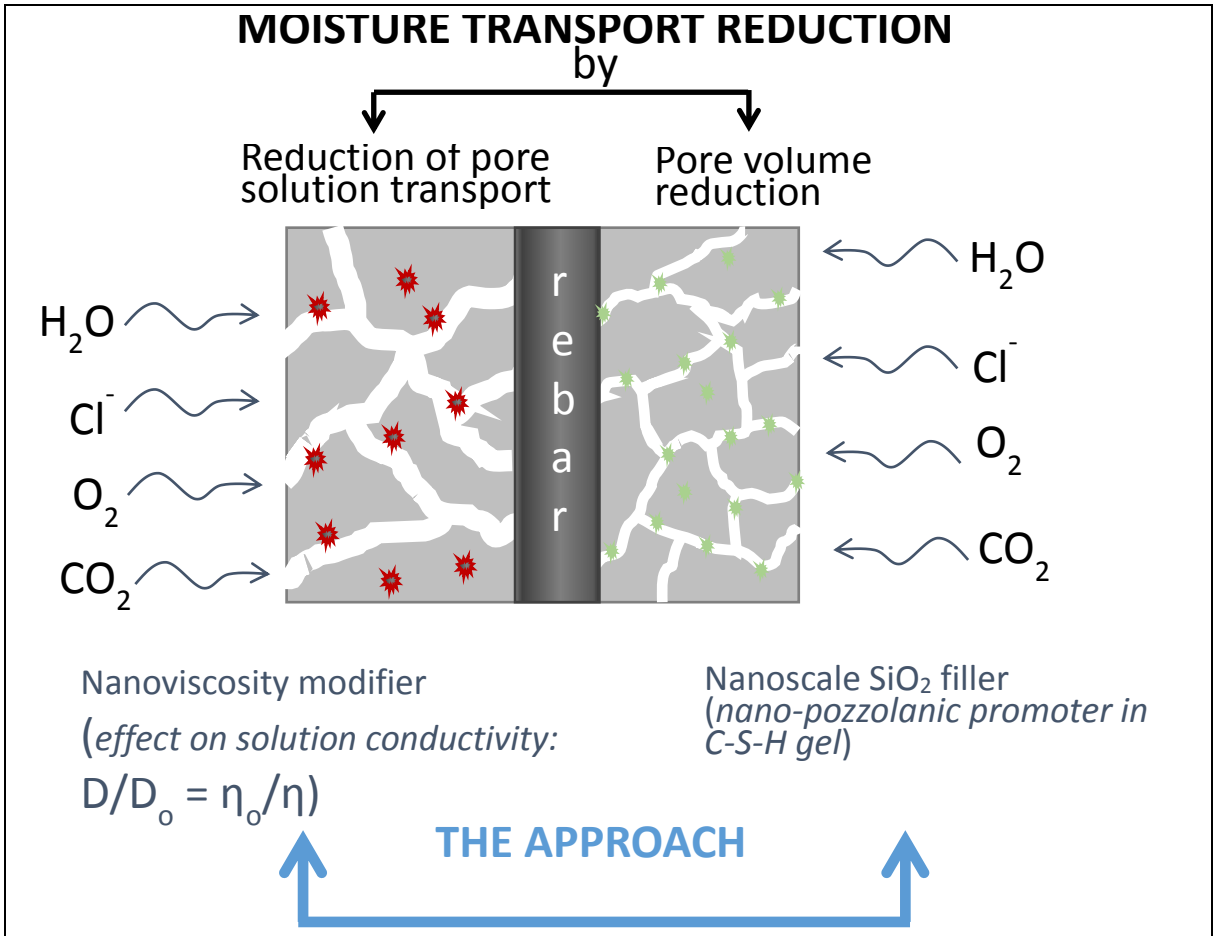

Fig. A-1 Illustration of methods used in moisture transport reduction. Left side is reduction of solution transport by viscosity adjustment. Right side is pore volume reduction with SiO_2 fillers. Also on the left side is the Bentz equation relating diffusion (D) and viscosity (η).

As previously mentioned, electrochemical (Echem) techniques were applied to measure additive effect on concrete permeability by observing steel corrosion. Echem techniques included, open circuit potential (OCP), linear polarization (LP), Tafel polarization, cyclic polarization (CP), and electrochemical impedance spectroscopy (EIS). These techniques measured corrosion mechanisms of steel in both a solid concrete matrix as well as in cement saturated solution (CSS). The CSS simulated actual concrete pore solution. The research on corrosion of reinforcement steel immersed in cement saturated solution played the role of control experiments, i.e. providing baseline comparison between steel in direct contact with cement saturated solution (CSS) and when steel is embedded in concrete.

The overall objective of the project is to reduce concrete moisture uptake and permeability to several corrosion inducing species (CO_2, H_2O, and Cl^-). However, a parallel objective is development of nondestructive techniques towards measuring corrosion rates of reinforcement steels in concrete structures. This development employed a novel use of a commercially available leak free Ag/AgCl reference electrode (see experimental procedures Section 4). Parallel to this was investigations into fully embedded silver (Ag) wires for measuring rebar corrosion. The stability of Ag voltage potential in the highly alkaline environment of concrete was tested over forty-six weeks.

SECTION 1.

ELECTROCHEMICAL ANALYSIS OF STEEL CORROSION AS A MEANS OF EVALUATION OF MOISTURE PERMEABILITY IN CONCRETE – EFFECT OF ADMIXTURES

1.1 Experimental procedures

The experimental procedure involved the electrode preparation, solution preparation and corrosion type of measurements in adequately prepared electrochemical cell. For steel embedded in concrete, the procedure involved machining (see previous reports) of steel into cylindrical shape, attachment of lead wire to the cylinder, and protection/insulation of the lead wire and cylinder ends by epoxy and heat shrinkable tubing, Fig. A-2. At this stage, to the cylinder electrode, a glass tube with 2.5mm internal diameter was affixed to the lead wire. The end of glass tube is right in the proximity of the edge of the steel cylinder, Fig A-2b. This prepared electrode then was placed and positioned in a PVC mold for casting of cement with particular composition. The composition of cement is the key parameter as it reflects the permeability modulation as the function of particular admixture.

After curing for at least 28 days, the concrete cylinder with embedded steel sample was ready for transfer to a jar for electrochemical measurements. Mo-wire coiled around the concrete cylinder served as the counter electrode. Reference electrode was introduced in the glass tubing. Each of these, steel as the working electrode, Mo wire as the counter electrode and Ag/AgCl as the reference electrode are all connected to the electrometer of the potentiostat (EG&G PAR Model 273A) for corrosion studies, Fig. A-4. It is important to state that the reference electrode (2mm diameter) was of a leak-free type, the important characteristic that ensures the absence of contamination by chloride ions by the reference electrode filling solution.

Some additional things of note, before embedding the electrodes in the concrete, the tip each glass tube was packed with cotton. The cotton serves a dual purpose, one to prevent cement from filling the end of the tube and the second to pull moisture from the concrete matrix and to create an ionic bridge between the reference electrode and steel electrodes. Furthermore, the tops of the concrete cells were covered with an AREMCO epoxy, the epoxy prevents expedient movement of salt solution down the sides of the glass tubing or lead wires.

After preparation and transfer of 3.5%wt NaCl solution, the pH before and after immersion of concrete cylinders into solution was measured. After waiting for minimum of 24hrs the reference electrode was inserted into the glass port, the electrode lead wires attached to the potentiostat (EG&G, Model 273 A) for

pertinent measurements to follow. The experiments were run in predetermined time intervals, such as 30, 90, 180 days, etc. The order of electrochemical testing was OCP followed by LP then Tafel and lastly CP.

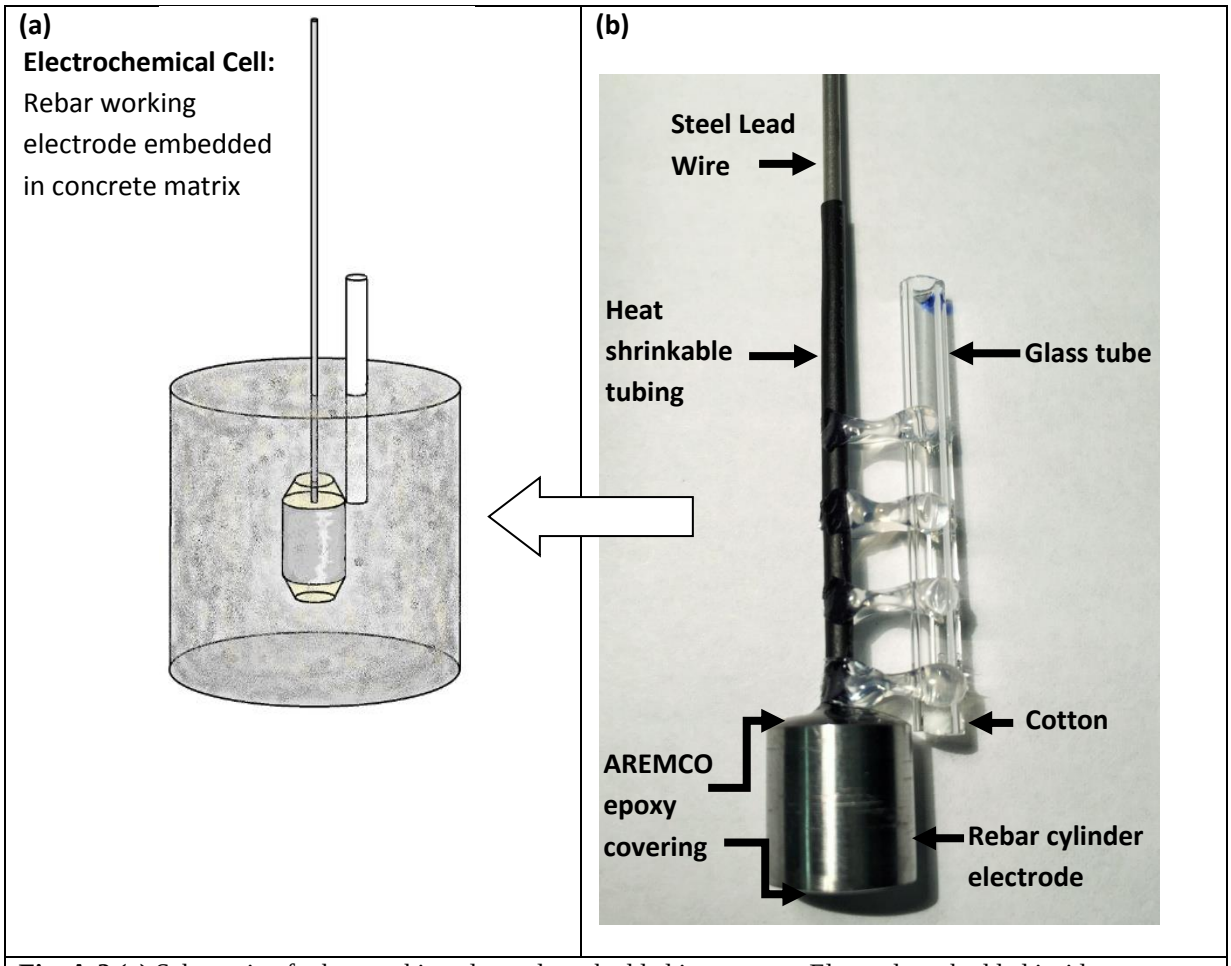

Fig. A-2 (a) Schematic of rebar working electrode embedded in concrete. Electrode embedded inside concrete matrix. **(b)** Rebar electrode ready to be cast in concrete. Glass tube provides reference electrode direct access to rebar cylinder edge.

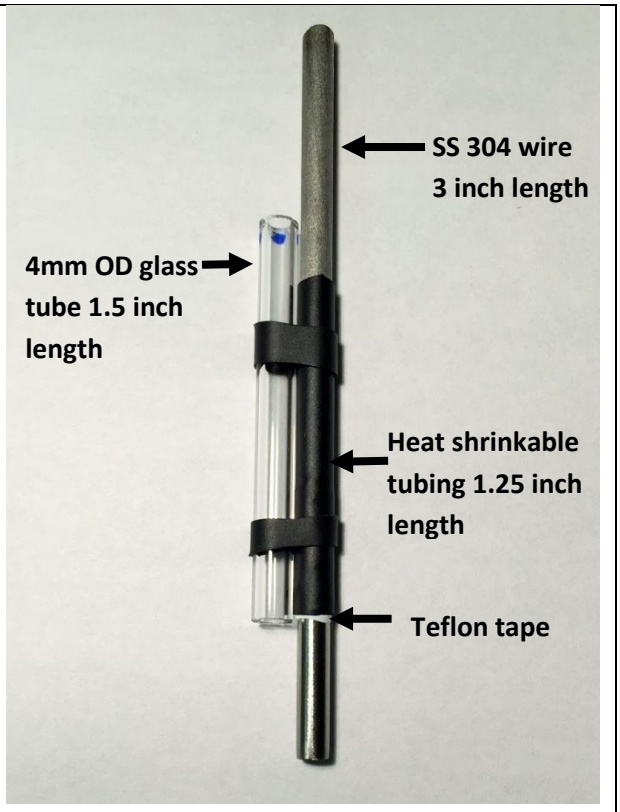

Fig. A-3 SS304 electrode ready to be cast in concrete. Glass tube provides reference electrode direct access to working electrode area.

Table 1. Experimental conditions used during corrosion studies of reinforcement steel (rebar) and stainless steel (SS304)

WE: SS304 (area 1.35 cm^2) or rebar cylinder (area 3.88 cm^2) CE: Molybdenum coil or steel wire RE: Ag/AgCl, 2mm diameter, leak free	Volume: 150ml Solution: 3.5 wt% NaCl Temp: 25^0 C Atmosphere: Air

Rebar composition – rebar supplied by Nucor Steel

Element	C	Mn	P	S	Si	Cu	Ni	Cr	Mo	V	Nb
wt%	0.41	1.23	0.017	0.044	0.20	0.25	0.08	0.15	0.019	0.0029	0.001

Experimental Parameters: The main experimental parameters were effect of additives during concrete preparation and effect of immersion time of concrete in 3.5% NaCl solution. The additives used were glycerol, micro silica, fumed silica, and colloidal silica in respective 0.5, 1.0 and 2.0 wt% amounts.

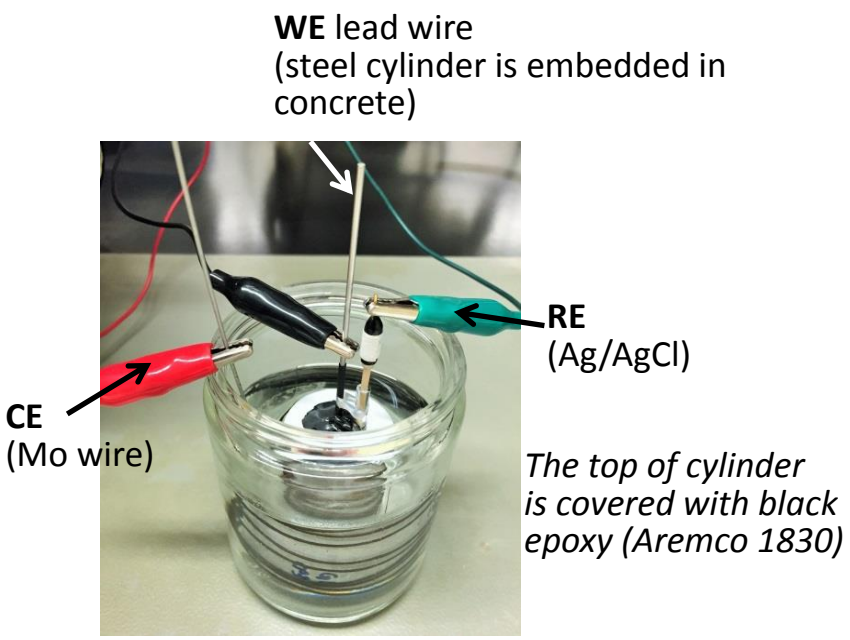

Fig. A-4 Electrochemical cell for corrosion studies of reinforcement steel (rebar) in concrete. Solution is 3.5 wt% NaCl.

1.2 Results and Discussion

1.2.1 Open Circuit Potential

OCP was studied as a function of time. Both stainless steel (SS304), Fig. A-3, and reinforcement steel (rebar), Fig. A-2, were embedded in concrete. Separate samples of concrete cells were prepared with additions of 0.5, 1.0, and 2.0 wt % glycerol, micro silica, fumed silica or colloidal silica. Each addition was introduced as wt% vs. cement binder. The control sample contains no additive.

Effect of Glycerol

Note there have been two consecutive trials for rebar encased in concrete. The results of the first trial for concrete cylinders containing the glycerol can be seen in Fig. A-5a-b, it was thought that the sudden cathodic drops in OCP were a result of poor protection of marine epoxy sealant about the glass tube used for REF electrode insertion. The second trial of samples used an AREMCO epoxy to prevent this possibility. However, redundancies in results indicate that the previous epoxy used was adequate and Cl^- arrival must be through the concrete porous pathways.

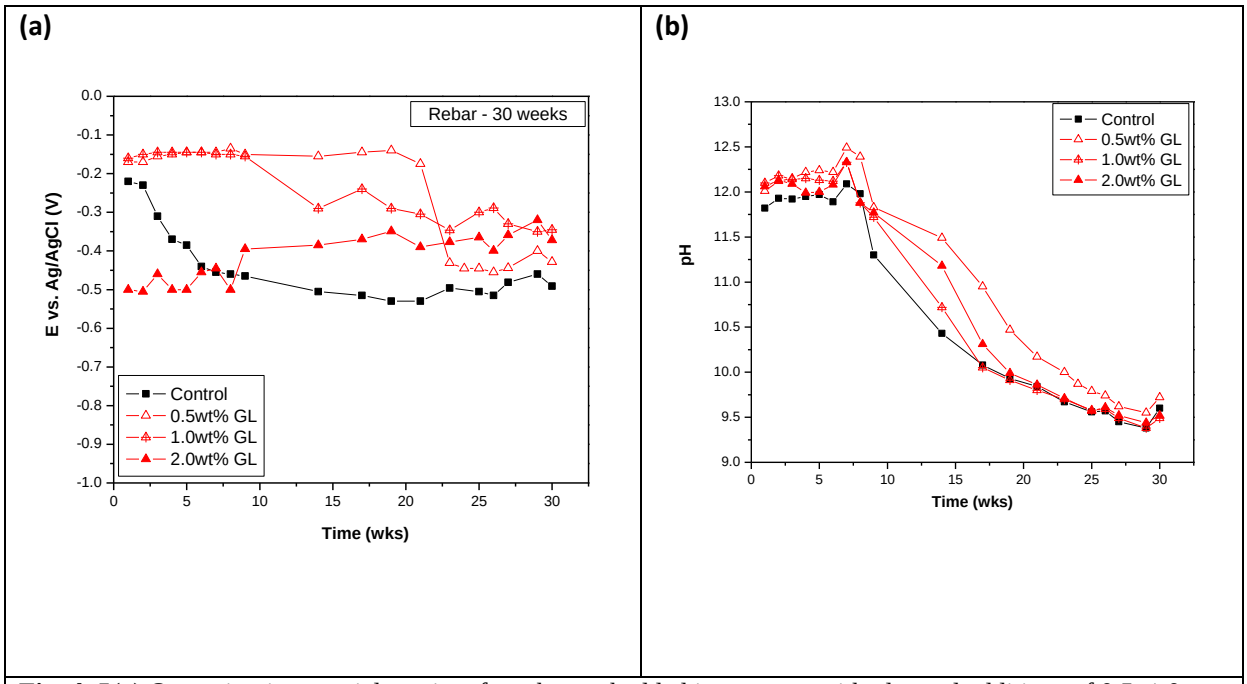

Fig. A-5(a) Open circuit potential vs. time for rebar embedded in concrete with glycerol additions of 0.5, 1.0, and 2.0 wt% (trial 1). **(b)** Variation of 3.5 wt% NaCl pH due to immersion of concrete cylinders. Concrete prepared with additions of 0.5, 1.0, and 2.0 wt% glycerol.

The resulting measurements for rebar in concrete mixed with glycerol additions can be seen in Fig. A-5a. Fig. A-5a represents OCP change for rebar over 30 weeks. For the given time interval (above) it can be seen that concrete samples containing glycerol eventually stabilize at more anodic corrosion potentials then the control experiment (no glycerol). The drop in rebar OCP for the glycerol 0.5wt% and glycerol 1.0wt% samples is most likely caused by the arrival of chloride anions to the electrode surface. This theory is supported by results for similar OCP measurements done on rebar in direct contact with saturated cement solution (see Section 2 *Corrosion of Rebar in Simulated Concrete Pore Solution: Effect of Glycerol and Silica Additives, Time, Carbonation, Oxygen Presence and Chloride Concentration*). The open circuit potentials for the rebar encased in concrete with glycerol 2.0wt%, differ from 0.5wt% and 1.0wt% results. Starting at an open circuit potential of -0.5V suggests that at this concentration of 2.0wt%, glycerol does not inhibit Cl^- migration through the concrete. However, as time progresses the potential moves more anodic. This could indicate either a slowing of Cl^- arrival, the development of a passive film, or formation of a glycerol chloride complex. Further research is needed to identify glycerol's role in the C-S-H chemistry. Note, concrete is characterized with a high pH property; the pH of the 3.5 wt% immersion solution was monitored in tandem with the open circuit potential. The results vary between pH 12.5 and 9.5. The drop in pH, Fig. A-5b, is most likely from carbonic acid formation due to carbon dioxide arrival.

The results of the second trial, including both rebar and SS 304 can be seen in Fig. A-6. For the second trial, the maximum concentration of glycerol added was 1.0wt%. Concentrations of glycerol at 2.0wt% were removed to limit the number of samples made and save time.

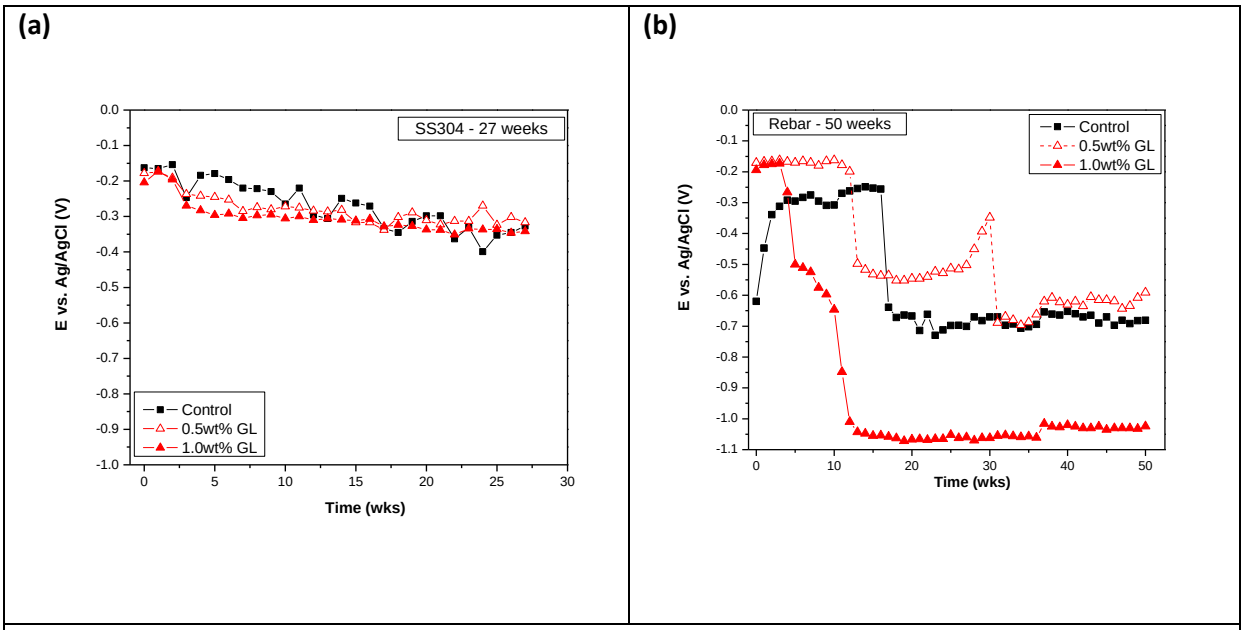

Fig. A-6 (a) Open circuit potential vs. time of SS304 and **(b)** rebar embedded in concrete with glycerol additions of 0.5 and 1.0 wt%.

The graphs above were for SS304 and rebar (trial 2) electrodes embedded in concrete. For the given time interval of 27 weeks, SS304 samples in concrete containing glycerol admixture have cathodic (negative) trending open circuit potentials. The drop in OCP for these samples is approximately -0.100V, Fig. A-6a. The OCP results for rebar in concrete containing glycerol additions can be seen in Fig. A-5b-a. Fig. A-6b represents OCP change over 50 weeks. In the case of rebar embedded in concrete with glycerol 1.0wt% admixture, the OCP stabilized at approximately -1.5V. Note the potential is so low that the rebar specimen is nearing cathodic protection. It could be the glycerol molecules OH^- functional groups factor into such negative potentials. However, the mechanism influencing open circuit potential variance needs further determination. Addition of glycerol at 0.5wt% holds OCP at a stable potential of approximately -0.15V for up to 15 weeks in sodium chloride solution. After 15 weeks the OCP drops to approximately -0.5 volts and is stable for 10 more weeks before showing a gradual increase in the anodic (positive) direction followed by a dramatic spike downwards to a more negative potential of -0.6V. This behavior could be related to a passive film endeavoring to reform ensued by an increase in the chloride concentration and reinitiating of active corrosion. The control (no glycerol) experiment of rebar

embedded in concrete, exhibited similar OCP trends to rebar in concrete containing 0.5wt% glycerol admixture.

The drop in rebar OCP for the glycerol 0.5wt% (G05) and glycerol 1.0wt% (G1) modulated concrete is likely caused by arrival of chloride anions to the electrode surface. This theory is supported by results for similar OCP measurements done on rebar in direct contact with saturated cement solution. The control samples starting open circuit potential of -0.65V suggests little to no inhibition of Cl^- migration through the concrete. However, as time progresses the potential moves more anodic. This could indicate either a slowing of Cl^- arrival or the development of a passive film at the steel concrete interface.

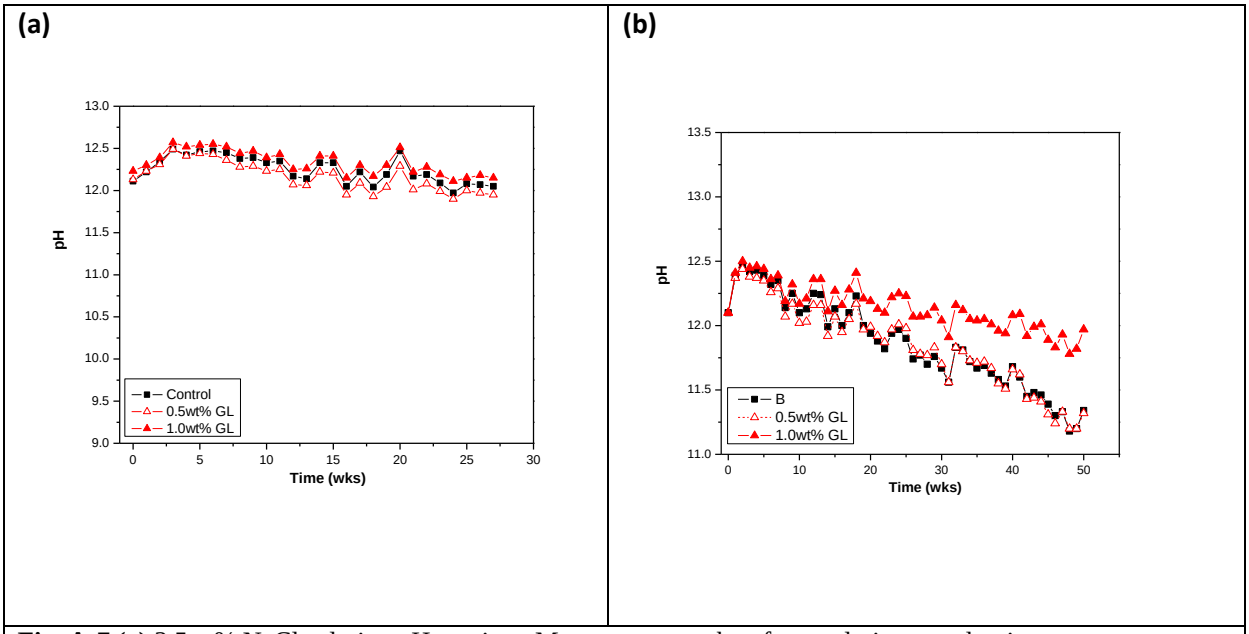

Fig. A-7 (a) 3.5wt% NaCl solution pH vs. time. Measurements taken from solutions used to immerse concrete cells with glycerol admixtures and SS304 embedded. **(b)** pH variation of 3.5wt% NaCl solution vs. time. Measurements taken from solutions used to immerse concrete cells with glycerol admixtures and rebar embedded.

Again, pH of the 3.5 wt% immersion solution was monitored in tandem with open circuit potential. These results vary between pH 12.5 and 11.5, Fig. A- 7a-b. Decrease in pH is accredited to carbonation (CO_2) reactions within the cement resulting in formation of carbonic acid and calcium carbonate. The concrete containing 1.0wt% glycerol shows a slower decrease in pH then that of concrete with 0.5wt% glycerol and concrete which contained no admixture (control), Fig. A-7b. The increase viscosity of glycerol could be limiting the kinetics of the carbonation reactions.

Effect of Micro, Fumed, and Colloidal Silica

The resulting OCP measurements for rebar in concrete containing silica additions can be seen in Fig. A-8a and Fig A-8b. Fig. A-8a shows the potential change with time for the first set of rebar samples over 12 weeks. The potentials during this time were mostly stable. However, there are large potential differences dependent upon the admixtures present. For instance, the potential measured on rebar in 1.0wt% fumed silica concrete has a potential around -0.550V vs. -0.300V potential for rebar in 0.5wt% micro silica concrete, Fig. A-8a. Fig. A-8b shows that over 20 weeks rebar embedded in concrete samples containing colloidal and micro silica 0.5wt% have stable OCP values around -0.2V. After 20 weeks the rebar embedded in 0.5wt% micro silica concrete shows a cathodic drop in OCP. The other samples all show OCP that have moved significantly in the cathodic direction. There are several noticeable cases in which the OCP drops abruptly to about -0.5V or more. This drop is believed to indicate the arrival of chloride anions (Cl^-) to the rebar's surface.

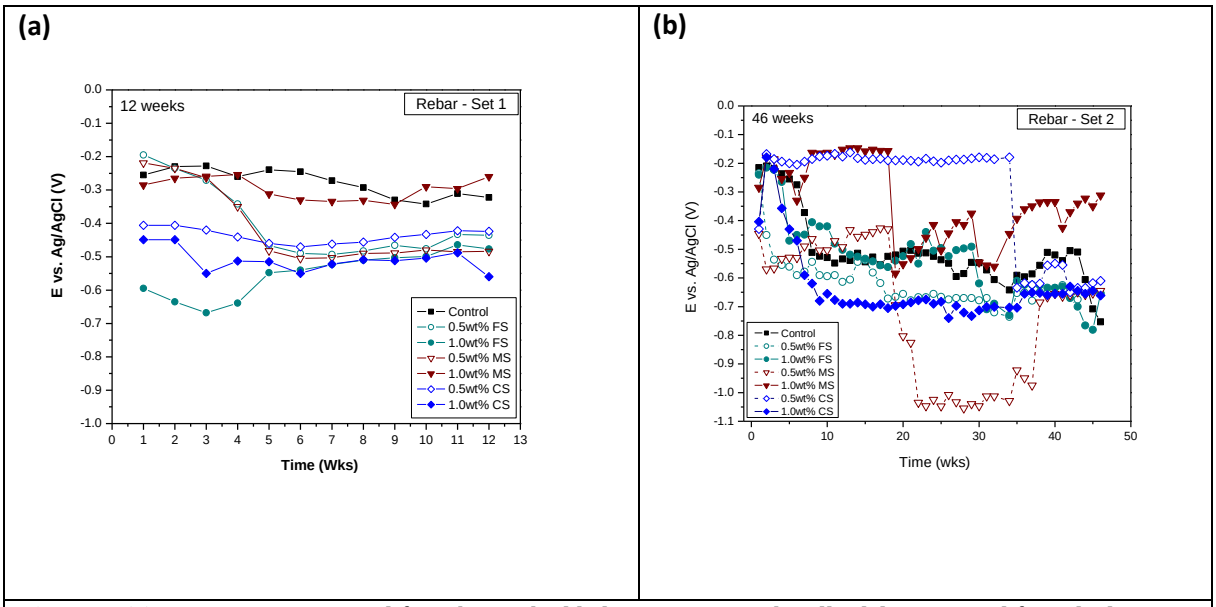

Fig. A-8 (a) Open circuit potential for rebar embedded in concrete with colloidal, micro and fumed silica admixtures for 12 weeks (rebar set 1) and **(b)** 46 weeks (rebar set 2). Concrete was immersed in 3.5wt% NaCl salt solution.

Fig. A-9a-b show the pH over time produced by concrete containing the silica admixtures with rebar embedded. The drop in pH seen in Fig. A-9a is most likely from the formation of carbonic acid due to carbon dioxide arriving from the air. Again, pH shows no relation to the OCP change.

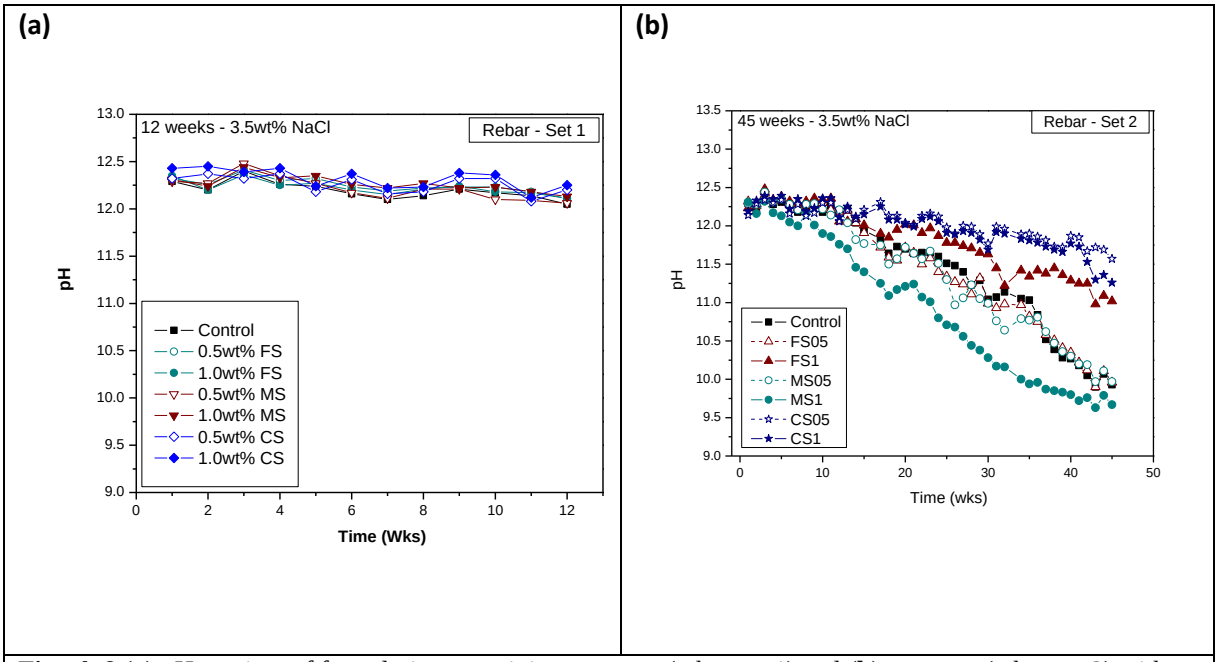

Fig. A-9 (a) pH vs. time of for solution containing concrete (rebar set 1) and **(b)** concrete (rebar set 2) with colloidal, micro and fumed silica admixtures. Note these sample sets are the same as those seen in Fig. 8a-b.

The resulting OCP measurements for SS 304 in concrete containing silica additions can be seen in Fig. A-10a-b. For the given time intervals it can be seen that concrete samples containing micro silica and fumed silica admixtures follow the same cathodic trending open circuit potential (OCP) as the control sample (no admixture). The drop in OCP for these samples is approximately -0.100V. The samples containing colloidal silica additive show the most stable open circuit potential, constant for twenty weeks, Fig. A-10b. This could suggest that colloidal silica is filling the porous pathways of the concrete matrix reducing the navigation of anions or is a functional contributor to thin film formation on the stainless steel. The mechanism influencing the variance in open circuit potentials needs further determination. Note the measurements in Fig. A-10a and 10b come from two separate and independent sample series, one to have electrochemical test run after 180 days immersed in solution the other to have tests run after 90 days. Duplicate samples were used to provide reproducibility of results.

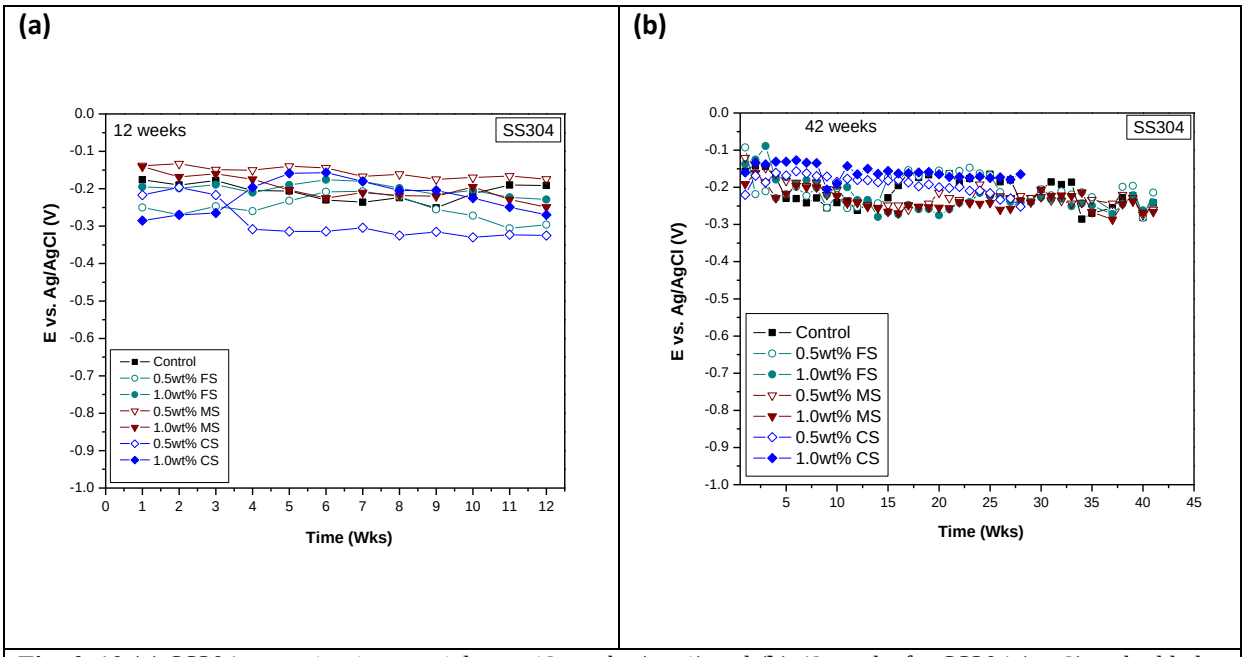

Fig. A-10 (a) SS304 open circuit potential over 12 weeks (set 1) and **(b)** 42 weeks for SS304 (set 2) embedded in concrete with colloidal, micro and fumed silica admixtures. Note, colloidal silica parameter was only measured out to 27 weeks (see report on cyclic polarization).

Concrete is characterized with a high pH property; the pH of the 3.5 wt% immersion solution was monitored in tandem with the open circuit potential. The results vary in a range between pH 11.0 and 12.5. Fig. A-11a-b show the pH over time produced by concrete containing the silica admixtures with SS304 embedded. The drop in pH seen in Fig. A-11b is most likely from the formation of carbonic acid due to carbon dioxide arriving from the air. Currently decreasing pH shows no relation to changes in OCP.

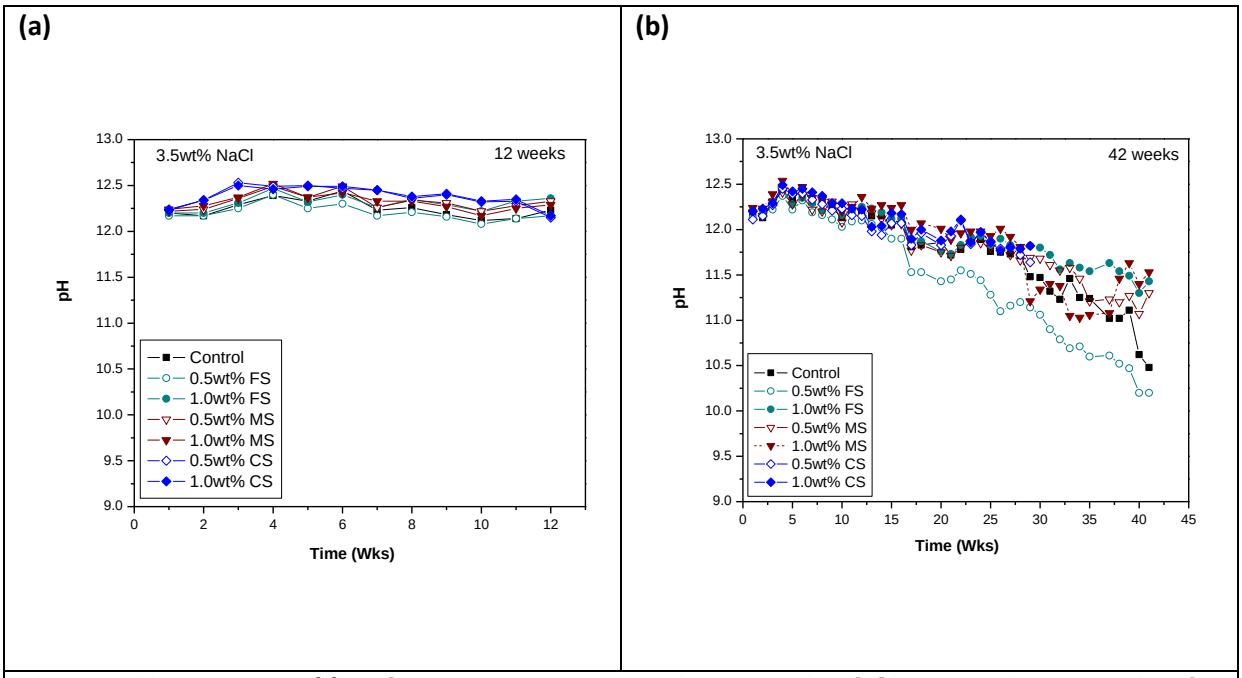

Fig. A-11 (a) pH vs. time of for solution containing concrete (SS304 set 1) and **(b)** concrete (SS304 set 2) with colloidal, micro and fumed silica admixtures. Note these sample sets are the same as those seen in Fig. 10a-b.

1.2.2 Linear and Tafel Polarization

Effect of Glycerol

A main objective of the current research is development of nondestructive techniques for modulating the permeability of concrete to moisture. In this respect, linear (LP) and Tafel polarization methods have been applied. The governing principle of this approach is that reinforcement steel and stainless steel are susceptible to corrosion from arrival of chloride ions through concretes porous pathways. The more chloride and other corrosion inducing species being transported by moisture to the rebar surface the weaker the resistance to corrosion. This polarization resistance (Rp) is synonymous to corrosion resistance. Both linear and Tafel polarization can evaluate polarization resistance of rebar and stainless steel embedded in concrete. LP and Tafel also provide the corrosion potential E_{corr} and corrosion current $i_{corr\ values}$ for the rebar and stainless steel embedded in concrete.

By monitoring Rp values with respect to time, permeability of concrete should be measurable. If glycerol slows the arrival of the corrosion inducing species, corresponding decreases in corrosion currents and increases in Rp values would be seen.

For the LP tests the potentiostat began WE polarization at -25mV from OCP and increased the potential at 0.166 mV/sec to a potential +25mV from OCP. The resulting graphs display linear sections through open

circuit potential and zero current (equilibrium), with a definable slope. The slope of this line is the resistance to polarization $R_p = \Delta E/\Delta i$. The greater the resistance to polarization the greater resistance to corrosion. In cases where no linear region was found, the slope of a tangent line using the 10 nearest data points each side of equilibrium, was used to extrapolate the resistance to polarization. An example LP graph is shown in Fig. A-12d, tangent extrapolation red line with slope values in upper left hand corner. Results for LP testing are summarized in Tables 2 and 3.

The Tafel tests function similar to LP tests however on a wider potential range. Instead of ± 25mV tests are run ± 250mV from OCP. Tafel tests are used to determine the Tafel coefficients β_a and β_c as well as the corrosion potential and corrosion current E_{corr} and i_{corr}. After Tafel tests are run Stern and Geary equation $i_{corr} = [1/2.303Rp][(\beta_a\beta_c)/(\beta_a+\beta_c)]$, can be utilized to solve for corrosion resistance or for corrosion current, depending on known values. Using the known values of i_{corr}, β_a and β_c, the resistance R_p can be calculated. The results of Tafel polarization are shown in Figures 16a-c. Electrochemical interpretation of the Tafel tests are tabulated, Tables 4 and 5.

Note, there were two separate experimental trials for rebar embedded in concrete. Tafel polarization results come from the first trial. As discussed previously the samples of this first trial had PC11 type marine epoxy to prevent solution wetting of the lead wire and glass tube for REF electrode insertion. A second series of samples were produced in which AREMCO epoxy was used to seal the top of the concrete cylinders. LP results come from this second series of samples in which SS 304 was studied along with rebar.

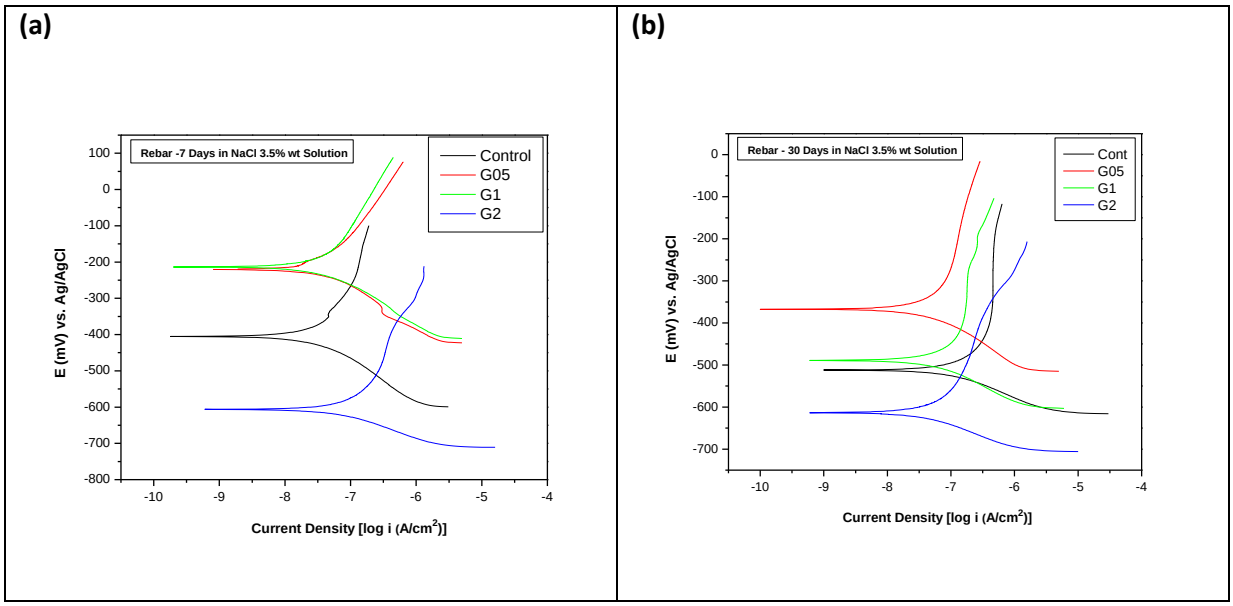

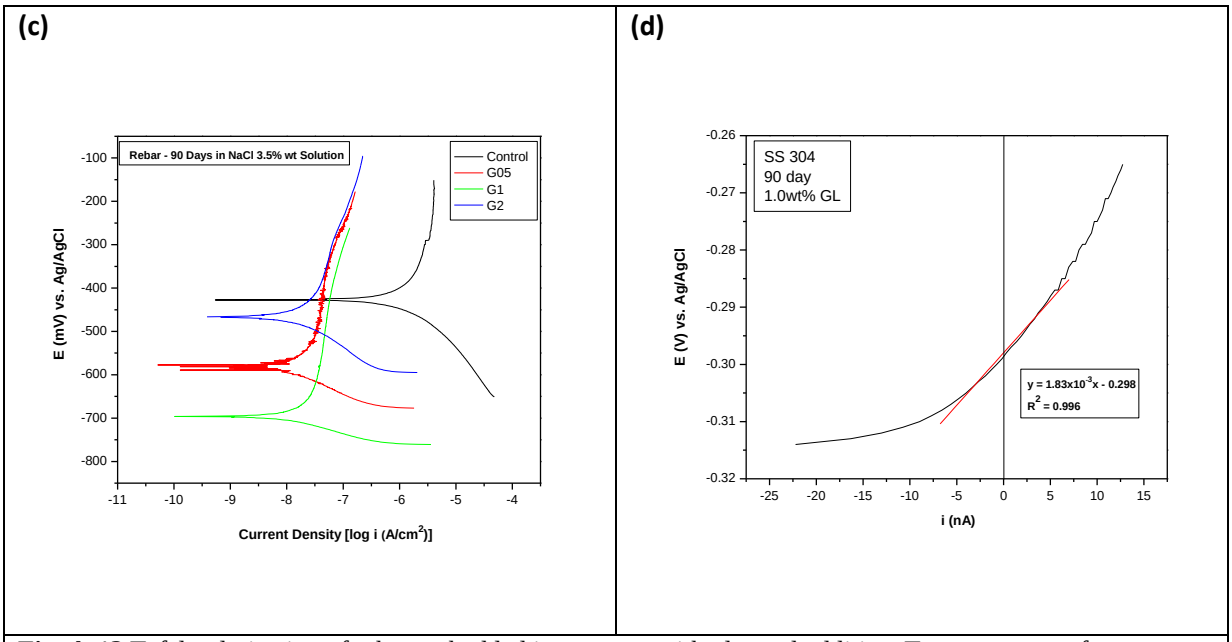

Fig. A-12 Tafel polarization of rebar embedded in concrete with glycerol additive. Tests were run after concrete had been immersed in simulated sea water (NaCl 3.5wt %) for **(a)** 7 days **(b)** 30 days and **(c)** 90 days. **(d)** Linear polarization of SS304 embedded in concrete with glycerol 1.0% admixture. Tests were run after concrete had been immersed in simulated sea water (NaCl 3.5wt %) for 90 days. Plot shows region used for Rp calculations.

Table 2. Tabulated values for Tafel polarization of rebar embedded in concrete, immersed in 3.5wt% NaCl for 7 days.

Admixture (%)	Exposure (days)	OCP (mV)	E_{corr} (mV)	I_{corr} ($\mu A/cm^2$)	R_p ($K\Omega \cdot cm^2$)	β_a (mV/decade)	β_c (mV/decade)
Control	7	-355.00	-408.78	0.1577	204.54	169.60	132.32
Glycerol	7	-175.00	-233.61	0.04159	827.24	259.80	114.00
Glycerol	7	-165.00	-216.12	0.04299	840.45	299.93	115.15
Glycerol	7	-465.00	-610.62	0.0658	134.03	29.87	63.55

Table 3. Tabulated values for Tafel polarization of rebar embedded in concrete, immersed in 3.5wt% NaCl for 30 days.

Admixture (%)	Exposure (days)	OCP (mV)	E_{corr} (mV)	I_{corr} ($\mu A/cm^2$)	R_p ($K\Omega \cdot cm^2$)	β_a (mV/decade)	β_c (mV/decade)
Control	30	-370.00	-513.58	0.094	106.75	36.92	62.38
Glycerol	30	-270.00	-377.20	0.0659	287.28	75.76	103.3
Glycerol	30	-360.00	-490.18	0.0544	232.14	46.76	76.93
Glycerol	30	-460.00	-615.92	0.0316	214.61	22.11	53.48

Table 4. Tabulated values for Tafel polarization of rebar embedded in concrete, immersed in 3.5wt% NaCl for a minimum 90 days.

Admixture (%)	Exposure (days)	OCP (mV)	E_{corr} (mV)	I_{corr} ($\mu A/cm^2$)	R_p ($K\Omega \cdot cm^2$)	β_a (mV/decade)	β_c (mV/decade)
Control	108	-405.00	-436.48	2.377	14.63	115.3	163.5
Glycerol	108	-430.00	-584.8	0.07508	367.244	469.6	73.45
Glycerol	103	-515.00	-698.36	0.0082	412.51	10.11	33.99
Glycerol	110	-350.00	-467.16	0.0171	851.93	53.59	89.73

The results of the Tafel polarization tests are separated by exposure time of concrete cell to 3.5wt% NaCl solution. At all three test times (7, 30, and 90 days) Rebar embedded in concrete containing glycerol admixtures exhibited lower corrosion currents and higher resistance to polarization then the control sample (no glycerol). However, low cathodic corrosion potentials and OCP indicative of chloride presence suggests, glycerol could be serving as a corrosion inhibitor instead of decreasing permeability.

Table 5. Tabulated values for linear polarization of SS 304 and rebar embedded in concrete, immersed in 3.5wt% NaCl solution for 30 and 90 day testing times.

SS 304				Rebar			
Admixture (%)	Exposure (days)	OCP (V)	Rp (KΩ)	Admixture (%)	Exposure (days)	OCP (V)	Rp (KΩ)
Control	30	-0.255	782	Control	30	-0.178	4910
Glycerol 0.5%	30	-0.214	726	Glycerol 0.5%	30	-0.330	1520
Glycerol 1.0%	30	-0.300	522	Glycerol 1.0%	30	-0.448	606
SS 304				Rebar			
Admixture (%)	Exposure (days)	OCP (V)	Rp (KΩ)	Admixture (%)	Exposure (days)	OCP (V)	Rp (KΩ)
Control	90	-0.229	822	Control	90	-0.729	595
Glycerol 0.5%	90	-0.260	6920	Glycerol 0.5%	90	-0.541	466
Glycerol 1.0%	90	-0.290	1830	Glycerol 1.0%	90	-0.523	432

The results for linear polarization were inconclusive. There is no discernable effect of glycerol addition to concrete and its effect on polarization resistance for the steel electrodes. Difficulty in LP measurements for steel embedded in concrete could result from the high pH environment. The large number of

hydroxides present in concrete could be forming an OH^- barrier on the rebar and SS 304 surfaces, interfering with sensitive LP measurements making the results difficult to interpret.

Effect of Micro, Fumed, and Colloidal Silica

The values of E_{corr} and i_{corr} were determined allowing the evaluation of silica additives. The example LP measurements for SS 304 in concrete containing silica additions can be seen in Fig. A-13a-d. LP measurements for SS 304 embedded in concrete with micro and colloidal silica additions are similar to that of the control sample when immersed for 90 days in salt water. Polarizations for the fumed silica, Fig. A-13b, parameter show ideal linearity compared to the polarizations of samples with micro, colloidal or control parameters. Table 10 contains the OCP and Rp values calculated from LP measurements, for SS 304 in concrete immersed in salt water for 30 and 90 days. The Rp values were lower at 90 days for control but concrete with silica additives remained mostly the same. This could mean that the silica additives are providing a longer and higher resistance to corrosion on SS304 steel.

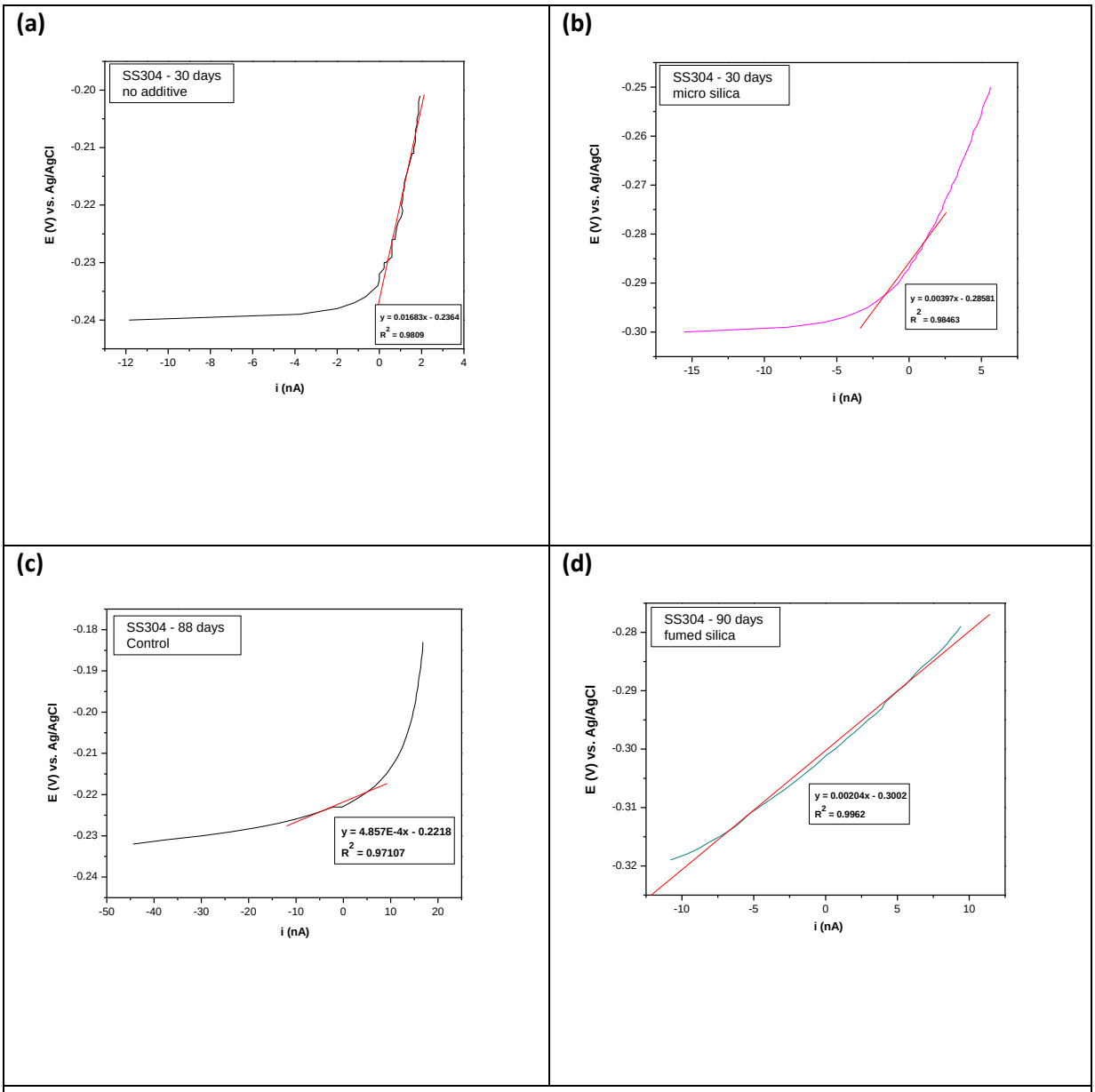

Fig. A-13 Linear polarization of SS304 embedded in concrete with **(a)** no silica admixture (control) and with **(b)** micro silica admixture. Tests were run after concrete had been immersed in simulated sea water (NaCl 3.5wt %) for 30 days. Samples containing colloidal and fumed silica exhibited similar LP graphs. Linear polarization of SS304 embedded in concrete with **(c)** no silica (control) and **with (d)** Fumed silica admixture. Test were run after concrete had been immersed in simulated sea water (NaCl 3.5wt %) for 90 days.

Table 6. Tabulated values for linear polarization of SS 304 embedded in concrete, immersed in 3.5wt% NaCl solution for 30 and 90 day testing times.

SS 304			
Admixture (%)	Exposure (days)	OCP (V)	Rp (KΩ)
Control	30	-0.209	48.4
Colloidal Silica 0.5 wt%	30	-0.184	4040
Colloidal Silica 1.0 wt%	30	-0.227	8160
Fumed Silica 0.5 wt%	30	-0.293	41.8
Fumed Silica 1.0 wt%	30	-0.256	2430
Micro Silica 0.5 wt%	30	-0.180	2090
Micro Silica 1.0 wt%	30	-0.277	3970
SS 304			
Admixture (%)	Exposure (days)	OCP (V)	Rp (KΩ)
Control	90	-0.223	16830
Colloidal Silica 0.5 wt%	90	-0.342	965
Colloidal Silica 1.0 wt%	90	-0.276	1040
Fumed Silica 0.5 wt%	90	-0.230	2450
Fumed Silica 1.0 wt%	90	-0.301	2040
Micro Silica 0.5 wt%	90	-0.171	1450
Micro Silica 1.0 wt%	90	-0.201	237

Example LP measurements for rebar in concrete containing silica additions can be seen in Fig. A-14a-d. LP measurements for rebar embedded in concrete with control, micro, fumed and colloidal parameters were taken after 30 and 90 days of salt water immersion. Table 7 contains the OCP and Rp values from LP measurements. All Rp values were about the same at 90 days as they were at 30 days.

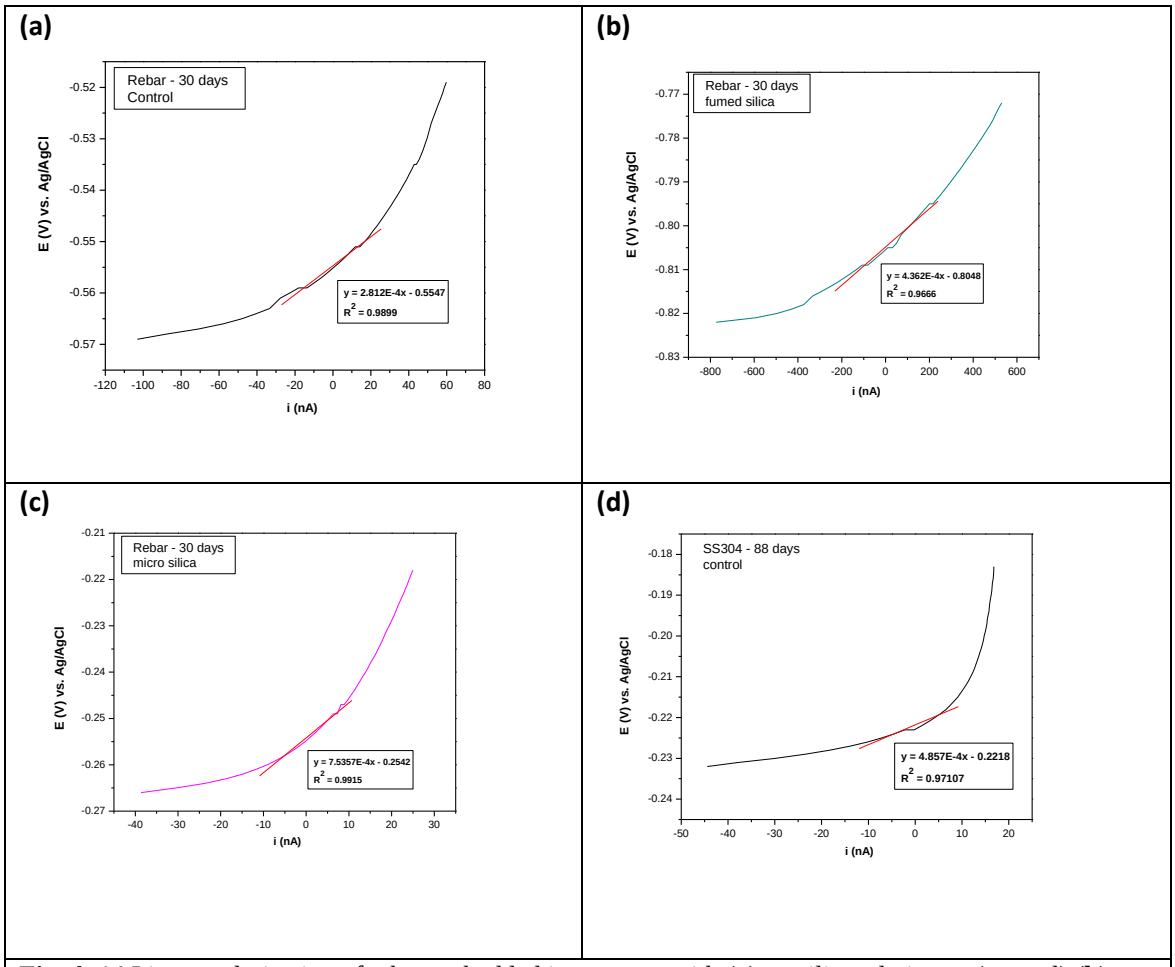

Fig. A-14 Linear polarization of rebar embedded in concrete with **(a)** no silica admixture (control) **(b)** with fumed silica and **(c)** with micro silica additives. Test were run after concrete had been immersed in simulated sea water (NaCl 3.5wt %) for 30 days. **(d)** Linear polarization of SS 304 embedded in concrete with no silica admixture. Test was run after concrete had been immersed in simulated sea water (NaCl 3.5wt %) for 90 days.

Table 7. Tabulated values for linear polarization of rebar embedded in concrete, immersed in 3.5wt% NaCl solution for 30 and 90 day testing times.

Rebar			
Admixture (%)	Exposure (days)	OCP (V)	Rp (KΩ)
Control	30	-0.314	99.9
Colloidal Silica 0.5 wt%	30	-0.200	477
Colloidal Silica 1.0 wt%	30	-0.540	651
Fumed Silica 0.5 wt%	30	-0.420	70.3
Fumed Silica 1.0 wt%	30	-0.456	31.3
Micro Silica 0.5 wt%	30	-0.494	38.2
Micro Silica 1.0 wt%	30	-0.244	75.4
Rebar			
Admixture (%)	Exposure (days)	OCP (V)	Rp (KΩ)
Control	90	-0.546	28.1
Colloidal Silica 0.5 wt%	90	-0.418	184
Colloidal Silica 1.0 wt%	90	-0.579	159
Fumed Silica 0.5 wt%	90	-0.559	26.3
Fumed Silica 1.0 wt%	90	-0.799	43.6
Micro Silica 0.5 wt%	90	-0.554	34.8
Micro Silica 1.0 wt%	90	-0.490	21.9

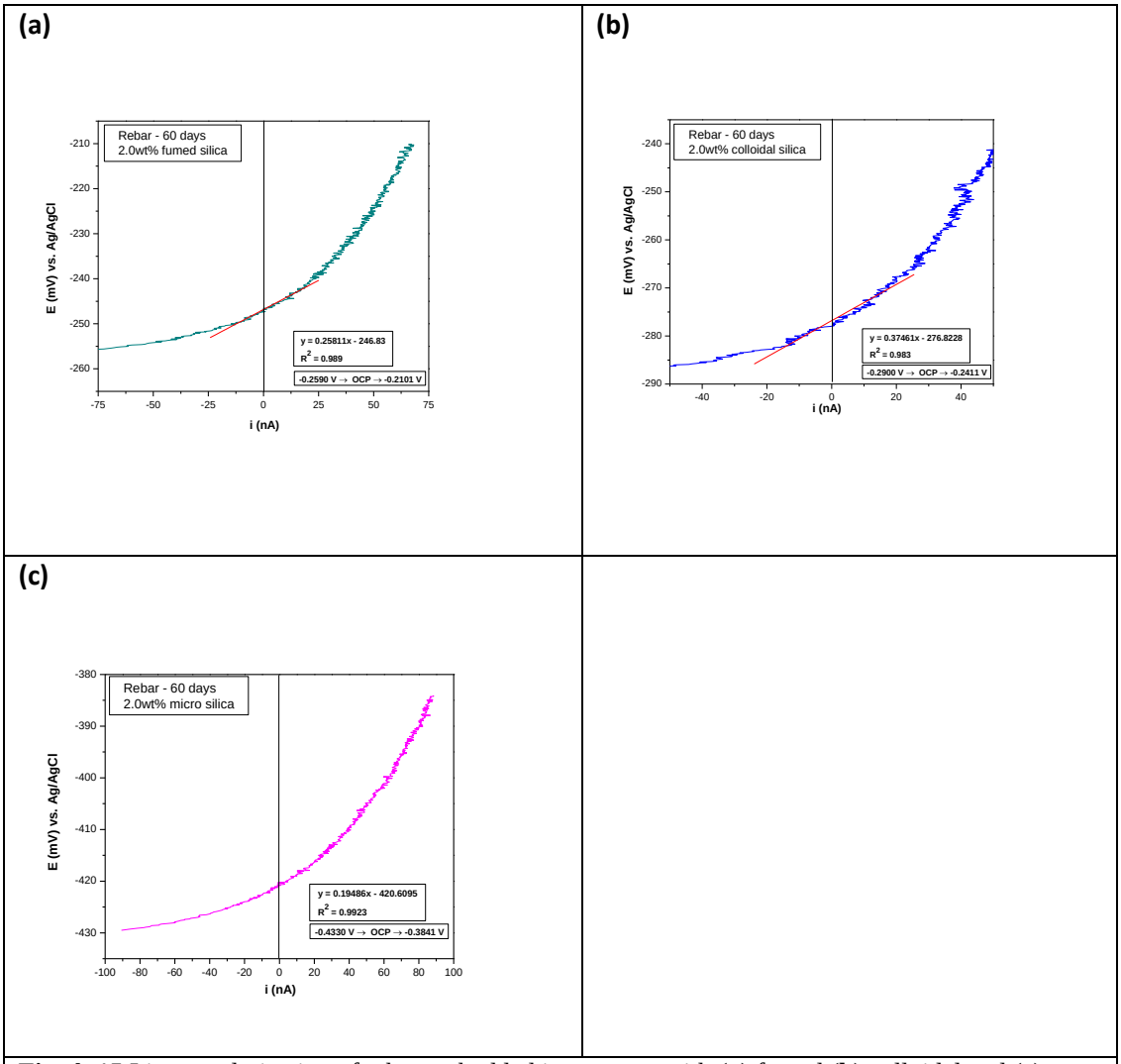

Fig. A-15 Linear polarization of rebar embedded in concrete with **(a)** fumed **(b)** colloidal and **(c)** micro silica additive. Test were run after concrete had been immersed in simulated sea water (NaCl 3.5wt %) for 60 days.

The resulting Tafel measurements for rebar in concrete containing silica additions can be seen in Fig. A-16a-c and Fig. A-17a-c. Fig. 20a-b show the Tafel polarizations after concrete had been immersed in simulated sea water (NaCl 3.5wt %) for 90 days. Tables 8 and 9 contain the values of Tafel measurements for rebar in concrete after immersion in salt water for 7 and 90 days, receptively. The fumed silica parameter at both 7 and 90 days showed the lowest corrosion rate and highest resistance to polarization. For 90 day of immersion in salt water only fumed and colloidal silica parameters showed improvement compared to the control.

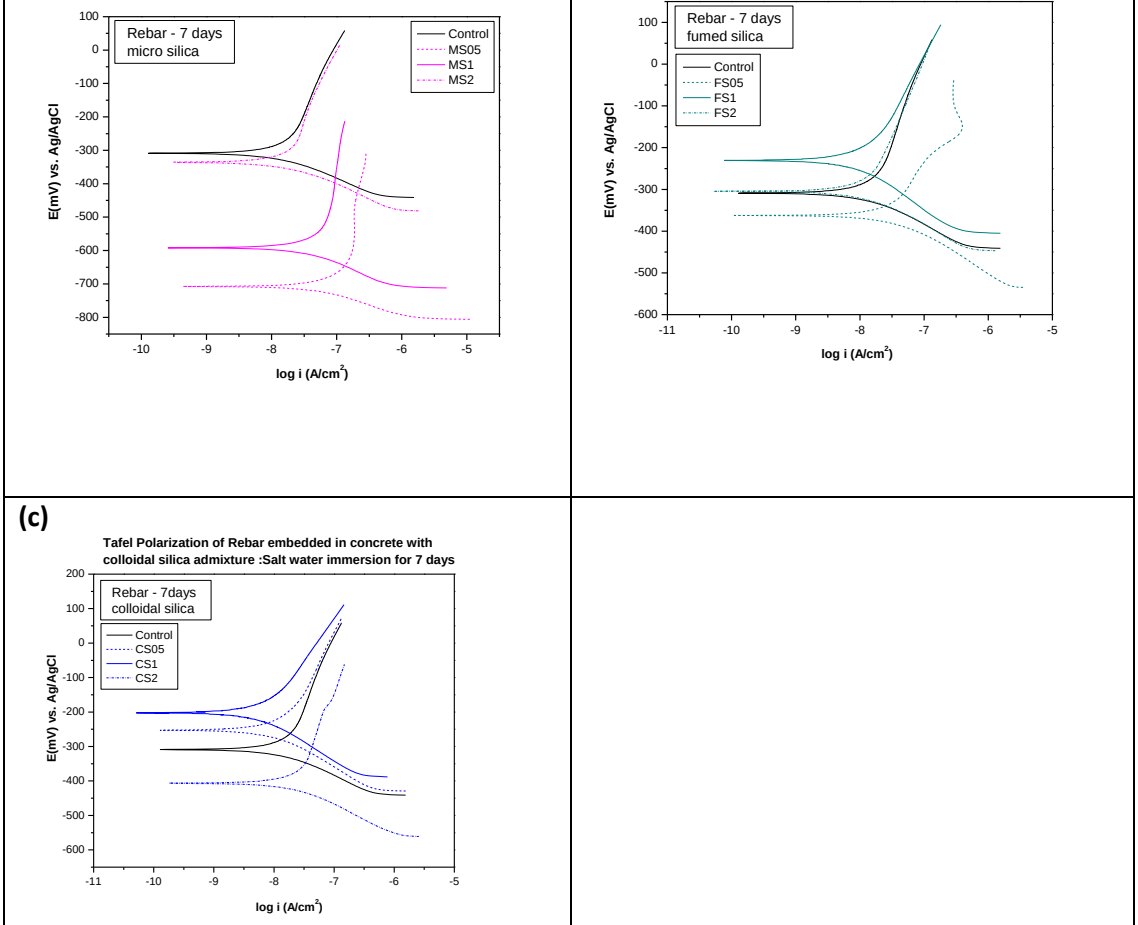

Fig. A-16 Tafel polarization of rebar embedded in concrete with **(a)** micro **(b)** fumed and **(c)** colloidal silica additive. Tests were run after concrete had been immersed in simulated sea water (NaCl 3.5wt %) for 7 days.

Table 8. Tabulated values for Tafel polarization of rebar embedded in concrete, immersed in 3.5wt% NaCl for a 7 days.

Admixture (%)	Exposure (days)	OCP (mV)	E_{corr} (mV)	I_{corr} ($\mu A/cm^2$)	R_p ($K\Omega \cdot cm^2$)	β_a (mV/decade)	β_c (mV/decade)
Control	7	-355.00	-408.78	0.1577	204.54	169.60	132.32
Colloidal Silica 0.5%	7	-185.00	-271.79	0.01417	2451.16	356.38	103.14
Colloidal Silica 1.0%	7	-145.00	-217.11	0.00641	4827.96	240.38	103.41
Colloidal Silica 2.0%	12	-315.00	-416.97	0.02599	1245.74	534.95	86.64
Fumed Silica 0.5%	9	-290.00	-360.19	0.02933	971.64	234.96	91.07
Fumed Silica 1.0%	9	-160.00	-251.33	0.01193	2809.43	293.73	104.70
Fumed Silica 2.0%	8	-215.00	-312.25	0.01312	2229.11	364.50	82.62
Micro Silica 0.5%	14	-560.00	-728.04	0.08491	294.11	766.11	62.18
Micro Silica 1.0%	14	-470.00	-621.78	0.06539	523.39	1447.09	83.36
Micro Silica 2.0%	12	-235.00	-333.77	0.01500	2011.16	409.409	83.675

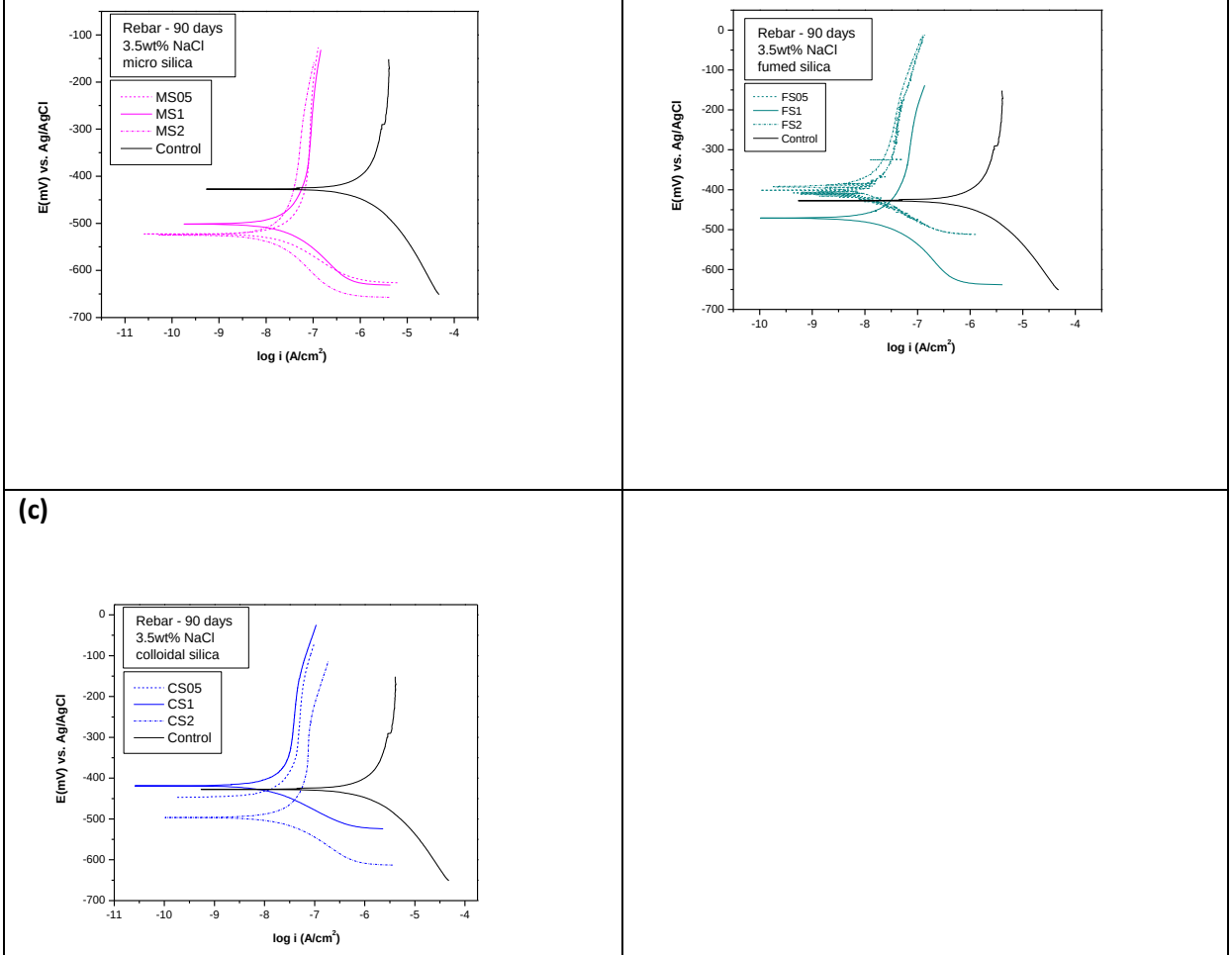

Fig. A-17 Tafel polarization of rebar embedded in concrete with **(a)** micro **(b)** fumed and **(c)** colloidal silica additive. Tests were run after concrete had been immersed in simulated sea water (NaCl 3.5wt %) for 90 days.

Table 9. Tabulated values for Tafel polarization of rebar embedded in concrete, immersed in 3.5wt% NaCl for a minimum 90 days.

Admixture (%)	Exposure (days)	OCP (mV)	E_{corr} (mV)	I_{corr} ($\mu A/cm^2$)	R_p ($K\Omega \cdot cm^2$)	β_a (mV/decade)	β_c (mV/decade)
Control	108	-405.00	-436.48	2.377	14.63	115.3	163.5
Colloidal Silica 0.5%	92	-320.00	-478.90	0.03498	833.08	1396.56	70.50
Colloidal Silica 1.0%	92	-275.00	-445.21	0.02629	898.50	1107.79	57.21
Colloidal Silica 2.0%	92	-463.00	-501.34	0.002344	11509.1	437.54	72.40
Fumed Silica 0.5%	93	-365.00	-423.71	0.01432	1701.19	428.76	64.55
Fumed Silica 1.0%	93	-390.00	-485.50	0.03802	640.74	428.76	64.55
Fumed Silica 2.0%	93	-270.00	-414.40	0.01413	1899.04	446.28	71.73
Micro Silica 0.5%	99	-377.00	-557.44	0.06123	405.77	1684.71	59.23
Micro Silica 1.0%	99	-360.00	-533.06	0.05433	629.37	1042.81	85.18
Micro Silica 2.0%	99	-410.00	-552.70	0.02483	1354.78	666.53	87.66

1.2.3 Cyclic Polarization

Cyclic Polarization measurements provide information on passive films and pitting for electrodes of interest. CP tests were run to evaluate the susceptibility of stainless steel and reinforcement steel to pitting corrosion. The extent of the pitting corrosion caused by chloride ions was measured. The expectation is that the greater extent of pitting the more permeable to moisture (and chloride) the concrete.

Effect of Glycerol

The tests, Fig. A-18a-d, below were run after 155 days of sample immersion in 3.5 wt% NaCl.

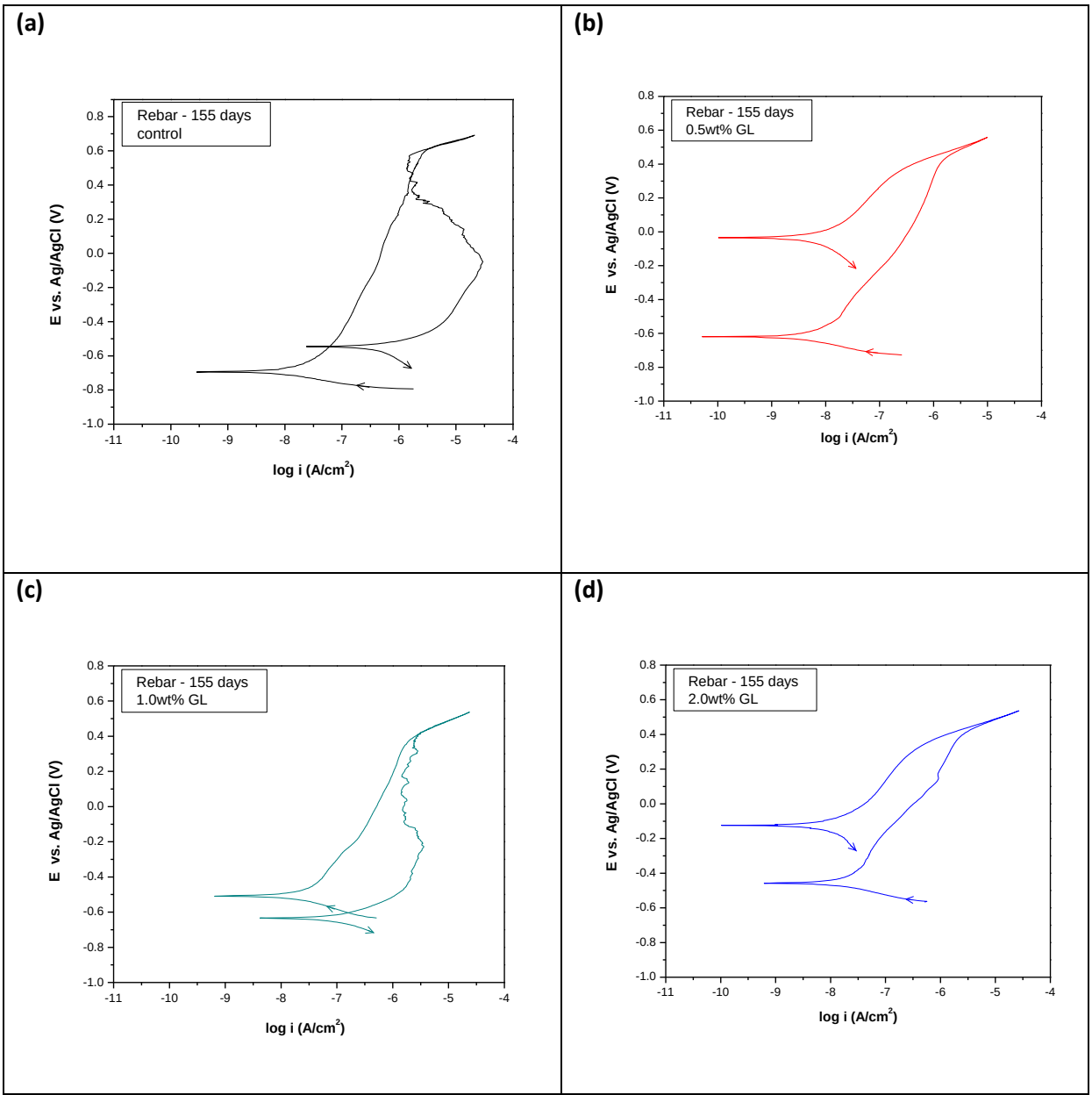

Fig. A-18 Cyclic polarization of rebar embedded in concrete with **(a)** no glycerol admixture, **(b)** glycerol 0.5wt% **(c)** glycerol 1.0wt% and **(d)** glycerol 2.0wt%. Experiments run after concrete had been immersed in simulated sea water (NaCl 3.5wt %) for 155 days.

Fig. A-18a-d are cyclic polarization graphs for series 1 of rebar electrodes cast in concrete. After 5 months immersed in salt water, the CP for rebar embedded in concrete without glycerol addition (control), exhibits a positive hysteresis, Fig. A-18a. The positive hysteresis indicates the formation of pits on the rebar surface. For rebar embedded in concrete with the glycerol additions, CP analysis indicates no pitting present at glycerol concentrations of 0.5 and 2.0wt%. Conversely, the glycerol 1.0wt% admixture

to concrete has pitting present on the rebar surface. In order to confirm the results of series 1, a second round of cyclic polarizations were performed Fig. A-19a-b, Fig. A-20a-b and Fig A-21a-b. The second round of testing also included SS304 electrodes. Immersion times in salt water before CP were 30, 90, 190 and 350 days.

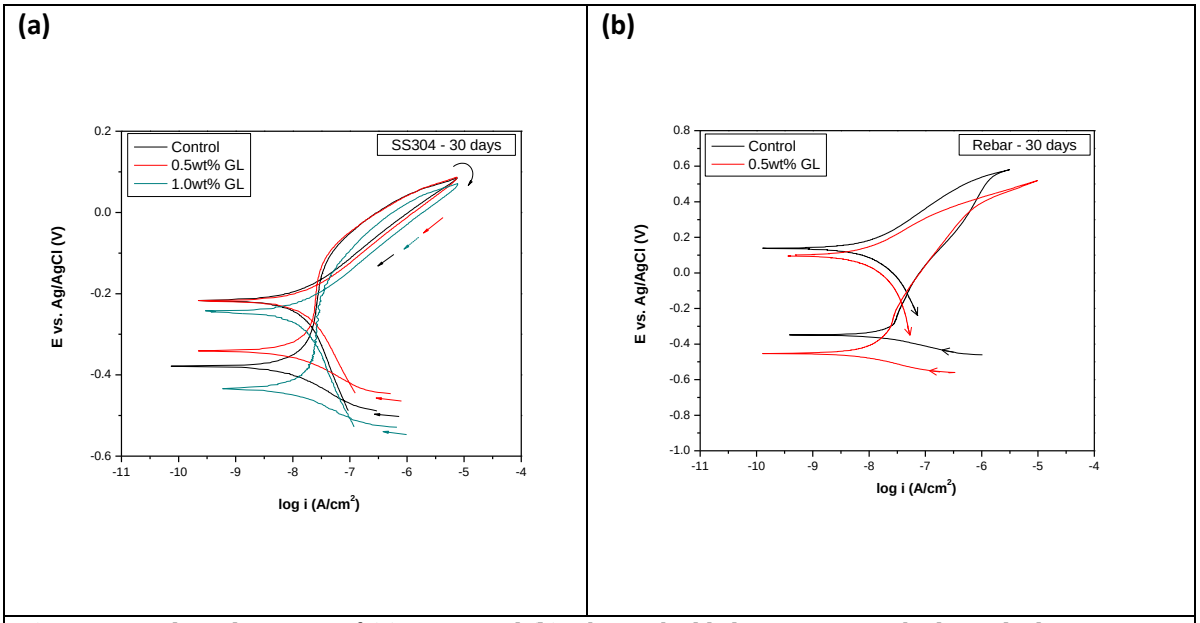

Fig. A-19 Cyclic polarization of **(a)** SS304 and **(b)** rebar embedded in concrete with glycerol admixtures. CP conducted after concrete had been immersed in simulated sea water (NaCl 3.5wt %) for 30 days.

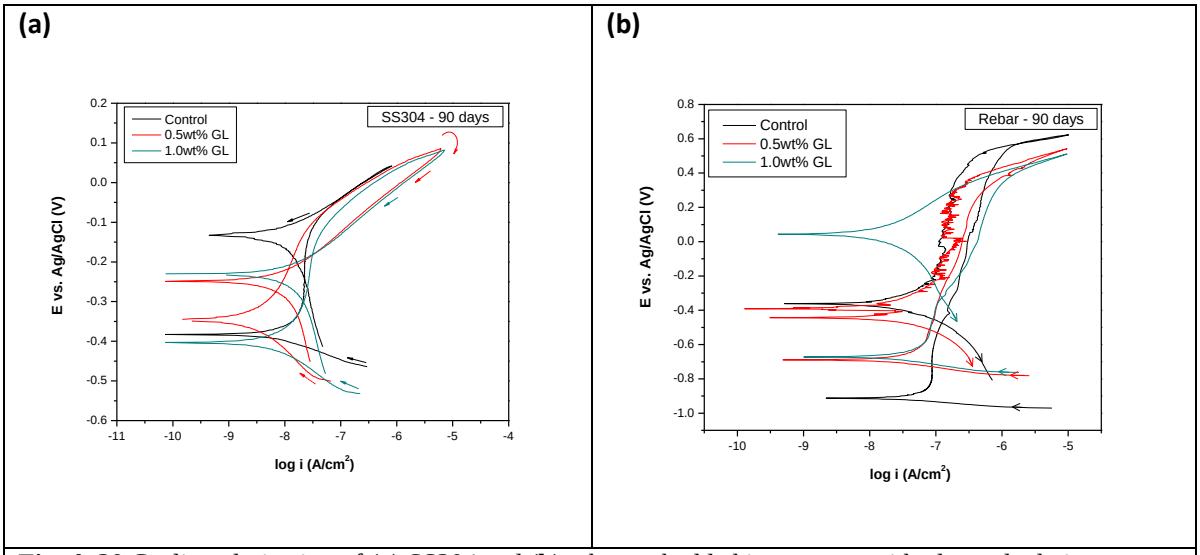

Fig. A-20 Cyclic polarization of **(a)** SS304 and **(b)** rebar embedded in concrete with glycerol admixtures. CP conducted after concrete had been immersed in simulated sea water (NaCl 3.5wt %) for 90 days.

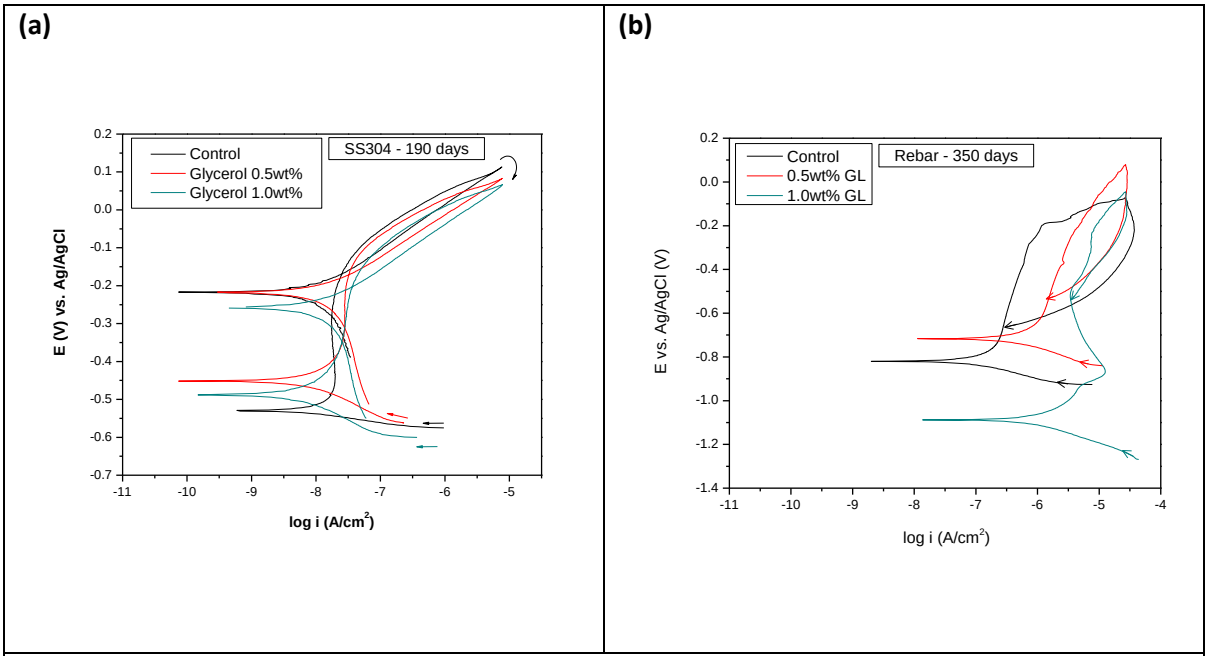

Fig. A-21 (a) Comparison for cyclic polarizations of SS304 embedded in concrete with glycerol admixtures. CP conducted after concrete had been immersed in simulated sea water (NaCl 3.5wt %) for 190 days. **(b)** Cyclic polarization of rebar embedded in concrete with and without glycerol admixture. Experiments run after concrete had been immersed in simulated sea water (NaCl 3.5wt %) for 350 days.

The cyclic polarization tests, resulted in positive hysteresis for SS304 in glycerol modified concrete cells. Furthermore, localized corrosion was detected on SS304 at each testing time (30, 90 and 190 days). This suggests that the permeability of concrete was not decreased through the presence of glycerol.
Rebar embedded in concrete containing glycerol showed no localized corrosion after 30 or 90 days, Fig A-19b and A-20b. Localized corrosion of the rebar was seen after 350 days of concrete cell immersion in salt solution, Fig. A-21b.

Effect of Micro, Fumed, and Colloidal Silica

Cyclic polarization (CP) tests were run to evaluate the susceptibility of the stainless steel and reinforcement steel to pitting corrosion. Tests were run on 30, 90 and 140 days of immersion in salt water. Separate samples of concrete cells were prepared with additions of micro silica, colloidal silica and fumed silica. Each addition was introduced at concentrations of 0.5, 1.0, or 2.0wt % vs. cement binder. The control sample contains no admixture. The following experiments show pitting corrosion of SS 304 embedded in concrete prepared with silica admixtures, Fig. A-22a-c, Fig. A-23a-c and Fig. A-24a-c. Interpretation of the plots is given after Fig. A-24c.

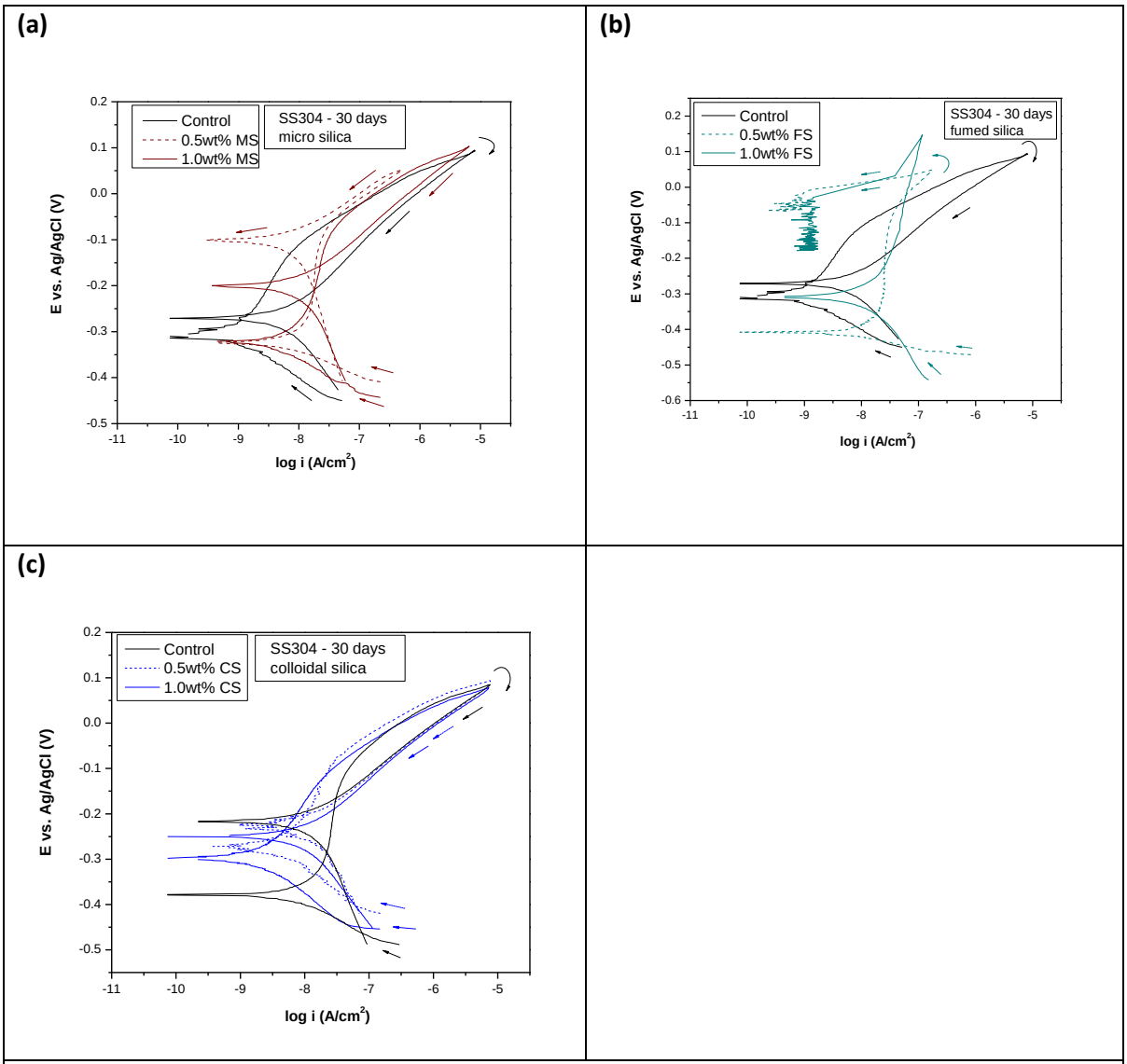

Fig. A-22 Cyclic polarization of SS304 embedded in concrete with **(a)** micro silica, **(b)** fumed silica and **(c)** colloidal silica admixture. Tests were run after concrete had been immersed in simulated sea water (NaCl 3.5wt %) for 30 days.

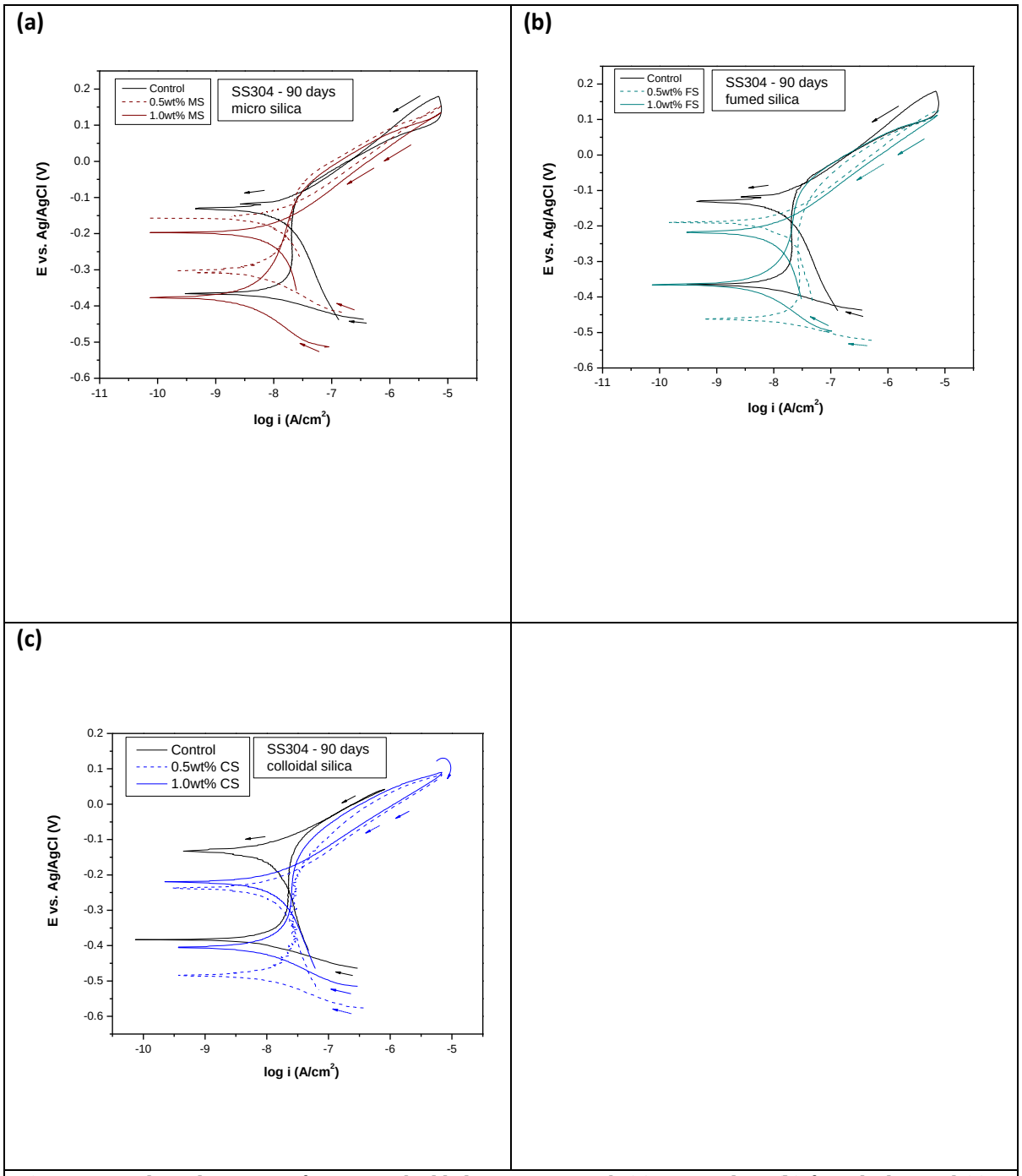

Fig. A-23 Cyclic polarization of SS304 embedded in concrete with **(a)** micro silica, **(b)** fumed silica and **(c)** colloidal silica admixtures. Tests were run after concrete had been immersed in simulated sea water (NaCl 3.5wt %) for 90 days. A control result is shown for comparison.

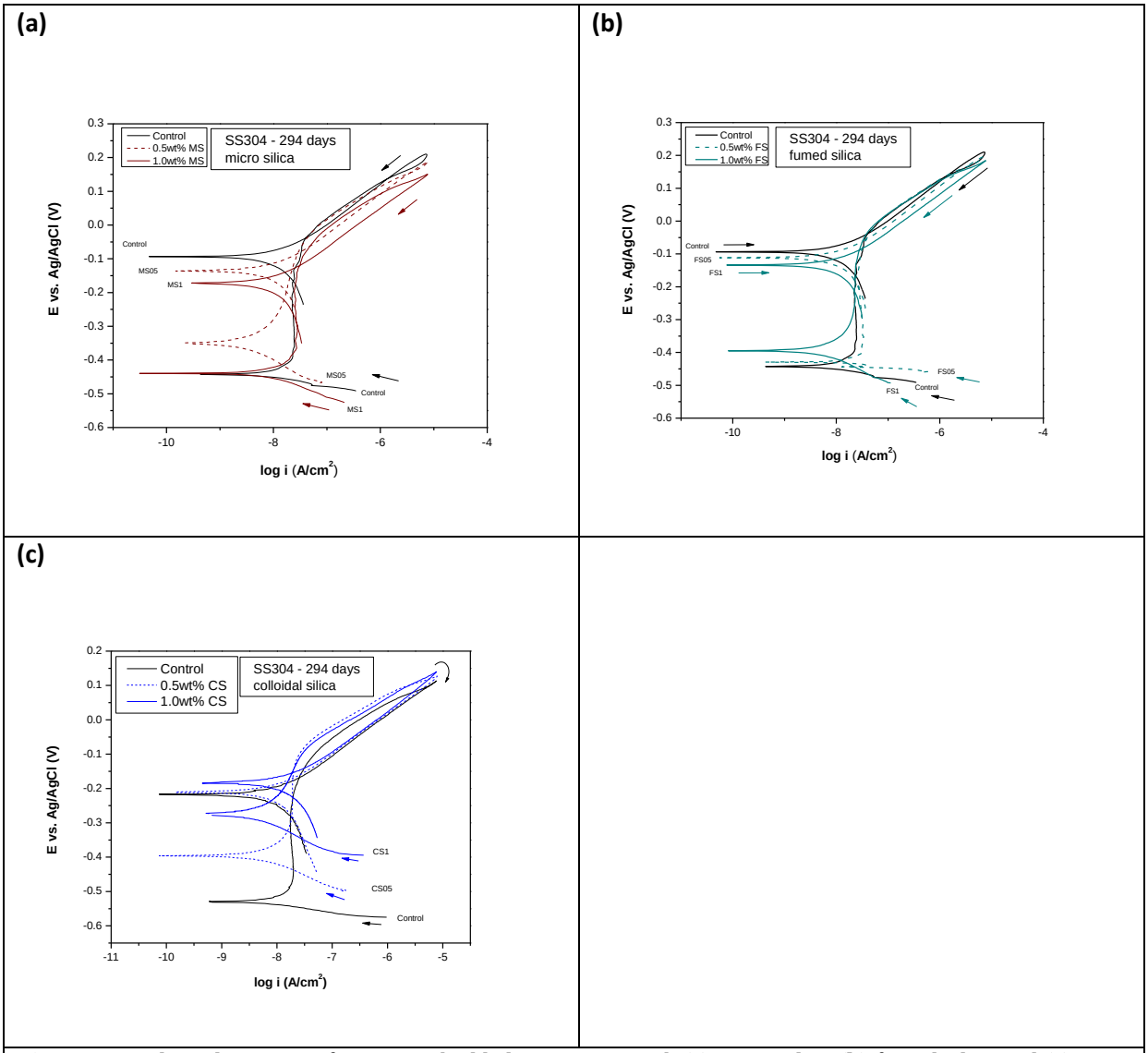

Fig. A-24 Cyclic polarization of SS304 embedded in concrete with (a) micro silica **(b)** fumed silica and **(c)** colloidal silica admixture. Tests were run after concrete had been immersed in simulated sea water (NaCl 3.5wt %) for 294 days.

The cyclic polarization tests at 30 days resulted in negative hysteresis for SS 304 in concrete containing micro and fumed silica. In contrast, the samples containing colloidal silica had positive hysteresis for cyclic polarization of SS 304. In terms of these results, micro and fumed silica additions either reduce the permeability of the concrete matrix to Cl^- or inhibit pitting corrosion. After 90, 190 and 294 days the only parameter which exhibited negative hysteresis (no pitting) was the control (no silica). This might indicate that with time of a stronger passive film develops on the SS 304 surface. Overall, permeability of concrete could not be determined from these results.

The following experiments, Fig. A-25a-c, Fig. A- 26a-c, Fig. A-27a-c, Fig. A-28a-c, and Fig. A-29a-c show CP graphs for rebar embedded in concrete prepared with silica admixtures.

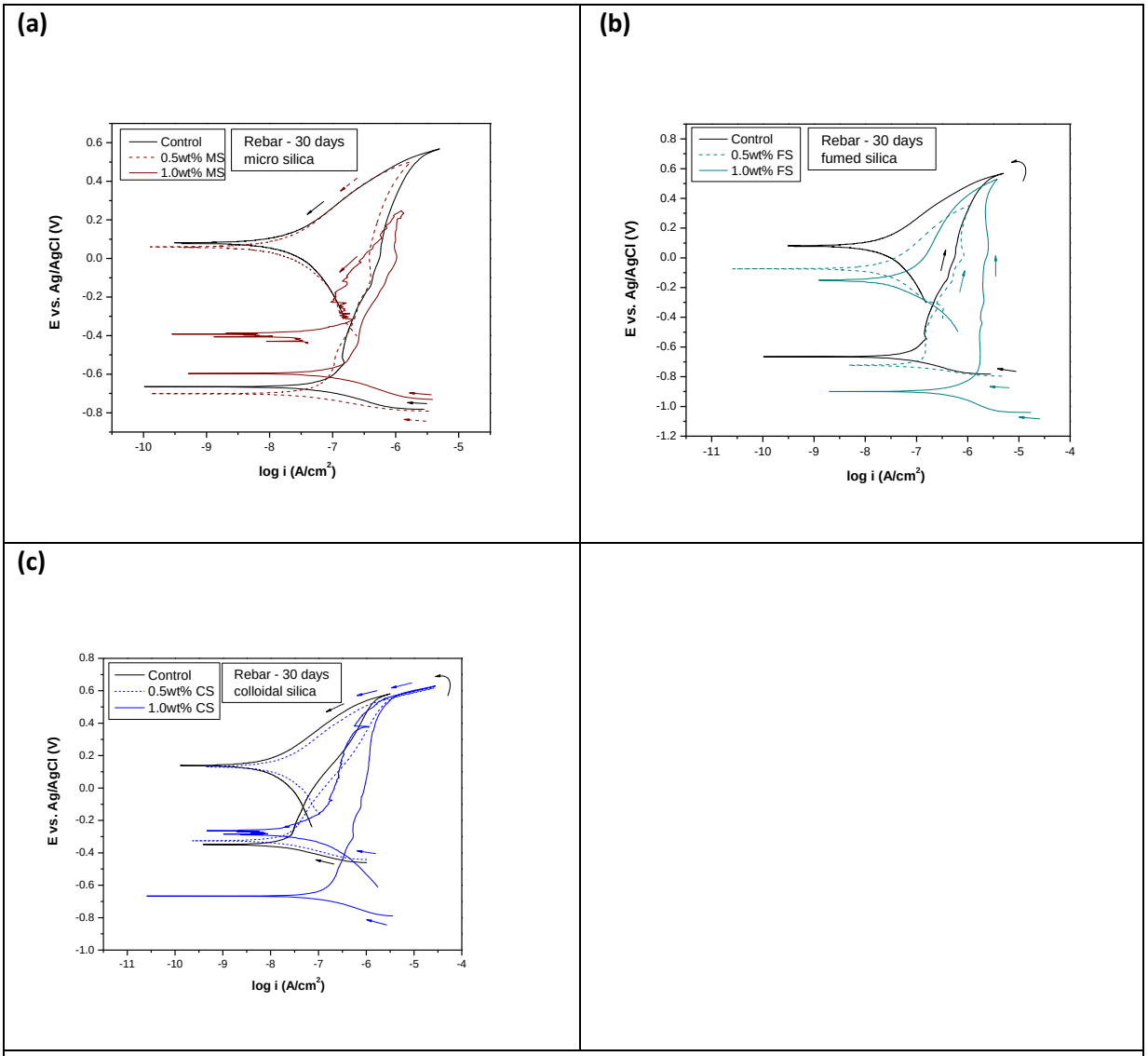

Fig. A-25 Cyclic polarization of rebar embedded in concrete with **(a)** micro silica, **(b)** fumed silica and **(c)** colloidal silica admixture. Tests were run after concrete had been immersed in simulated sea water (NaCl 3.5wt %) for 30 days. A control result is shown for comparison.

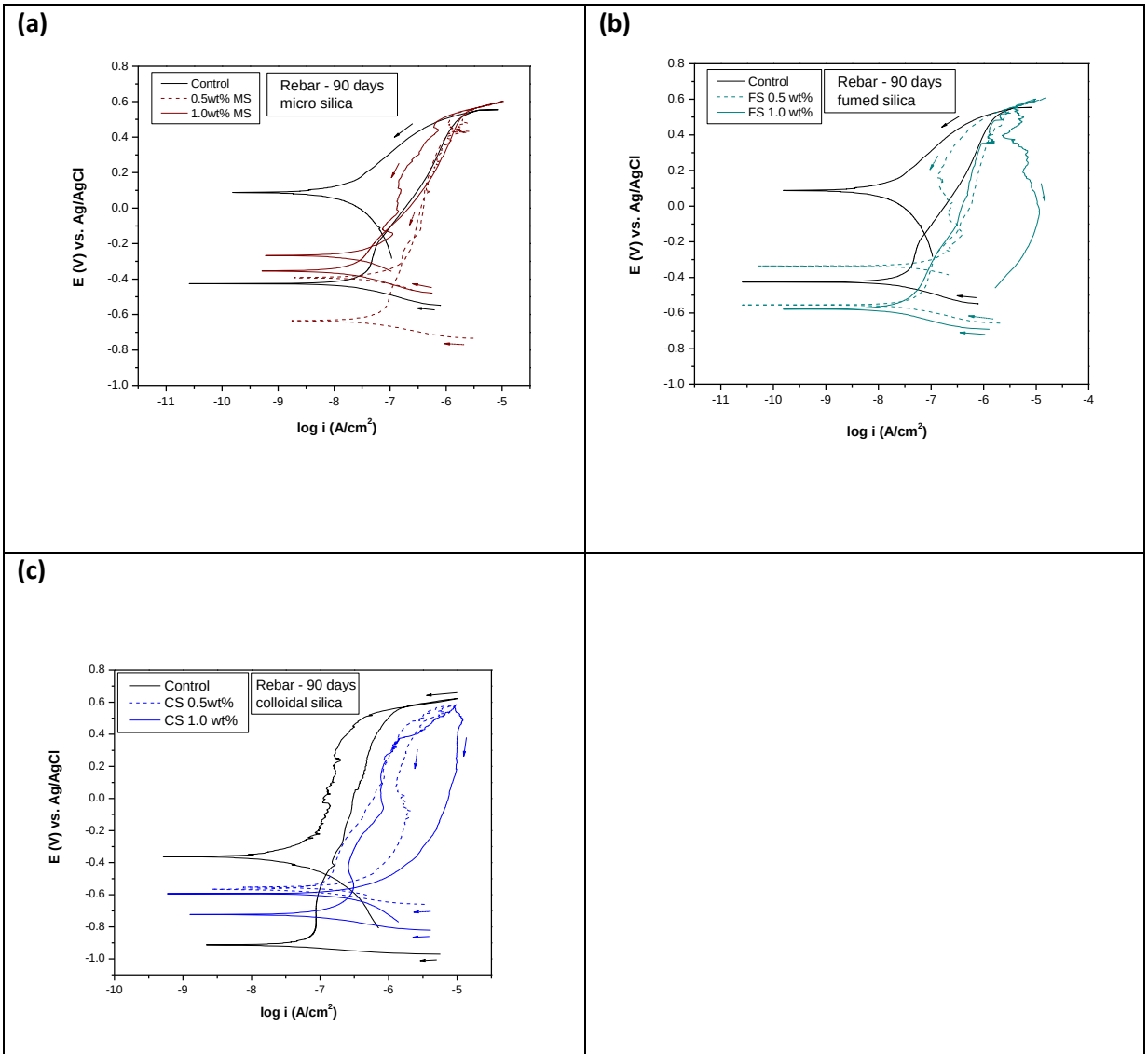

Fig. A-26 Cyclic polarization of rebar embedded in concrete with **(a)** micro silica, (b) fumed silica and (c) colloidal silica admixtures. Tests were run after concrete had been immersed in simulated sea water (NaCl 3.5wt %) for 90 days. A control result is shown for comparison.

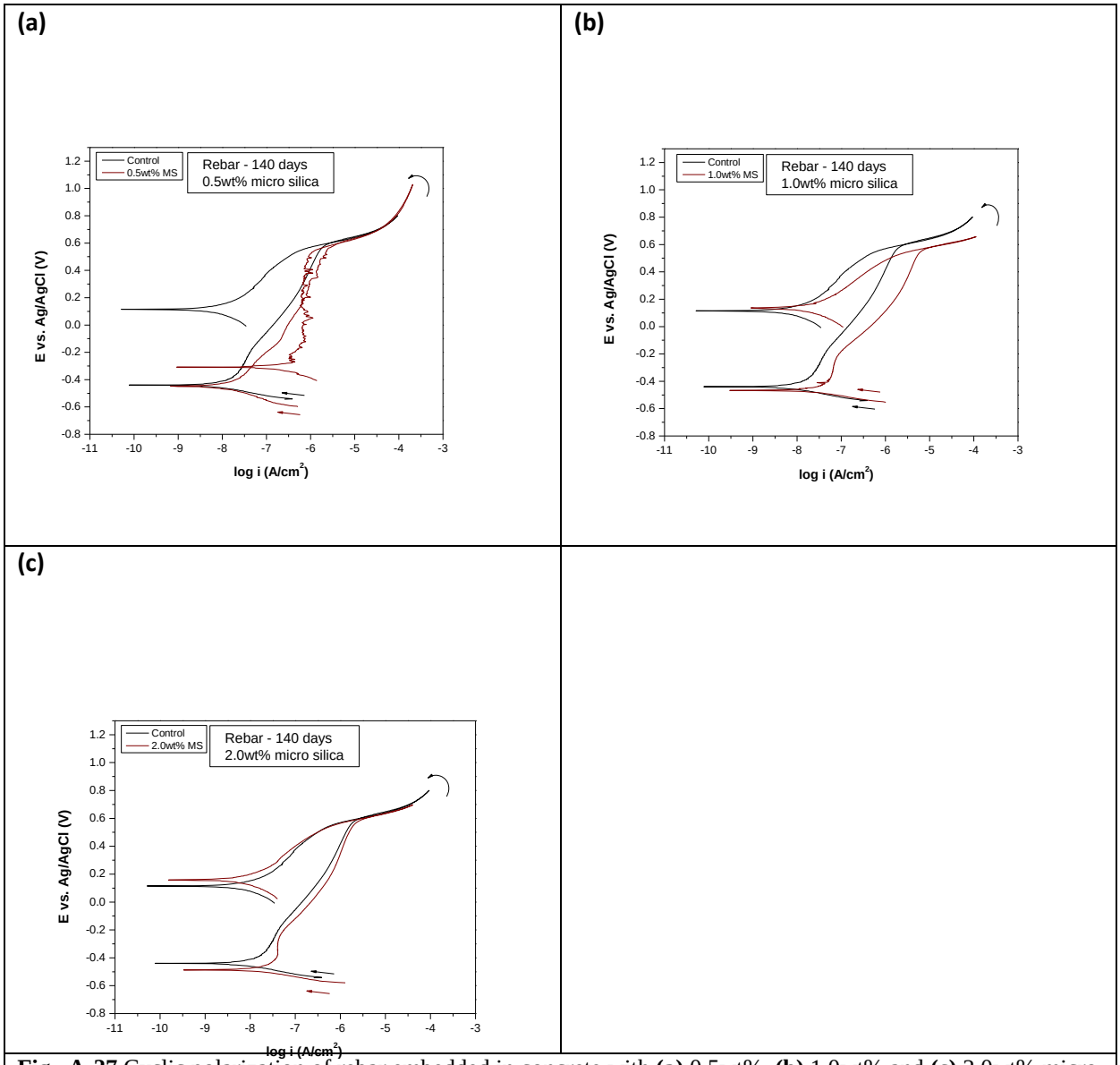

Fig. A-27 Cyclic polarization of rebar embedded in concrete with **(a)** 0.5wt%, **(b)** 1.0wt% and **(c)** 2.0wt% micro silica admixture. Tests were run after concrete had been immersed in simulated sea water (NaCl 3.5wt %) for 140 days.

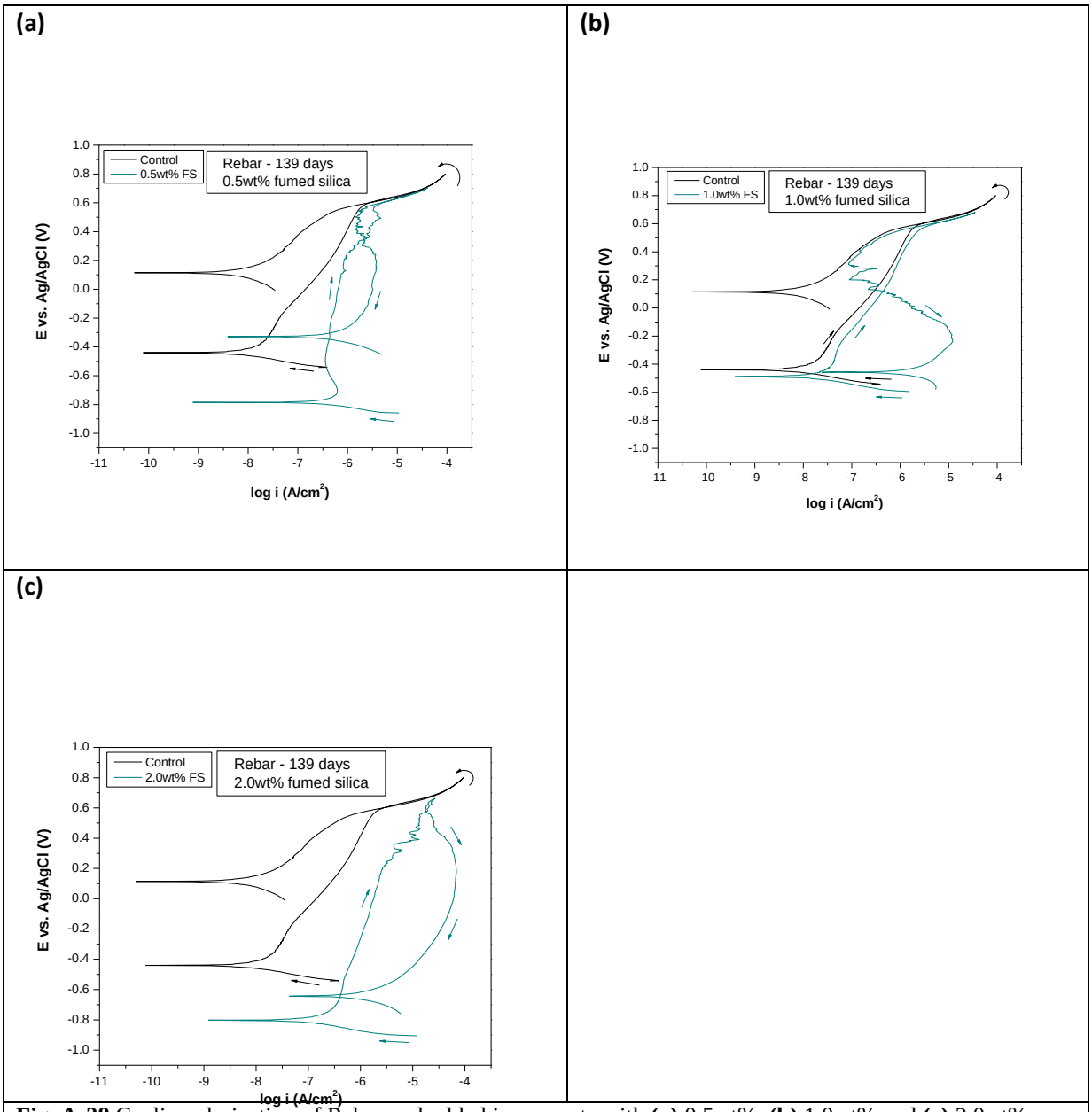

Fig. A-28 Cyclic polarization of Rebar embedded in concrete with **(a)** 0.5wt%, **(b)** 1.0wt% and **(c)** 2.0wt% fumed silica admixture. Tests were run after concrete had been immersed in simulated sea water (NaCl 3.5wt %) for 140 days.

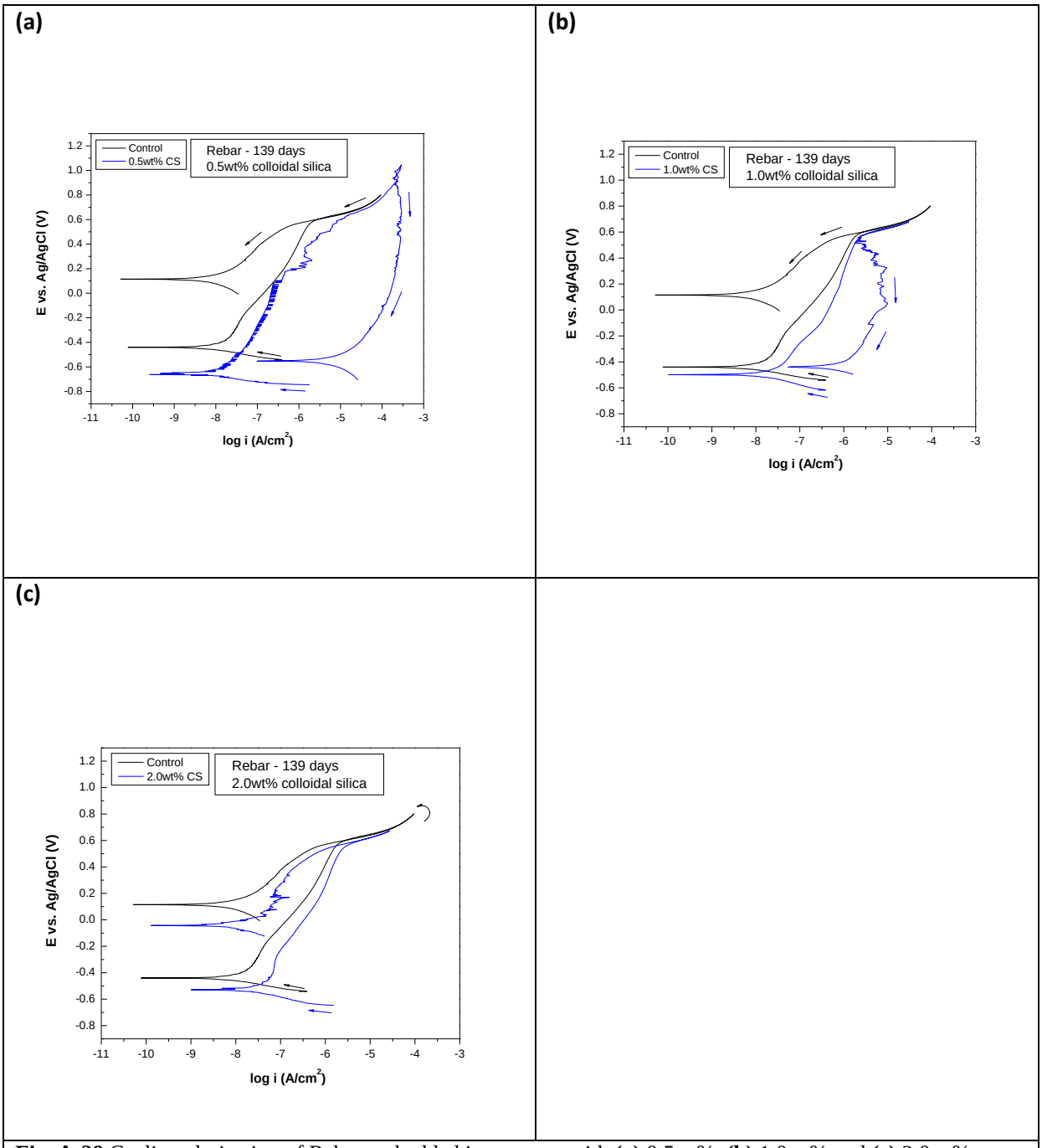

Fig. A-29 Cyclic polarization of Rebar embedded in concrete with **(a)** 0.5wt%, **(b)** 1.0wt% and **(c)** 2.0wt% colloidal silica admixture. Tests were run after concrete had been immersed in simulated sea water (NaCl 3.5wt %) for 140 days.

Rebar embedded in concrete containing micro silica admixtures showed primarily negative hysteresis (no pitting). In contrast rebar embedded in concrete containing colloidal and fumed silica show cases of positive hysteresis (pitting). This suggests either the permeability of concrete was increased through the

presence of colloidal and fumed silica or theses admixtures inhibit the formation of passive films on the rebar surface.

An additional series of Cyclic polarization (CP) tests were run to evaluate the susceptibility reinforcement steel to pitting corrosion. Tests were after 330 days of immersion in salt water. Separate samples of concrete cells were prepared with additions of micro silica, colloidal silica and fumed silica. Each addition was introduced at concentrations of 0.5, and 1.0wt % vs. cement binder. The control sample contains no admixture.

The following experiments, Fig. A-30a-c, show CP graphs for rebar embedded in concrete prepared with silica admixtures.

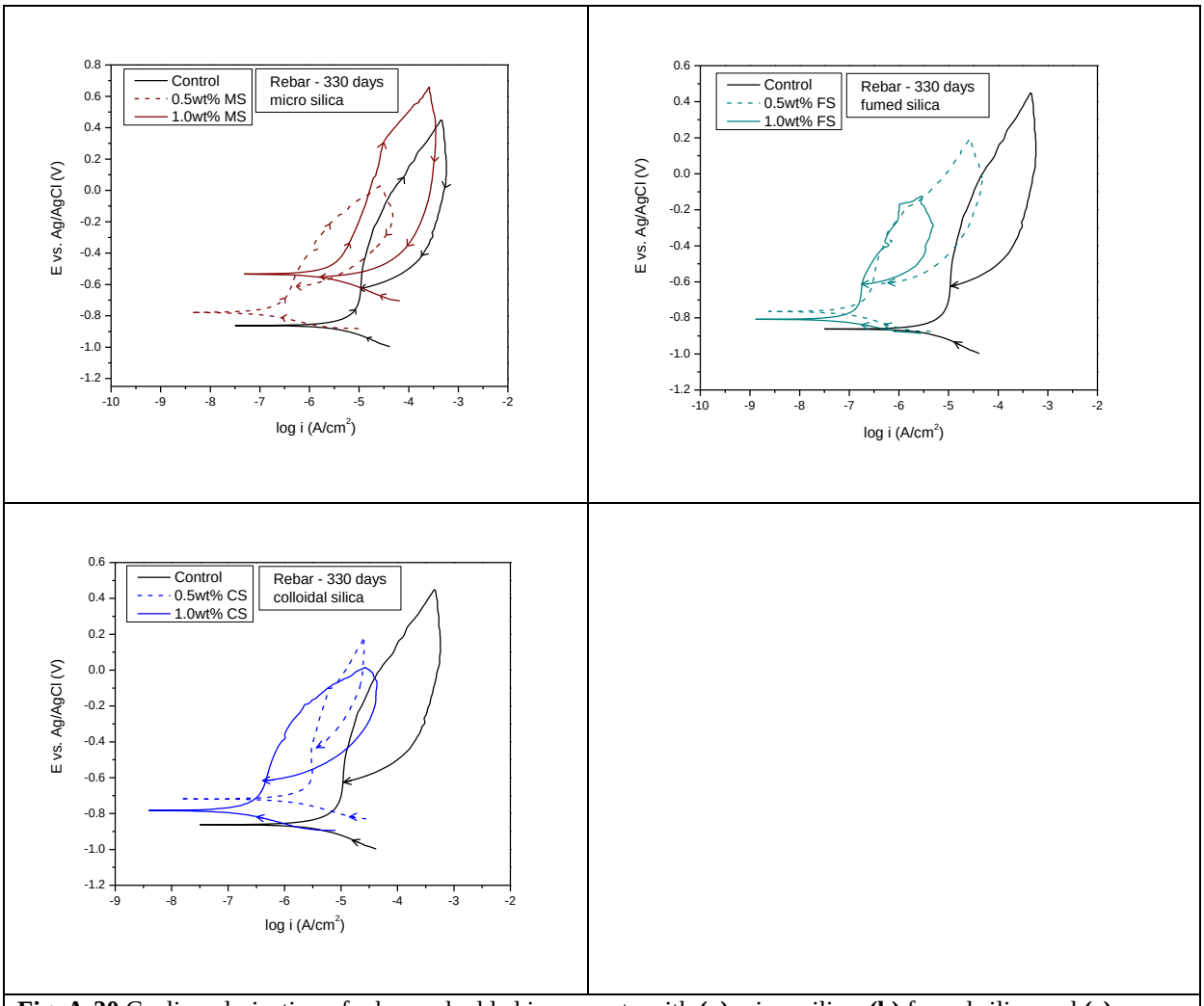

Fig. A-30 Cyclic polarization of rebar embedded in concrete with **(a)** micro silica, **(b)** fumed silica and **(c)** colloidal silica admixtures. Concrete had been immersed in simulated sea water (NaCl 3.5wt %) for 330 days.

Cyclic polarization of rebar embedded in concrete with and without silica admixtures all showed positive hysteresis (pitting) after 330 days. However, current densities were lower when silica admixtures were present. This suggests either the permeability of concrete was decreased through the presence of colloidal, micro or fumed silica or theses admixtures enhance the formation of passive films on the rebar surface.

1.3 Conclusions

1. OCP measurements have yet to provide conclusive information on the effect of glycerol on concrete permeability. However, the addition of glycerol seems to have a stabilizing effect on the OCP of both SS 304 and rebar.

2. The optimal concentration for glycerol to limit permeability is 0.5wt%. Admixtures of glycerol at 0.5 wt% stabilized OCP at approximately -0.15V for up to 20 weeks, while other concentrations show cathodic trending OCP earlier.

3. The addition of colloidal or micro silica at 0.5wt% anodically stabilized OCP for both SS304 and rebar.

4. Admixtures of colloidal and micro silica at 0.5 wt% stabilized OCP to approximately -0.2V, while other admixture ratios show cathodic trending OCP.

5. OCP measurements have yet to provide conclusive information on the effect of admixtures on concrete permeability.

6. Cyclic polarization of SS304 embedded in concrete is largely inconclusive.

7. Cyclic polarizations of rebar indicate a positive effect of glycerol additions in terms of preventing localized corrosion.

8. Cyclic polarization of SS 304 embedded in concrete is inconclusive.

9. Cyclic polarization of rebar indicates a negative effect of colloidal and fumed silica additions in terms of preventing pitting corrosion.

10. Micro silica addition corresponds with increased resistance to pitting corrosion.

11. Micro silica limits permeability, but could also be a corrosion inhibitor and is functional in passive film formation at the rebar surface.

12. From Tafel polarization: Rebar embedded in concrete containing glycerol admixtures exhibits lower corrosion currents and higher resistance to polarization then the control sample (no glycerol). However, low cathodic corrosion potentials and OCP indicative of chloride presence suggests glycerol could be serving as a corrosion inhibitor instead of decreasing permeability.

13. Results for linear polarization were inconclusive. There is no discernable effect of glycerol addition to concrete and its effect on polarization resistance for the steel electrodes. Difficulty in LP measurements for steel embedded in concrete could result from the high pH environment.

14. Linear polarization of SS 304 and Rebar embedded in concrete is largely inconclusive in terms of identifying the silica admixtures effect on permeability of concrete. Tafel polarizations of rebar indicate an increased resistance and smaller corrosion rate for colloidal and fumed silica additions. In contrast micro silica additions indicate an increasing rate of corrosion.

SECTION 2

CORROSION OF REBAR IN CEMENT SATURATED SOLUTION (CSS) - EFFECT OF GLYCEROL AND SILICA ADDITIVES, TIME, CARBONATION, OXYGEN PRESENCE, AND CHLORIDE CONCENTRATION

2.1 Experimental procedures

The research on corrosion of reinforcement steel with simulated cement pore solution plays the role of "control experiments", i.e. providing the baseline for comparison when steel is in direct contact with simulated pore solution to those conditions when steel is contact with actual cement pore solution while embedded in concrete. Our experiments are unique in that our simulated pore solution is prepared by leeching Portland cement in RO water for a period of at least three days and then filtering. The end result is a cement saturated solution (CSS) that has an ideal mineral content and alkalinity.

In regards to the alkalinity an important topic is carbonation reactions within concrete. The pH of concrete pore solution will be in the range 12.5 -13.5. At this high pH, steel has a strong protective passive film. However, as CO_2 permeates from the atmosphere into the structure, it participates in a carbonation reaction with the water and calcium hydroxide present within the pores. The chemical reactions for formation of carbonate and bicarbonate from OH and $CO_2$are.

$$CO_2 + Ca(OH)_2 \rightarrow CaCO_3 + H_2O$$

$$CO_2 + H_2O \rightarrow H_2CO_3$$

$$H_2CO_3 \rightarrow HCO_3^- + H^+$$

This carbonation reaction consumes the calcium hydroxide and creates carbonic acid which lowers the pH over time to between 11 and 9. Therefore corrosion of rebar was studied in CSS solution at three different pH values, 12.5, 11.0 and 9.0.

The effects of free chloride ions and oxygen on the corrosion behavior of the rebar samples were also investigated. Chloride ions permeating through the concrete microstructure can participate in an autocatalytic reaction once they reach the rebar surface and initiate localized pitting corrosion on the surface. Oxygen molecules can also permeate through the porous microstructure so their effect on the corrosion behavior of rebar steels in simulated solution was studied. With the strong passive film steel has at high pH, a significant amount of chloride will have to be present in order to break down said passive film and initiate localized corrosion. If the proposed additives affect the level of chloride

necessary to begin localized corrosion on the rebar surface, their benefits could be two-fold. Not only would they slow diffusion of corrosive species through solid concrete, but also help protect the rebar once the corrosive species reach the steel surface.

These experiments determined if any of the glycerol or silica additives could act as an inhibitor to corrosion of the rebar surface. This was accomplished by studying cement saturated solutions with percentages of each additive present in turn. Classical electrochemical techniques of Open Circuit Potential (OCP), Linear Polarization (LP), Tafel Polarization, and Cyclic Polarization (CP) were used to characterize additive effect on steel corrosion.

2.1.1 Solution Preparation

Cement Saturated Solution (CSS) was prepared by leeching 4kg of Portland Type II cement within 10L of RO water. For a period of three days, the solution was kept constantly agitated with a mixer to prevent settling. After three days of mixing the solution was allowed to settle for one day before it was pressure filtered to remove particulates. The pH of solution after filtering was approximately 12.5. Experimental solutions were prepared using this CSS as stock. A variety of solutions were prepared according to pH and additive. The pH could be lowered by bubbling CO_2 gas through the solution, and raised as necessary by adding NaOH. The chloride addition was carried out by dissolving required amounts of NaCl in the cement solution. Any additives of interest were measured out on a balance and introduced to solution after pH adjustment.

2.1.2 Electrode Preparation

Disk Electrodes

Rebar disks were cut from bar stock using a band saw. Each disk was polished by hand with metallographic papers up to 2000 grit count, then polished using 1μm diamond slurry on a polishing wheel. An Ultrasonic methanol bath followed each polishing step. Once polishing was complete the steel disks were immediately dried and stored in a desiccator. Prior to any electrochemical test a steel sample was given a final polish by hand with a 1μm diamond slurry, ultrasonicated in methanol and dried with air. A polished electrode sample can be seen below in Fig. A-31.

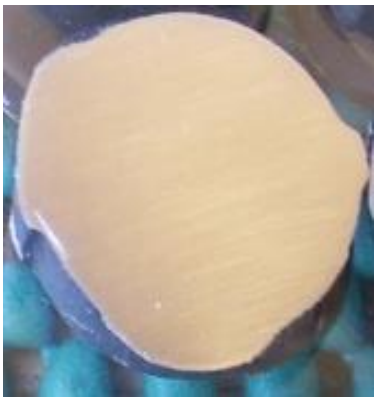

Fig. A-31. Polished rebar disk electrode.

Metallographically polished rebar steel discs (Supplied by Nucor Steel) of 3/4" diameter were used in the polarization experiments. The composition of the steel was 0.42% C, 1.16% Mn, 0.01% P, 0.045% S, 0.19% Cu, 0.08% Ni, 0.08% Cr, 0.019% Mo, 0.0007% V, and Fe balance. The elongation, yield, and tensile strengths were: 13%, 470 MPa, and 757 MPa, respectively.

Hanging Electrodes

Rebar wafers were machined to 1cm diameter and had a stainless steel lead welded to the top. The chemical composition of reinforcement steel used is provided below, Table 10. To protect it from solution, each sample was cold mounted in epoxy and the stainless steel leads wrapped with heat shrink tubing. A representative sample can be seen below in Fig. A-32.

Table 10. Chemical composition of rebar samples for use as hanging electrodes.

Element	C	Mn	P	S	Si	Cu	Ni	Cr	Mo	V	Nb
wt%	0.41	1.23	0.017	0.044	0.20	0.25	0.08	0.15	0.019	0.0029	0.001

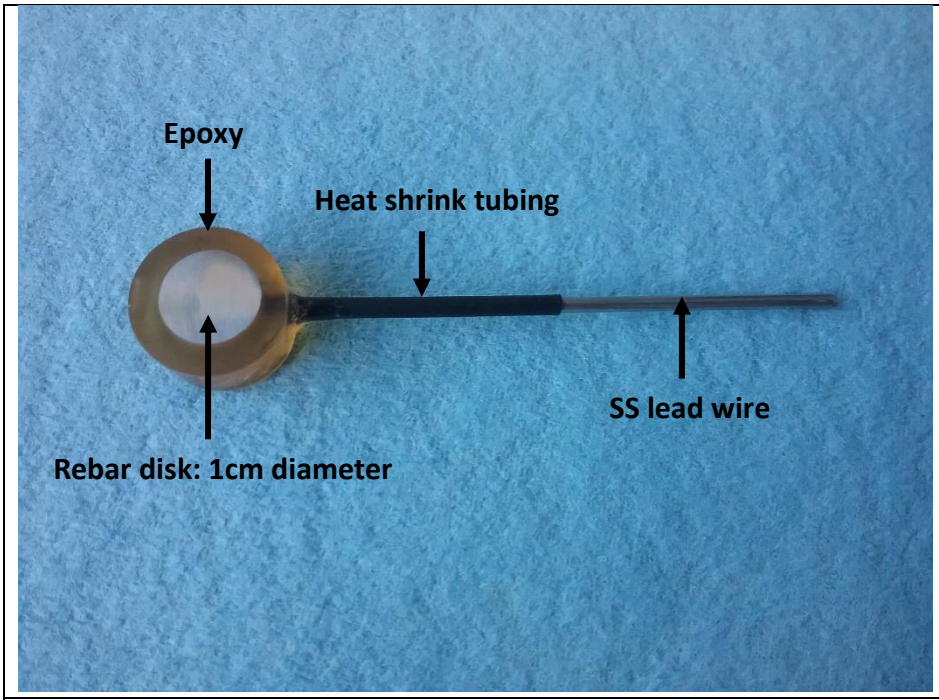

Fig. A-32 Working electrode sample used to study corrosion of rebar in direct contact with cement saturated solutions. Referred to as a hanging electrode for the way it is suspended in solution.

Initially polished using metallographic papers up to 800 grit, electrodes received polishing by hand with 1.2µm Alumina compound. After polishing each electrode would be ultrasonicated in methanol and placed in an argon purged desiccator to prevent oxidation. Prior to being loaded into their jars (Echem cell), samples were lightly polished by hand with 1µm silicon oxide compound, ultrasonicated and rinsed with DI water.

2.1.3 Experimental Set Up

Three separate electrode cell designs were used to conduct a myriad of electrochemical techniques. Each cell designed shared a common three electrode system. The first experimental set up can be seen in Fig. A-33 below. These electrodes were connected to a Princeton Applied Research EG&G Model 273A potentiostat. This set up with electrodes "hanging" in the electrolyte was used for preliminary testing, the techniques used here were OCP, LP, Tafel and CP. The additive and solution parameters are tabulated, Table 11.

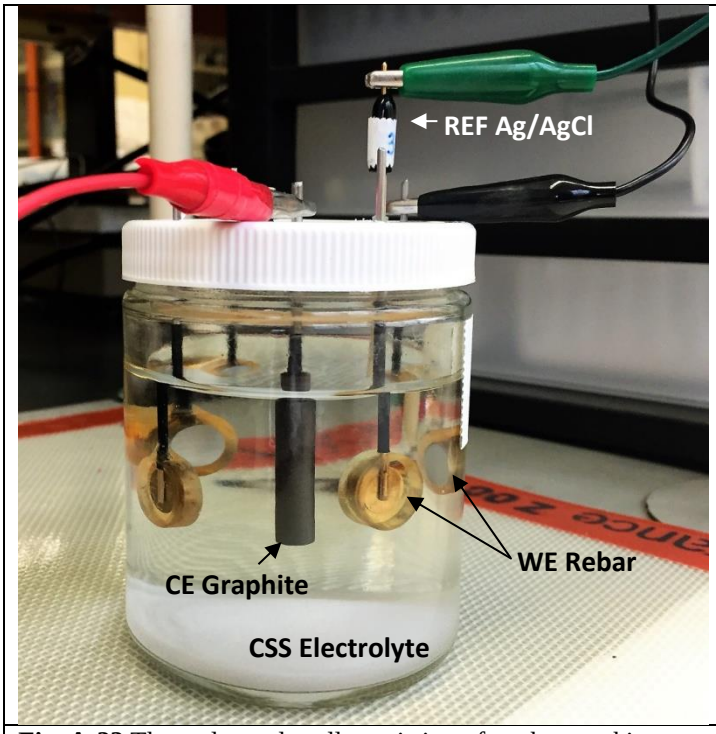

Fig. A-33 Three electrode cell consisting of a rebar working electrode, Ag/AgCl reference electrode, and graphite cylinder counter electrode. Each of these jars contained multiple working electrodes, each scheduled for testing at particular time intervals.

Table 11. Solution composition to study the effects of glycerol, chloride, and oxygen

No NaCl	0.25wt% Glycerol	No Oxygen	Jars 1,3
		With Oxygen	Jars 5,7
	1.0wt% Glycerol	No Oxygen	Jars 2,4
		With Oxygen	Jars 6,8
3.5wt% NaCl	0.25wt% Glycerol	No Oxygen	Jars 9,11
		With Oxygen	Jars 13,15
	1.0wt% Glycerol	No Oxygen	Jars 10,12
		With Oxygen	Jars 14,16
Control: No NaCl	Control: No Glycerol	No Oxygen	Jars 17,19
		With Oxygen	Jars 18,20

Table 12. Standard experimental condition used throughout electrochemical tests

WE: Nucor rebar electrode A=0.785 cm^2	Solution: Cement Saturated Solution
CE: Graphite	pH: ~12.5
RE: Ag/AgCl, 2mm diameter, leak-free	Glycerol Concentration: 0.25wt% or 1wt%
Volume: 100ml	Cl^- Concentration: 0 or 3.5wt%
Temp: 25 C	Atmosphere: air or argon purged

Open circuit potential (OCP) experiments were performed by monitoring the OCP for approximately 15 to 20 minutes to obtain a stable reading. Linear Polarization (LP) experiments were performed using a voltage range of +/- 0.025V and a scan rate of 0.1667mV/s. OCP and LP experiments were performed

weekly. Tafel Polarization experiments were performed at 0, 4, and 8week time intervals, using a voltage range of +/- 0.250V and a scan rate of 0.1667 mV/s. Cyclic Polarization (CP) experiments were started at -0.200V vs the OCP and the scan reversed when the current reached 1E-04 Amps using a scan rate of 0.1667mV/s. *CP experiments were only performed at zero weeks of exposure time.

The second electrochemical cell was designed in such a way that an Ag/AgCl reference electrode can be inserted directly adjacent to the top of the rebar disk. A platinum foil counter electrode was positioned opposite the working electrode. A picture of the experimental setup can be seen below in Fig. A-34. This design was efficient for running multiple CP tests one after another. This setup was used for studying the effect of silica concentration on pitting of rebar in CSS.

Fig. A-34 Experimental setup used for electrochemical testing.

Clamped to the side of the cell a rebar disk could be conditioned in CSS for 30 minutes. During this time OCP was monitored. Once the 30 minutes was passed, a linear polarization was run. Directly after the linear polarization was completed, a cyclic polarization was begun. Table 13 presents additional experimental conditions.

Table 13. Experimental condition for experiments with rebar immersed in saturated cement solutions.

Working electrode:	Nucor rebar steel	Area:	0.636 cm^2
Reference electrode:	Ag/AgCl	Temperature:	25 C
Counter Electrode:	Graphite	Solution volume:	200mL
Solution:	CSS at pH 11	Atmosphere:	Air

Table 14 provides the experimental procedure used in cyclic polarization studies. Cyclic polarization studies were run until the current density reached 0.1mA/cm^2 on the forward scan. At this point the scan was reversed and the hysteresis examined.

Table 14. Experimental procedures used during CP analysis of rebar samples.

Initial Potential:	0mV vs OCP
Critical Current Density:	0.1mA/cm^2
Final Potential:	-0.2 V vs OCP
Scan Rate:	1 mV/s

Experimental parameters included: chloride ion presence, and silica additive concentration. Solutions used in the electrochemical analyses are listed below.

1. pH 11 CSS + 10mM chloride + 0.5wt%, 1wt%, 2wt% colloidal silica (CS)
2. pH 11 CSS + 10mM chloride + 0.5wt%, 1wt%, 2wt% micro silica (MS)
3. pH 11 CSS + 10mM chloride + 0.5wt%, 1wt%, 2wt% fumed silica (FS)

The third electrochemical cell design consisted of the rebar working electrode, a homemade Ag/AgCl reference electrode and a platinum foil counter electrode. A complete picture of the experimental setup can be seen below in Fig. A-35. This electrochemical cell was used to run, Potentiostatic, EIS, and Mott-Schottkey tests.

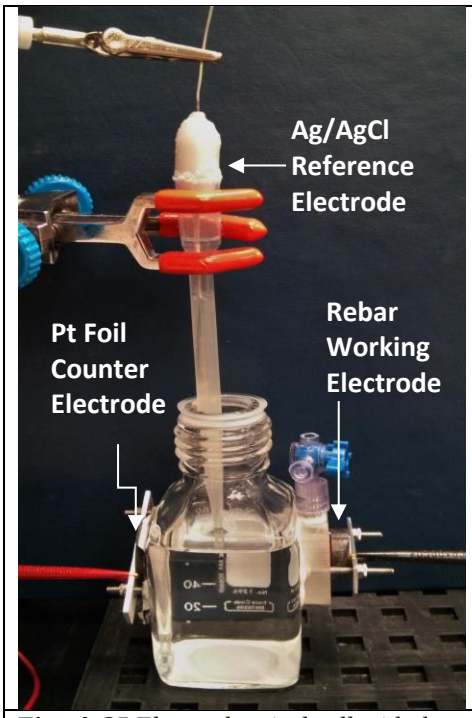

Fig. A-35 Electrochemical cell with three electrode setup.This set up was used for EIS.

The experimental procedure was as follows. After final polishing the electrode is immersed in solution and a potentiostatic polarization performed for 1 hour over a predetermined potential range. If the current density increased to above 0.1mA/cm^2 this was taken to be the onset of pitting corrosion and the potentiostatic experiment was terminated and electrochemical impedance spectroscopy begun. EIS was run between a frequency range of 10 kHz to 10mHz using 5 points per decade intervals. Once the EIS was completed, Mott-Schottkey analysis was performed. A frequency of 100hZ was used in the Mott-Schottkey analysis

Table 15. Standard experimental conditions used throughout EIS experiments

WE: Nucor rebar electrode A=0.636 cm^2 CE: Graphite RE: Homemade Ag/AgCl Volume: 100ml Temp: 25 C	Solution: Cement Saturated Solution pH: 9, 11, 12.5 Cl^- Concentration: Varies Silica Concentration: 2wt%

2.2 Results and Discussion

2.2.1 Open Circuit Potential Variation with Time

The variation of rebar OCP with time while in cement saturated solutions was studied as a function of glycerol, chloride and oxygen additions. The results for solutions with 0.25wt% glycerol and 1.0wt% glycerol are plotted below in Fig. A-36a-b respectively.

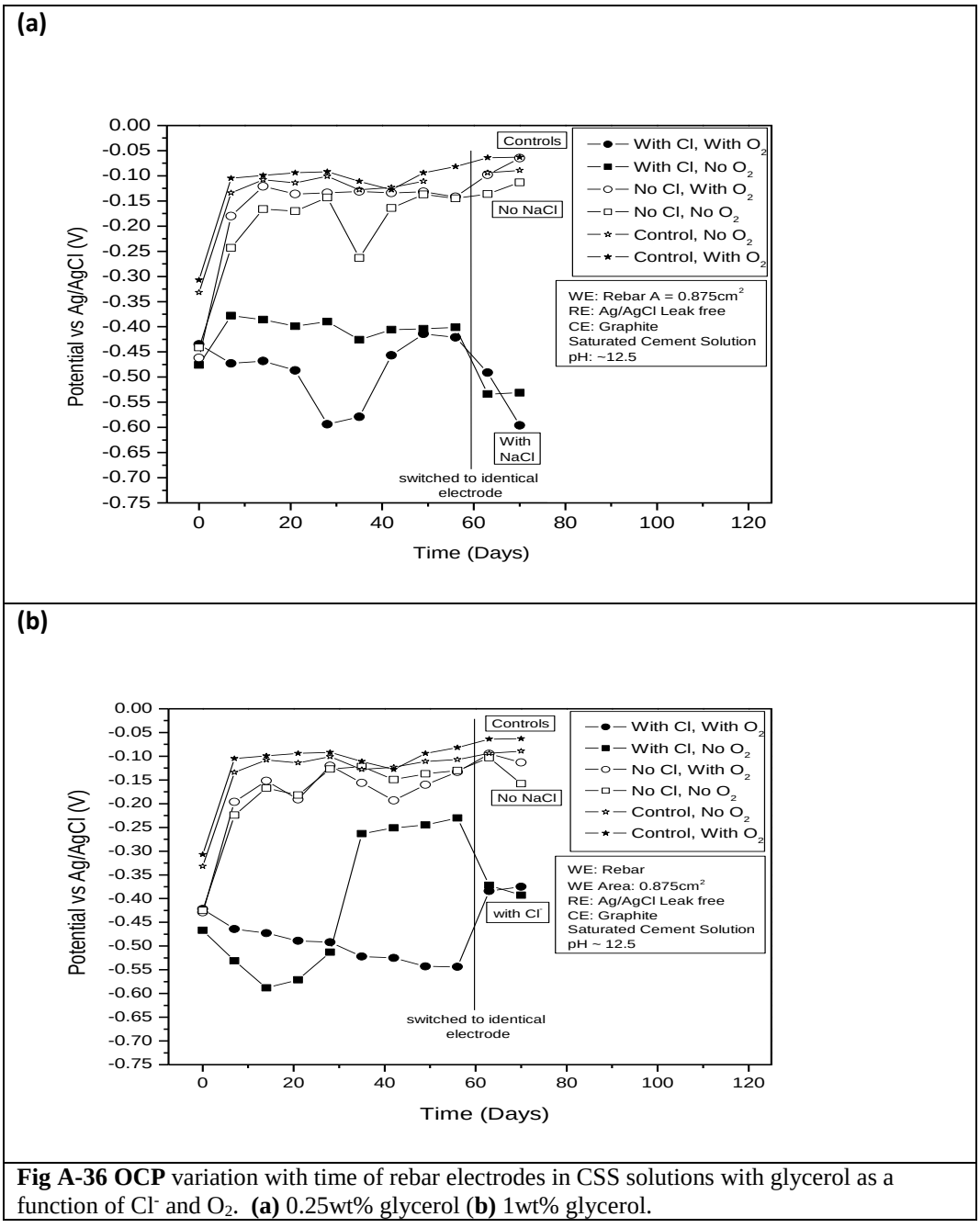

Fig A-36 OCP variation with time of rebar electrodes in CSS solutions with glycerol as a function of Cl^- and O_2. **(a)** 0.25wt% glycerol (**b)** 1wt% glycerol.

In Fig. A-36b, the sharp increase in OCP for steel in solution with chloride and without oxygen (the four data points of filled-in black squares), could be explained by a Tafel polarization experiment performed on another working electrode in the same jar. This Tafel experiment could have produced a species on the counter electrode that migrated over and anodically influenced the OCP of the sample being monitored.

After 8 weeks (56 days), Tafel experiments were scheduled for electrodes previously used to monitor OCP. Therefore, at 8 weeks, OCP monitoring was changed to another electrode in a jar with identical experimental conditions. This transition between electrodes could explain the sudden jumps in the final two data points in Fig. A-37a and b indicated by the vertical solid line.

From Fig.A-36a and b it can be seen that glycerol is not affecting the open circuit potential. For samples with no chloride and control solution, the OCP moves anodically from -0.300V to -0.100 volts and stays constant throughout the three week test. For samples with chloride present the potential drops cathodically to approximately -0.500V. From FigA-36a and b, it can be seen that chloride presence has a significant impact on the OCP. Without chloride, the OCP's proceed to -0.100V, whereas with 3.5wt% chloride the potentials rapidly drop to -0.500V. From Fig. A-36a and b it can be seen that oxygen does not have a prominent effect during these experiments. However, the effects of oxygen can be seen in CP experiments presented later in this report.

2.2.2 Linear Polarization (LP) Analysis

LPs were performed in solutions with two different concentrations of glycerol, 0.25wt% and 1.0wt%, while simultaneously monitoring for any effects from Cl^- or O_2. Experimental results for LP analysis are presented in Tables 16 and 17 below. Results from Tables 16 and 17 are presented graphically in Fig. A-37a and b respectively.

Table 16. Rp (kΩ) Calculated values for 0.25wt% Glycerol Admixture Concentrations

	With NaCl		Without NaCl		Control	
Time (days)	With O_2	Without O_2	With O_2	Without O_2	Without O_2	With O_2
0	24	53	77	113	160	101
7	14	32	56	68	981	1600
14	190	18	669	772	600	633
21	9	14	456	705	480	694
28	3	16	456	407	430	624
35	3	12	450	278	603	729
42	5	14	490	594	540	560
49	6	14	453	740	510	670
56	6	13	550	610	405	710
63	9	5	590	420	580	1020
70	6	5	870	450	570	930

Table 17. Rp (kΩ) Calculated values for 1.0wt% Glycerol Admixture Concentrations

	With NaCl		Without NaCl		Control	
Time (days)	With O_2	Without O_2	With O_2	Without O_2	Without O_2	With O_2
0	66	84	69	99	160	101
7	17	8	61	75	981	1600
14	9	190	499	419	600	633
21	11	22	561	272	480	694
28	11	17	560	529	430	624
35	11	39	496	400	603	729
42	12	48	510	220	540	560
49	12	46	444	490	510	670
56	11	57	770	400	405	710
63	14	15	710	510	580	1020
70	15	12	710	450	570	930

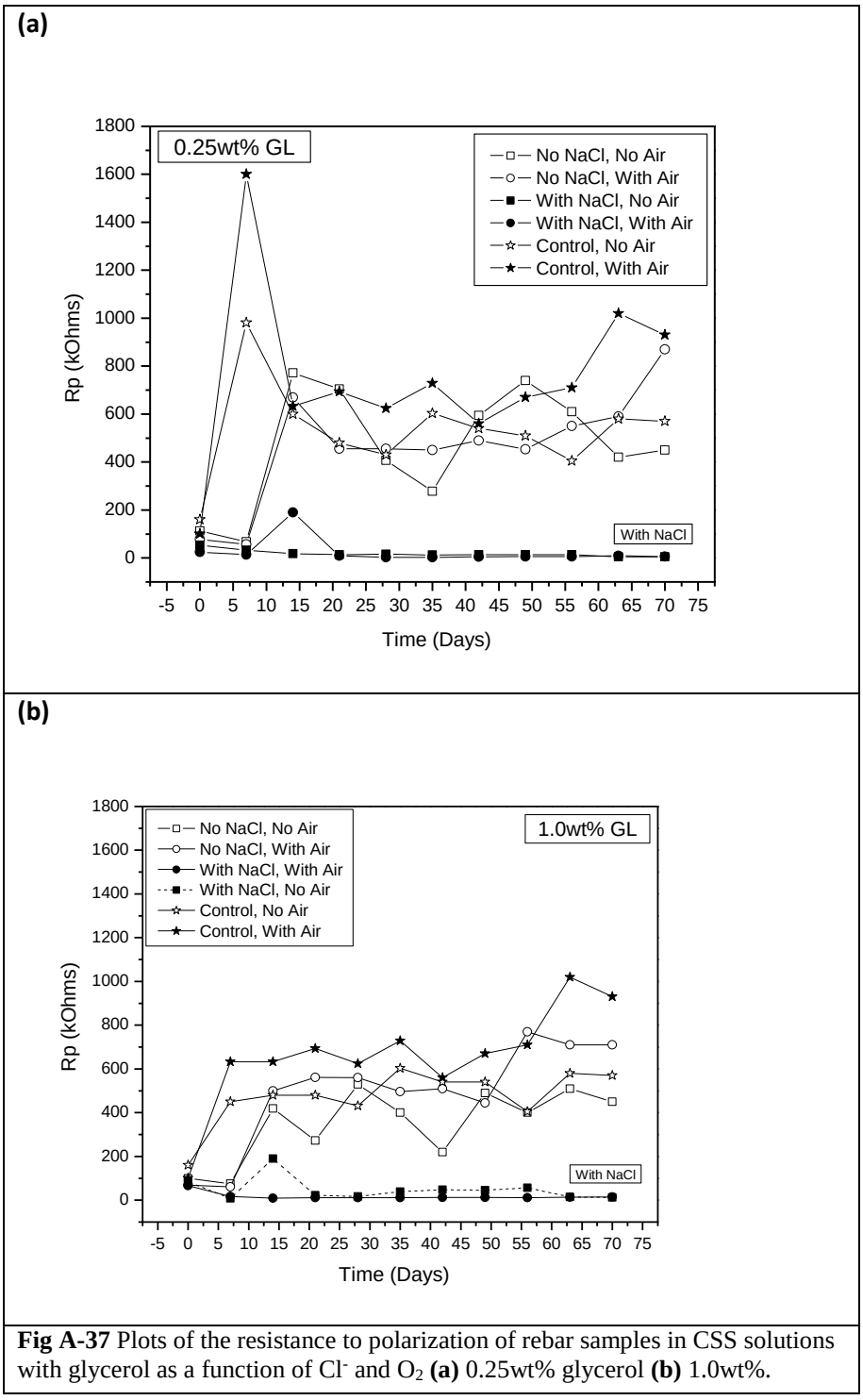

Fig A-37 Plots of the resistance to polarization of rebar samples in CSS solutions with glycerol as a function of Cl^- and O_2 **(a)** 0.25wt% glycerol **(b)** 1.0wt%.

Tables 16 and 17 and Fig.A-37a and b show that there is no significant effect on the Rp value from even a factor four increase in glycerol concentration. Tables 16 and 17 demonstrate that chloride has a significant effect on the Rp values. A chloride concentration of 3.5wt% causes the Rp's to decrease by at

least an order of magnitude. Oxygen has a negligible effect when there is no chloride present. However, in samples with both chloride and oxygen present the Rp is consistently smaller than the Rp of samples with chloride but without oxygen.

2.2.3 Tafel Polarization Analysis

Tafel polarizations were performed on rebar samples immersed in cement saturated solutions containing either 0.25wt% or 1.0wt% glycerol. The effect of time was studied in the presence and absence of chloride and oxygen. Results for Tafel analysis are presented in Tables 18, 19, and 20 below. The calculated corrosion rates for solutions with 0.25wt% glycerol and 1wt% glycerol are plotted in Fig. A-38a and b respectively.

Table 18. Initial (0 Wk) Results for Tafel Polarization Experiments

Experimental Conditions			Time (Wks)	OCP (V)	Ecorr (V)	Icorr (A/cm^2)	β_c (mV/dec)	β_a(mV/dec)
No Sodium Chloride	0.25wt% Glycerol	No Oxygen	0	-0.507	-0.551	4.99E-7	-195.13	70.67
		With Oxygen	0	-0.393	-0.404	2.90E-7	-162.04	53.12
	1.0wt% Glycerol	No Oxygen	0	-0.512	-0.665	1.27E-9	-180.7	58.98
		With Oxygen	0	-0.446	-0.442	5.34E-7	-99.891	96.305
3.5wt% Sodium Chloride	0.25wt% Glycerol	No Oxygen	0	-0.452	-0.427	7.30E-10	-301.88	119.91
		With Oxygen	0	-0.437	-0.451	1.27E-9	-267.56	50.008
	1.0wt% Glycerol	No Oxygen	0	-0.484	-0.637	2.43E-12	-287.79	67.748
		With Oxygen	0	-0.448	-0.449	1.10E-9	-246.44	99.78
Control: No Sodium Chloride	Control: No Glycerol	No Oxygen	0	-0.360	-0.344	5.60E-10	-224.94	180.29
		With Oxygen	0	-0.365	-0.495	5.93E-11	-198.94	177.57

Table 19. Tafel polarization results after 4 weeks of immersion

Experimental Conditions			Time (Wks)	OCP (V)	Ecorr (V)	Icorr (A/cm^2)	β_c (mV/dec)	β_a (mV/dec)
No Sodium Chloride	0.25wt% Glycerol	No Oxygen	4	-0.136	-0.247	1.94E-8	-88.58	30.03
		With Oxygen	4	-0.126	-0.380	1.34E-6	-101.8	41.32
	1.0wt% Glycerol	No Oxygen	4	-0.123	-0.232	5.03E-8	-97.81	10.76
		With Oxygen	4	-0.166	-0.215	3.06E-8	-99.67	61.22
3.5wt% Sodium Chloride	0.25wt% Glycerol	No Oxygen	4	-0.401	-0.472	7.23E-7	-111.34	57.84
		With Oxygen	4	-0.432	-0.559	1.31E-6	-72.7	43.83
	1.0wt% Glycerol	No Oxygen	4	-0.432	-0.508	6.60E-7	-105.26	56.26
		With Oxygen	4	-0.384	-0.452	7.60E-7	-121.09	91.08
Control: No Sodium Chloride	Control: No Glycerol	No Oxygen	4	-0.088	-0.199	1.38E-8	-82.815	42.33
		With Oxygen	4	-0.081	-0.175	1.24E-8	-98.76	52.35

Table 20. Tafel polarization results after 8 weeks of immersion

Experimental Conditions			Time (Wks)	OCP (V)	Ecorr (V)	Icorr (A/cm^2)	β_c (mV/dec)	β_a(mV/dec)
No Sodium Chloride	0.25wt% Glycerol	No Oxygen	8	-0.123	-0.210	2.18E-08	-101.84	55.59
		With Oxygen	8	-0.174	-0.259	2.55E-08	-97.4	56.12
	1.0wt% Glycerol	No Oxygen	8	-0.146	-0.260	2.71E-08	-89.73	33.16
		With Oxygen	8	-0.150	-0.248	1.57E-08	-90.82	53.08
3.5wt% Sodium Chloride	0.25wt% Glycerol	No Oxygen	8	-0.395	-0.468	7.85E-07	-101.5	50.24
		With Oxygen	8	-0.400	-0.533	9.93E-07	-54.34	28.54
	1.0wt% Glycerol	No Oxygen	8	-0.191	-0.238	3.03E-07	-144.22	51.07
		With Oxygen	8	-0.543	-0.601	1.61E-06	-125.11	84.66
Control: No Sodium Chloride	Control: No Glycerol	No Oxygen	8	-0.124	-0.197	1.57E-08	-83.66	54.14
		With Oxygen	8	-0.056	-0.203	4.83E-09	-55.47	27.4

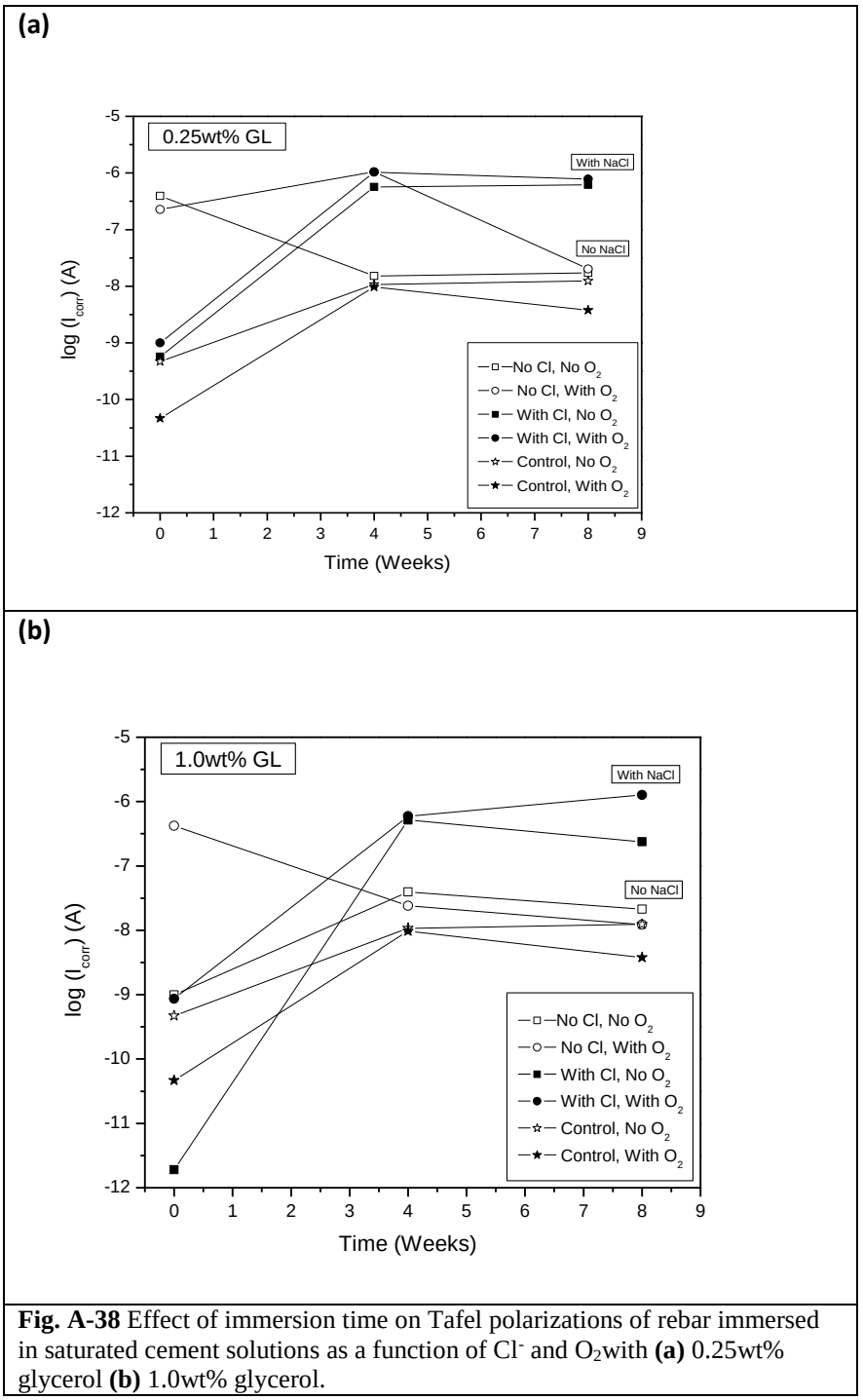

Fig. A-38 Effect of immersion time on Tafel polarizations of rebar immersed in saturated cement solutions as a function of Cl^- and $O_2$with **(a)** 0.25wt% glycerol **(b)** 1.0wt% glycerol.

According to the results plotted in Fig. A-38a and b it can be seen that changing the concentration of glycerol does not affect the corrosion rate. Corrosion rates for the glycerol experiments are consistent with the corrosion rates of the control experiments. When chloride was present, the corrosion rates were

consistently higher compared to when no chloride was present. As with previous experiments, oxygen was seen to compound the effects of chloride. In experiments in which no chloride was present the corrosion rates were almost identical to one another at the 8 week test time.

2.2.4 Cyclic Polarization Studies

Cyclic polarizations (CP's) are used to determine if a metal sample in contact with a solution will be vulnerable to pitting corrosion. If on the return scan the current density returns with lower values than the forward scan, the CP has negative hysteresis and the metal sample is not experiencing pitting corrosion. If on the return scan the current density returns with higher value that the forward scan, the CP has positive hysteresis and the metal sample is vulnerable to localized corrosion.

Effect of Glycerol

CP studies were performed on rebar samples immersed in cement saturated solutions to determine if glycerol served as an inhibitor to pitting corrosion. The effect of time was studied in the presence and/or absence of chloride and/or oxygen. Results for CP analysis are presented in Fig. A-39 and 40 and in Table 21.

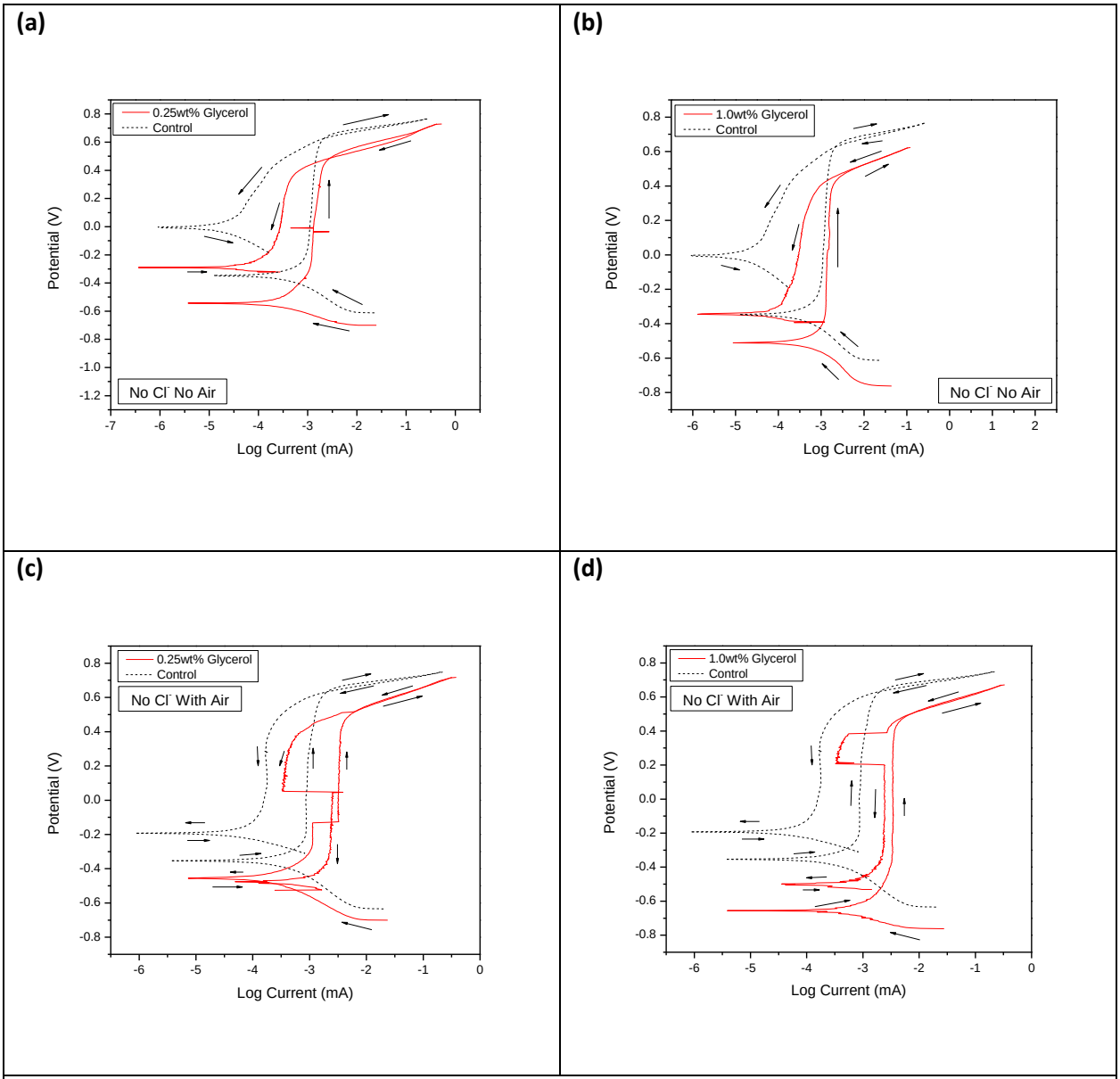

Fig. A-39: Cyclic polarizations of rebar working electrodes in direct contact with saturated cement solutions with no sodium chloride as a function of glycerol concentration and oxygen presence. **(a)** 0.25wt% glycerol, no oxygen **(b)** 1wt% glycerol, no oxygen **(c)** 0.25wt% glycerol, with oxygen **(d)** 1wt% glycerol, with oxygen.

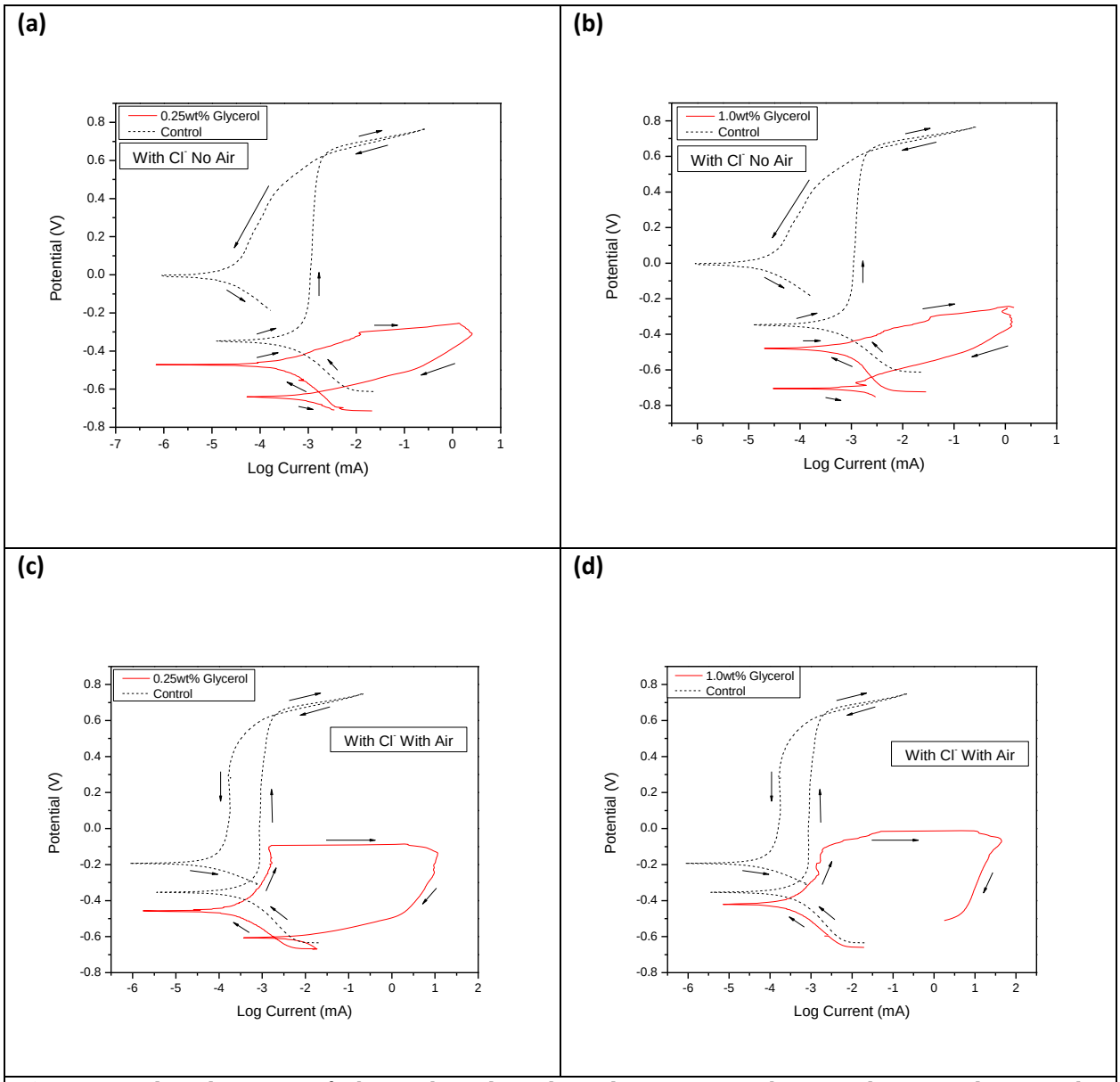

Fig. A-40 Cyclic polarizations of rebar working electrodes in direct contact with saturated cement solutions with 3.5wt% sodium chloride as a function of glycerol concentration and oxygen presence. **(a)** 0.25wt% glycerol, no oxygen **(b)** 1wt% glycerol, no oxygen **(c)** 0.25wt% glycerol, with oxygen **(d)** 1wt% glycerol, with oxygen.

Table 21. Results for cyclic polarization studies of reinforcement steel.

No NaCl	0.25wt% Glycerol	No O_2	Negative Hysteresis
		With O_2	Negative Hysteresis
	1.0wt% Glycerol	No O_2	Negative Hysteresis
		With O_2	Negative Hysteresis
3.5wt% NaCl	0.25wt% Glycerol	No O_2	Positive Hysteresis
		With O_2	Positive Hysteresis
	1.0wt% Glycerol	No O_2	Positive Hysteresis
		With O_2	Positive Hysteresis
Control: No NaCl	Control: No Glycerol	No O_2	Negative Hysteresis
		With O_2	Negative Hysteresis

Changing the concentration of glycerol had no effect on the cyclic polarizations of the rebar steel. Adding 1wt% of glycerol is insufficient to protect the rebar samples from pitting corrosion. Chloride concentration expectedly had a major impact on these experiments. Without chloride, all experiments return with negative hysteresis, while experiments with 3.5wt% chloride all show pronounced pitting. Oxygen has little effect on experiments when chloride was absent from solution, Fig. A-39a-d. The main difference between these graphs is the abrupt jumps in current seen on the reverse scans in Fig.A-40c-d but not in Fig. A-40a-b. This could be attributed to a reaction of glycerol and oxygen, as the jumps are not seen in the control experiment performed with oxygen alone. When oxygen is present in experiments alongside chloride, the pitting observed is worse than in experiments with chloride but no oxygen.

Effect of Micro, Fumed and Colloidal Silica

The following experiments examined the effect of silica additions to CSS on the CP curves of rebar. Three different morphologies of silica were used: colloidal silica (CS), micro silica (MS), and fumed silica (FS). Previous experiments conducted were done within solid concrete cells with varying concentrations of silica admixtures. Therefore the experiments presented below were conducted to determine if changing silica concentration within the CSS had any effect on the CP curves of rebar.

Results for CP scans of rebar in pH 11 CSS mixed with chloride and silica additives are presented below, Fig. A-41a-c.

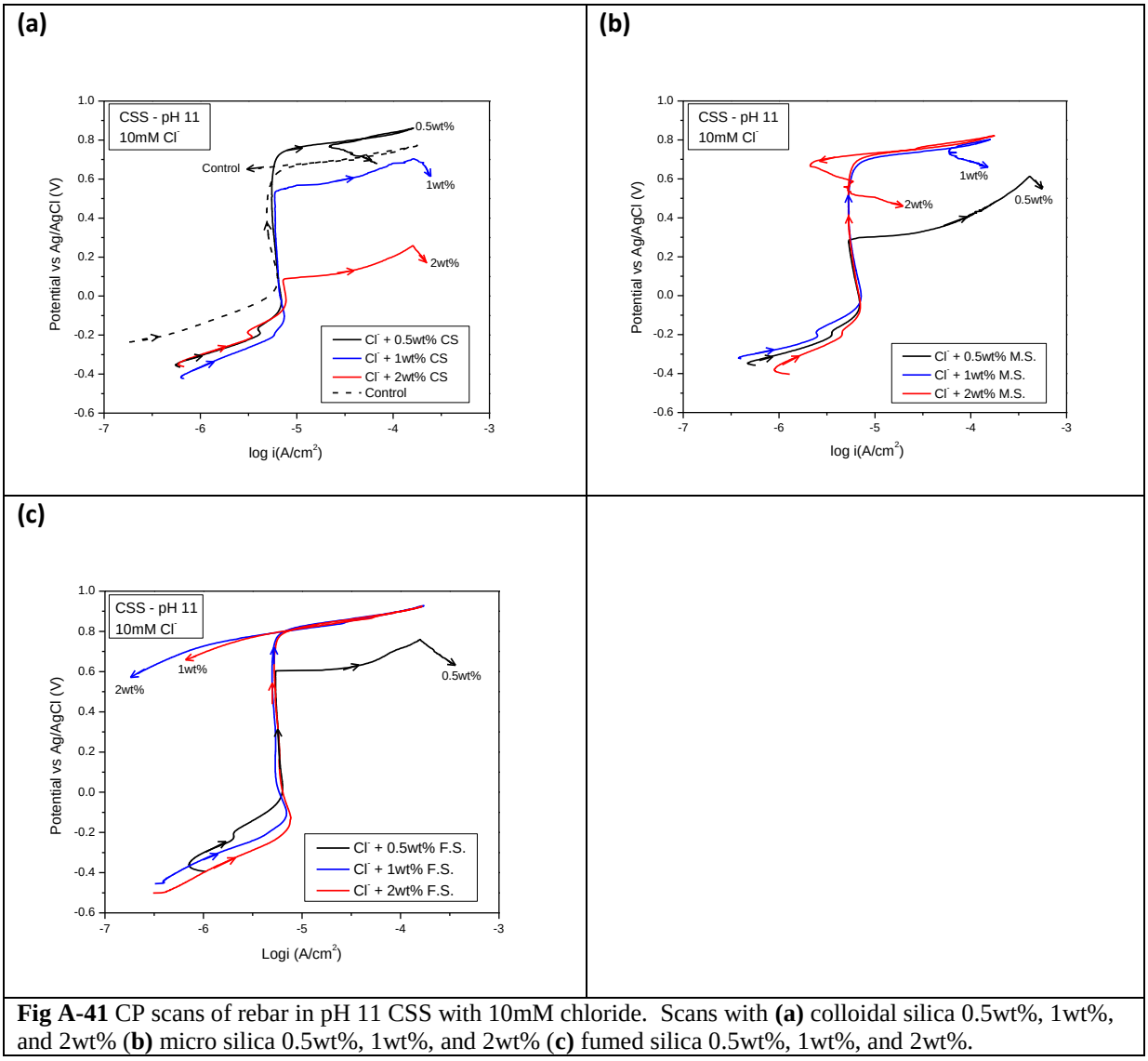

Fig A-41 CP scans of rebar in pH 11 CSS with 10mM chloride. Scans with **(a)** colloidal silica 0.5wt%, 1wt%, and 2wt% **(b)** micro silica 0.5wt%, 1wt%, and 2wt% **(c)** fumed silica 0.5wt%, 1wt%, and 2wt%.

Fig. A-41a demonstrates that as the concentration of colloidal silica increases, the poorer the corrosion resistance of the rebar. Increasing concentrations of colloidal silica lead to earlier film breakdown potentials as well as increased return scans current densities. The CP with 0.5wt% colloidal silica has the lowest return scan current density compared to the experiments with 1wt% and 2wt% colloidal silica. Colloidal silica is not serving as an inhibitor and may even be impeding the passive film formation. Colloidal silica is the smallest particle morphology studied and the interaction of any particles with the metal surface during critical film formation could prevent a protective passive film forming.

As opposed to colloidal silica, the addition of micro silica improves corrosion resistance. Initially with a micro silica concentration of 0.5wt%, the return current density is always larger than forward scan with

pronounced localized corrosion. With the addition of 1wt% and 2wt% micro silica, there are some portions of the return scan that have either smaller or identical current densities to the forward scan, especially in the case of 2wt% micro silica. The higher concentrations also increase the film breakdown potential as compared to the 0.5wt% sample. This morphology of silica has the smallest surface area of the three silica's tested.

The final admixture of fumed silica is presented in Fig. A-41c. These scans showed that fumed silica performed the best of the three silica's. Additions of 1wt% and 2wt% fumed silica resulted in total negative hysteresis for both scans, indicating good protection from localized corrosion. However the rebar CP scan in solution with 0.5wt% fumed silica exhibited a quicker film breakdown and more aggressive localized corrosion. Fumed silica has the highest surface area at ~400m^2/g of the silica's and the effects of this large area should be further examined.

2.2.5 Effect of Silica Additives on Pitting Chloride Threshold

The following experiments study whether silica admixtures have any effect on the electrochemical processes of the rebar corrosion under the chloride attack. With the strong passive film steel has at high pH, a significant amount of chloride will have to be present in order to break down that film and begin localized corrosion of the steel. If the silica additives are able to increase the threshold chloride concentration, their benefits could be two-fold. Not only would they slow diffusion of corrosive species, but they could help protect the rebar from the corrosive species once they have eventually reached the surface. The following experiments were performed to examine this hypothesis.

Cyclic Polarization Studies

Cyclic polarization was carried out on the rebar steel specimens by scanning the potentials from open circuit potential (OCP) into trans-passive potentials until a current density of 100 µA/cm^2 (or 0.1mA/cm^2) was reached, and reversing the potential scan back towards OCP. A scan rate of 1 mV/s was used in all cyclic polarization experiments. Fig. A-42 below are CP results for rebar in pH 12.5 CSS with colloidal (CS), micro (MS), and fumed (FS) silica admixtures. CP were used to determine the minimum concentration of chloride necessary to begin pitting corrosion.

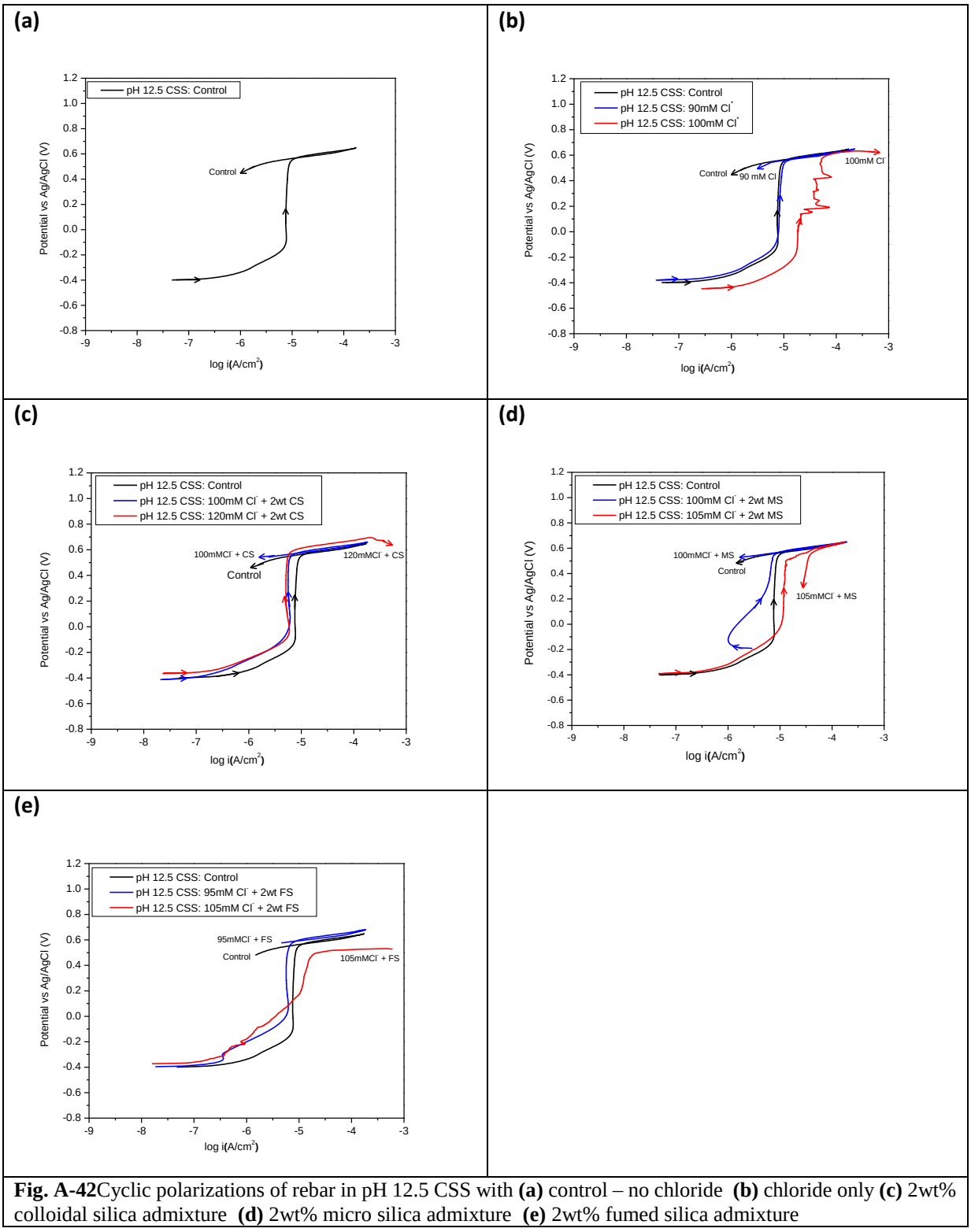

Fig. A-42 Cyclic polarizations of rebar in pH 12.5 CSS with **(a)** control – no chloride **(b)** chloride only **(c)** 2wt% colloidal silica admixture **(d)** 2wt% micro silica admixture **(e)** 2wt% fumed silica admixture

By interpreting identical CP experiments conducted at pH's 11 and 9, the threshold concentrations for chloride required to initiate localized corrosion is increased from 0.6 to ~8mM. At the natural concrete pH

of 12.5 the chloride threshold required for pitting is ~100mM. Chloride concentration thresholds in CSS for each silica additive (2wt%) are given as follows:

Table 22. Rebar Chloride Pitting thresholds as a function of silica additive and pH of CSS

	pH 12.5	pH 11.0	pH 9.0
Chloride Only	95mM Cl^-	8mM Cl^-	0.6mM Cl^-
Colloidal Silica	110mM Cl^-	5mM Cl^-	0.3mM Cl^-
Micro Silica	100mM Cl^-	2mM Cl^-	0.4mM Cl^-
Fumed Silica	100mM Cl^-	7mM Cl^-	0.45mM Cl^-

In all cases except at pH 12.5, fumed silica performs the best of any of the silica admixtures. At pH 12.5 all silica admixtures raise the threshold concentration of chloride required to initiate localized corrosion with colloidal silica performing the best, followed closely by micro and then fumed silica. However, at pH's 11 and 9, silica admixtures lower the amount of chloride required to begin pitting. This could be explained by examining the stability of silica at high pH. At high pH 12.5, the silica settles rapidly out of solution and remains a solid in the bottom of the jar. At the lower pH of 9 and 11, the silica remains suspended in solution much longer and colloidal never fully settles from solution at pH 9. As the pH's drops, the silica's could become more stable in solution with an established equilibrium between solid and soluble silica. At pH 12.5 the silica is totally insoluble and remains a solid. These silica admixtures have a very high surface area (colloidal: 200m^2/g, micro: 2m^2/g, fumed: 400m2/g) and the solid silica could be adsorbing chloride out of solution. If the silica's become unstable and chloride is allowed to remain in solution, the silica would be detrimental in preventing corrosion at a pH of 9 or 11.

In Fig. A-42b as the current density reached a value of 100µA/cm^2, the potential scan was reversed, and negative hysteresis of I-V behavior observed. When 90mM chloride was in the reverse scan current density was much lower than forward scan current density once potentials were lower than the transpassive range. This behavior indicated that the passivation of steel was not locally disrupted at high polarization potentials. Therefore, the transpassivity could be related to oxygen evolution and uniform oxidative dissolution of the passive layer following the reactions:

$$4OH^- \rightarrow 2H_2O + O_2 + 4e^- \quad (1)$$

$$Fe_2O_3 + 6OH^- \rightarrow 2Fe^{3+} + 3H_2O + 3O_2 + 12e^- \quad (2)$$

$$Fe^{3+} + 4H_2O \rightarrow FeO_4^{2-} + 8H^+ + 3e^- \quad (3)$$

Increasing the chloride concentration to 100mM was observed to cause passive layer breakdown, as the reverse scan did not trace back through the transpassive region.

Potentiostatic Studies

Potentiostatic passivation was carried out at fixed potentials for one hour. Usually the current decayed with time as the passive film continued to thicken. If the passive film became unstable, then the current increased instead of decaying. In such cases, the test was interrupted when the current density reached 100 $\mu A/cm^2$ or $0.1mA/cm^2$. These poteniostatic studies were carried out for two reasons. The first reason was to study the stability of the passive films formed by different anodically imposed potentials. The second reason was to prepare passive films on the rebar in order to study the film with electrochemical impedance spectroscopy (EIS), the results of which will be presented in later sections. Fig. A-43 below present the results for potentiostatic studies at pH 12.5 with chloride and silica admixtures present.

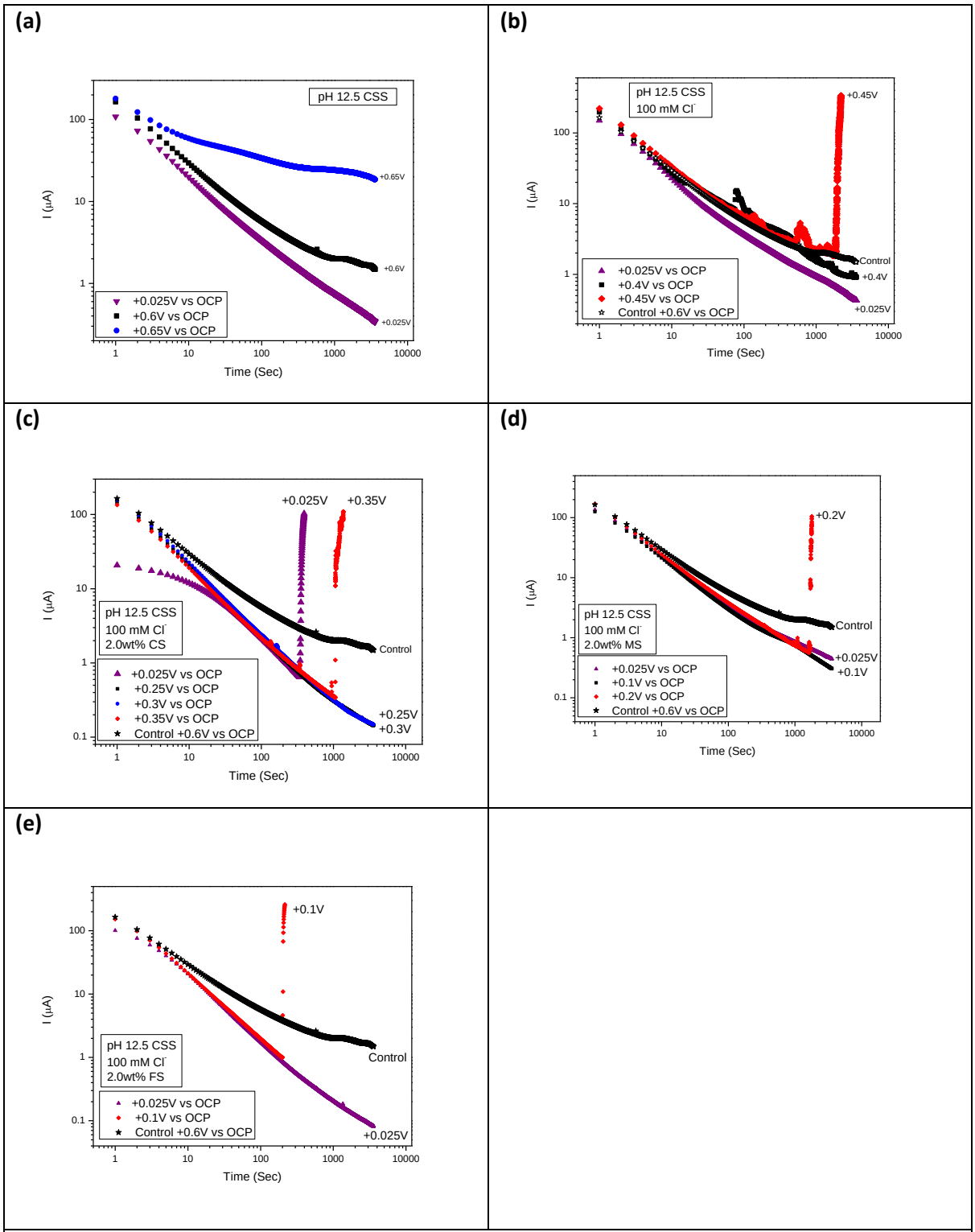

Fig. A-43 Potentiostatic polarization studies of rebar in pH 12.5 CSS solutions with **(a)** Control – no chloride **(b)** Chloride only 100mM **(c)** chloride + 2wt% colloidal silica admixture **(d)** chloride + 2wt% micro silica admixture **(e)** chloride + 2wt% fumed silica admixture.

The *I-t* plots of rebar steel in pH 12.5 cement solution without chloride are given in Fig. A-43. The current decay shows a linear trend when plotted in log-log scale for the potentiostatic control at $0.025V_{Ag/AgCl}$. The 0.025 $V_{Ag/AgCl}$ was in the middle of the passive potential range seen during cyclic polarization. The current decay behavior can be expressed as

$$i=\alpha t^{-n}$$

Where i = passivation current density at time t, α = a constant related to exchange current density of the fresh steel surface in the test environment and n = passivation kinetic exponent. The higher the value of 'n' faster the passivation kinetics. The passivation kinetic exponents of the potentiostatic plots seen in Fig. A-43 above and for identical experiments conducted at pH's 9 and 11, are presented in Table 23.

Table 23. Passivation Kinetic Exponents at pH's 9, 11, and 12.5.

Experiments at pH 9		
	Potential vs OCP (V)	n
Control	+0.025	-0.37
	+0.70	-0.72
	+0.75	-0.99
Cl^- Only	+0.025	-0.37
	+0.70	-1.09
	+0.75	-1.10
	+0.80	-0.89
Cl^- + Colloidal	+0.025	-0.63
	+0.45	-0.98
	+0.50	-1.02
Cl^- + Micro	+0.025	-1.05
	+0.70	-1.05
	+0.75	-1.04
Cl^- + Fumed	+0.025	-0.91
	+0.90	-0.93
	+0.95	-1.00

Experiments at pH 11		
	Potential vs OCP (V)	n
Control	+0.025	-0.841
	+0.6	-0.821
	+0.65	-0.966
Cl^- Only	+0.025	-0.904
	+0.1	-0.988
	+0.15	-1.044
Cl^- + Colloidal	+0.025	-0.988
Cl^- + Micro	+0.025	-0.999
Cl^- + Fumed	+0.025	-1.015

Experiments at pH 12.5		
	Potential vs OCP (V)	n
Control	+0.025	-0.679
	+0.6	-0.617
	+0.65	-0.244
Cl^- Only	+0.025	-0.605
	+0.4	-0.628
	+0.45	-0.635
Cl^- + Colloidal	+0.025	-0.865
	+0.3	-0.849
	+0.35	-0.848
Cl^- + Micro	+0.025	-0.688
	+0.1	-0.644
	+0.2	-0.74
Cl^- + Fumed	+0.025	-0.854
	+0.1	-1.025

These values indicate that increasing the potential resulted in slower passivation kinetics, even in the absence of chloride. Furthermore, higher the applied potential larger the current densities at initial (t=1s) and final (t=1h) time durations. These higher currents and slower passivation kinetics imply that dissolution of the passive layer was predominant at higher potentials rather than at lower potentials. The passivation kinetic exponents did not vary significantly with pH changes.

EIS Studies

Electrochemical impedance spectroscopy was carried out on previously passivated specimens. During each EIS run10 mV amplitude of *ac* voltage was super imposed over the film formation potentials and frequency scanned from 100 kHz to 0.01 Hz using a three electrode configuration and a potentiostat (Gamry Instruments, USA, model: Reference 600).

Representative Bode and Nyquist plots are show below in Fig. A-44 for a typical sample scan. Results for Equivalent Electrical Circuit (EEC) modeling of these results are given in the Tables below. Fig. A-44 below provides a graphical representation of the EECs used to model these experiments. The passive layers grown at high potential showed depressed semicircles in the Nyquist plot, and the passive film grown at 0.025V showed very high impedance at low frequencies. These EIS data were fitted to an equivalent electrical circuit consisting of two hierarchical parallel RC loops in series with the resistance of the electrolyte as proposed by Sanchez et.al. The equivalent circuits used are illustrated in Fig. A-45.

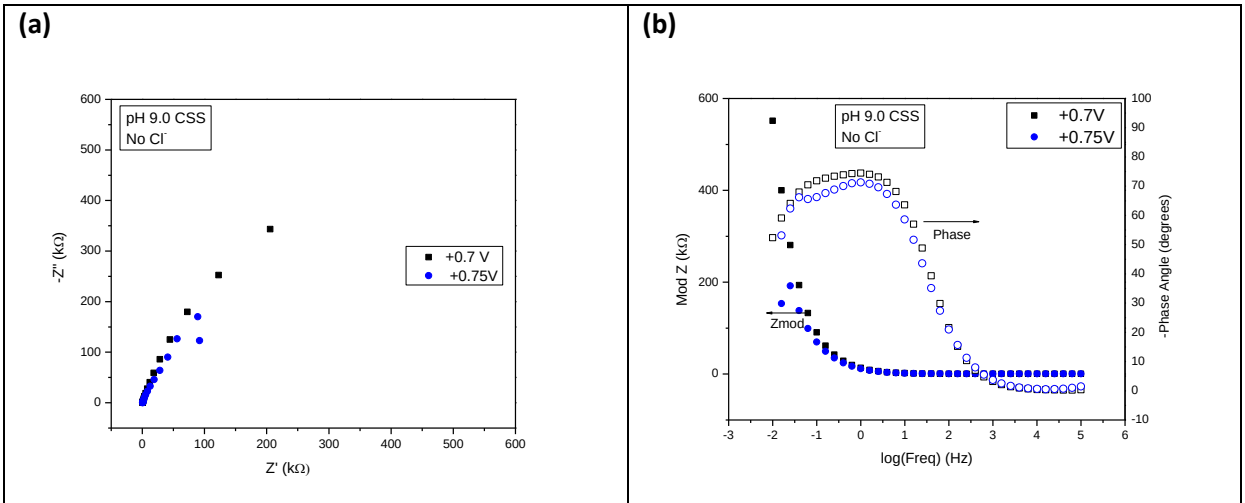

Fig A-44 Representative EIS results. Rebar in pH 9 CSS control solution. **(a)** Nyquist plots **(b)** Bode plots

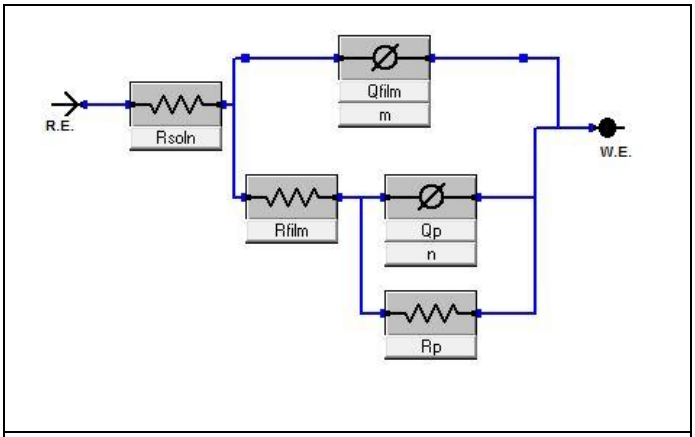

Fig A-45 Equivalent Electrical Circuits used to model EIS experiments

Tables 24-28 summarize values for the circuit elements. The element R_s represents resistance due to electrolyte, R_f represents the charge transfer resistance, R_p corresponds to resistance due to redox reactions involving the re-precipitated passive layer, Q_f is a constant phase element associated with interfacial capacitance and Q_p represents capacitance associated with the passive layer [19]. The element Lp symbolizes an inductor. This term is needed to capture the adsorption behavior of the silica experiments conducted at pH 11. The values of R_f and R_p decreased with increase in the applied potentials whereas C_f and C_p increased with increase in potentials. It is reported that higher resistance values and lower capacitance values result in good passivity. The EIS data correlated well with potentiostaic*I-t* data where the passivation at 0.025V was found to result in a more protective passive film.

Table 24. EEC Modeling of EIS Experiments at pH 9

	Control			Cl Only		
E vs OCP	+0.025	+0.7	+0.75	+0.025	+0.7	+0.75
Rs (Ohm)	541.6	5.32E+02	374.6	498	559.8	549
Rp (Ohm)	4.29E+05	2.23E+06	8.37E+10	1.39E+05	4.38E+05	4.51E+07
Rf (ohm)	6.75E+05	7.34E+00	185.7	9.06E+05	2.25E+04	1.94E+11
Cp	3.23E-13	8.95E-07	1.75E-05	4.58E-13	2.34E-05	1.67E+01
Cf	2.76E-05	1.52E-05	3.73E-06	2.57E-05	1.72E-05	2.09E-05

Table 25. EEC Modeling of EIS Experiments at pH 9 with silica admixtures

	Colloidal			Micro		
E vs OCP	+0.025	+0.45	+0.5	+0.025	+0.7	+0.75
Rs (Ohm)	457.3	517.5	493.4	472	520.8	531.3
Rp (Ohm)	4.87E+08	5.88E+05	1.08E+04	1.81E+06	1.57E+06	2.60E+03
Rf (ohm)	7.72E+05	1.50E+06	3.96E+03	5.11E+05	12.27	1.26E+03
Cp	1.20E-05	9.28E-06	7.12E-06	3.50E-06	5.57E-06	1.55E-05
Cf	2.73E-05	1.24E-05	8.83E-06	2.33E-05	1.16E-05	7.46E-06

	Fumed		
E vs OCP	+0.025	+0.9	+0.95
Rs (Ohm)	500	515.2	534.5
Rp (Ohm)	6.82E+05	6.49E+04	6.89E+03
Rf (ohm)	4.81E+06	245.5	1.03E+03
Cp	8.80E-06	1.80E-05	3.60E-06
Cf	2.32E-05	1.36E-05	3.34E-05

Table 26.EEC Modelling of EIS Experiments at pH 11

	E vs OCP (V)	Rs	Rp	Rf	Qp	Qf	
Control	+0.025	429.4	8.09E+06	1.66E+05	3.55E-06	2.44E-05	
	+0.6	429.8	6.81E+05	3.61E+05	3.43E-06	1.29E-05	
	+0.65	417.5	3.97E+05	2.22E+02	1.36E-05	6.53E-06	
Cl Only	+0.025	376.2	7.95E+05	4.14E+05	8.70E-06	2.23E-05	
	+0.1	336.5	9.36E+05	2.96E+05	6.53E-06	1.93E-05	
	+0.15	349.9	9.59E+02	9.84E+02	9.46E-06	1.33E-05	
	E vs OCP (V)	Rs	Rp	Rf	Qp	Qf	Lp
Colloidal	+0.025	3.62E+02	1.09E+03	1.15E+03	1.43E-05	1.63E-05	1.53E-01
Micro	+0.025	4.01E+02	3.91E+01	1.87E+03	2.42E-03	2.52E-05	3.60E+02
Fumed	+0.025	3.42E+02	1.30E+03	1.18E+03	1.07E-05	1.42E-05	2.72E-02

Table 27. EEC Modelling of EIS Experiments at pH 12.5

	Control			Cl Only		
Potential vs Ag/AgCl (V)	0.025	0.6	0.65	0.025	0.4	0.45
Rs(Ohm)	51.54	80.7	71.14	50.41	89.35	94.55
Rp (Ohm)	2.30E+14	4.13E+04	1.53E+03	3.31E+05	4.15E+04	3.09E+03
Rf (ohm)	3.29E+04	4.31E+01	1.45E+01	9.65E+04	4.88E+01	2.17E+01
Cp	2.71E-05	3.08E-05	9.51E-05	3.21E-05	3.67E-05	6.63E-05
Cf	1.73E-05	2.65E-05	3.16E-05	1.88E-05	2.61E-04	3.39E-05

Table 28.EEC Modelling of EIS Experiments at pH 12.5 with silica admixtures

	Colloidal			Micro		
Potential vs Ag/AgCl (V)	0.025V	0.3V	0.35V	0.025V	0.1V	0.2V
Rs (Ohm)	141.8	83.46	80.8	52.38	3.86E+01	5.30E+01
Rp (Ohm)	6.99E+02	1.00E+06	6.42E+03	9.87E+06	1.29E+06	2.35E+03
Rf (ohm)	3.53E+02	3.99E+05	5.30E+03	4.51E+04	5.37E+04	3.22E+03
Cp	8.29E-06	4.85E-06	2.28E-04	2.56E-05	8.07E-06	2.33E-04
Cf	1.11E-04	1.11E-05	1.13E-05	1.78E-05	1.43E-05	1.36E-05
	Fumed					
Potential vs Ag/AgCl (V)	0.025V	0.1V				
Rs (Ohm)	139	133.4				
Rp (Ohm)	1.16E+06	44.72				
Rf (ohm)	9.00E+05	315.9				
Cp	3.22E-06	3.49E-05				
Cf	1.27E-05	1.05E-05				

All experiments were modeled with the equivalent electrical circuit shown in Fig. A-45 except for the experiments conducted at pH 11 with silica admixtures. These experiments all performed at +0.025V vs OCP, showed pitting corrosion and visible reaction product formed on the surface. Bode and Nyquist plots showed areas of positive imaginary impedance and positive phase angle indicating adsorption of the silica's. The model was therefore modified to include the inductor element to capture this behavior. These indicators of silica adsorption onto the rebar surface were not seen in the experiments conducted at pH's 9 and 12.5 indicating a change in the stability of silica admixtures at pH 11. These experiments were modeled using a modified equivalent electric circuit.

Mott-Schottkey Studies

Mott-Schottky measurements were conducted at a frequency (*f)* of 100 Hz by scanning the potential of the sample from the film formation potential to OCP at 100 mV steps for every two seconds. The capacitance (*C*) of the space charge layer was calculated from the imaginary impedance (*Z"*) using the relation

$$C = -1/(2\pi f Z'')$$

All potentials reported here are relative to the Ag/AgCl (immersed in saturated KCl) reference electrode. Fig. A-46a-b below presents representative Mott-Schottkey plots of rebar in direct contact with CSS. Values for the charge carrier density and flat band potential for all experiments are given below in Table 29.

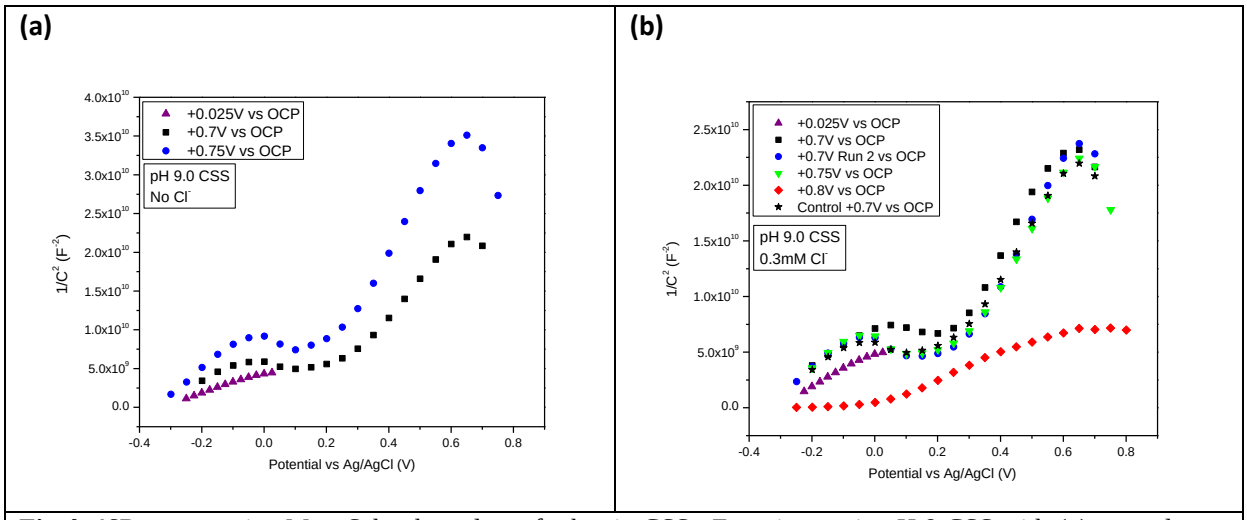

Fig A-46 Representative Mott-Schottkey plots of rebar in CSS. Experiments in pH 9 CSS with **(a)** control – no chloride **(b)** chloride only [8mM].

From the slopes of these Mott-Schottkey plots the charge carrier densities are calculated.

Table 29. Calculated charge carrier densities for experiments with rebar in CSS at **(a)** pH 9 **(b)** pH 11**(c)** pH 12.5.

(a)			**(b)**		
	Potential vs OCP (V)	Charge carrier density (cm^{-3})		Potential vs OCP (V)	Charge carrier density (cm^{-3})
Control	+0.025	3.59E+20	Control	+0.025	5.91E+20
	+0.7	2.92E+20		+0.6	2.55E+20
	+0.75	1.56E+20		+0.65	2.43E+20
Cl Only	+0.025	3.10E+20	Cl Only	+0.025	5.28E+20
	+0.7	3.15E+20		+0.1	5.17E+20
	+0.75	2.34E+20		+0.15	2.89E+21
	+0.8	3.93E+20	Colloidal	+0.025	1.82E+21
Colloidal	+0.025	4.49E+20	Micro	+0.025	9.85E+20
	+0.45	2.14E+20	Fumed	+0.025	3.82E+20
	+0.5	2.38E+20			
Micro	+0.025	3.78E+20			
	+0.7	1.20E+20			
	+0.75	1.50E+20			
Fumed	+0.025	3.36E+20			
	+0.85	1.16E+20			
	+0.9	1.69E+20			
	+0.95	1.38E+20			
(c)					
	Potential vs OCP (V)	Charge carrier density (cm^{-3})			
Control	+0.025	4.96E+20			
	+0.6	2.76E+20			
	+0.65	3.05E+20			
Cl Only	+0.025	7.50E+20			
	+0.4	2.30E+20			
	+0.45	6.92E+23			
Colloidal	+0.025	8.89E+22			
	+0.25	2.65E+20			
	+0.3	2.48E+20			
	+0.35	5.70E+20			
Micro	+0.025	6.62E+20			
	+0.1	6.07E+20			
	+0.2	2.24E+21			
Fumed	+0.025	1.60E+20			
	+0.1	4.93E+22			

The formation of a less protective passive layer at high applied potentials as seen in the previous discussion on EIS, can be further confirmed by looking at the Mott-Schottky results presented in Fig. A-46. In this

diagram, linear regions with both positive and negative slopes can be seen. The positive slopes of the potentials vs. $1/C^2$ indicate *n*-type behavior and negative slopes indicate p-type semiconducting behavior. It is well documented that the passive film of iron exhibits *n*-type conductivity. The charge carrier densities determined for the *n*-type behavior were $4.9x10^{20}$, $2.77x10^{20}$and $3x10^{20}cm^{-3}$ for the passive films formed at 0.025, 0.6 and $0.65V_{Ag/AgCl}$ respectively. These values are similar to those reported by other investigators. At potentials nobler than $0.4V_{Ag/AgCl}$, p-type behavior was observed in this study and by other researchers as well. Williamson and Isgor attributed the *p*-type behavior to formation of an inversion layer enriched with holes due to very large band bending caused by the anodic polarization. An alternated explanation is based on the following reaction that could occur on the electrode:

$$2Fe^{3+} + 2[O] + 2H_2O \rightarrow 2Fe^{5+} + 4OH^- \qquad (10)$$

At potentials more positive than 0.3 $V_{Ag/AgCl}$ in pH 12.5, oxygen evolution is thermodynamically possible. Oxygen could oxidize the Fe^{3+} in the passive layer to Fe^{5+}creating cation vacancies in the passive film. These vacancies are produced by chemical dissolution in order to maintain charge neutrality. According to the point defect model, these cation vacancies are precursors for passive film breakdown. Formation of cation vacancies also make the passive layer less protective. The charge carrier densities of the p-type layer were $1.1x10^{20}$ and $9.6x10^{19}cm^{-3}$ at 0.6 and $0.65V_{Ag/AgCl}$ respectively. The reaction (10) should in fact, go from right to left and not the other way as proposed here. However, it should be noted that the oxygen evolution reaction (OER) requires over potentials and occurs in multiple steps as given below:

$$Fe^* + OH^- \rightarrow Fe^*\text{-}OH_{ads} + e^- \qquad (11)$$

$$OH^- + Fe^*\text{-}OH_{ads} \rightarrow Fe^*\text{-}O_{ads} + H_2O + e^- \qquad (12)$$

$$2O_{ads} \rightarrow O_2 \qquad (13)$$

Here Fe* represents the catalytic site of the passive iron surface. The onset of OER on hydrous iron oxide has been reported to occur at about $0.7V_{Ag/AgCl}$ in pH 12.5 electrolyte, with an over potential at about $0.4V_{Ag/AgCl}$. Therefore, at potentials between 0.4 and $0.7V_{Ag/AgCl}$, the intermediate steps occur and make the reaction (10) a possible step. Furthermore, hole localization on 'O' was suggested as a necessary step for water oxidation reaction. Formation of Fe cations with valence state higher than +3 can be considered as hole accumulation. The hole formation and formation of higher valent Fe cations (Fe(IV) – Fe(VI)) are similar phenomena in line with formation of an inversion layer due to high band bending or electron depletion. The hole accumulation on the top surface layer could be considered a precursor for electrostatic attraction of chloride ions which lead to passivity breakdown. Based on Mott-Schottky results, it is proposed

that at high applied potentials the top surface of the passive layer is *p*-type and the bottom layer of the passive film is n-type.

2.3 Conclusions

1. The addition of 0.25wt% and 1.0wt% glycerol produced no significant effect in any of the experiments performed. Adding glycerol, even up to 1wt%, was insufficient to protect the rebar samples when chloride is present at concentrations of 3.5wt%.

2. Chloride had a pronounced effect on all experiments measured in this report. When chloride was present, dramatic corrosion was observed. OCP's for experiments with chloride were more cathodic that those without chloride. In LP experiments the RP values were a factor of ten smaller for samples with chloride compared to samples without chloride. Tafel polarizations showed that corrosion rates for samples with chloride were consistently larger than for samples without chloride. CP's showed some of the most pronounced effects of chloride. Samples with chloride pitted and corroded dramatically, while those that did not have chloride present repassivated. In samples without chloride, the passive region was characterized by a vertical line that spanned approximately 1 volt of potential.

3. Oxygen was found to compound the negative effects of chloride if the chloride was added. However, oxygen had no noteworthy effect if there was no chloride present. In OCP experiments, oxygen had no observable effect. LP experiments showed that samples with oxygen and chloride had smaller Rp's than samples with chloride but no oxygen. Tafel polarizations presented no observable effects of oxygen on the corrosion rate. CP analysis demonstrated much worse pitting for samples with both oxygen and chloride compared to samples with chloride but without oxygen. This difference in severity of pitting can be seen by the size of area enclosed by the CP plots.

4. Colloidal silica: Increased amounts of colloidal silica lead to earlier film breakdowns and all concentrations showed localized corrosion present.

5. Micro silica: Additions of micro were beneficial. Increasing the micro silica concentration increased the film breakdown potential and lead to decreased localized corrosion currents.
6. Fumed silica: Fumed silica performed the best out of the three silica's in terms of reducing the corrosion of rebar samples. One the concentration reached 1wt%, the sample was protected from

localized corrosion and both scans returned with negative hysteresis. Based on these studies, fumed silica is the recommended morphology for silica admixture.

7. The threshold concentration of chloride required to initiate localized corrosion were determined to be as follows:

    pH 12.5

    - Chloride Only: 95mM
    - Colloidal Silica: 110mM
    - Micro Silica: 100mM
    - Fumed Silica: 100mM

    pH 11

    - Chloride only: 8mM
    - Colloidal silica: 5mM
    - Micro silica: 2mM
    - Fumed silica: 7mM

    pH 9

    - Chloride Only: 0.6mM chloride
    - Colloidal silica: 0.3mM chloride
    - Micro silica: 0.4mM chloride
    - Fumed silica: 0.45mM chloride

8. The passivation kinetics of the rebar steel generally increased in the presence of silica admixtures at all pH conditions.
9. The electronic properties of the passive layers were not altered by the addition of silica admixtures.
10. The charge carrier densities were not affected by the presence of silica admixtures.

SECTION 3

CYCLIC VOLTAMMETRY OF REINFORCEMENT STEEL AND STAINLESS STEEL 316 IN CEMENT SATURATED SOLUTION (CSS) AND CEMENT SOLUTION SIMULATED WITH SODIUM HYDROXIDE

3.1 Experimental procedure

Previous work focused on rebar corrosion in CSS solution by means of linear polarization (LP) and cyclic polarization (CP). Now the electrode/solution interface of rebar/cement saturated solution will be analyzed using Cyclic Voltammetry (CV). Literature has been extensively published on steel in alkaline solutions created by NaOH or $Ca(OH)_2$ to simulate concrete environments. Our CSS is leached directly from actual Portland cement and pressure filtered, creating a more accurate representation of the mineral species present in real concrete pore solution. The following experiments have been performed to characterize the many species present in the leach solution and their effect on rebar and SS 316 electrochemistry. These experiments will also contest whether NaOH solution provides a valid representation of real cement solution. Four different parameters were considered.

1) Effect of working electrode composition: rebar vs SS 316.
2) Effect of solution composition: real cement solution vs NaOH, pH 12.5, 11, 9.
3) Effect of carbonation of NaOH solution: pH 12.5, 11, 9.
4) Effect of atmosphere and silica additions: colloidal silica, micro silica, fumed silica

3.1.1 Electrode Preparation

A rebar working electrode was machined from a Nucor #5 steel rod. The composition of the steel was 0.42% C, 1.16% Mn, 0.01% P, 0.045% S, 0.19% Cu, 0.08% Ni, 0.08% Cr, 0.019% Mo, 0.0007% V, and Fe balance. The elongation, yield, and tensile strengths were: 13%, 470 MPa and 757 MPa, respectively. This electrode is unique in that it was created by Dr. Pesic to have two different surface areas. The smaller area is best suited to cyclic voltammetry which can be distorted by large currents. The larger area can be used for cyclic polarizations which evaluate the resistance to pitting corrosion. This electrode can be seen below in Fig. A-47a. An identical electrode of stainless steel 316 (SS 316) was also created and can be seen below in Fig A-47b.

Once mounted in the epoxy, electrodes were polished with metallographic papers up to 2000 grit count. Electrodes were then polished on a wheel using 1μm alumina compound. Final polishing was performed by hand with 1μm diamond slurry. Between each step the electrode was rinsed with DI water and dried with compressed air. Note between each CV run electrodes were polished with diamond slurry ensuring a fresh surface.

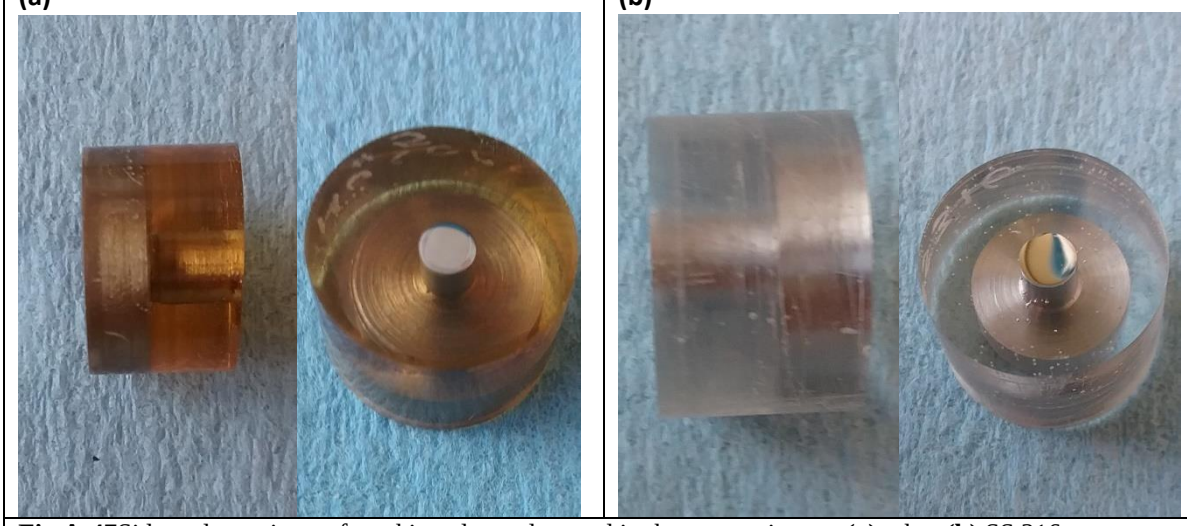

Fig A-47 Side and top views of working electrodes used in these experiments **(a)** rebar **(b)** SS 316.

3.1.2 Solution Preparation

Two types of solution were studied, Type 1) and Type 2). First was the real cement saturated solution (CSS), and second a sodium hydroxide solution. The sodium hydroxide solution was in turn prepared in two separate ways described below, method a) and method b).

1) CSS was prepared by mixing 4 kg of commercial Type II Portland cement in 10 liters of de-ionized water. The Portland cement composition was 41-43 % CaO, 28-32% SiO_2, 7-10% Al_2O_3, 4.9-6% Fe_2O_3, 1-2% MgO, 2.4-2.8% SO_3, and 3.0-3.5% fly ash. To leach out the ionic species from the cement and prevent settling, the solution was constantly stirred over a three day period. The solution was then allowed to settle and subsequently pressure filtered to remove particulates. This filtered solution is referred to as cement saturated solution (CSS) and the pH was ~12.5. The pH was further lowered by bubbling CO_2 gas through the solution, and raised as necessary by adding NaOH.

2) The sodium hydroxide solutions were prepared with reagent grade NaOH crystals dissolved in DI water. The sodium hydroxide solutions were prepared by two different methods described below
    a) Sodium hydroxide solutions we prepared to pH's 9, 11, and 12.5 by dissolving NaOH crystals in DI water and adjusting as necessary with the NaOH dropper bottles.

b) Sodium hydroxide solutions were also prepared to pH's 9, 11, and 12.5 by dissolving NaOH crystals in DI water up to a pH of 13 and then adjusting the pH to the desired level using CO_2 gas. This method of solution preparation simulated the formation of carbonates that would occur in cement solutions exposed to the atmosphere.

3.1.2 Experimental Set up

A three electrode electrochemical cell was used. The Echem cell consisted of a steel working electrode, a Ag/AgCl reference electrode, and a glassy carbon counter electrode. A picture of the complete experimental setup can be seen below in Fig. A-48.

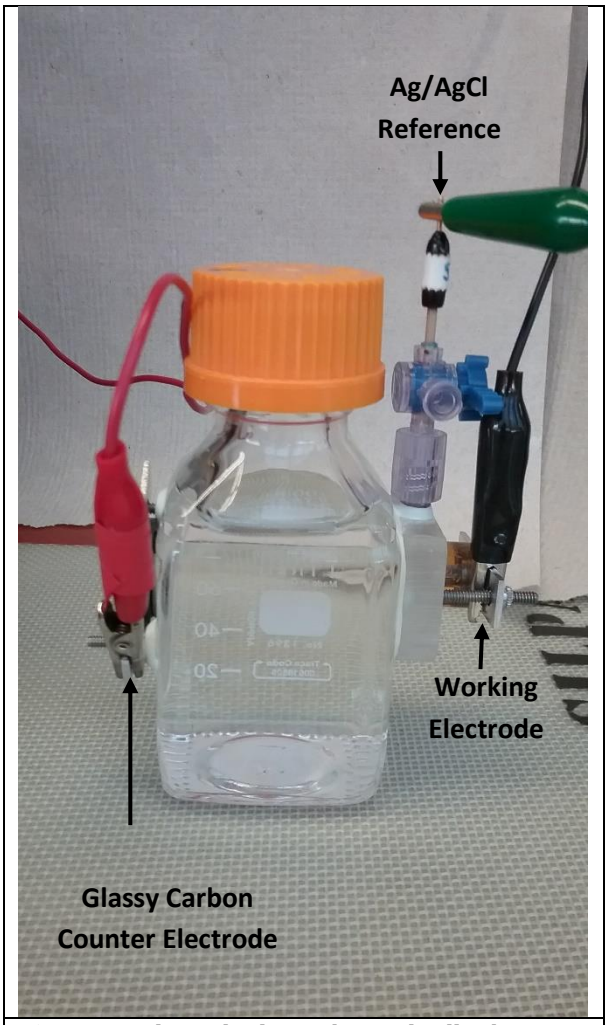

Fig A-483-Electrode electrochemical cell. The working electrode is side-mounted to the Echem cell wall.

The experimental procedure for CV was as follows. After polishing an electrode would be mounted onto the side of the Echem cell and solution poured in. The OCP was allowed to stabilize for 5 minutes. Once OCP was stable CV's were performed over desired potential ranges at preselected scan rates. For experiments where no corrosion was seen, had a 5 cycle CV scan run to examine the oxidation/reduction behavior. Scans with severe corrosion present were only run for 2 scans to avoid excessively damaging the electrode. Once the CV's were completed, steel electrodes were removed and re-polished.

Table 30 Standard experimental condition used throughout electrochemical tests

WE: Nucor rebar or SS316, A=0.071 cm^2	Solution: Cement Saturated Solution (CSS) or NaOH solution
CE: Glassy carbon	pH: 9, 11, 12.5
RE: Leak-free Ag/AgCl	Silica concentration (if added): 2wt%
Volume: 100ml	Atmosphere: air, unless otherwise stated
Temp: 25 C	

3.2 Results and Discussion

3.2.1 Effect of working electrode composition: Nucor rebar vs SS 316

Cyclic voltammetry was performed on rebar and SS 316 working electrodes to determine if alloy composition had any effect on oxidation/reduction peaks. Fig. A-49a-c present the results for rebar (Nucor #5, plain C steel) in CSS pH 12.5, pH 11, and pH 9. Fig. A-50a-c present the results for SS 316 under identical conditions.

49(a)

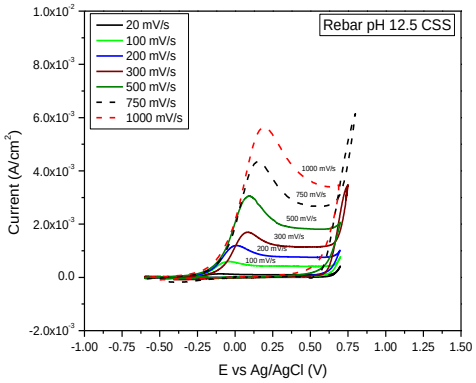

50(a)

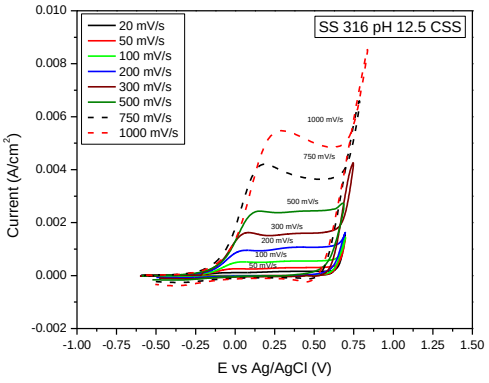

49(b)

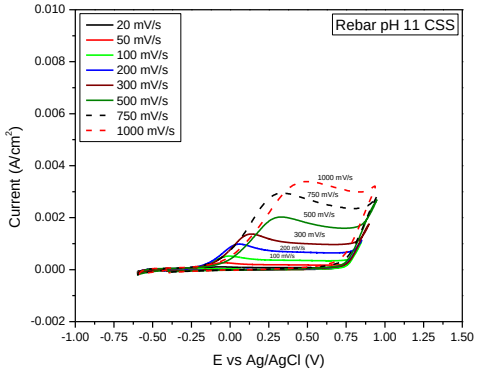

50(b)

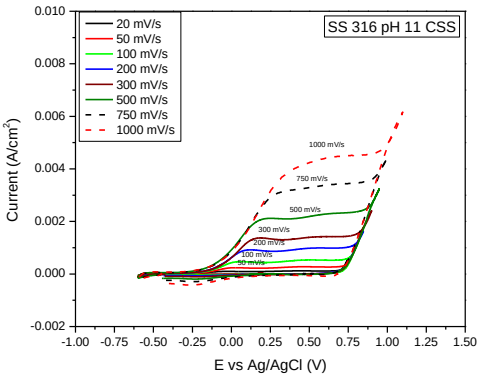

49(c)

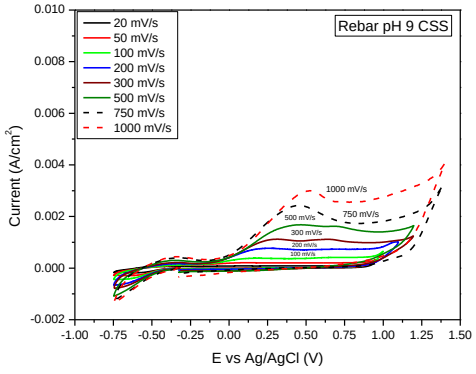

50(c)

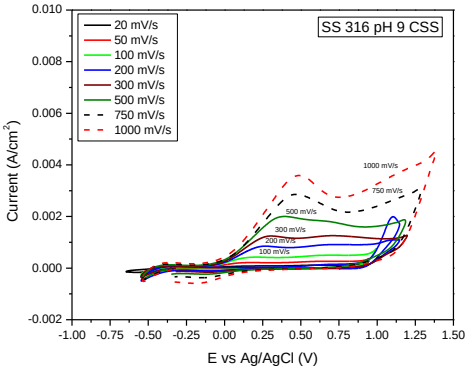

Fig. A-49 Cyclic voltammograms of rebar in CSS solutions at **(a)** pH 12.5 **(b)** pH 11 **(c)** pH 9

Fig. A-50 Cyclic voltammograms of SS 316 in CSS solutions at **(a)** pH 12.5 **(b)** pH 11 **(c)** pH 9

These scans were interpreted using the Randles-Sevcik equation with results presented below in Fig. A-51.

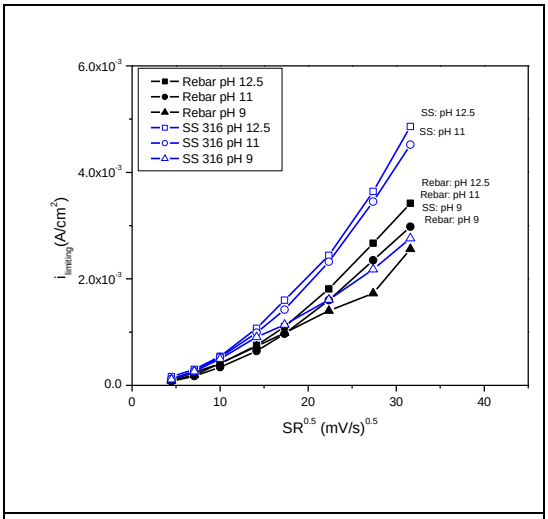

Fig. A-51 Randles-Sevcik equation plot as a test of reaction reversibility.

By examining Fig. A-49a-c it can be seen that as pH is lowered to 11 and 9, the overall anodic current decreases. The peak location, particularly from Figure 3a, is evidence of hydroxide ion oxidation. The reaction is presented below.

$$4OH^- \leftrightarrow 2H_2O + O2 + 4e^- \qquad E^\circ = 0.401V \text{ vs RHE} \qquad (1)$$

Considering this reaction, it follows that as hydroxide ion concentration and pH decrease the anodic currents also decrease.

It can be seen that the plots are essentially identical for SS 316 to the Nucor rebar across all pH's, Fig. A-50a-c. Thus the assumption that the surface reaction occurring in these experiments is controlled by composition of solution, and not by the alloy composition of the working electrode.

Fig. A-51 further affirms this assumption, it demonstrates that the behavior of the Randles-Sevcik equation is similar for both rebar and SS 316. From Fig. A-51 there is obvious non-linear behavior. The non-linearity could be caused by an interfering homogeneous chemical reaction between oxidation products and species present in the solution. Further studies could be conducted to examine this possibility.

3.2.2 Effect of solution composition: CSS vs NaOH

Two different solutions were studied (CSS solution and NaOH solution) to determine if the additional species present in CSS, such as Al, Ca, Mg, Si, effected CV scans differently than NaOH solution. Researchers commonly approximate concrete pore solution with NaOH solution and these experiments

examine if this approximation is valid over a range of pH's. The results for CV of rebar in CSS solutions at pH 12.5, 11, and 9 are presented below in Fig. A-52a-c. Identical experiments for rebar in NaOH solutions are presented in Fig. A-53a-c.

52(a)

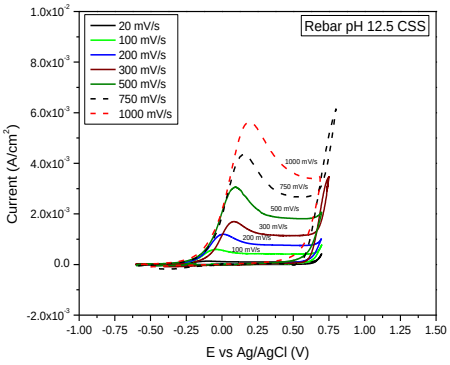

53(a)

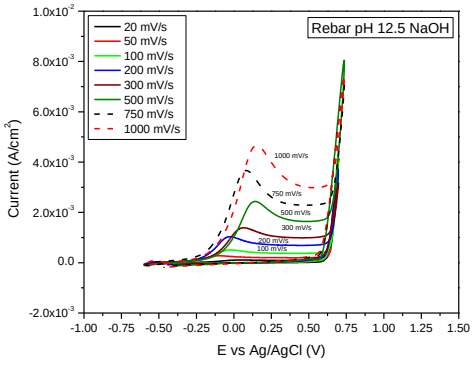

52(b)

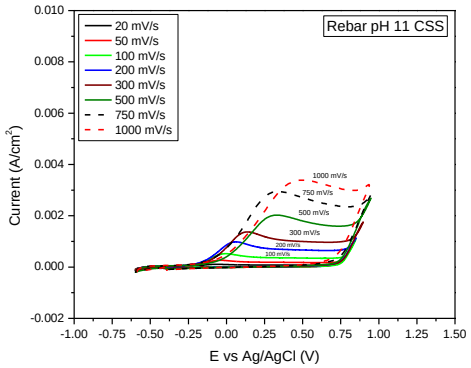

53(b)

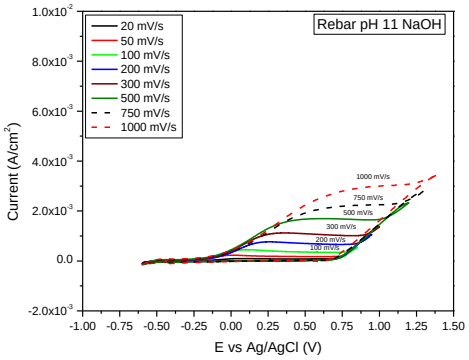

52(c)

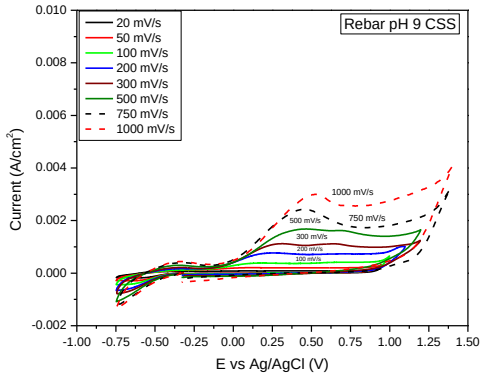

53(c)

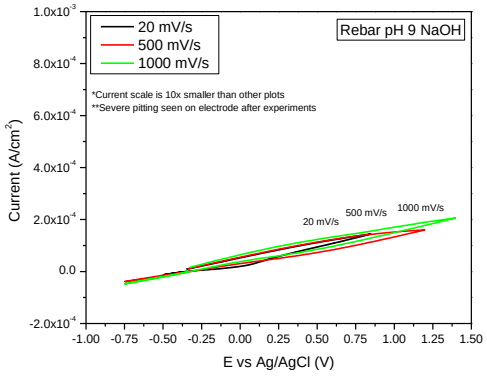

Fig. A-52 Cyclic voltammograms of rebar in CSS solutions at **(a)** pH 12.5 **(b)** pH 11 **(c)** pH 9

Fig. A-53 Cyclic voltammograms of rebar in NaOH solutions at **(a)** pH 12.5 **(b)** pH 11 **(c)** pH 9

Fig. A-52a-c and 53a-c were analyzed to determine the limiting current value for each scan. These values were then plotted verses the square root of scan rate to determine if the Randle's-Sevcik equation was applicable. The results are plotted below in Fig. A-54.

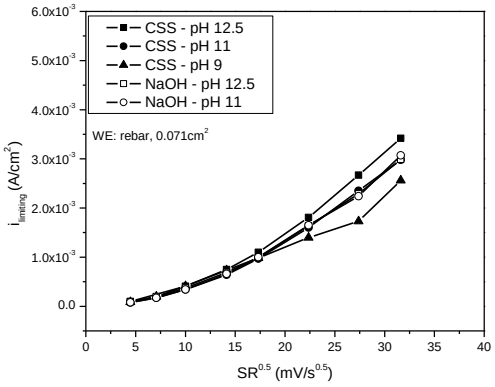

Fig A-54 Randle's-Sevcik equation analysis of rebar in CSS and NaOH.

It can be seen that at concrete's natural pH of 12.5, CVs of rebar in CSS and in NaOH are identical, Fig. A-52a and 53a. However, at pH 11 differences can be seen between the two solutions. For solution prepared to pH 11 with NaOH, Fig. A-53b, there are no pronounced peaks compared to those seen in Fig. A-52b, (CSS pH 11.0). This peaking is attributed to carbonate ions present in CSS solution as a result of CO_2 bubbling used to reduce the pH from 12.5 to 11.0. In NaOH solution that was prepared directly to pH 11 with NaOH crystals, the amount of carbonates present should be negligible.

At pH 9 a drastic difference appears between the CSS and NaOH solution, Fig. A-52c and 53c. Rebar in CSS shows results consistent with other experiments, Fig. A-52c, with lower currents. The lower currents can be attributed to a lack of hydroxides to be reduced. However, in NaOH solutions at pH 9 all passivity is lost and the plot is linear without any peaks or evidence of passivation. Even though the currents are much smaller, corrosion is visible on the electrode surface. To the naked eye the surface has a yellow tint, and investigation with optical microscopy confirmed surface corrosion. Micrographs taken before and after the experiments are presented below in Fig. A-55. Any passivation in a CO_2 adjusted CSS solution compared to corrosion in a pure NaOH solution has been attributed to carbonates. This assumption will be further expanded on shortly.

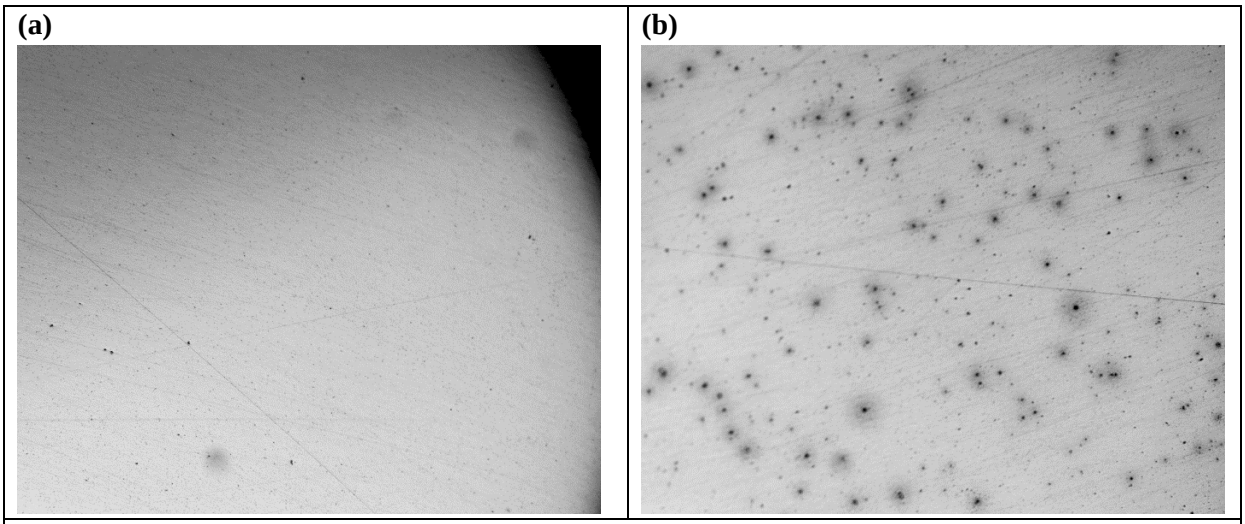

Fig A-55 Micrographs of rebar working electrode used in CV at pH 9 NaOH at 1000 mV/s. **(a)** before and**(b)** after CV run. All micrographs taken at 50x magnification.

3.2.3 Effect of carbonation of NaOH solution on CV of rebar

To determine the effect of carbonates, experiments were performed with rebar in two different types of NaOH solutions. The first type was prepared by adding enough NaOH to achieve the desired pH with no CO_2 additions; these experiments are shown above in Fig. A-56a-c and are reproduced below for comparison. The second type was prepared by adding NaOH to achieve a pH of 13 and then bubbling CO_2 gas to reduce the pH, these experiments are shown below in Fig. A-57a-c.

56(a)

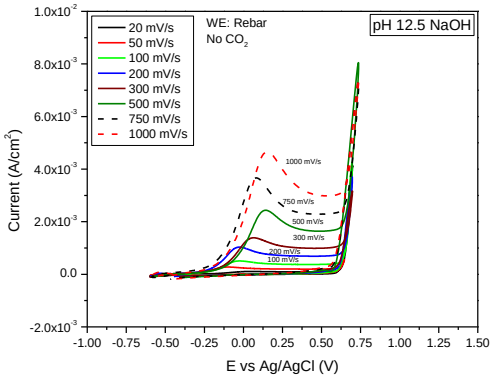

57(a)

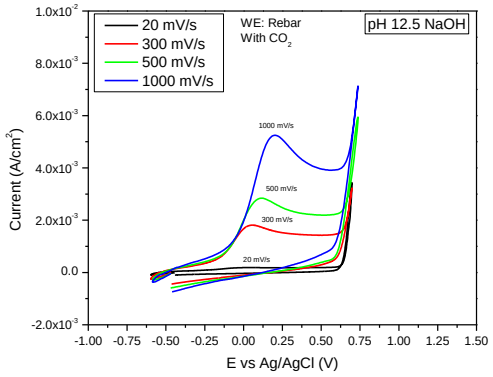

56(b)

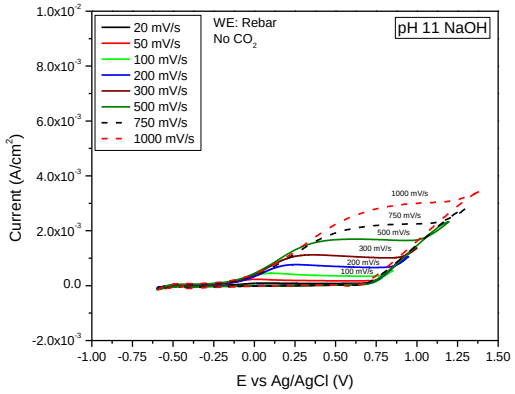

57(b)

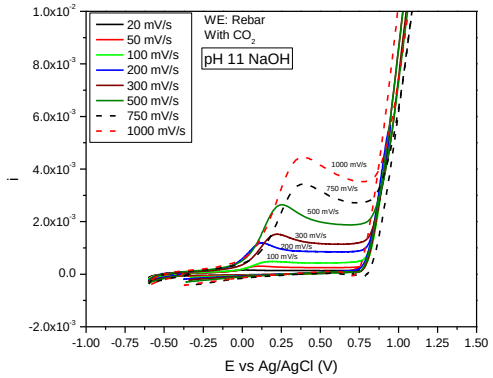

56(c)

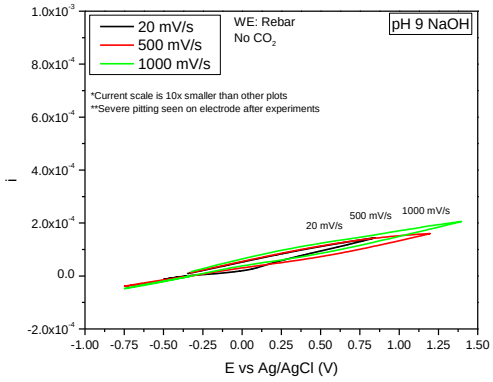

57(c)

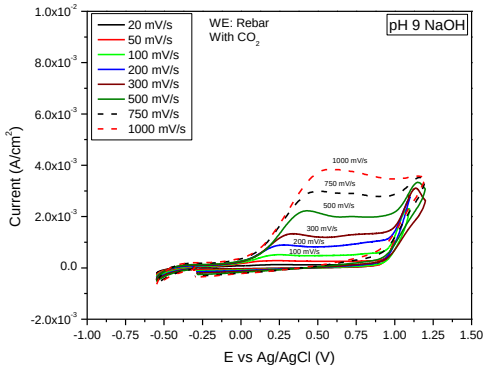

Fig. A-56 Cyclic voltammograms of rebar in NaOH solutions at **(a)** pH 12.5 **(b)** pH 11 **(c)** pH 9

Fig. A-57 Cyclic voltammograms of rebar in NaOH solutions at **(a)** pH 12.5 **(b)** pH 11 **(c)** pH 9

The limiting currents from CV scans in Fig. A-56a-c and Fig. A-57a-c were analyzed with the Randle's-Sevcik equation and plotted below in Fig. A-58.

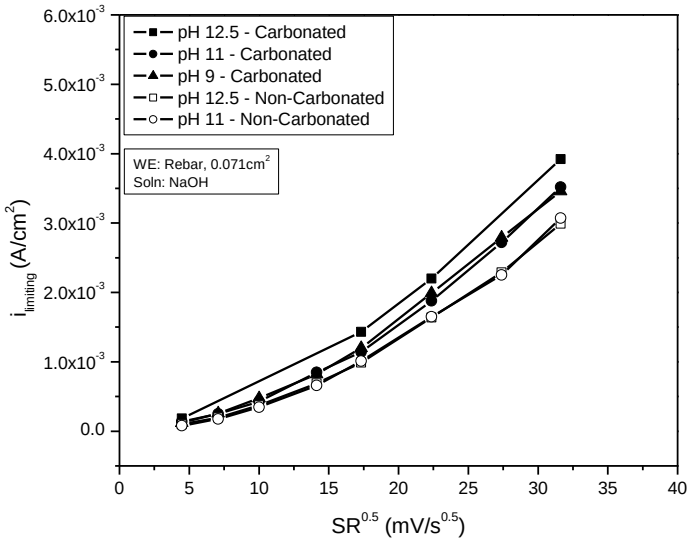

Fig A-58 Randle's-Sevcik equation plots for rebar exposed to NaOH solutions with and without CO_2 purging.

Fig. A-56a and 57a demonstrate that at pH 12.5, the effect of carbonates is negligible due to the high concentrations of hydroxides present. Fig. A-56b and 57b show that at pH 11, the effect of carbonates begins to appear. While Fig. A-56b without CO_2 purging shows no noticeable peaks, Fig. A-57b shows noticeable peaks, especially at the larger scan rates. The most noticeable difference comes in Fig. A-56c and Fig. A-57c. Fig. A-56c with no CO_2 purging showed aggressive corrosion on the surface as mentioned above. However, Fig. A-57c shows results similar to those found in Figures 52c, 53c, and 55c. This behavior is attributed to the formation of a protective iron carbonate film that formed when the carbonates were present. The proposed reactions are presented below [5]:

$$CO_{2\,(Aq)} + H_2O \leftrightarrow H_2CO_3 \qquad (2)$$

H_2CO_3 is unstable and decomposes as see in Eqn 3

$$H_2CO_3 \rightarrow HCO_3^- + H^+_{\,(Aq)} \qquad (3)$$

Ferrous ions would be readily available due to the oxidizing potentials applied

$$Fe^{0}_{(S)} \leftrightarrow Fe^{2+}{}_{(Aq)} + 2e^{-} \qquad E^{\circ} = -0.447V \text{ vs RHE} \qquad (4)$$

With

$$Fe^{2+}_{(Aq)} + CO_3^{2-}{}_{(Aq)} \leftrightarrow FeCO_{3(S)} \qquad (5)$$

Given the above reactions, it is proposed that the protection shown in Fig. A-57c is attributed to a passive film which has been fortified by a solid $FeCO_3$ product. The product cannot form without the dissolved CO_2 as in Fig. A-56c, where the instability of $Fe(OH)_2$ leads to the dissolution of the film. Active dissolution of the iron surface is evidenced by visible corrosion.

3.2.4 Effect of atmosphere and silica additions

CV tests were carried out on rebar in pH 9 NaOH solutions. The solutions also had an addition of 2wt% silica (colloidal, micro, or fumed silica) to determine if silica helped prevent surface corrosion. Furthermore during these CV trials oxygen or argon gas was bubbled through the solutions to determine atmosphere effect. Fig. A-59a-d below present the effects of atmosphere and silica additions on the CV of rebar in pH 9 NaOH.

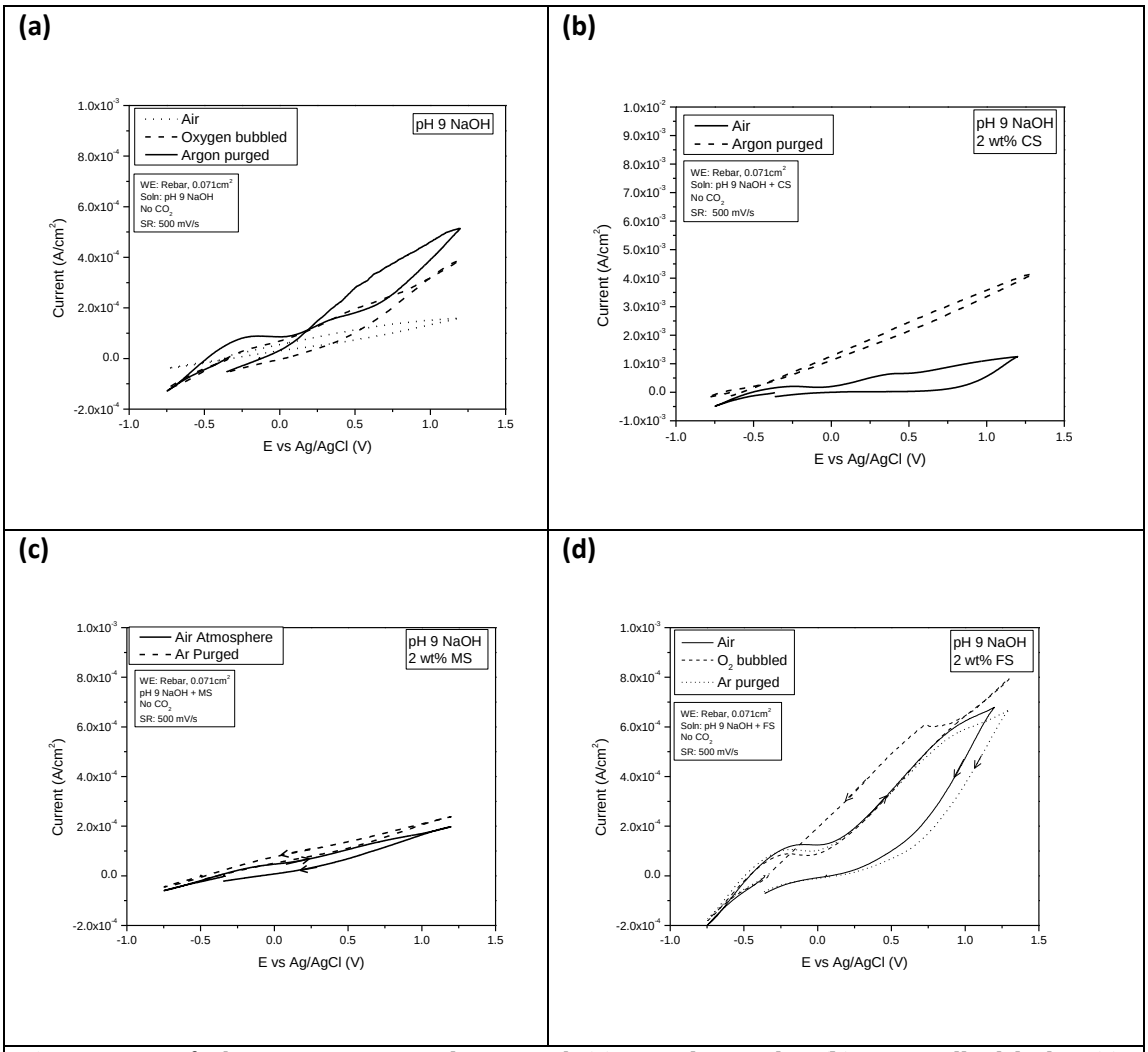

Fig. A-59 CV of rebar in pH 9 NaOH solutions with **(a)** control – no silica **(b)** 2wt% colloidal silica **(c)** 2wt% micro silica **(d)** 2wt% fumed silica.

Argon purging increases the CV currents regardless of silica additive. This is consistent with idea that argon is purging oxygen out of the solution. With little oxygen remaining in the solution, the electrode is unable to form a protective oxide film and thus the anodic current densities are larger. Fig. A-59b shows colloidal silica as reactive, in that it increases current densities by an order of magnitude above those seen in the control (no silica additive), micro, or fumed CVs. Fig. A-59d shows that fumed silica addition restored some typical CV behavior. Optical micrographs taken after each experiment are presented below in Fig. A-60a-d. All micrographs were taken at 50x magnification.

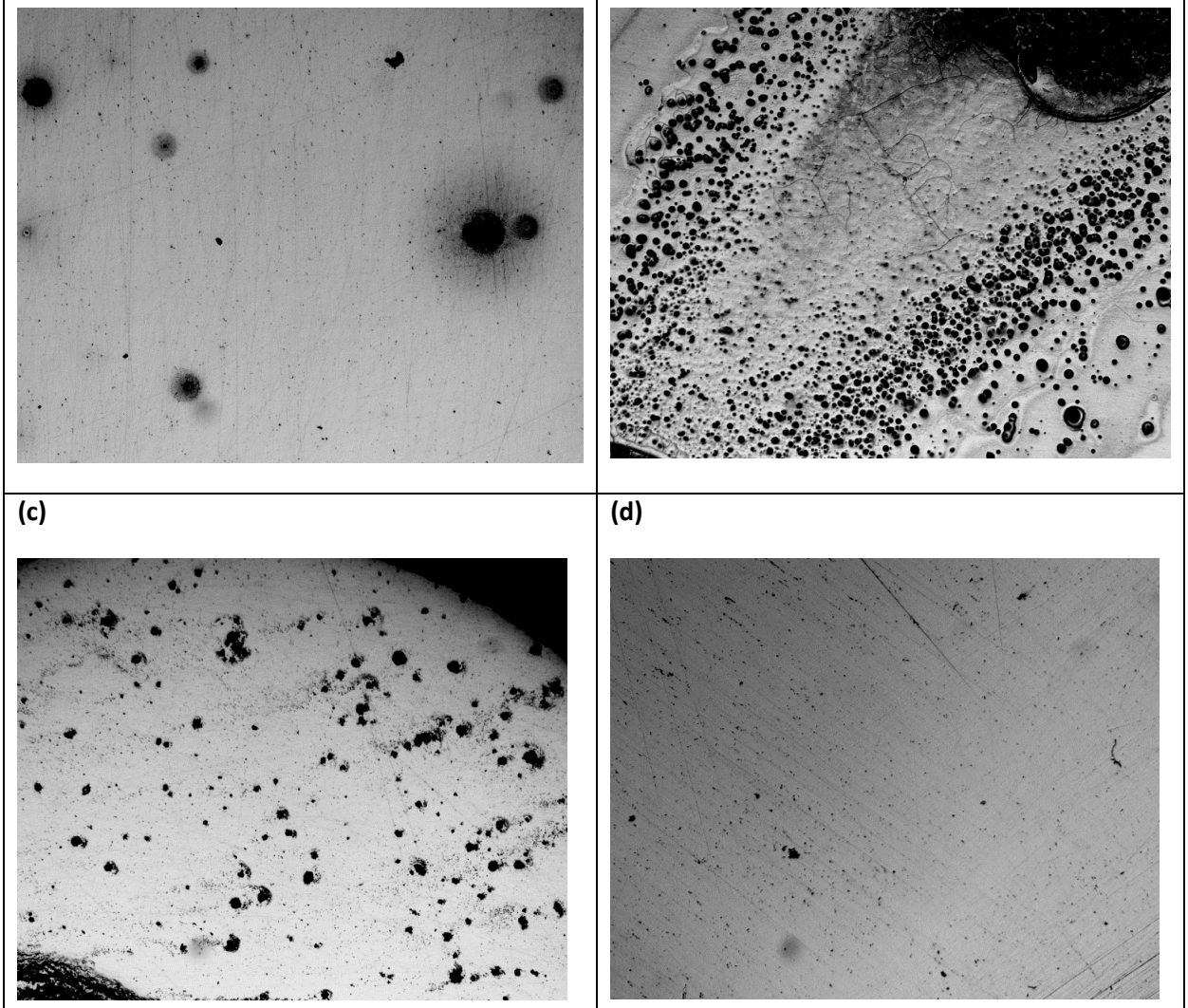

Fig. A-60. Optical micrographs of rebar electrodes after experiments in pH 9 NaOH solutions with **(a)** control – no silica **(b)** 2wt% colloidal silica **(c)** 2wt% micro silica **(d)** 2wt% fumed silica. All samples were prepared with an air atmosphere, 500 mV/s scan rate, and were taken at 50x magnification.

From Fig. A-60d it can be seen that fumed silica provides the rebar surface the best protection from localized corrosion. Further work is recommended to determine by what mechanism the fumed silica is protecting the surface.

3.3 Conclusions

1. Effect of working electrode composition: Two different working electrodes were studied (Nucor #5, and SS 316) to study their behaviors in CSS at 3 different pH's. No difference between the two electrodes was noticeable in the CV's indicating the surface reaction is controlled by the species present in the solution and not the electrode surface.

2. Effect of solution composition: Two different solutions were studied (real CSS solution and NaOH solution) to determine if the additional species present in real CSS had any effect on CV compared to a controlled NaOH solution.

    a. At the natural pH condition of 12.5, there was no difference in the CV's.

    b. At the pH condition of 11, solutions prepared with just NaOH showed no prominent peaking and only a limiting current behavior, compared to the real CSS solution which showed peaking at all pH's.

    c. At the pH condition of 9, NaOH solutions showed a loss of typical CV behavior and severe corrosion was seen on the electrode after the scans. The real CSS showed typical CV behavior with no pitting.

    d. Preparing NaOH solutions to pH 13 with NaOH, then bubbling with CO_2 to pH's 11 and 9 restored the pronounced peaks at pH 11 and restored protection at pH 9. This is attributed to a $FeCO_3$ film protecting the surface.

3. Effect of atmosphere and silica additions: Purging the pH 9 NaOH solutions with argon was found to increase the severity of the localized corrosion. This is attributed to lack of oxygen to form oxide passive films. Colloidal silica was found to increase the severity of corrosion and the magnitude of the corrosion currents. Micro silica caused negligible changes while fumed silica showed a positive effect by shutting off the surface to corrosion.

SECTION 4.

DEVELOPMENT OF SILVER WIRE REFERENCE ELECTRODES FOR IN-SITU MEASUREMENT OF REBAR CORROSION

4.1 Experimental procedures

Initially silver was selected as a candidate working electrode. Silver was chosen for its high degree of reactivity towards free chloride. It was thought the arrival of free chloride through the concretes porous pathways would be indicated by a marked change in the open circuit potential (OCP) of the silver. However, preliminary testing in cement saturated solution (simulates internal environment of concrete) showed remarkable stability in silver's OCP regardless of chloride and oxygen presence. The fixed potential of silver is thought to be a consequence of the high alkaline solution. It is speculated that a protective film of silver oxides forms on the surface of the solid silver, rendering the silver resistant to reactions induced by increases in chloride or oxygen. In aqueous environments of high alkalinity, silver oxide films will preferentially form.

$$2Ag + 2OH^- \rightarrow Ag_2O + H_2O + 2e^- \qquad (1)$$

Unfortunately, this added resistance renders the silver moot as a chloride indicator and thus the silver wires embedded in the concrete cannot be used to assess the concrete permeability. Because of the unchanging OCP, silver is now being studied as a possible in-situ reference electrode (REF). Similar to the standard Ag/AgCl electrode already in use, silver will be embedded in concrete next to a rebar cylinder and used as an in-situ REF, Table 31. Results of OCP measurements will be cross checked with measurements made on the exact same rebar samples using a standard Ag/AgCl REF.

A series of single silver wires embedded in solid concrete served as control experiments. Any effect admixtures of colloidal silica, fumed silica, and glycerol have on silver OCP was of interest. Experimental procedures included fabrication of the silver wire electrodes, casting of concrete cells, and partial immersion in salt solution. Individual silver electrodes were cut in 3 inch increments from silver wire with a diameter of 2mm. Each increment was then straightened, sanded down, smoothed and ultra-sonicated. The silver electrodes were attached to glass tubes (to accommodate a commercial Ag/AgCl REF). A total of twelve silver working electrodes were produced.

Fig. A-61, shows a completed electrode with individual components labeled. The Teflon tape and heat shrink tubing should prevent wetting of the silver anywhere except on the standardized area. The silver wires were then cast inside concrete. The concrete castings varied in both admixture and aggregate type. Admixtures included glycerol, colloidal silica, and fumed silica; the aggregates were rounded and crushed

river rock. Cement only castings served as the baseline experiments. After the 28 day curing time, samples were immersed in 3.5wt% NaCl salt solution. Once in solution, open circuit potentials were measured using a voltmeter.

Table 31. Experimental conditions used during OCP studies of silver embedded in concrete.

WE: Silver wire or Rebar RE: Ag/AgCl, 2mm diameter, leak free	Volume: 150ml Solution: 3.5 wt% NaCl Temp: 25^0 C Atmosphere: Air

Experimental Parameters: The experimental parameters were effect of additives in concrete and time of immersion of concrete in 3.5% NaCl solution. The additives of fumed silica, colloidal silica, and glycerol were introduced at 1.0 wt% vs. cement binder. Aggregate type was also an experimental parameter. How these parameters affected Ag OCP was of interest.

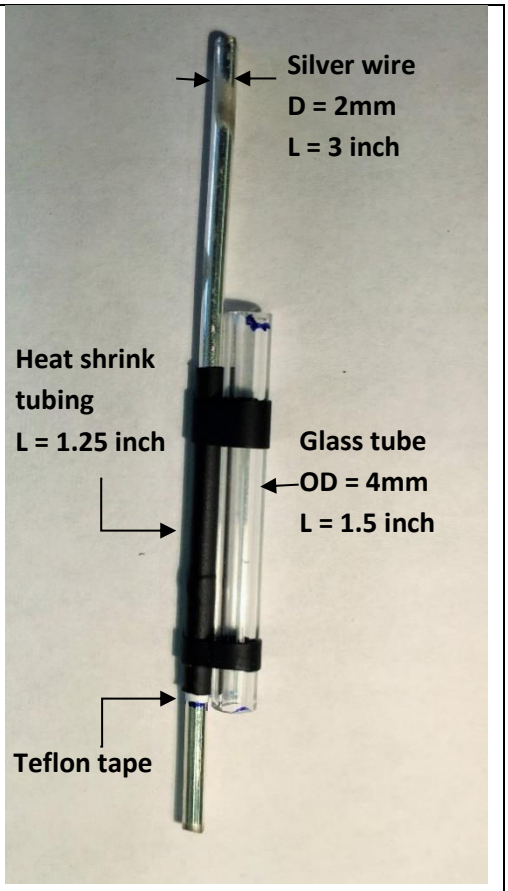

Fig. A-61 Silver wire electrode to be cast inside concrete.

Following the control experiments the *in-situ* electrodes were ready for preparation. Experimental procedures included fabrication of the silver wire electrodes, casting of concrete cells, and partial immersion in salt solution. Individual silver electrodes were cut in 1.75 inch increments from silver wire with a diameter of 1.6mm. Each increment was then straightened, sanded down, smoothed and ultra-sonicated. The silver electrodes were attached to glass tubes (to accommodate commercial Ag/AgCl REF) and glued to the rebar cylinders in such a way that both the in-situ electrode and the Ag/AgCl electrode are in close proximity but not touching the rebar working electrode. The rebar and silver wires were then cast inside concrete.

A total of seven silver reference electrodes were produced. Fig. A-62, shows a completed silver reference electrode, a reference electrode and glass tube attached to a rebar working electrode, and a concrete casting. Several different admixtures and aggregate types were used while casting the concrete, Table 32.

Table 32. Cement and concrete parameters

CEMENT	CONCRETE
Cement Only (Control)	Lane Mt Aggregate
Cement + 2wt% Glycerol	Lane Mt Aggregate + 2wt% Glycerol
Cement + 1wt% Fumed Silica	Lane Mt Aggregate + 1wt% Fumed Silica

After the 28 day curing time, samples were immersed in 3.5wt% NaCl salt solution. Once in solution, open circuit potentials were measured, Fig. A-63a, using a voltmeter. After 46 weeks of OCP monitoring the *in-situ* silver wires were validated as reference electrodes by running both Tafel and Cyclic Polarization tests on the rebar working electrodes. Each rebar sample underwent two Tafel tests, one test conducted in which the reference electrode was a purchased leak free Ag/AgCl/ electrode. After waiting 24hrs the same Tafel test would be run except an *in-situ* silver wire would function as the reference electrode. Results from the duplicated Tafel trials were compared and contrasted. The cyclic polarization experiments were conducted exclusively with the *in-situ* silver wires as reference. An added bonus of these additional electrochemical studies is the reinforcement steel corrosion data.

Fig. A-62 (Left) Silver wire to be used an in-situ REF, glass tube to accommodate Ag/AgCl REF. (Middle) Silver REF and tube attached to rebar WE using glue gun. (Right) Embedded silver and rebar in concrete cast.

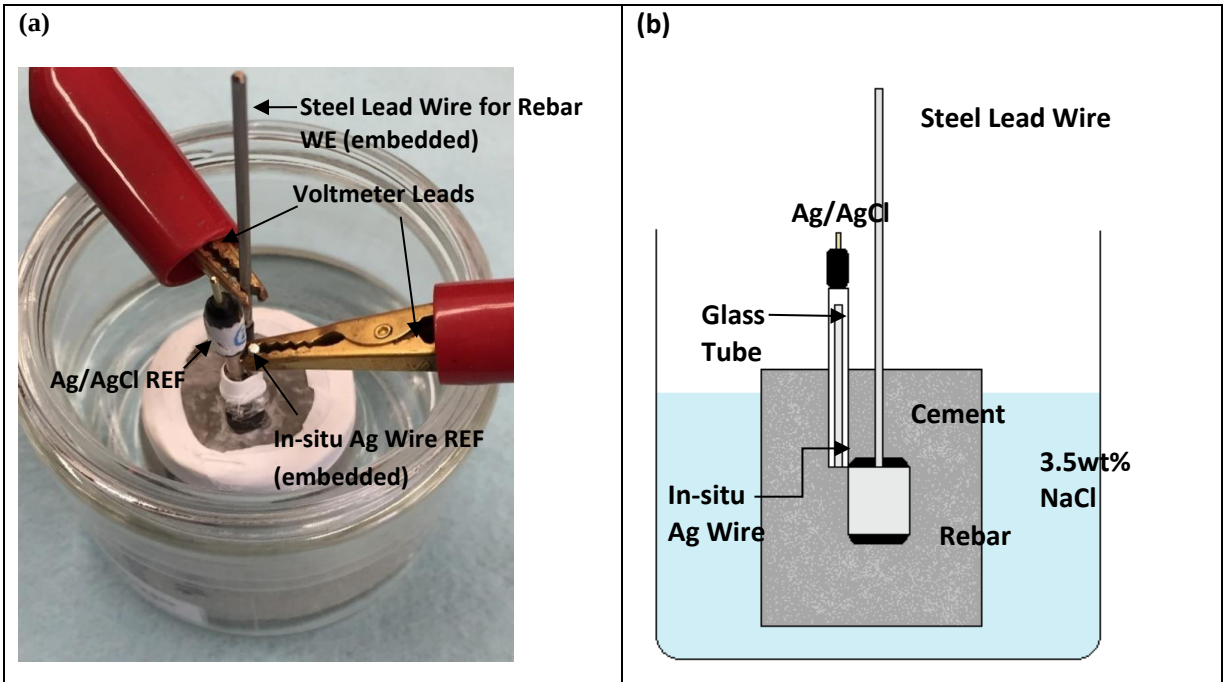

Fig. A-63 (a) Electrochemical cell: concrete matrix, in-situ Ag wire as REF, Ag/AgCl as cross reference and rebar cylinder WE. **(b)** Cross sectional schematic of electrochemical cell for in-situ silver REF electrode studies.

4.2 Results and Discussion

4.2.1 Control Experiments

Experimental results for silver embedded in concrete are shown, Fig. A-64a-d. The OCP was measured against a standard Ag/AgCl electrode. Initially all silver wires were approximately 150mV more cathodic than Ag/AgCl. The exception being the silver wires embedded in cement/ concrete which had been mixed with a glycerol admixture. The silver potential in these cases were 25-50 mV less than the control. The lower potential could be accredited to additional hydroxyl (OH^-) groups supplied by glycerol.

The difference in standard potentials for AgCl and Ag_2O is 132mV. The 150mV difference in the embedded silver wire and the Ag/AgCl reference is very close to the 132mV difference. Taken into account a degree of error and fluctuations in the Ag/AgCl ref electrode, it was postulated that the high pH of the concrete pore solution is promoting the formation of a protective silver oxide film on the silver and stabilizing the OCP.

The sudden rise in potential occurring at 50 days and 250 days resulted from a switch in REF electrodes. Three different electrodes have been used over the course of the experiment. This is in part due to the experiments long duration and in part to the harsh environment. The caustic concrete pore solution over time could break down the membrane of the leak free Ag/AgCl electrodes. Also, mineral packing of the ref electrode tip could be occurring. For this reason the ref electrodes are cleaned in hydrochloric acid after each use or replaced if unstable.

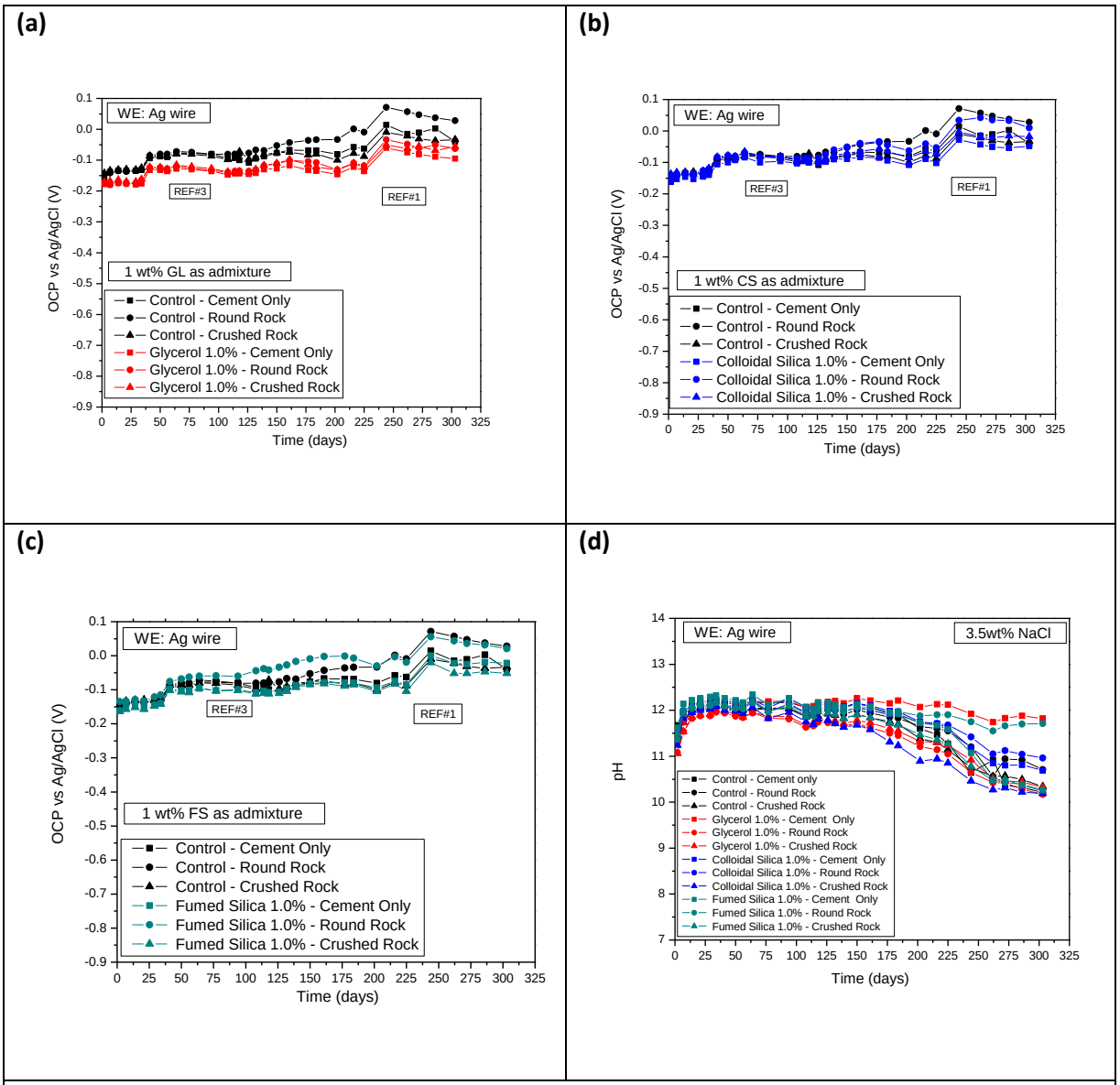

Fig. A-64 Open circuit potential of silver embedded in concrete. **(a)** Experiment on effect of aggregate type and glycerol on silver potential. **(b)** Experiment on effect of aggregate type and colloidal silica on silver potential. **(c)** Experiment on effect of aggregate type and fumed silica on silver potential. **(d)** pH of 3.5wt% NaCl solution containing concrete cells.

Silver wires embedded in cement/concrete containing no admixture served as the control series. For the control set, the silver wire potential was stable at an average of -120mV vs. Ag/AgCl for 150 days. After 150 days the silver potential between each concrete cell begin to drift apart. Silver in concrete with round rock aggregate trended upwards in potential to more anodic regions, while silver in cement or concrete with crushed rock aggregate maintained the original potential.

This behavior was replicated in both fumed and colloidal silica series. The silver potential in colloidal silica cement/concrete begins to spread out around 150 days, similar to the control series. Furthermore, divergence in potentials becomes pronounced at 250 days, Fig. A-64b. In the case of the fumed silica series, potentials begin to drift apart much earlier. After only 75 days there is a disparity between silver embedded in round rock concrete vs silver in cement or crushed rock concrete, Fig. A-64c.

pH of solution surrounding each concrete cell was measured periodically throughout the experiment, Fig. A-64d. The solution pH does not reflect perfectly the internal pH of the cement but provides a point of reference. After 175 days carbonation effect becomes noticeable. Form 175 – 300 days the bulk of the samples decreased from an average of pH 12.0 to an average of pH 11.0. This decline corresponds with the increases in silver potential embedded in round rock control and round rock colloidal silica. The supplementary broadening between silver potential in colloidal silica mixed cement vs concrete occurring at 250 days is explained by the continuing drop in pH. Also, there is a barely noticeable and gradual increase in potential across all samples, this too can be explained by progressive drop in pH.

Note, in all three cases, control, colloidal and fumed silica, the morphology that moves away from the tight grouping is the round river rock aggregate. The only silver electrode in a round rock aggregated concrete that does not show anodic trending potential is the one which contains the glycerol admixture. The most stable potentials are seen with silver embedded in the cement/concrete cast with glycerol at 1.0wt% vs. binder. Potentials for all three silver wires remainwithin20mV from each other, now for almost 300 days.

4.2.2 *In-situ* Ag REF Experiments

Experimental results for the in-situ silver reference electrodes can be seen below, Fig. A-65a -c. The figures represent three separate measurement types, the potential of embedded rebar versus the purchased Ag/AgCl standard, the rebar potential versus the in-situ Ag wire (also embedded) and the potential of the in-situ Ag wire versus the purchased Ag/AgCl standard. Comparison in OCP values for rebar measured using the standard Ag/AgCl and the in-situ Ag, Fig. A-65a and 65b, show almost identical trends. The similar trends validate embedded silver wires as functional reference electrodes. This is confirmed by measuring the potential difference of in-situ silver versus Ag/AgCl REF. For 325 days the in-situ silver electrodes show stable and fixed potentials around -0.15 V.

The pH of the immersion salt solution is progressively monitored, this is to catch any changes in the electrodes that might occur from reduction in alkalinity. For 190 days the pH of the immersion solutions

was stable at values between pH 12.0 and pH 12.5. After 200 days a minor reduction in pH can be observed, Fig. A-65d.

Note the characteristic drop in rebar potential as seen in previous OCP experiments (see Section 1) was registered by both the standard Ag/AgCl REF as well as the in-situ silver wires, Fig. A-65a-b.

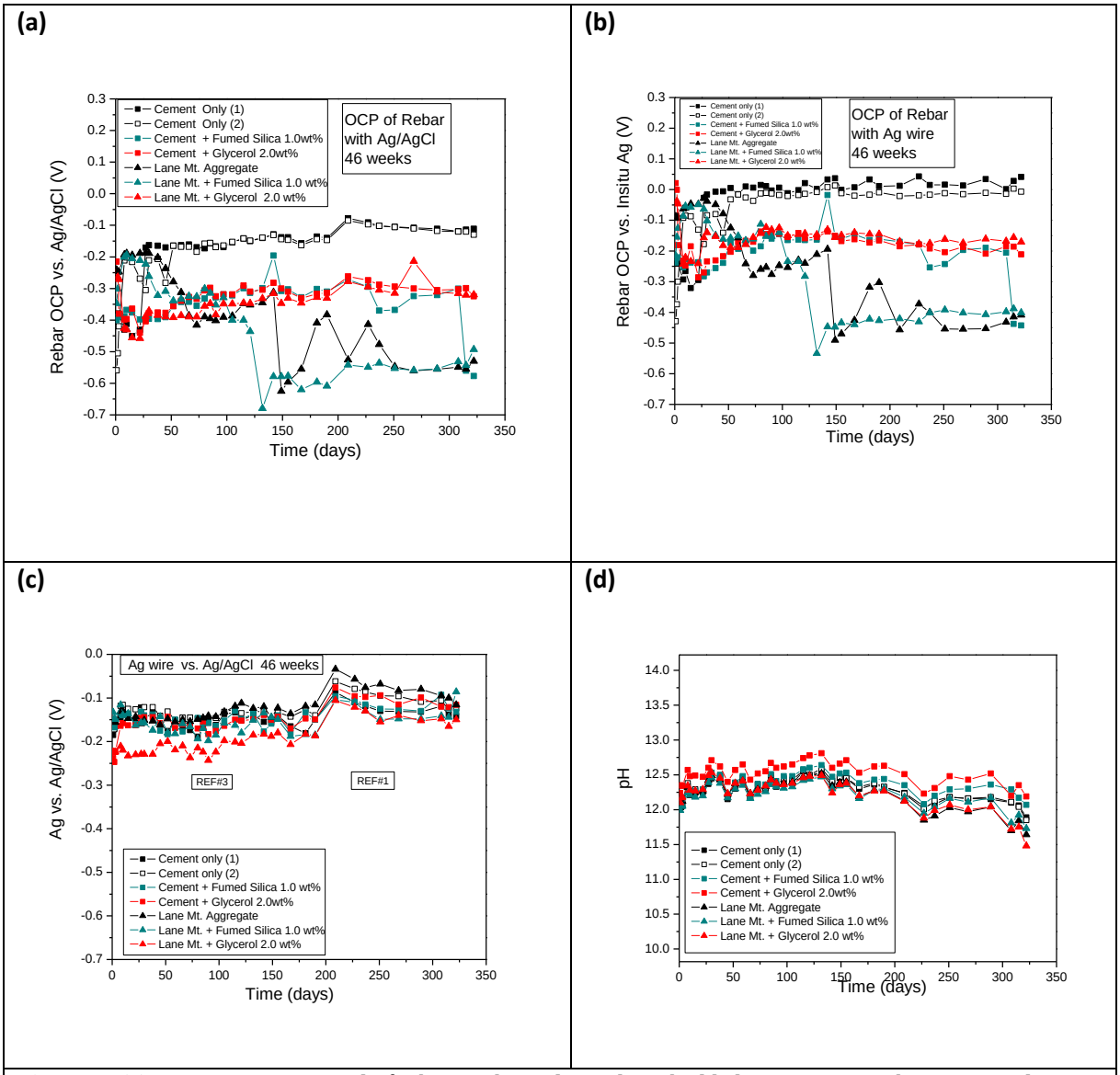

Fig. A-65 (a) Open circuit potential of rebar working electrode embedded in concrete. *Rebar measured against Ag/AgCl REF*.**(b)** Open circuit potential of rebar working electrode embedded in concrete. *Rebar measured against Insitu Ag REF wires.***(c)** Open circuit potential of silver wire electrode embedded in concrete. *Potential difference vs. Ag/AgCl REF*.**(d)** pH of 3.5wt% NaCl solution containing concrete cells

To reiterate , in a highly alkaline solution, research supports that at the surface of solid silver a mono-layer of Ag-OH will form followed by a secondary reaction to form Ag_2O. [6][7] It is believed that the *in-*

situ silver wires embedded as reference electrodes have a layer of Ag_2O which is sustained by the high concentrations of hydroxide. If there is any disruption in the silver oxide layer caused by chloride it can be immediately repaired. In this way the silver wires are held at constant potential not directly influenced by the potential of the pore solution. However this stability is dependent upon pH. Studies have shown that other metal/metal oxides embedded in concrete have a stability dependent upon pH [8][9][10]. The solid silver wires will be effective reference electrodes until carbonation sufficiently lowers pH.

The pH within the concrete pore solution will often be decreased by carbonation reactions. A Brief follow up experiment contested silver potential as a function of pH. The results for potential of silver versus pH of solution are shown, Fig. A-66a and 66b. The difference in silver potential seen in solutions of pH8 and pH9 are indistinguishable. Potential values between pH 11 and pH 12.5 are almost the same; pH 11 is fractionally more anodic. Overall the difference between silver potential in pH8 or 9 and ph11 or 12.5 is only +100mV. Furthermore, the potential change when chloride was introduced was at most 50mV. Therefore, it is assumed that the in-situ reference electrodes will be functional in the concrete environment even when carbonation effect reduces the pH (usually no less then pH 9).

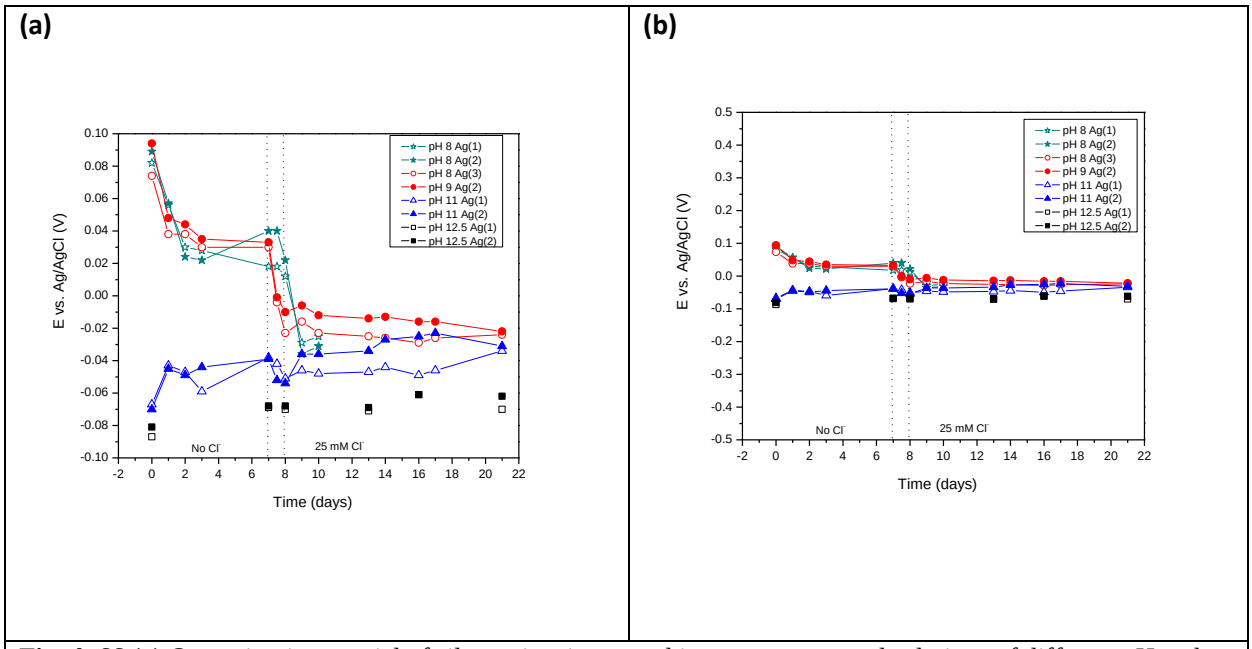

Fig. A-66 (a) Open circuit potential of silver wires immersed in cement saturated solutions of different pH and with and without chloride. **(b)** Open circuit potential of silver wires immersed in cement saturated solutions of different pH and with and without chloride. Voltage range expanded out to 1 volt.

4.2.3 Tafel Polarization

The following are results for Tafel Polarization experiments contesting the use of simple silver wires in place of commercially available Ag/AgCl electrodes. The graphs facilitate a compare and contrast between Tafel curves measured with Ag/AgCl and *in-situ Ag.* The graphs are labeled according to the additives and aggregates present in the cement sample. However considering this experiment was a proof of concept test for the *in-situ* measurement techniques it is more important to examine the similarity of the two Tafel curves on each graph and not necessarily the corrosion behavior of the rebar in the cement. However, the shapes and behavior of the anodic branches of the Tafel curve suggest an additive effect on the corrosion mechanisms for rebar in the concrete.

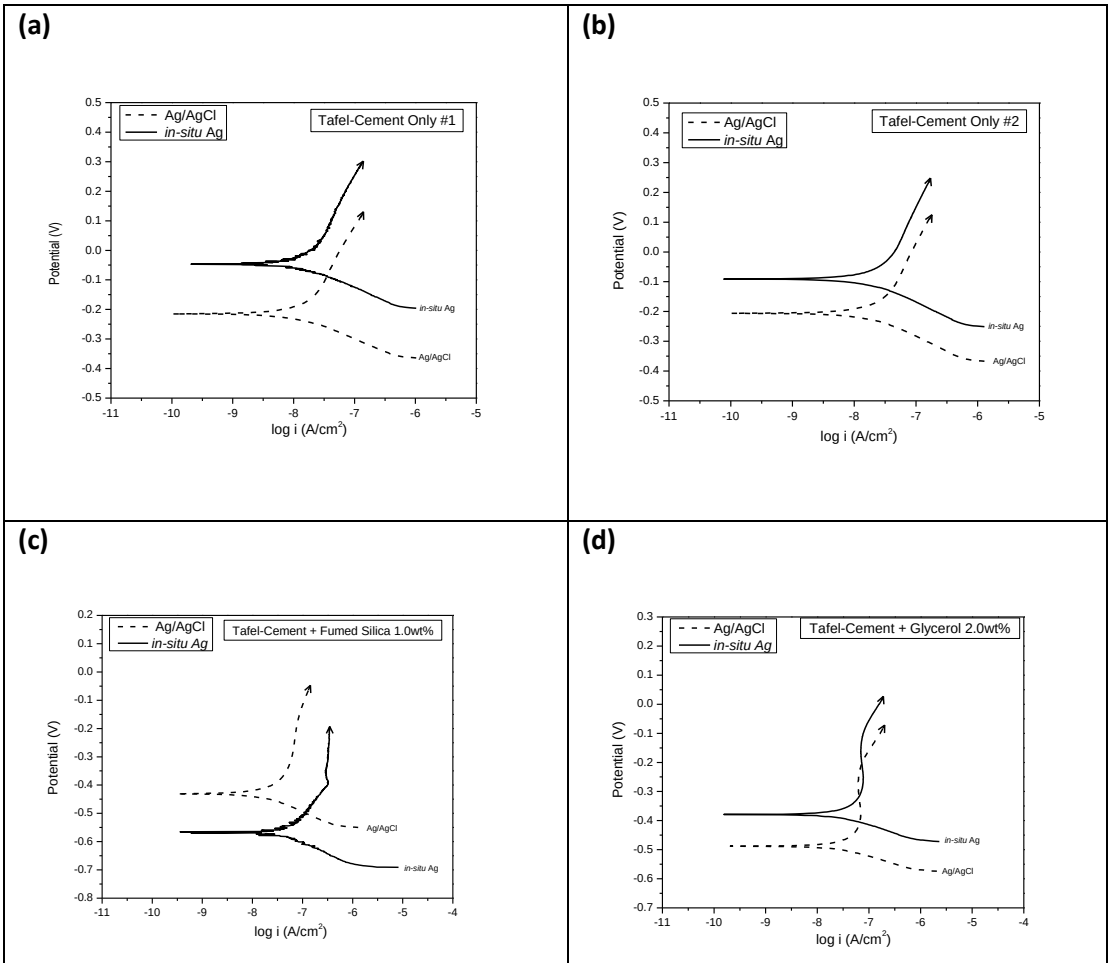

Fig. A-67 Tafel polarizations of rebar WE measured against a standard commercially available Ag/AgCl REF and then against simple silver wire REFs. The experiment was repeated multiple times in different cement mixtures **(a)** cement mortar control sample 1 **(b)** cement mortar control sample 2 **(c)** cement mortar with fumed silica additive and **(d)** cement mortar with glycerol additive.

Fig. A-67a and b were baseline experiments. These two samples were replicates of each other, two separate rebar cylinder were embedded in cement only (no additives). The cement cells had been submerged in salt water for 325 days. Over this time the OCP for both Cement Only 1 and 2 remained stable and nearly identical in value (for review consult Fig. A-68 below). This behavior was repeated in the Tafel tests. The curves were nearly fully reproducible. Furthermore, the functionality of the *in-situ* silver REF electrodes was confirmed. The behavior of both the cathodic and anodic branches were identical between an experiment run with the Ag/AgCl REF and an experiment run with the *in-situ* REF.

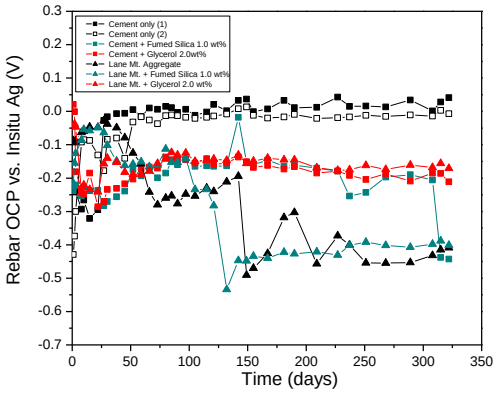

Fig. A-68 Open circuit potential of rebar working electrode embedded in concrete. *Rebar OCP measured against in-situ Ag REF wires.*

As previously mentioned the standard reduction/oxidation potentials for silver oxide and silver chloride are 0.342V and 0.222V a 120mV difference. This means that the Tafel polarization curves with *in-situ* silver wire as reference will be 120mV apart from curves measured with a standard Ag/AgCl electrode. This was observed in the results shown in both Fig. A-67 above and Fig. A-69 below. For each Tafel the in-situ curve (solid black line) is positioned 120-150mV more positive than standard Ag/AgCl (dashed line). There is only one exception to this shown in Fig. A-67c, where the curve for *in-situ* run is shifted 200mV below the Ag/AgCl run. This is due to a shift in corrosion activity which is highlighted by the observable drop in rebar OCP of the cement + Fumed Silica 1.0wt% sample. In this case the first set of Tafels was run at -0.200 V vs. In-situ silver after 300days and the second trial was run at -0.450V vs *in-situ* silver a week later. During that one week interval the OCP was encouraged to move cathodically most likely caused by an increase in corrosion activity corresponding to either a drop in internal pore solution caused by carbonation reactions or by increased concentration of Cl- at the rebar surface. In any

event the change in orientation between the two Tafel trials in Fig. A-67c was not caused by any resistance or imperfection in the in-situ reference electrodes performance.

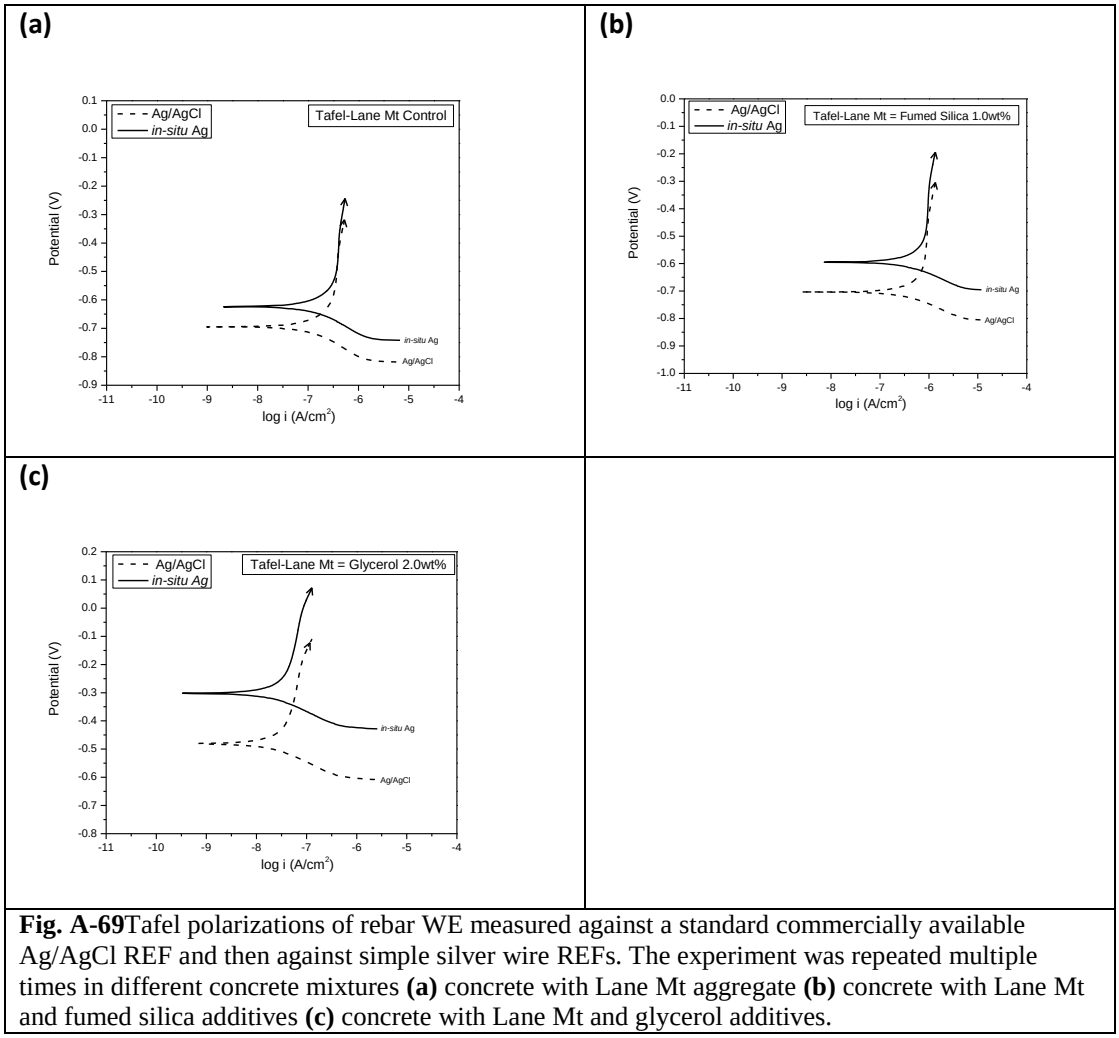

Fig. A-69 Tafel polarizations of rebar WE measured against a standard commercially available Ag/AgCl REF and then against simple silver wire REFs. The experiment was repeated multiple times in different concrete mixtures **(a)** concrete with Lane Mt aggregate **(b)** concrete with Lane Mt and fumed silica additives **(c)** concrete with Lane Mt and glycerol additives.

Again the functionality of in-situ silver wire as a ref electrode was confirmed during the second group of Tafel experiments. For Fig. A-69a-c the Tafel curves are fully reproducible between Ag/AgCl and *in-situ* Ag.

4.2.4 Cyclic Polarization

The following are results for Cyclic Polarization experiments contesting the use of simple silver wires in place of commercially available Ag/AgCl electrodes. The same parameters mentioned in Section 1.2.3 were used for the CP scans below.

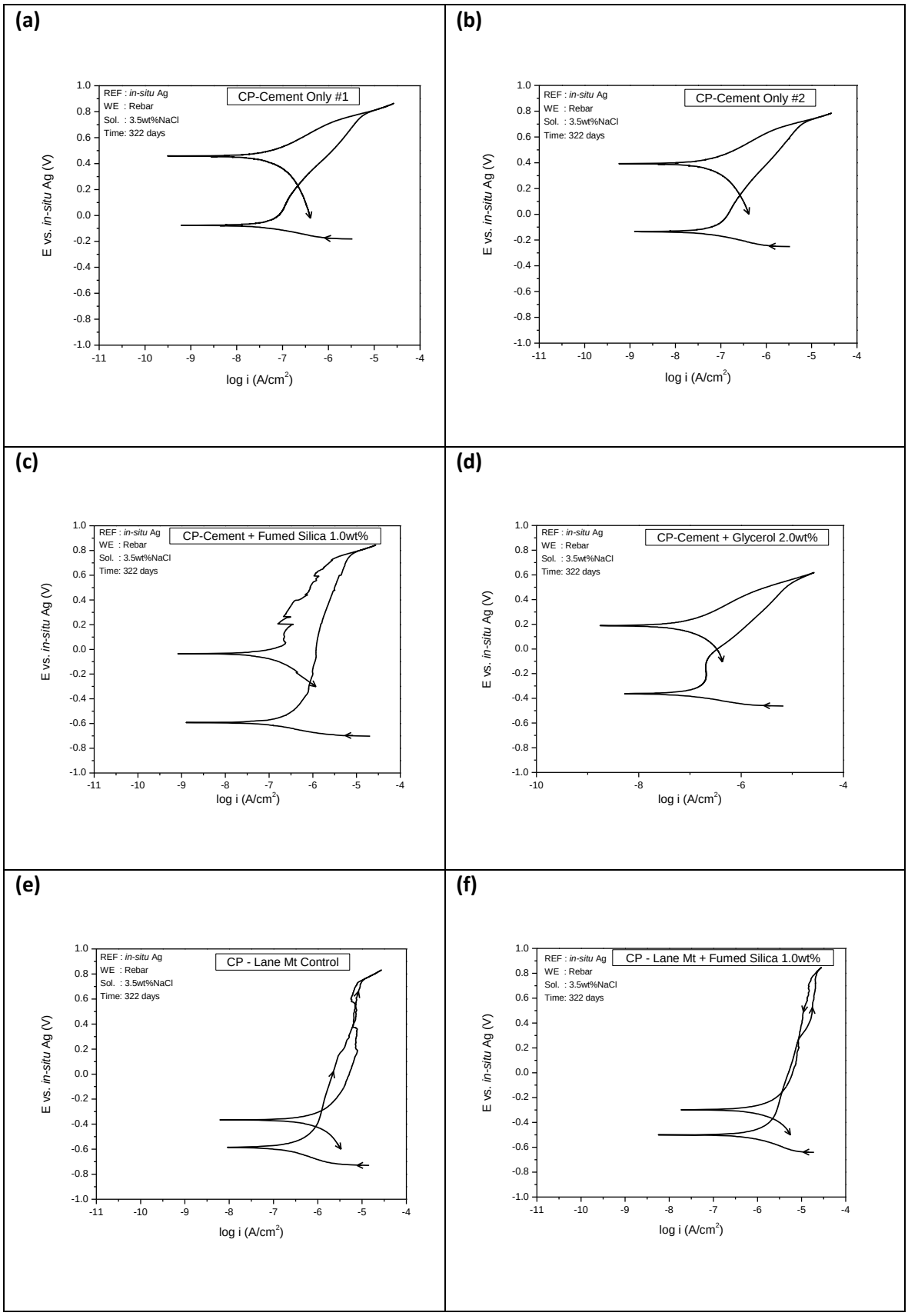
(a)
REF : in-situ Ag
WE : Rebar
Sol. : 3.5wt%NaCl
Time: 322 days
CP-Cement Only #1
E vs. in-situ Ag (V)
log i (A/cm2)
(b)
REF : in-situ Ag
WE : Rebar
Sol. : 3.5wt%NaCl
Time: 322 days
CP-Cement Only #2
E vs. in-situ Ag (V)
log i (A/cm2)
(c)
REF : in-situ Ag
WE : Rebar
Sol. : 3.5wt%NaCl
Time: 322 days
CP-Cement + Fumed Silica 1.0wt%
E vs. in-situ Ag (V)
log i (A/cm2)
(d)
REF : in-situ Ag
WE : Rebar
Sol. : 3.5wt%NaCl
Time: 322 days
CP-Cement + Glycerol 2.0wt%
E vs. in-situ Ag (V)
log i (A/cm2)
(e)
REF : in-situ Ag
WE : Rebar
Sol. : 3.5wt%NaCl
Time: 322 days
CP - Lane Mt Control
E vs. in-situ Ag (V)
log i (A/cm2)
(f)
REF : in-situ Ag
WE : Rebar
Sol. : 3.5wt%NaCl
Time: 322 days
CP - Lane Mt + Fumed Silica 1.0wt%
E vs. in-situ Ag (V)
log i (A/cm2)

(g)

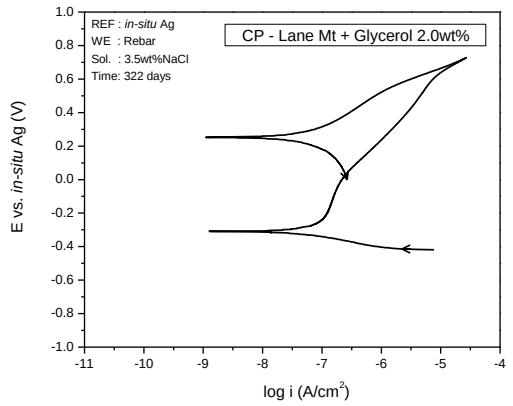

Fig. A-70 Cyclic polarization scans of rebar electrodes embedded in **(a)** cement only (1), **(b**) cement only (2), **(c)** cement + fumed silica 1.0wt%, **(d)** cement + glycerol 2.0wt% **(e)**Lane Mt concrete, **(f)** Lane Mt + fumed silica 1.0wt% concrete and **(g)**Lane Mt + glycerol 2.0wt%. CP tests were conducted after cement and concrete cells had been immersed in 3.5wt% NaCl solution for 325 days.

Taking into account the rebar equilibrium potentials measured over 325 days, Fig. A-68, pitting would be expected on the steel embedded in concrete with Lane Mt aggregate (Lane Mt agg.), Lane Mt aggregate plus fumed silica (Lane Mt + Fumed Silica 1.0wt%) and possibly in cement with fumed silica (cement + Fumed Silica 1.0wt%). This was confirmed in the above results. Evidence of pitting is seen for the rebar in both Lane Mt aggregate concrete and Lane Mt plus fumed silica concrete. It is evident by the return scans crossing back over the forward scans. Pitting was not identified on the rebar embedded in cement plus fumed silica cement, the return scan had lower current density then the forward scan. This is probably because aggressive localized corrosion had just been initiated prior to the test. If the CP had been run a week or two weeks later pitting would most likely have occurred.

4.3 Conclusions

1. Initial potential difference between silver embedded in concrete and Ag/AgCl is approximately -120mV which corresponds to the standard potential difference between AgCl (±222mV) and Ag_2O (±132mV).
2. Results indicate silver is functional as an in-situ reference electrode for electrochemical observation of reinforcement steel, so long as there is no significant reduction in pH.
3. Tafel polarization trials show exceptional reproducibility between tests run with a standard Ag/AgCl reference electrode and an in-situ silver reference electrode.

4. In-situ silver wire performed well as a reference electrode for cyclic polarization experiments.
5. Results verify silver wire being functional as an in-situ reference electrode for electrochemical observation of reinforcement steel.

SECTION 5

ADDITIVE EFFECT ON CHLORIDE PERMEABILITY WITHIN CONCRETE BLOCKS CONTAINING GLYCEROL OR SILICA

5.1 Experimental procedures

To study the diffusion of Cl^- ion, a series of concrete blocks were cast then subjected to extended ponding in simulated sea water solution. Over time the chloride ions present in the salt water diffuse into the concrete blocks. Additive effect on chloride permeability was of interest, additives included glycerol, fumed silica, micro silica, and colloidal silica. Additives were introduced as admixtures to the concrete during the casting process. The glycerol admixture was added as a viscosity modifier; objectively glycerol will slow the diffusion of chloride carrying moisture through the porous pathways of the concrete block. The silica additives were chosen for their microscale to nanoscale sized silica particulates. The nanoscale silica particles have a high specific surface area that contribute to enhanced C-S-H chemistry and decreased pore free volume. The silica admixtures should effectively reduce the size of the transport pathways within the concrete matrix. After a period of approximately 1.5 years, the blocks were removed from the salt bath. The chloride concentration profile with depth was then determined via progressive drill sampling and ion chromatography (IC).

Although results from concrete ponding experiments were satisfactory, the experiment duration from start to finish was nearly 2 years. Time was necessary to allow for the slow ingress of chloride through the large concrete blocks. Thus, a novel approach for accelerated chloride penetration by application of pressure was proposed. To best study the diffusion of Cl^- ion, a series of small concrete cylinders were cast then immersed in salt water and placed in an autoclave. The high pressures attainable inside an autoclave would theoretically increase of moisture and chloride ingress into the concrete. The effectiveness of the proposed method was investigated. This method allowed for quicker acquisition of results. The results obtained from the autoclave trials would be confirmation for the original method of prolonged salt bath exposure.

5.1.1 Concrete Block Preparation

Preparation consisted of mixing Portland cement, aggregate, admixture and water, casting, curing and placing in a plastic container filled with 3.5% NaCl for an extended time followed by drill sampling and IC analyses. Additive effect on chloride permeability was of interest, additions included glycerol, fumed silica, micro silica, and colloidal silica. These admixtures were added to the concrete during the casting process. For a single control (no additive) block, 600g cement + 600g sand + 240ml RO H_2O was used.

The standard procedure first mixed cement and sand together as a dry mixture, using a metal stirring whisk. Dry mixing was carried out within a fume hood. Next admixtures and water solutions were progressively added until concrete was at optimum casting consistency. For the glycerol 2.0 wt% admixture, two extra mixing parameters were studied (A and B).

Mixing procedure A: Cement + (H_2O + Glycerol) → Aggregate; first 12g of glycerol was added to the 240ml H_2O and stirred in, then the water/glycerol solution was poured directly into the cement binder and stirred energetically. This was done to insure a thorough combination of glycerol, water, and cement, only after this was the aggregate mixed in.

Mixing procedure B: Aggregate + (H_2O + Glycerol) → Cement; first 12g of glycerol was added to the 240ml H_2O and stirred in. Next the water/glycerol was poured directly into the sand aggregate and stirred energetically. This was done to insure a thorough coating of the sand aggregate particulates with the glycerol and water, only after this was the cement mixed in.

Following mixing, the concrete slurry would be scooped into cubic molds (Type 1 or Type 2) and packed down with a plastic rod. Once hardened, concrete blocks were cured for 28 days in a humid atmosphere, then ponding began.

Concrete block sizes were 8.5 x 8.5 x 8.5 [cm] *(Type 1 mold)* or 8 x 8 [cm] base, 7.5 [cm] height and 8.5 x 8.5 [cm] top *(Type 2 mold).*

Ponding Duration: Start - November 6, 2014 End - May 24, 2016

5.1.2 Concrete Cylinders for Autoclave Treatment

Experimental procedures included casting and curing of concrete cylinders, protection of cylinder sides, and immersion in salt solution followed by autoclave treatment. Subsequent drilling and IC analysis determined chloride concentration depth profiles.

Standard concrete cylinders were prepared with aggregate (Lane Mountain) for immersion in 3.5% NaCl chloride solution. Also prepared were cylinders made exclusively of cement binder. These cement only cylinders would serve as control samples. Further preparation included coating the outside wall with PC Concrete Epoxy (overnight cure) and wrapping aluminum tape over the epoxy, Fig. A-40a. Only the "faces" of the concrete/cement cylinders were free for sorption of moisture/chloride. Next, cylinders were placed in jars with 3.5% NaCl saltwater filled exactly to the brim. Over the brim, double walled flexible latex (purple glove with cut off fingers) was stretched and affixed with a rubber band, Fig. A-72b.

The gloves purpose was preclusion of nitrogen dissolution into NaCl solution. The jar (solution plus cylinder plus the latex cover) is placed in an autoclave and pressurized with nitrogen, Fig. A-72c-d. The parameters to study are related to the autoclave conditions (pressure and time) and concrete conditions (admixtures, aggregates, etc.).

5.1.3 Drilling and Dissolution

After ponding, blocks were gently washed by dipping each block into a tap water reservoir bucket for 5 dips, water was constantly flowing in and out of the bucket ensuring no buildup of chloride ions. After the tap water, each block was immediately rinsed clean with RO water. The RO wash was a three dip cycle in a RO reservoir bucket, the RO water was refreshed every three blocks. Chloride gradient within the concrete could be measured by progressive drill sampling from the top, bottom and/or sides of the concrete blocks, Fig. A-71a-b. The chloride concentration profile was found by analyzing powdered concrete samples taken at different drill depths. Drilling extended 35mm into each block, 7mm increments for a total of 5 powder samples. The drilled concrete samples received additional grinding by mortar and pestle. 100 ml DI H_2O was used to dissolve 1.0 gram of concrete sample powder gathered from each particular drilling depth. Upon dissolution, the solution was left to settle down upon which 3ml of solution was withdrawn by a syringe and filtered through 0.45 micron PTFE disk filter under syringe pressure. These solutions were analyzed for Cl^- presence using ion chromatography(IC). The procedures used during the autoclave study mimicked those described above, see comments after Fig. A-73.

(a)

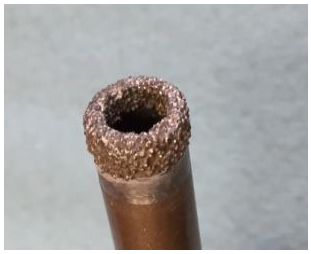

(b)

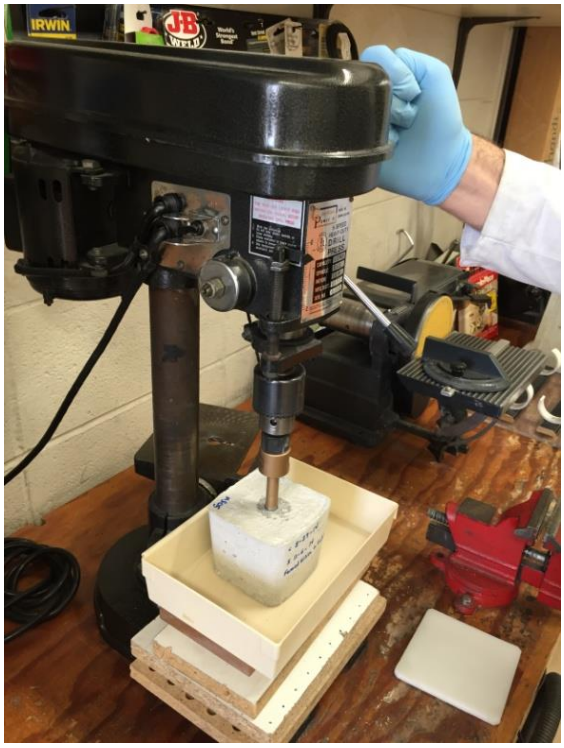

Fig. A-71(a) Diamond studded drill (Ø ½'' DAMO). **(b)** Drilling into a concrete block using a drill press, process carried out over a plastic tray.

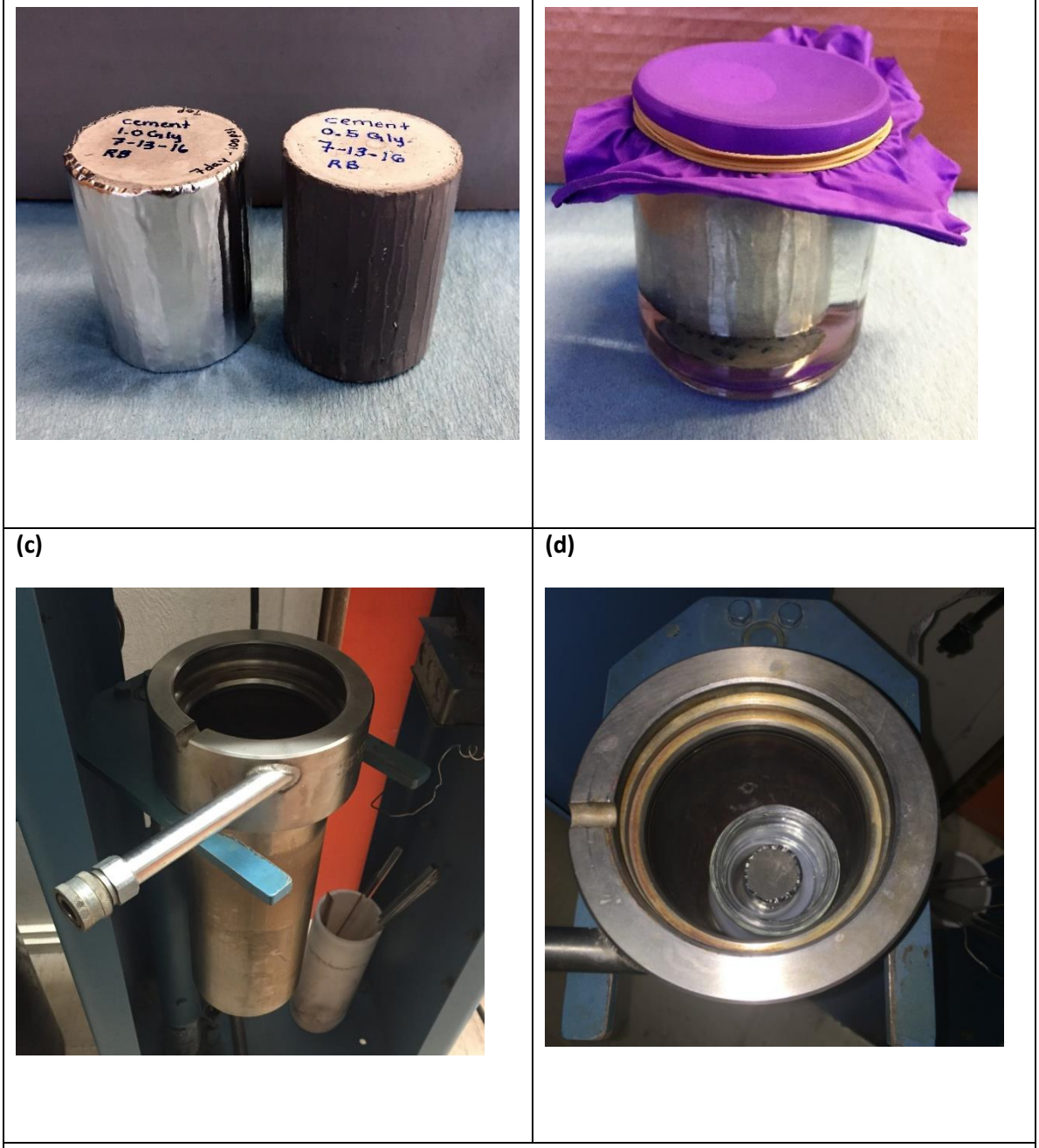

Fig. A-72 (a) Cement cyliders sealed with PC epoxy and wrapped in aluminum tape. **(b)** Purple nitrile glove (double layered) to act as diaphragm resistant to NO_2 permeation. Glove concaved from autoclave pressure.**(c)** Autoclave pressure vessel (stainless steel chamber) **(d)** Concrete sample immersed in 3.5wt% NaCl salt solution, sample placed inside steel chamber.

Following autoclave pressure treatment, Table 33, the cement or concrete cylinder is removed from the autoclave and inspected. Each cylinder is rinsed three times under RO water and patted dry with a paper

towel. The samples top and base surfaces are then fully dried using an air gun. Once dry the samples are ready for drilling and IC analysis.

The concrete cylinders are each ~50mm in height. Therefore, drilling was done incrementally for five steps at 5mm each. The cored drill samples were then powdered and stored in glass vials for dissolution. The dissolutions are later analyzed with an ion chromatograph for chloride presence; by this chloride concentration (ppm) is measured at each incremental depth.

5.2 Results and Discussion

Drilling directions into the concrete blocks included top-down, bottom-up and side-in. The results from any of the three directions show a similar trend. For example, the chloride concentrations with depth have been presented, Fig. A-73a-c, for the top down drilling direction. Fig. A-73d, displays the chloride concentration gradients for the side drilling direction. It can be seen that the presence of glycerol increases the slope of the line indicating a greater decrease in chloride presence moving towards the center of the blocks, Fig. A-73a. Furthermore, in blocks containing the glycerol admixtures, the chloride concentration achieves values at and below 1ppm near the center of the block. This is much lower than other admixtures (silica) and the controls. Additionally glycerol was studied in tandem to micro and fumed silica. In blocks that contained equal parts silica (1.0 wt%) and glycerol (1.0 wt%), the chloride concentrations decreased below the values seen for the silica exclusively, Fig. A-73c.

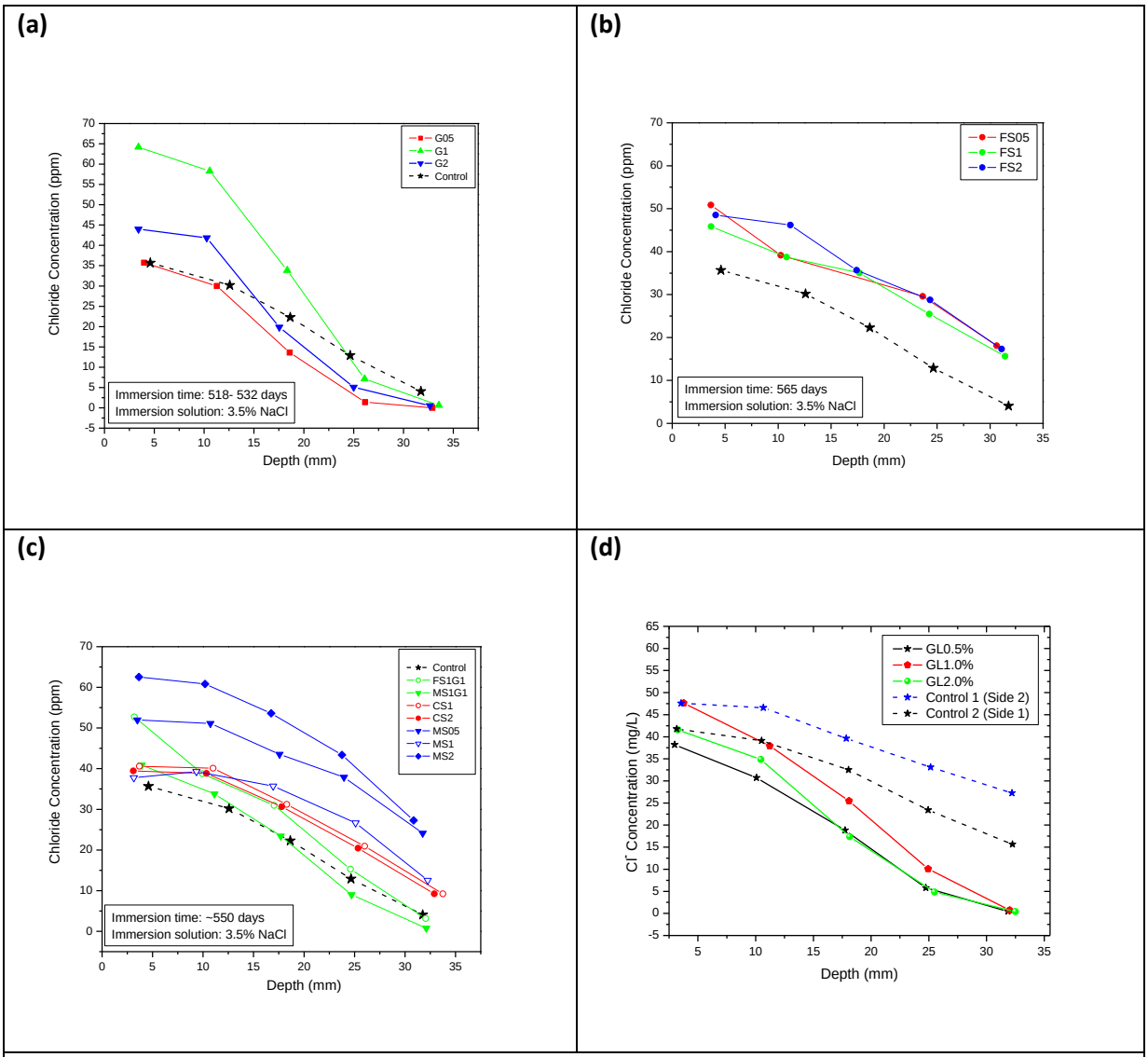

Fig. A-73 Chloride concentration with depth, concrete containing **(a)** glycerol, **(b)** Fumed silica and **(c)** concrete containing colloidal silica, micro silica, and silica + glycerol.

Table 33. Experimental parameters for autoclave pressure at 100psi

100 psi – Sample Set		
Time (days-hrs)	Aggregate/Additive	Pressure (psi)
1 day (24hrs)	LnMt-Control	100psi
3 day (72hrs)	LnMt-Control	100psi
7 day (168hrs)	LnMt-CollS2.0	100ps
200 psi – Sample Set		
Time (days-hrs)	Aggregate/Admixture	Pressure (psi)
1 day (24hrs)	LnMt-Coll.S. 2.0	200psi
3 day (72hrs)	LnMt-Coll.S. 2.0	200psi

It was found that the time parameters of 1 and 3 days had little to no effect on chloride penetration into the concrete. Conversely, adjustment in pressure from 100psi to 200psi saw increasing chloride penetration, Fig. A-74. However, at 200psi inspection of samples revealed cracking on the surface of the samples. This cracking was believed to be caused by overwhelmingly high pressure.

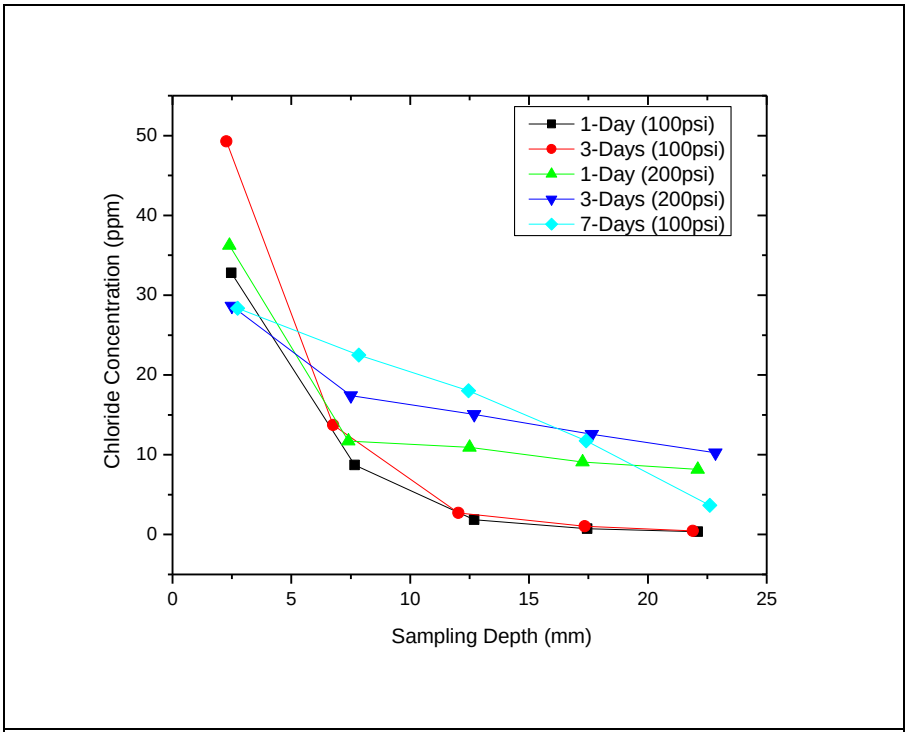

Fig. A-74 Chloride concentration profiles within concrete after immersion in 3.5wt% NaCl and subjected to autoclave pressures (100-200psi)

Note, at both pressures the lines representing the chloride profiles are not linear, but have two distinct sections. The first section representing 0-7mm depth has a steep line marking a rapid decrease in chloride presence; the second section is a plateau of constant chloride concentration from 10-25mm depth. Therefore, time was extended to 7 days to allow for more ingress of chloride ions. The 7 –day 100 psi autoclave treatment produced a chloride profile represented by the green line with diamond markers. This profile is unique from the others. Instead of curving sharply downwards, the profile has a gradual almost linear decrease in chloride with depth. Finding the cause profile change would require more experimentation.

Results shown in Fig. A-74, are trial experiments as proof of concept for autoclave application. All samples used were concrete with LnMt aggregate. Additional experiments with cement only (control) cylinders were tried. Unfortunately usable results for cement only cylinders were never generated. Fig. A-75 illustrates how chloride concentration drops dramatically after a few mm of depth and after 10mm there is essentially zero chloride present. Because of this, it is difficult to calculate a diffusion coefficient. The cement-only samples may be too dense for any substantial chloride intrusion (by moisture). It was thought that concrete with Lane Mountain aggregate would be a better option for autoclave testing. The silica aggregate has wetting properties that enhance moisture migration through the inter-granular transition zones between the cement CSH gel and the sand. In this way the samples are "weakened" to moisture absorption driven inwards by the increased pressure.

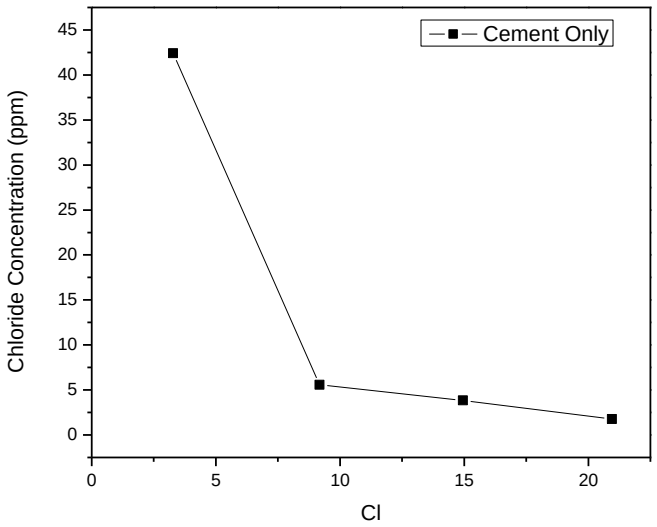

Fig. A-75 Chloride concentration gradient for cement only cylinder subjected to 100 psi over 7 days.

5.2.1 Calculating Diffusion Coefficients

Silica additives did not restrict chloride inclusion into the concrete blocks, therefore diffusion coefficients were calculated solely for control concrete (no additive) and concrete containing the glycerol additive. For example, the chloride concentrations with depth have been re-presented for concrete containing glycerol additions, Fig. A-76a-e.

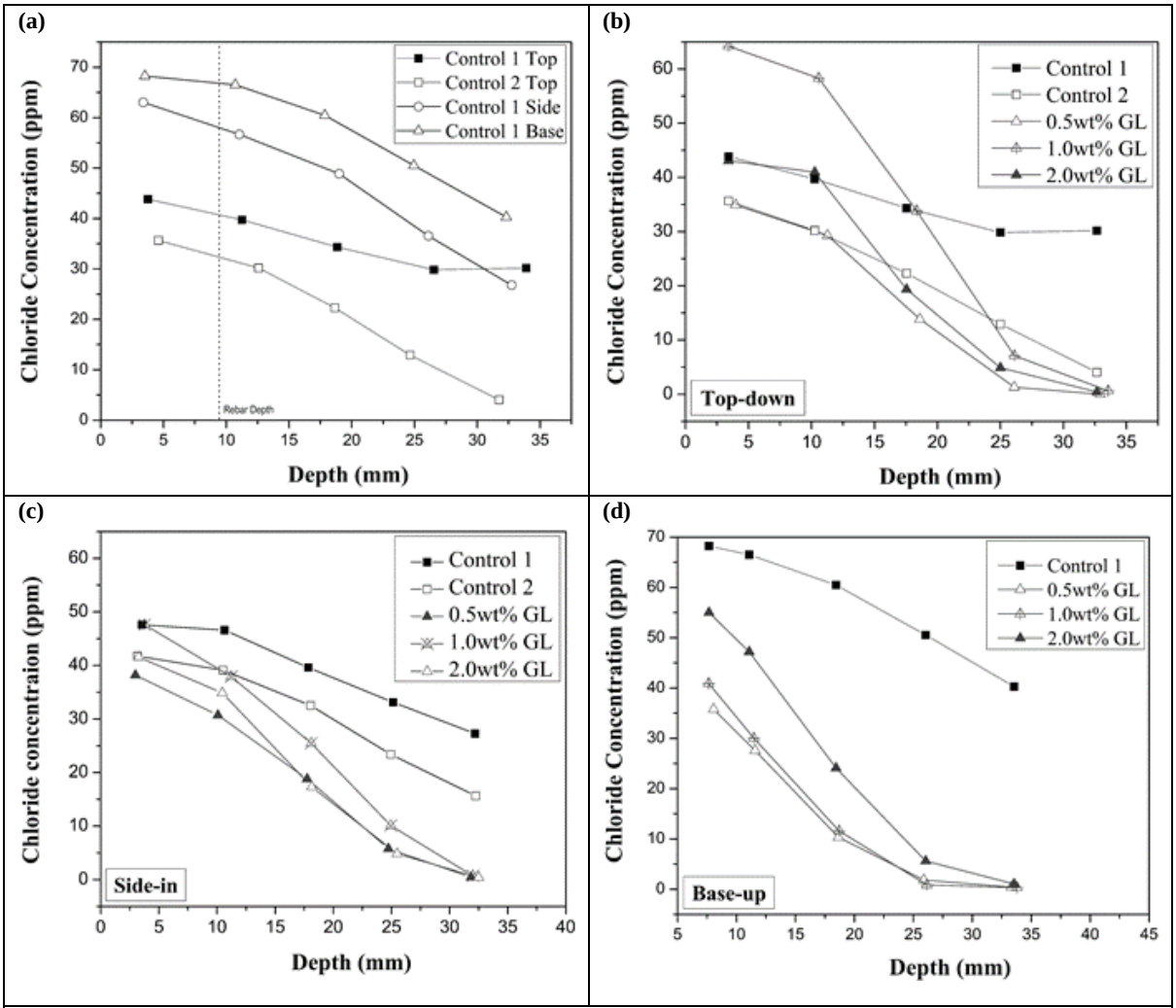

Fig. 76 Chloride concentration profiles for concrete **(a)** control samples, **(b)** glycerol admixtures profiles from top-down direction of drilling, **(c)** glycerol admixtures profiles from side-in direction of drilling, **(d)** glycerol admixtures profiles from base-up direction of drilling.

It can be seen in Fig. A-76b-d, that glycerol increases the slope (concentration gradient) of the lines, indicating a greater decrease in chloride presence moving towards the center of the blocks. Furthermore, in blocks containing glycerol, chloride concentration values are at and below 1ppm near the center of the block. The lowest chloride concentrations were seen in the block with 0.5 wt.% glycerol. It could be at higher concentrations of 1.0 and 2.0 wt.%, glycerol slightly inhibits C-S-H chemistry and prevents formation of a denser microstructure. Regardless at any concentration of glycerol the chloride profiles are much steeper than the controls.

By application of Crank's solution to Fick's 2nd law, the diffusion coefficients *D* as a function of glycerol admixture were calculated. [11]

$$\frac{C_x - C_o}{C_s - C_o} = 1 - erf\left[\frac{x}{2\sqrt{Dt}}\right] \quad (4)$$

Here C_x is the concentration of chloride in ppm at a certain depth *x*. C_s is the concentration of chloride at the surface of the concrete which was assumed to be 3.5wt% equivalent to 35000 ppm. C_o is the concentration of chloride within the concrete at time 0, this was assumed to be zero, there is a certain amount of bound chloride (0.2ppm) present in the cement before casting but it is assumed to be negligible. The time of exposure is represented by *t* which for this experiment was *t* = 550 days. Note calculations were done for the side-in drilling direction alone. The degree of difference between control 1 and 2 was smallest for the side in direction. Additionally, drilling side in-wards negates the error that could arise from evaporation loss (top face exposed to air) and in the middle gradation effects are averaged.

Table 34. Effect of glycerol admixture on concrete diffusivity

Admixture (wt.%)	Concentration gradients (ppm/mm)	Diffusion coefficients (cm^2/s)
Control 1	-0.754	$0.97x10^{-8}$
Control 2	-0.935	$0.89x10^{-8}$
Glycerol 0.5%	-1.39	$0.56x10^{-8}$
Glycerol 1.0%	-1.73	$0.59x10^{-8}$
Glycerol 2.0%	-1.53	$0.58x10^{-8}$

The calculated diffusion coefficients are shown in Table 34. There is some discrepancy in values between the control samples. The percentage difference between the controls was 8.6%, if the values are averaged the control concrete has diffusivity of $0.93x10^{-8}$ cm^2/s. The greatest percentage difference between glycerol augmented concrete samples was 5.2%, if the values are averaged the glycerol concrete has diffusivity of $0.58x10^{-8}$ cm^2/s. These results show that the factor for chloride diffusivity between concrete with glycerol and concrete without glycerol is 1.6 times smaller for the glycerol modulated concrete.

5.3 Conclusions

1. Glycerol inhibits chloride ion penetration into concrete.
2. Silica admixtures show little positive effect in limiting chloride ion penetration
3. Time parameters of 1 and 3 days had little to no effect on chloride penetration into the concrete. Conversely, adjustment in pressure from 100psi to 200psi saw increasing chloride penetration.
4. 200psi pressure is too high, samples are prone to cracking. Future experiments should only apply 100psi.
5. Proposed autoclave method for accelerated studying of chloride penetration into concrete has proven to be effective. Experimental method will standardize autoclave conditions at 100psi over a 7-day interval.
6. Chloride diffusivity is 1.6 times slower in concrete with glycerol additions than concrete without glycerol or with silica additions.

REFERENCE

[1] Bentz, D.P.; Snyder, K.A.; Cass, L.C.; Peltz, M.A. Doubling the Service Life of Concrete Structures. I: Reducing Ion Mobility Using Nanoscale Viscosity Modifiers. Cem. and Concr. Compos. 2008, 30, 674-678.

[2] Bentz, D.P.; Snyder, K.A.; Peltz, M.A. Doubling the Service Life of Concrete Structures. II: Performance of Nanoscale Viscosity Modifiers in Mortars. Cem. and Concr. Compos. 2010, 32, 187-193.

[3] Cheng, S.; Shui, Z.; Li, Q.; Sun, T.; Yang, R. Properties, Microstructures and Hydration Products of Lightweight Aggregate Concrete with Metakaolin and Slag Addition. Const. Build. Mater. 2016, 127, 59-67.

[4] Fajardo, G.; Valdez, P.; Pacheco, J. Corrosion of Steel Rebar Embedded in Natural Pozzolan Based Mortars Exposed to Chlorides. Const. Build. Mater.2009, 23, 768-774.

[5] Singer, P., et al. The Solubility of Ferrous Iron in Carbonate-Bearing Waters. American Water Works Association. Vol 62, No 3 (Mar 1970) pp 198-202.

[6] Jovic, B.M.; Jovic, V.D.; Stratford G.R. Cyclic Voltammetry on Ag (111) and Ag (100) Faces in Sodium Hydroxide Solutions. Electrochem. Commun. 1999**,** 1, 247-251.

[7]Zemlyanov, D.Y.; Savinova, E.; Scheybal, A.; Doblhofer, K.; Schlogl R. XPS Observation of OH Groups Incorporated in an Ag(111) Electrode. Surf. Sci.1998, 418, 441-456.

[8] Duffo, G.S., Farina, S.B., Giordano, C.M., Characterization of Solid Embeddable Reference Electrodes for Corrosion Monitoring in Reinforced Concrete Structures. Electrochem. Acta. 2009, 54, 1010-1020.

[9] Muralidharan, S., Ha, T.H., Bae, J.H., Ha, Y.C., Lee, H.G., Kim, D.K. A Promising Potential Embeddable Sensor for Corrosion Monitoring Application in Concrete Structures. Measurement. 2007**,** 40, 600-606.

[10] Gandía-Romero, J.M., Campos, I., Valcuende, M., García-Breijo, E., Marcos, M.D., Pay, J., Soto J. Potentiometric Thick-Film Sensors for Measuring the pH of Concrete. Cem. and Concr. Compos. 2016, 68, 66-76.

[11] Crank J, The mathematics of diffusion, Oxford University Press, 1975

DOE/NEUP Project: M2NU-3-ID-UI

-0401-0132: Effect of concrete mix design parameters on the temperature dependents CTE – Task B

&

-0401-0136: The effect of concrete admixtures on RILEM tube test method – Task E

by

Yunping Xi and Yao Wang

Abstract

This report provides details of two research tasks of this DOE/NEUP project, effect of concrete mix design parameters on the temperature dependent CTE, which is Task B, and the effect of concrete admixtures on RILEM tube test method, which is Task E. For each task, the report describes the topics from the important accomplishments, objectives, experimental approaches, experimental results and conclusions, and recommendations for future study.

Task B. Effect of concrete mix design parameters on the temperature dependent CTE.

Executive summary

There were three closely related parts in this task. The first part was the study on the behavior of concrete samples under the moisture and temperature variations simultaneously. We considered that the moisture transfer is not only driven by the moisture gradient but also by the temperature gradient. The simultaneous temperature and moisture variation is commonly seen during service life of concrete structures. The effect of temperature variation on moisture transfer is called “Soret effect”, which can be represented by a coupling parameter in the moisture flux equation. An experimental setup was designed and used in this study to determine the internal relative humidity distributions in concrete under different thermal gradients, and then a theoretical formulation was developed to determine the value of coupling parameter using the test data. By considering the coupling effect, the moisture transfer in concrete can be estimated more accurately and this is important to improve durability of concrete structures.

The second part in this task was focused on the damage of concrete due to the ice formation under low temperatures. Strain variations and changing in the modulus of elasticity under low temperatures were studied. For the strain variations, the temperature dependent Coefficient Thermal Expansion (CTE) of various concrete was measured under continuous cooling. A reversal in the curve of strain variation from contraction to expansion and then contraction can be used as an indication of the damage in concrete due to ice formation. The test data showed that proper amount of Air-Entraining Agent (AEA) can reduce the reversal and thus reduce the freezing damage of concrete. For the modulus of elasticity under continuous cooling, a theoretical model was developed based on Mori-Tanaka method. Given necessary material parameters and a cooling temperature profile, the model can estimate the variation of modulus of elasticity of a specific concrete sample. The model can characterize the two opposing trends: the stiffening effect due to the formation of solid ice in pores; and the weakening effect due to the damage of excessive ice formation.

The last part investigated the effect of added nanoscale viscosity modifiers in concrete. Most of previous researches have focused on improving mechanical properties of concrete through addition of nanoscale viscosity modifiers into concrete, and little research was done on the effect of the additive on durability properties, especially the freeze-thaw resistance of concrete. Two admixtures were used in this study: Glycerol and Fumed Silica. Compressive strength, chloride diffusion, water adsorption, total porosity, and freeze-thaw resistance were measured from the concrete samples with and without the nanoscale viscosity modifiers. The test data showed positive effect of glycerol and Fumed Silica on the durability properties of concrete.

Objectives

Most concrete structures and buildings are under temperature and moisture variations simultaneously. Thus, the moisture transfer in concrete always is driven by moisture gradient as well as temperature gradient. The temperature effect on moisture transfer is called "Soret effect". In order to accurately estimating the moisture distribution profiles in concrete, it is necessary to consider the effect of temperature gradient, which was the first objective of this task.

The behaviors of concrete under low temperature is different from those under the ambient temperature. When a concrete structure is under a cooling period, concrete may expand instead of contract under a certain temperature range. The possible expansion is due to ice formation which is associated with a large volume expansion of 9%. This dilation part may result in crack and damaging the concrete. This type of damage occurred in many large concrete water tanks in Canada (Grieve et al. 1987) and may be responsible for the deterioration of concrete containment structures and dry storage systems. Reducing the expansion of concrete under low temperature by improving internal structure of concrete was the second objective of this task.

Recently nano-technology has been used to improve the durability of concrete. Two types of nano additives, Glycerol and Fumed Silica, were used to improve durability of concrete, which was the third objective of this task. Fumed Silica was in powder form, while Glycerol was in liquid form. Thus, two different mixing procedures were used to handle the two forms of nano-particles. Various mechanical and transport properties of concrete were measured and optimized.

Experimental approach and Results

1. The effect of temperature on moisture transfer in concrete

The moisture transfer in concrete is affected by the environmental conditions, especially the temperature difference between the internal temperature of concrete and the environmental temperature. There are two types of temperature effects: the effect of elevated temperature with a uniform temperature distribution in concrete structure, and the effect of temperature gradient. Both types of temperature effects were studied.

The flux of moisture in concrete includes the flux due to the gradient of moisture concentration according to Fick's first law as well as the flux due to the gradient of temperature due to the Soret effect. The governing flux equation including both effects is shown below:

$$J = -D_{HH}.grad\ H - D_{HT}.grad\ T \quad (1)$$

where:

$J =$ the flux of moisture in concrete;

$H, T =$ the pore relative humidity and temperature in concrete, respectively;

$D_{HH} =$ the coefficient of moisture diffusion;

$D_{HT} =$ the coupling parameter for the effect of temperature on moisture transport;

Combining with the conservation of mass, the balance of moisture is:

$$\frac{\partial w}{\partial H}\frac{\partial H}{\partial t} = \nabla(-J) \quad (2)$$

where:

$\frac{\partial w}{\partial H}$ = the moisutre capacity of concrete;

The basic ideas of the experimental study are shown in Figure 1. Figure 1(a) shows the experimental setup of isothermal test. With different levels of isothermal temperature conditions, the moisture distributions in concrete samples are measured. If they are almost the same, we can conclude that the temperatures in the range of room temperature without a gradient have little effect on moisture transfer.

Figure 1(b) shows the experimental setup for non-isothermal test. In this case, both ends of the specimen have the same moisture concentrations but different levels of temperature, so there are temperature gradients in the specimens. If the moisture profile for the higher temperature gradient is higher than the profile from lower temperature gradient (with the lowest gradient as zero from the isothermal conditions), the effect of temperature gradient can be identified. In addition, the moisture profiles measured under different temperatures can be used to determine the coupling coefficient D_{HT} by Eq. 2.

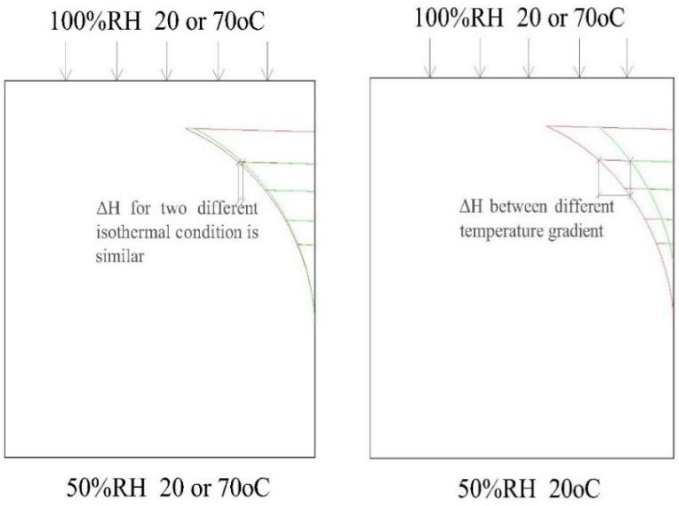

Figure 1 Theoretical model for the study topic: (a) Isothermal condition test and (b) Non-isothermal condition test

Specimen	Top side		Bottom side	
	RH	T (oC)	RH	T (oC)
I-20	100%	20	50%	20
I-70	100%	70	50%	70
N-40	100%	40	50%	20
N-60	100%	60	50%	20
N-70	100%	70	50%	20

Table 2 Experimental strategy adopted (I stands for Isothermal and N stands for Non-isothermal; 20 stands for the value of temperature)

The specimens were 6 x 12inches (diameter x height) concrete cylinders. All samples were made by the mix design shown in Table 2.

w/c=0.6; s/c=2.4; g/c=2.9; loss factor=1.1			
Component	Mass (g)	Consider the loss factor (g)	
cement	2278	2505	Type I Portland Cement
water	1367	1503	Fresh water
sand	5466	6013	All-purpose sand
aggregate	6605	7265	½ inch aggregate

Table 3 Mix proportions of concrete specimens

After 28 days of curing, three sensors were installed in each sample at depths of 2.5, 5.5 and 8.5inches from the heated surface (the top surface). Then the side wall of cylinder was covered with silicone gel and insulated by cotton fibers to ensure that the moisture and heat can only transfer from the top surface (see Figure 2). The top of each specimen had a 4inches deep water reservoir. The test data of temperature and moisture in concrete were recorded by a data logger every minute.

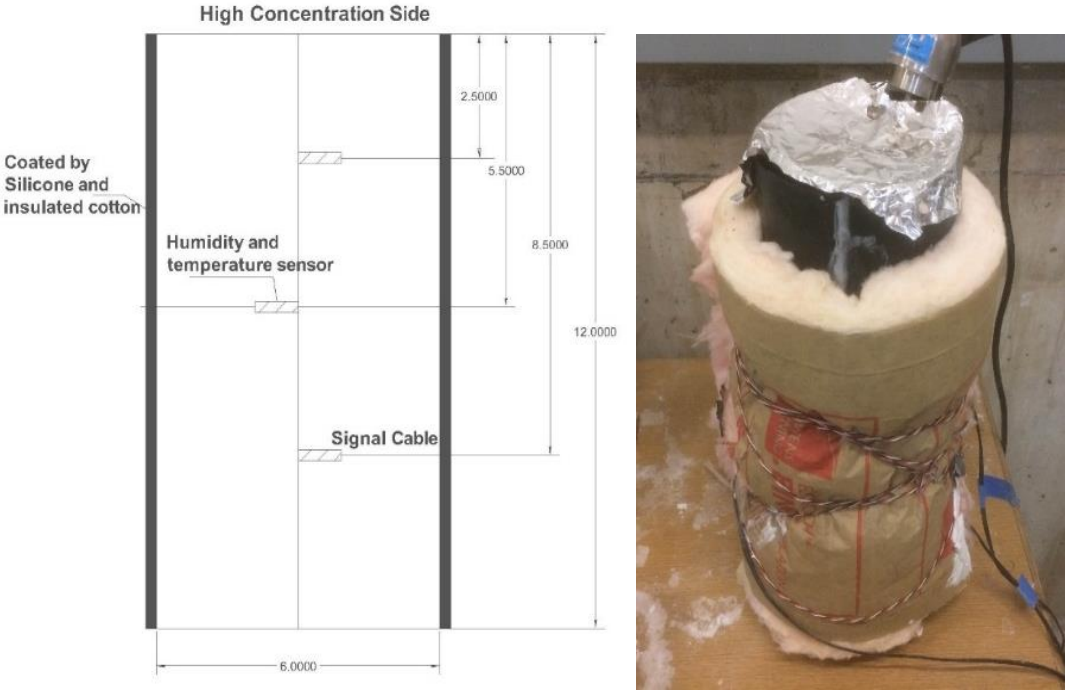

(a) (b)

Figure 1 (a) Schematic illustration of the experimental set-up (unit: inch); (b) a typical testing specimen

The samples are named by the experimental condition and boundary temperature. For example, I-70 is for the samples under the isothermal condition with temperature equal to 70^{o}C, while N-60 is for the samples under the non-isothermal condition and the upper side is heated up to 60^{o}C.

Figures 3-5 show the experimental data collecting from the inserted sensors.

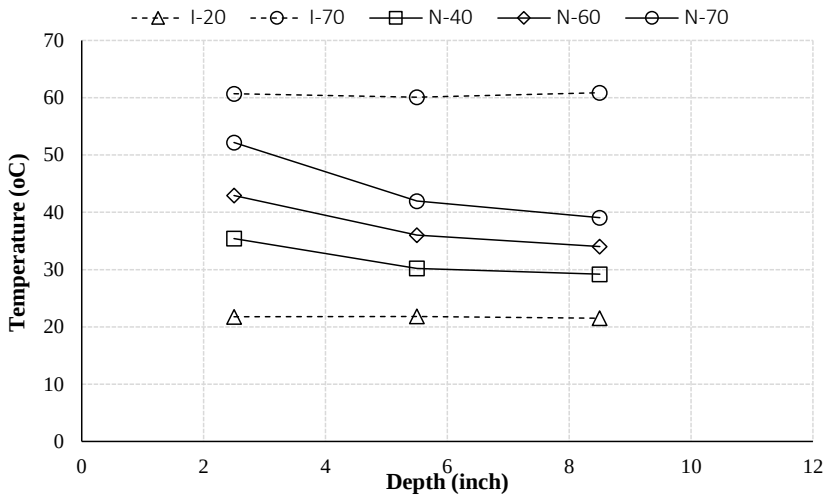

Figure 2 Temperature distribution profiles for all samples at the same time (t=10day)

Figure 3 shows the temperature distribution profiles in all samples after 10 days. From this figure, one can see that the internal temperatures of I-20 and I-70 both kept uniform at different depths, while the profile of I-70 was higher than I-20. However, the non-isothermal samples were under the temperature gradients. Additionally, they show that the temperature gradients depend on the boundary condition. The gradient is higher with a higher temperature on the boundary.

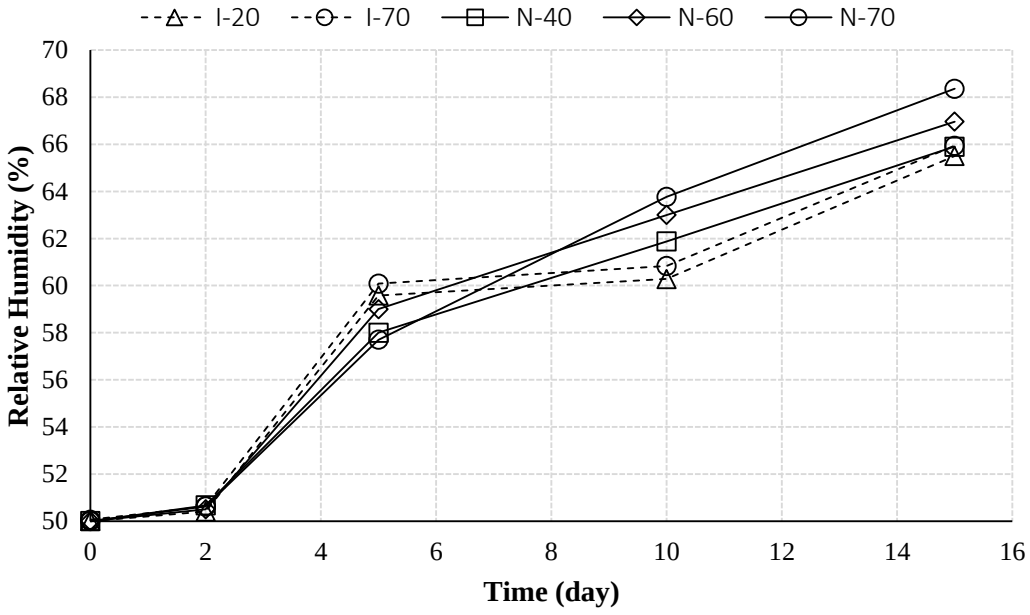

Figure 3 Relative humidity profiles for all samples varies with time increasing at same depth (x=5.5inch)

Figure 4 shows the moisture profiles in all samples at the same depth that *x* equals to 5.5inches. As one can see, all samples started from the same initial condition. The moisture profiles of I-20 and I-70 continuously increased, which resulted from the driving force of moisture gradient. Moreover, these two profiles vary in a similar way. It indicates that the levels of temperature without a temperature gradient do not have a significant effect on moisture transport. Instead, the profiles of the three non-isothermal cases have different increasing rate and moisture value. It shows that the sample with higher temperature boundary condition has the larger value of moisture.

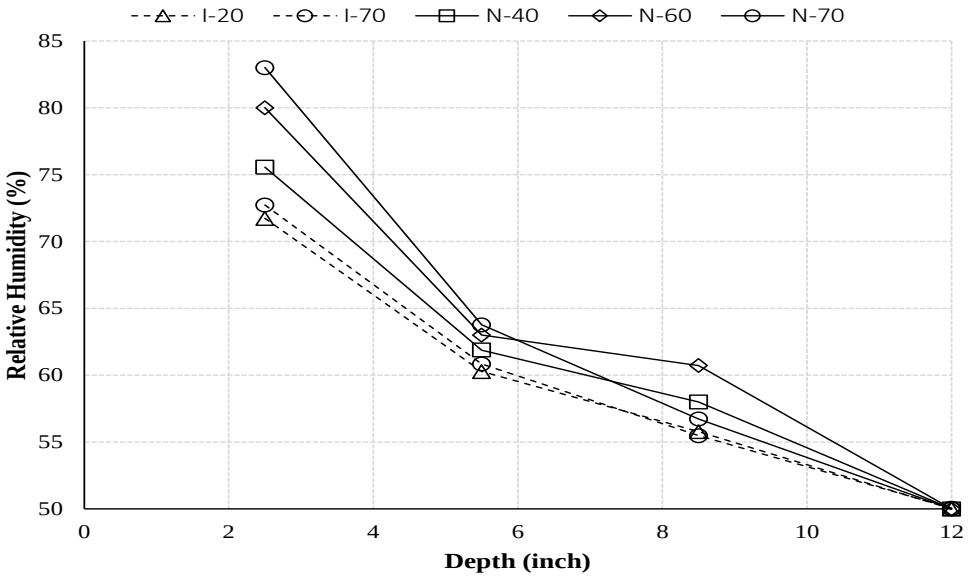

Figure 4 Relative humidity distribution profiles for all sample at the same time (t=10day)

Figure 5 shows the moisture distributions profiles for all samples after 10 days. From this figure, one can see that at a fixed depth, moisture profile has a larger value with a higher temperature boundary condition. In addition, a higher temperature gradient resulted in a faster increasing slope of moisture distribution. These results indicated clearly that the temperature gradient is a driving force for moisture transfer.

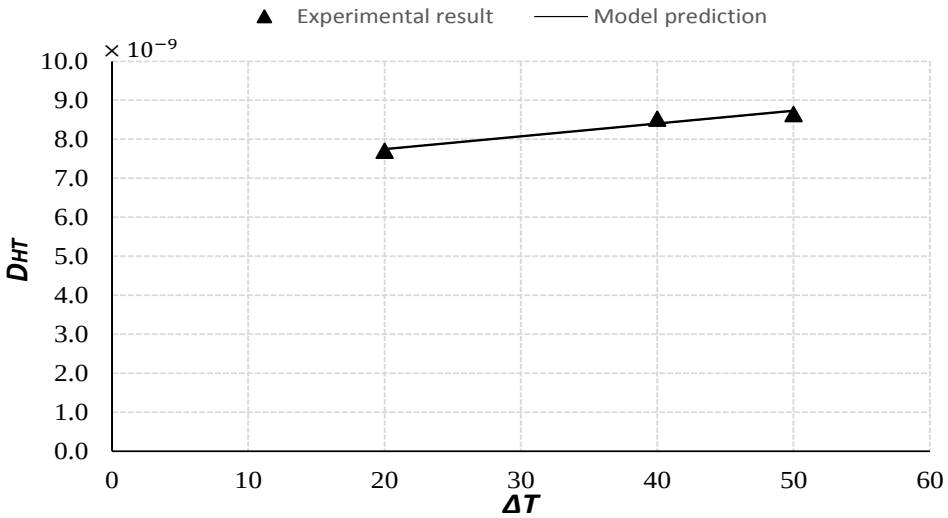

Figure 5 Comparison of experimental results and model prediction of D_{HT}

Figure 6 presents the values of D_{HT} for three different temperature gradients. As one can see, the coefficient for the high temperature gradient has a higher value, which means the coupling parameter is temperature dependent. Thus, a simplified model for the coupling parameter D_{HT} can be derived as a linear function depending on the temperature gradient:

$$D_{HT} = a\Delta T + b \quad (3)$$

The constants a and b can be obtained by a proper curve fitting:

$$D_{HT} = (0.0328 \times \Delta T + 7.0881) \times 10^{-9} \quad (4)$$

In which, D_{HT} is the coefficient of temperature effect on moisture transfer in concrete (%·m^{-2}·s^{-1}·^{o}C^{-1}).

Figure 6 compares the experimental results and model prediction of the D_{HT}. They agree reasonably well. It should be mentioned that the proportional constants in Eq. 4 depend on concrete mix design parameters, i.e. the water-cement ratio and aggregate volume fraction. A different mix design will result in a different material parameter. Therefore, more systematic studies will need to be conducted to determine the effect of concrete mix design on the coupling parameter.

2. Temperature dependent CTE under low temperature

In order to increasing the strength, we selected the size No.7 ASTM C33 to obtain a good gradation of aggregate which is shown in Figure 7. The specimens were used for two tests: (2.1) the compressive strength and (2.2) the CTE under the continuous cooling. The specimens were 3 x 6inch cylinders. The cement was type I/II Portland cement, and the sand was all-purposed normal sand. Two sizes of coarse aggregate were used, 3/8 and 1/2inch. The percentage of each aggregate is shown in Table 3. Air Entraining Agent (AEA) was a product from Sika Company. The details of mixing design are shown in Table 4.

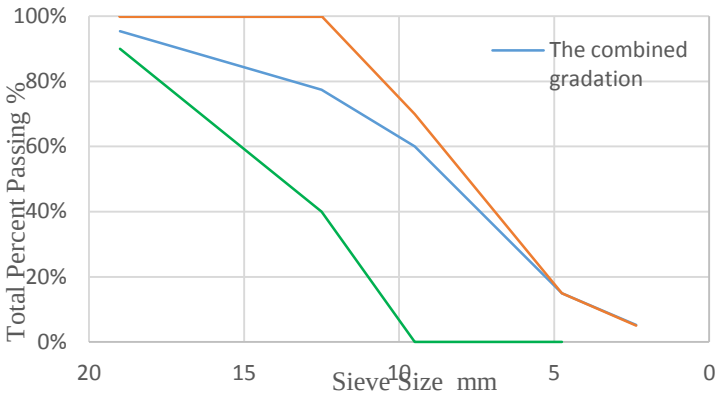

Figure 6 The gradation curves according to ASTM C33

Coarse Aggregate Size (in)	Approximate Percentage (%)
Large 1/2	65
Small 3/8	35

Table 4 The percentage for each type of aggregate

Group ID	w/c	a/w_tot	s/g	AEA
I	0.35	0.78	0.82	0
II	0.35	0.78	0.82	3
III	0.35	0.78	0.82	6
IV	0.4	0.78	0.82	0
V	0.4	0.78	0.82	3
VI	0.4	0.78	0.82	6
VII	0.45	0.78	0.82	0
VIII	0.45	0.78	0.82	3
IX	0.45	0.78	0.82	6

Table 5 Concrete mix design details

2.1 Compressive strength

After 28 curing days of curing, the compression tests were conducted by a MTS load frame with a displacement control of 0.0005 inch/sec. The test data are shown in Table 5.

Figure 7 the sample under compression test

Group ID	Mix Design		Pu kips	Stress ksi
	w/c	AEA		
I	0.35	0%	88	7.00
II	0.35	3%	85	6.76
III	0.35	6%	78	6.21
IV	0.4	0%	84	6.70
V	0.4	3%	79	6.31
VI	0.4	6%	71	5.66
VII	0.45	0%	70	5.58
VIII	0.45	3%	63	5.00
IX	0.45	6%	59	4.66

Table 6 The compression test results

From the results, we can see that the compressive strengths are closely related to the water-cement ratio and dosage of AEA. The strength decreases as w/c increases and as the dosage of AEA increases. The average compressive strength of these nine groups of concrete specimens is around 6 ksi.

2.2 Temperature Dependent CTE

After 28 days of curing, the cylinders glued two nuts by epoxy. During the test, the length changing between the two nuts represented the length changing of the cylinder. The caliber was used to measure the length.

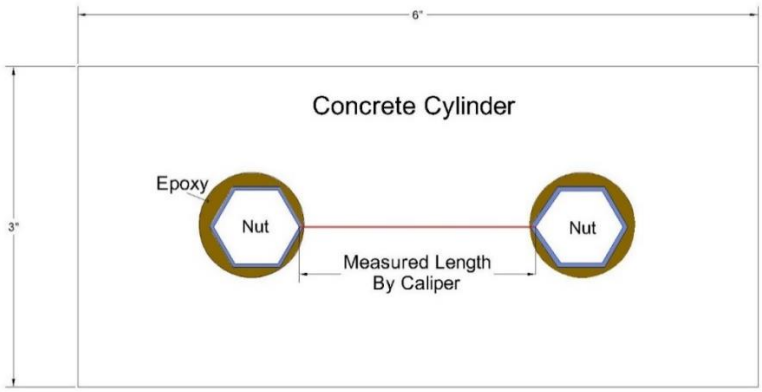

Figure 8 How to measure the length changing

Concrete specimens were tested in the freeze thaw machine. A smart control model was used for the machine to run a continuous cooling curve. The temperature started at 20°C. And then dropped 5 °C in 30 minutes and stayed constant for 3 hours. The end point of the constant part was the measuring point. The detail of curve is shown in Figure 11.

Figure 9 Cylinders in the freeze thaw machine

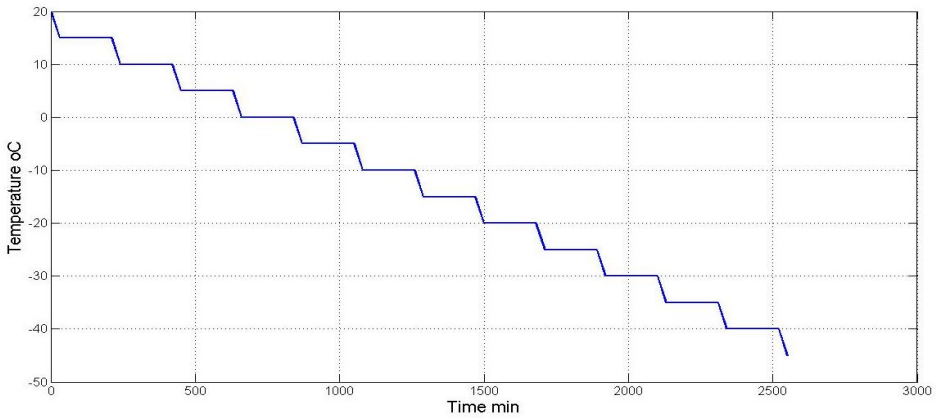

Figure 10 Details of the continuous cooling program

Tables 6 and 7 show the measured length variations and calculated strains during the cooling process, respectively. The strain was calculated by the following equation:

$$\varepsilon_n = \frac{l_n - l_{n-1}}{l_{n-1}} \qquad (5)$$

where ε_n is the strain at temperature n, l_n is the length measured at temperature n, and l_{n-1} is the length measured at temperature n-1.

Figures 12, 13, and 14 show the strain variations with the temperature drops for the specimens of a fixed *w/c* (*w/c* = 0.35, 0.4, and 0.45) and the three different dosages of AEA, respectively. Comparing these figures, we can see that the addition of AEA can effectively decrease the variation of strains upon cooling; and thus the group with lower dosage of AEA has larger slope than the other two groups (the slope is the CTE). Similarly, Figures 15, 16, and 17 show the strain variations with the temperature drops for the specimens with fixed dosages of AEA and three different w/c, respectively. Comparing these curves, we can see that increasing w/c can effectively decrease the variation of strains upon cooling. These variations of thermal strains are due to the increase of internal porosity in the concrete when AEA is added or when w/c is increased: more pores are available to accommodate the ice formed in concrete.

Group ID	Length (inch)								
	15 °C	5 °C	0 °C	-5 °C	-10 °C	-15 °C	-25 °C	-30 °C	-35 °C
I	1.815	1.823	1.812	1.816	1.812	1.817	1.818	1.816	1.815
II	1.841	1.844	1.842	1.846	1.845	1.836	1.839	1.835	1.829
III	1.920	1.920	1.927	1.924	1.918	1.920	1.920	1.921	1.919
IV	1.825	1.830	1.823	1.834	1.826	1.814	1.829	1.827	1.831
V	1.840	1.846	1.842	1.843	1.841	1.854	1.848	1.843	1.840
VI	1.876	1.875	1.876	1.874	1.878	1.875	1.868	1.865	1.861
VII	1.696	1.703	1.700	1.696	1.700	1.695	1.699	1.696	1.695
VIII	1.871	1.867	1.875	1.865	1.862	1.868	1.862	1.857	1.855
IX	1.785	1.784	1.787	1.787	1.790	1.787	1.785	1.782	1.776

Table 7 Length variations under the cooling process

Group ID	Strain								
	15 °C	5 °C	0 °C	-5 °C	-10 °C	-15 °C	-25 °C	-30 °C	-35 °C
I	0.000	0.004	-0.006	0.002	-0.002	0.003	0.001	-0.001	-0.001
II	0.000	0.002	-0.001	0.002	0.000	-0.005	0.002	-0.002	-0.003
III	0.000	0.000	0.003	-0.002	-0.003	0.001	0.000	0.001	-0.001
IV	0.000	0.003	-0.004	0.006	-0.005	-0.007	0.008	-0.001	0.002
V	0.000	0.003	-0.002	0.001	-0.001	0.007	-0.003	-0.003	-0.002
VI	0.000	0.000	0.001	-0.001	0.002	-0.002	-0.003	-0.002	-0.002
VII	0.000	0.004	-0.002	-0.002	0.002	-0.003	0.002	-0.002	-0.001
VIII	0.000	-0.002	0.004	-0.006	-0.001	0.003	-0.003	-0.003	-0.001
IX	0.000	0.000	0.001	0.000	0.002	-0.002	-0.001	-0.001	-0.003

Table 8 Strains calculated during the cooling process

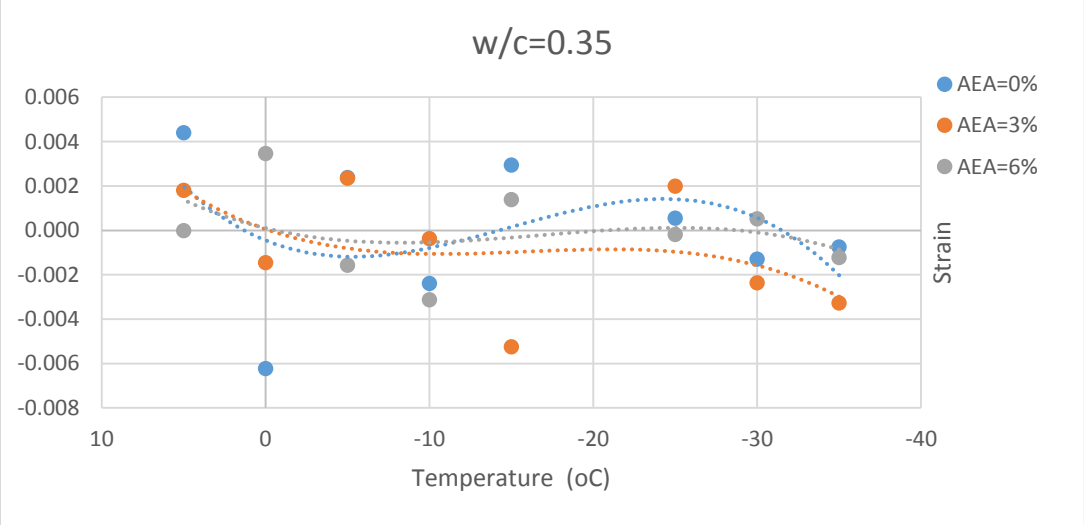

Figure 11 Strain variations of concrete samples with three different dosage of AEA for w/c=0.35

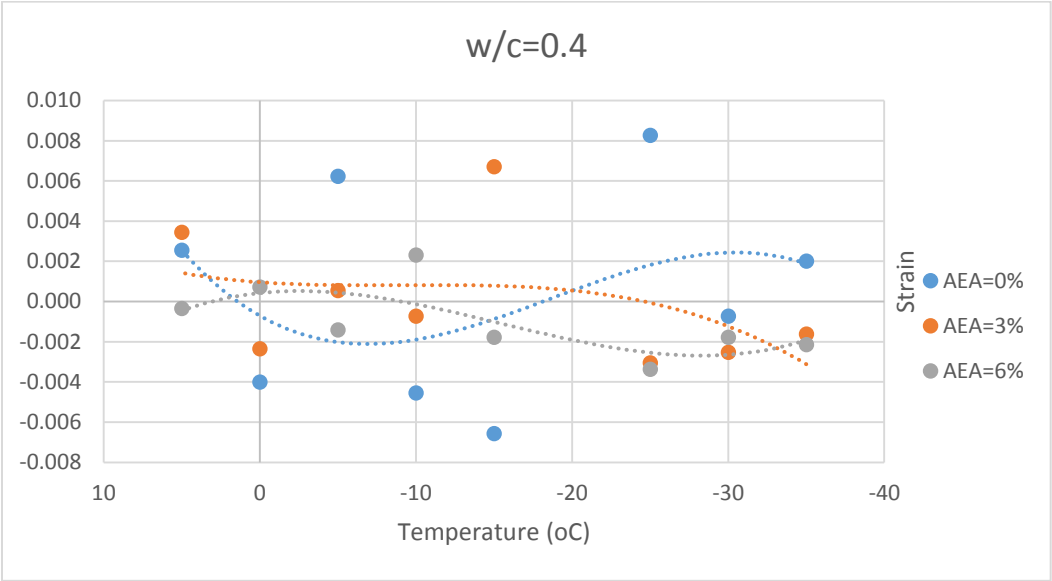

Figure 12 Strain variations of concrete samples with three different dosage of AEA for w/c=0.4

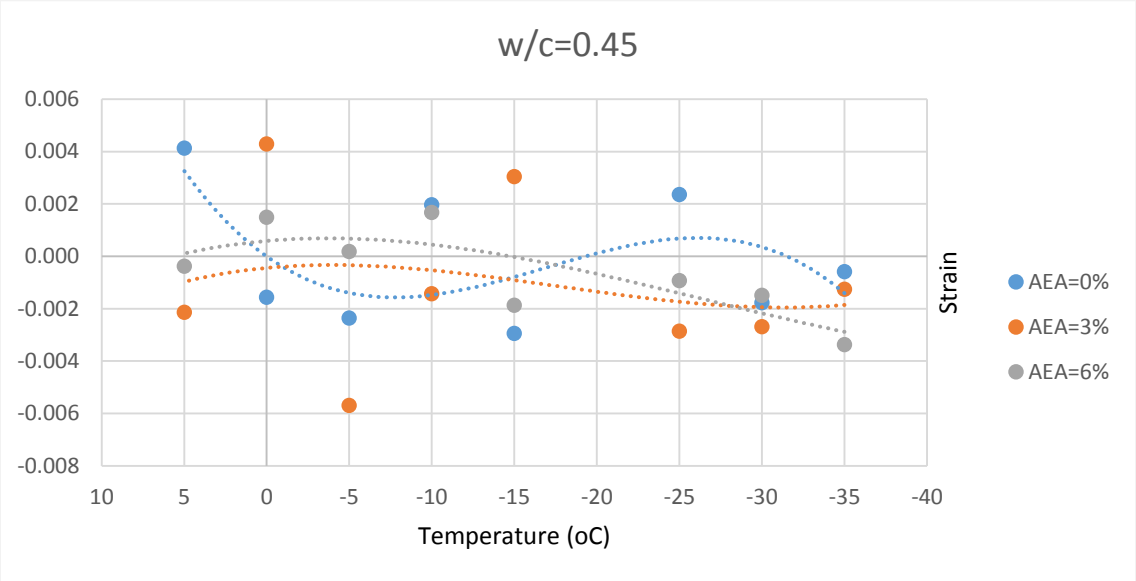

Figure 13 Strain variations of concrete samples with three different dosage of AEA for w/c=0.45

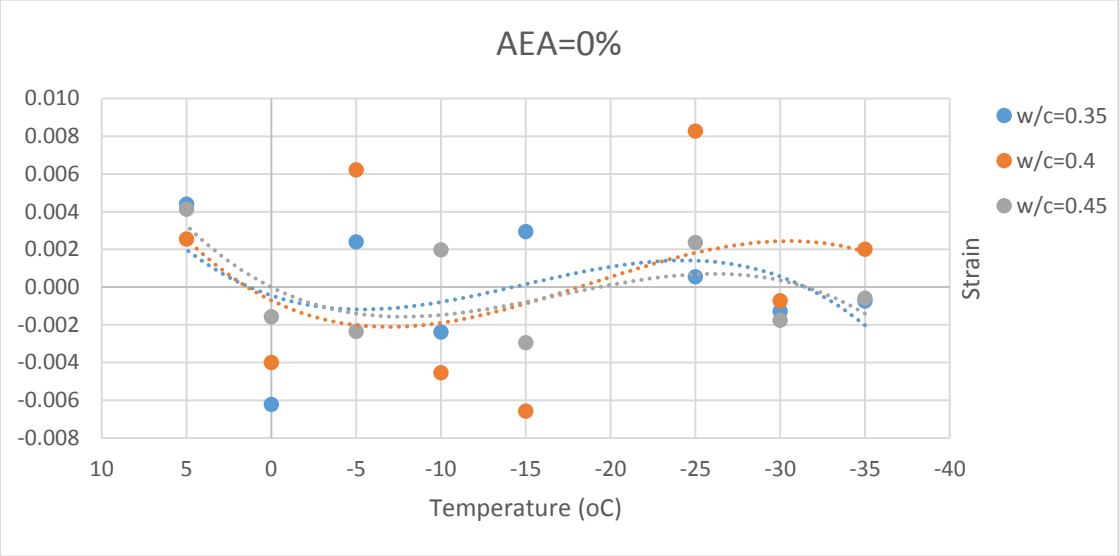

Figure 14 Strain variations of concrete samples with three different w/c for AEA=0%

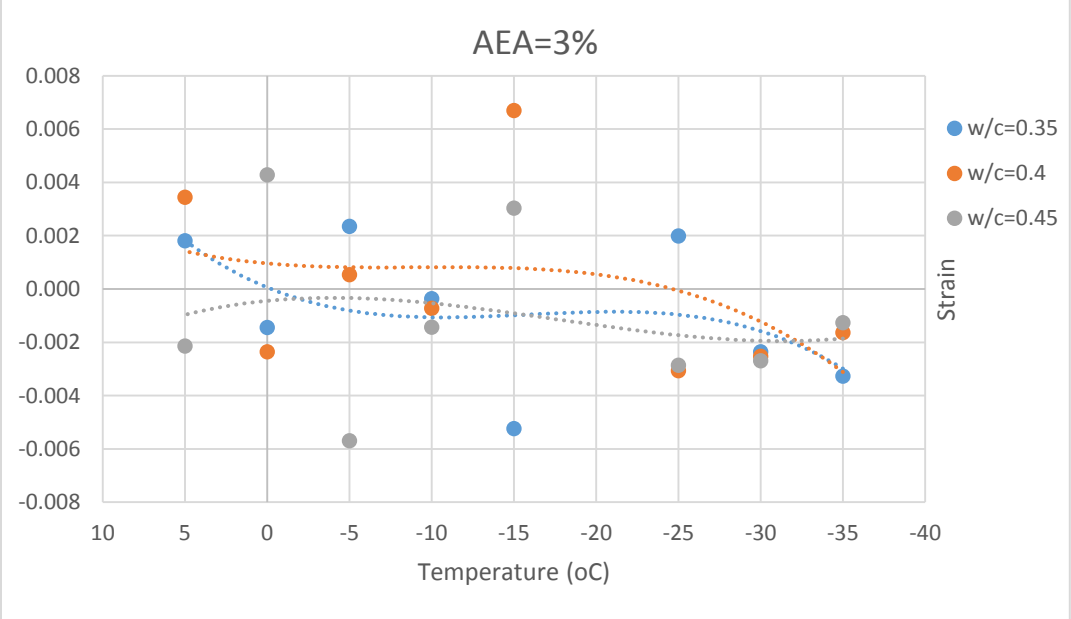

Figure 15 Strain variations of concrete samples with three different w/c for AEA=3%

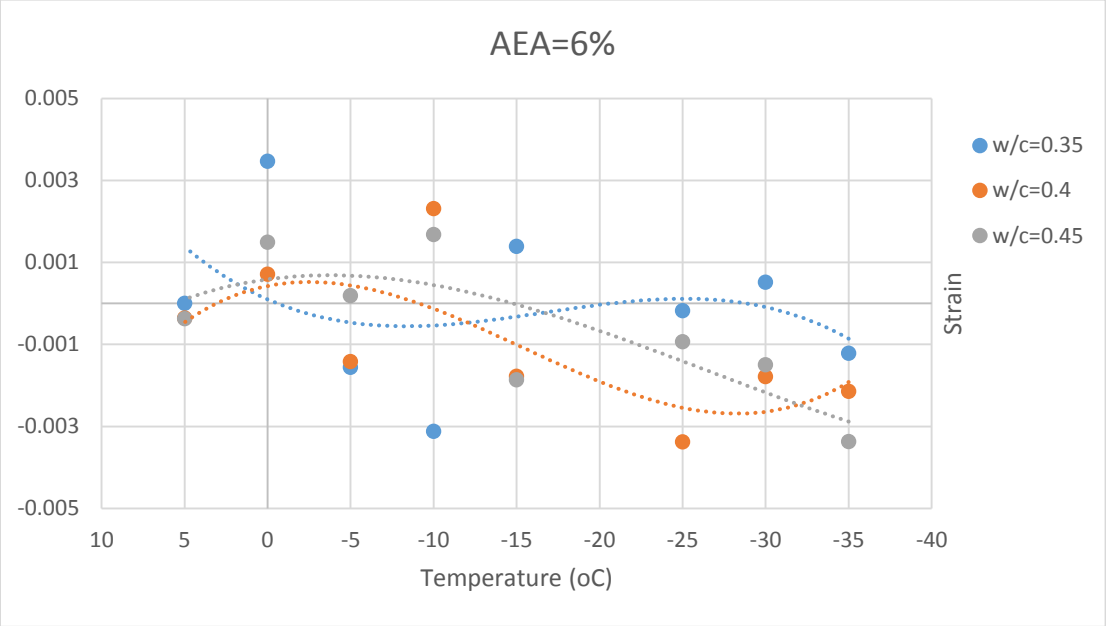

Figure 16 Strain variations of concrete samples with three different w/c for AEA=6%

3. Mori-Tanaka's model for Young's modulus of concrete under low temperature

Mori-Tanaka method, one of the multiscale methods, can provide an effective approach to estimate the overall behavior of composite material from behavior of the inclusions, through a mechanical homogenization technique in which the heterogeneous complex body is replaced by an Equivalent Homogeneous Medium (EHM) that behaves globally in the same way. The Figure 18 shows the general case for composite material and Eq. 6 is the general equation.

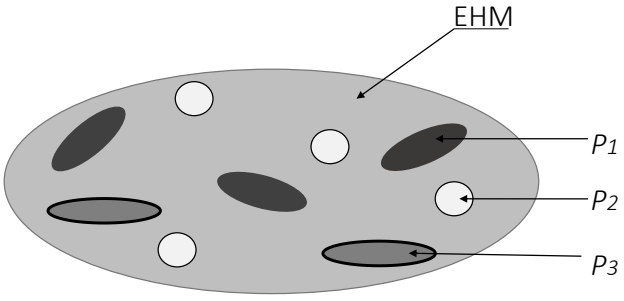

Figure 17 Random representation of a composite material

$$C_{comp} = \sum_{p=P1,P2,P3,M} f_p C_p : A_p$$

$$A_p = \left[I + S_p : \left(C_M^{-1} : C_p - I\right)\right]^{-1} : \left\{\sum_q f_q \left[I + S_q : \left(C_M^{-1} : C_q - I\right)\right]^{-1}\right\}^{-1} \quad (6)$$

Where

f_p = the volume fraction of phase p;

C_p = the fourth order stiffness of phase p;

A_p = the fourth order strain concentration tensor of phase p;

The simulating of concrete is separated into two major steps: modelling of cement paste and modelling of concrete. Figures 19 and 20 show the theoretical model for cement paste and concrete, respectively.

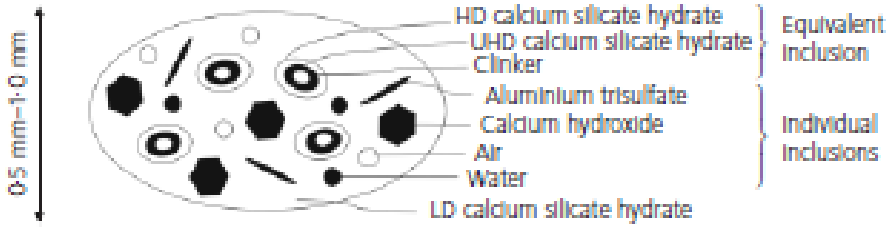

Figure 18 Theoretical model representing each inclusion's morphology

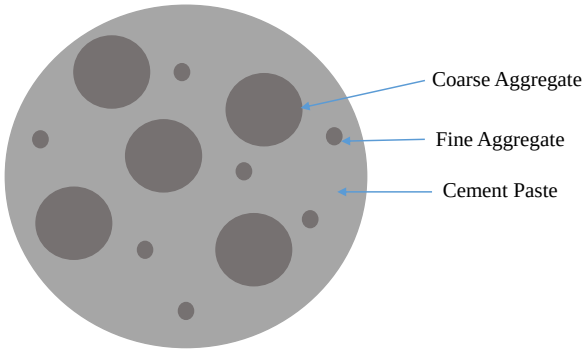

Figure 19 Theoretical model for concrete

3.1 The flowchart of the micromechanical model

- Input parameters: *w/c*, hydration degree and moduli of elasticity of microstructural components.
- Calculate the volume fractions and elastic stiffness tensors of microstructural constituents by Eq. (7).

$$f_{clinker}(\xi) = \frac{20(1-\xi)}{20+63w/c}$$

$$f_{water}(\xi) = \frac{63(w/c - 0.42\,\xi)}{20+63w/c}$$

$$f_{air}(\xi) = \frac{3.31\,\xi}{20+63w/c}$$

$$f_{LD}(\xi) = 0.7 \times \frac{1.66 \times 43.15\,\xi}{2.29 \times (20 + 63w/c)}$$

$$f_{HD}(\xi) = f_{microCH}(\xi) + f_{nanoCH}(\xi) = 0.3 \times \frac{1.66 \times 43.15\,\xi}{2.29(20+63w/c)}$$

$$\mathrm{f_{CH}}(\xi) = \frac{0.63 \times 43.15\,\xi}{2.29(20+63w/c)} \qquad (7)$$

- Calculate the relative volume fraction of components in equivalent inclusion.

$$f_{EI} = f_{clin} + f_{HD} + f_{UHD}$$
$$f_{clin}^{EI} = \frac{f_{clin}}{f_{EI}}$$
$$f_{HDa}^{EI} = \frac{f_{HD}}{f_{EI}}$$
$$f_{UHD}^{EI} = 1 - f_{clin}^{EI} \qquad (8)$$

- Calculate the elastic stiffness tensor of the equivalent inclusion by Eq. (9) based on the Mori Tanaka's scheme.

$$\mathrm{C_{EI}} = \left\{ \sum_{p=clin,UHD} \mathrm{f_p^{EI}}\, \mathrm{C_p} : \left[\mathrm{I} + \mathrm{S_p} : \left(\mathrm{C_{HD}^{-1}} : \mathrm{C}_p - \mathrm{I} \right) \right]^{-1} + \mathrm{f_{HD}^{EI}}\, \mathrm{C_{HD}} \right\}$$

$$: \left\{ \sum_{q=clin,UHD} f_q^{EI} \left[I + S_q : \left(C_{HD}^{-1} : C_p - I \right) \right]^{-1} + f_{HD}^{EI}\, I \right\}^{-1} \quad (9)$$

where, *C* is the fourth-order elastic stiffness, *f* is the volume fraction, *S* is the Eshelby tensor and *I* is the unit tensor.

- Calculate the elastic stiffness tensor of hardened cement paste by Eq. (10).

$$\begin{aligned}
\mathrm{C_{CP}} = & \left\{ \mathrm{f_{LD}\, C_{LD}} + \sum_{p=air,water} \mathrm{f_p\, C_p} : \left[\mathrm{I} + \mathrm{S_p^M} : \left(\mathrm{C_{LD}^{-1}} : \mathrm{C_p} - \mathrm{I} \right) \right]^{-1} \right. \\
& + \mathrm{f_{EI}\, C_{EI}} : \int_{\theta=0}^{\pi} \int_{\phi=0}^{2\pi} \left[\mathrm{I} + \mathrm{S_{EI}^M}\,(\theta, \phi) : \left(\mathrm{C_{LD}^{-1}} : \mathrm{C_{EI}} - \mathrm{I} \right) \right]^{-1} \frac{\sin(\theta)}{4\pi}\, \mathrm{d}\theta\, \mathrm{d}\phi \\
& + \mathrm{f_{AFt}\, C_{AFt}} : \int_{\theta=0}^{\pi} \int_{\phi=0}^{2\pi} \left[\mathrm{I} + \mathrm{S_{AFt}^M}(\theta, \phi) : \left(\mathrm{C_{LD}^{-1}} : \mathrm{C_{AFt}} - \mathrm{I} \right) \right]^{-1} \frac{\sin(\theta)}{4\pi}\, \mathrm{d}\theta\, \mathrm{d}\phi \\
& \left. + \mathrm{f_{microCH}\, C_{CH}} : \int_{\theta=0}^{\pi} \int_{\phi=0}^{2\pi} \left[\mathrm{I} + \mathrm{S_{CH}^M}(\theta, \phi) : \left(\mathrm{C_{LD}^{-1}} : \mathrm{C_{CH}} - \mathrm{I} \right) \right]^{-1} \frac{\sin(\theta)}{4\pi} \mathrm{d}\theta\, \mathrm{d}\phi \right\} \\
& : \left\{ \mathrm{f_{LD}\, I} + \sum_{p=air,water} \mathrm{f_p} : \left[\mathrm{I} + \mathrm{S_p^M} : \left(\mathrm{C_{LD}^{-1}} : \mathrm{C_p} - \mathrm{I} \right) \right]^{-1} \right. \\
& + \mathrm{f_{EI}} : \int_{\theta=0}^{\pi} \int_{\phi=0}^{2\pi} \left[\mathrm{I} + \mathrm{S_{EI}^M}\,(\theta, \phi) : \left(\mathrm{C_{LD}^{-1}} : \mathrm{C_{EI}} - \mathrm{I} \right) \right]^{-1} \frac{\sin(\theta)}{4\pi}\, \mathrm{d}\theta\, \mathrm{d}\phi \\
& + \mathrm{f_{AFt}} : \int_{\theta=0}^{\pi} \int_{\phi=0}^{2\pi} \left[\mathrm{I} + \mathrm{S_{AFt}^M}(\theta, \phi) : \left(\mathrm{C_{LD}^{-1}} : \mathrm{C_{AFt}} - \mathrm{I} \right) \right]^{-1} \frac{\sin(\theta)}{4\pi}\, \mathrm{d}\theta\, \mathrm{d}\phi \\
& \left. + \mathrm{f_{AFt}} : \int_{\theta=0}^{\pi} \int_{\phi=0}^{2\pi} \left[\mathrm{I} + \mathrm{S_{AFt}^M}(\theta, \phi) : \left(\mathrm{C_{LD}^{-1}} : \mathrm{C_{AFt}} - \mathrm{I} \right) \right]^{-1} \frac{\sin(\theta)}{4\pi}\, \mathrm{d}\theta\, \mathrm{d}\phi \right\}^{-1} \quad (10)
\end{aligned}$$

- Calculate the elastic stiffness tensor of concrete by Eq. (11), considering the fine and coarse aggregate:

$$\mathrm{C_{concrete}} = \left\{ \sum_{p=coarse,\,fine} \mathrm{f_p C_p} : \left[\mathrm{I} + \mathrm{S_p} : \left(\mathrm{C_{cp}^{-1}} : \mathrm{C_p} - \mathrm{I} \right) \right]^{-1} + \mathrm{f_{cp}\, C_{cp}} \right\}$$
$$: \left\{ \sum_{p=coarse,\,fine} \mathrm{f_p} : \left[\mathrm{I} + \mathrm{S_p} : \left(\mathrm{C_{cp}^{-1}} : \mathrm{C_p} - \mathrm{I} \right) \right]^{-1} + \mathrm{f_{cp}\, I} \right\}^{-1} \quad (11)$$

3.2 The volume fractions of ice and damage solids

According to the Gibbs-Thompson equation (Eq. (12)), one can see that the freezing temperature of a pore is inversely proportional to the pore size. Thus, if the low temperature value is given, we can calculate the critical size of pore with ice by Eq. (12):

$$T(p_L, x) - T_\infty = -\frac{\gamma_{CL}}{x \Delta S_{fv}} \quad (12)$$

The Drucker-Prager plasticity failure criterion is used to calculated the volume of damaged solid (Eq. (13)):

$$r_{n+1} = r_n + \Delta x = r_n \sqrt[3]{1 + \frac{3\Delta p (f_c + f_t)}{4 f_c f_t}} \quad (13)$$

3.3 A case study

Table 8 gives the material parameters of the sample and Figure 21 shows the calculating results by the Mori-Tanaka method.

Specimen	w/c	T (K)	t (day)	cement type	Hydration degree
Concrete	0.5	300	100	1	0.8

Specimen	Diameter (mm)	Volume fraction	Young's modulus (GPa)	Poisson's ratio

Gravel	12.7	0.7	6	0.2
Sand	0.3	0.1	0.2	0.15

Component	Young's modulus (GPa)	Poisson ratio v	References
UHD CSH	44.5	0.24	Vandamme and Ulm (2009)
HD CSH	29.4	0.24	Constandines and Ulm (2004)
LD CSH	21.7	0.24	Constandines and Ulm (2004)
Calcium hydroxide	42.0	0.315	Moteiro and Chang (1995)
Water	0	0	Ulm et al. (2004)
Air	0	0	
C3S	135	0.3	Velez et al. (2001); Acker (2001)
C2S	130	0.3	Velez et al. (2001); Acker (2001)
C4AF	125	0.3	Velez and Sarrentino (2001); Acker (2001)
C3A	145	0.3	Velez et al. (2001); Acker (2001)
Ettringite	50	0.34	Zohdi et al. (2008); Speziale et al. (2002

Table 9 Material parameters of the specific concrete sample

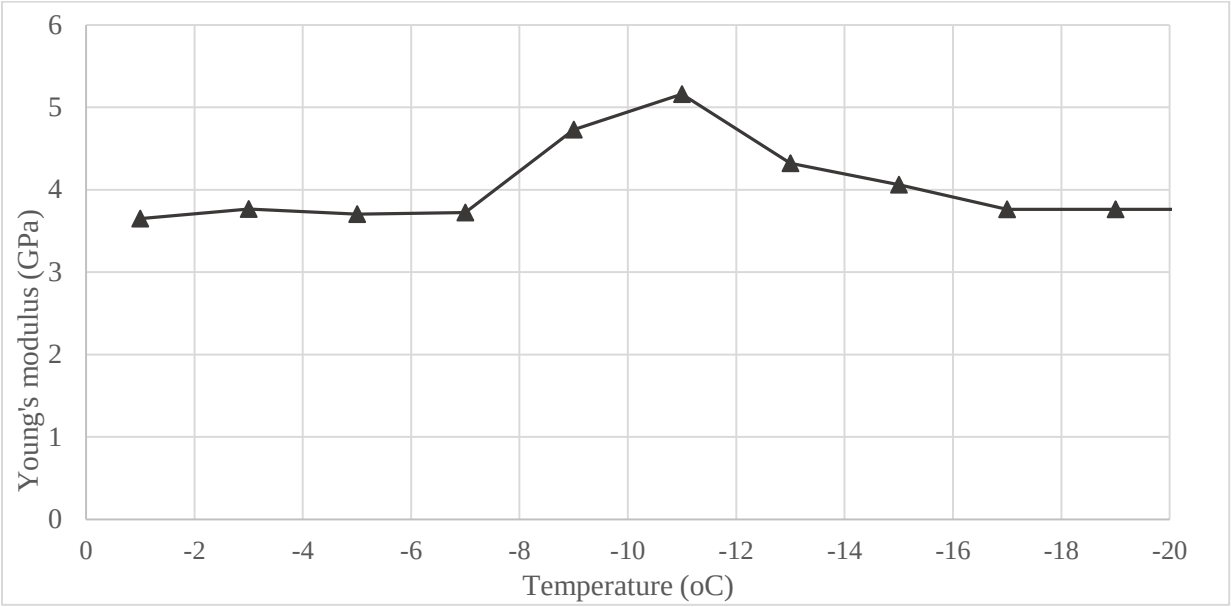

Figure 20 The effective Young's modulus of specific concrete sample under low temperature

From the Figure 21 one can see that at the beginning stage, the modulus increases with the decreasing temperature. This is due to the initial ice formation in pores, and the stiffness of solid ice is higher than that of water. This effect is called "Stiffening Effect". However, the effective modulus starts to decrease with further decease of temperature. This is because the damage due to the excessive ice formation starts to play an important role and the overall stiffness of the composite is weakened. This effect is called "Weakening Effect".

4. Effect of Nano-particle size viscosity modifiers on properties of concrete

In this section, we used two different Nano-particle size viscosity modifiers, Glycerol and Fumed Silica. Among these two admixtures, the Fumed Silica is the powder form, while the Glycerol is the liquid form, and this resulted in different mixing procedures used in the study. Table 9 shows the details of each admixture.

Glycerol	Clear in appearance (APHA<10); Purest form of Glycerin USP (99.7%)
Fumed Silica	Particle size of Powder is around 600 mesh (16μ)

Table 10 Details of admixture

4.1 Temperature dependent CTE and Ponding test of concrete with Glycerol

The sample was 4 by 8inch (diameter x length) cylinder. The mixing detail is shown in Table 10. Cement was Type I/II and sand was the all-purposed normal sand. The size of aggregate was 3/8''. Cause the Glycerol is the liquid form that don't have any dispersing problem, we add it into the water directly and then mix with the solid materials. The samples were demolded after 24hours. For the first 7days, the sample were submerged in lime water to prevent the early dry shrinkage. Then, they were placed in the ambient temperature and high humidity environment for 28days.

Label	Glycerl-cement	Water-cement	Sand-cement	Gravel-cement
1	0%	0.4	2.4	2.9
2	1%	0.4	2.4	2.9
3	2%	0.4	2.4	2.9

Table 11 The mix design for sample with Glycerol

4.1.1 Temperature dependent CTE

The experimental approach is the same with the previous test. A continuous cooling program was set, that started from 20°C, then dropped 10oC in an hour and held for 3hours. Length measurement was taken at the end of the 3hours holding period. Figure 22 shows the cooling program curve and Figure 23 shows the testing results.

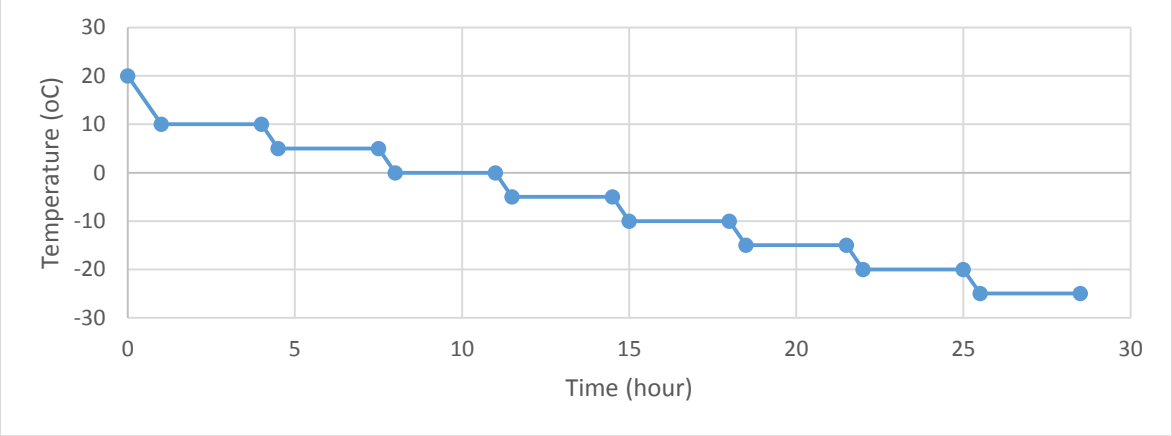

Figure 21 The cooling program curve

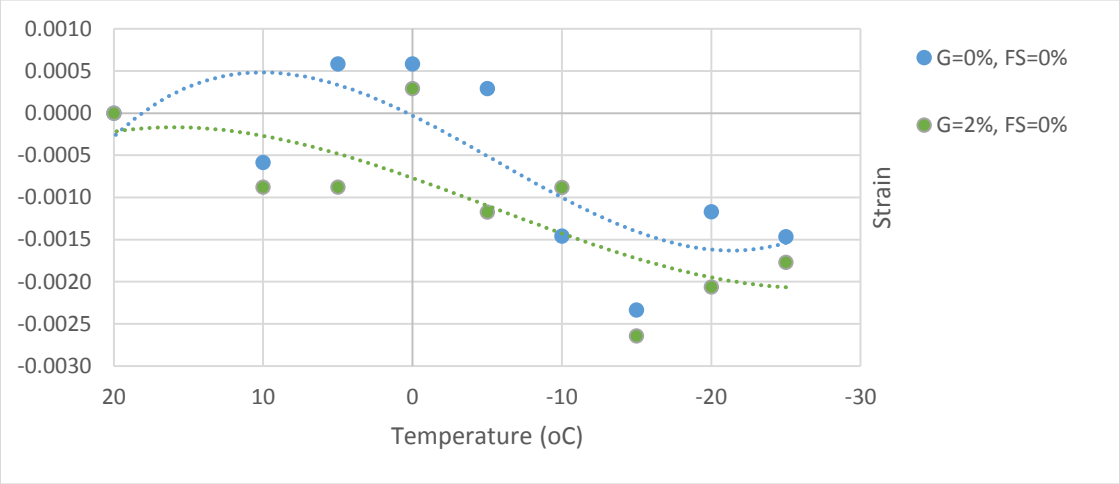

Figure 22 Strain variations of concrete with and without Glycerol

Figure 23 shows the strain variations with the temperature drops for the specimens of two different percentage of Glycerol, respectively. The blue dots are the test data for the specimens without any additives, and the yellow dots are the test data for the specimens with 2% Glycerol. The two dashed curves are the curve fitting for the two sets of test data. Because of the scattering of test data, the two curves can represent the general trends better. One can see that the curve with Glycerol is almost linear: decreasing strains with the decreasing temperature. While the other curve shows a strain reversal with the maximum strain at about 0ºC, which is due to the expansion during ice formation. Therefore, the Glycerol can reduce/prevent the expansion during the cooling process.

4.1.2 Ponding Test

1. In order to ensure the chloride transport in one dimension, the later surface of sample was coated with Silicone.
2. According to the standard AASHTO T259, the high concentration is provided by 3.0% NaCl solution, we used the plastic sheet to create a side seal and dam on the top surface of cylinder for chloride solution.
3. The depth of solution was 10 mm and remained at the constant depth through the whole test.
4. The total chloride concentration profiles were obtained by measuring total chloride concentrations at different depths from the surface exposed to the NaCl solution and different time.
5. The RCT equipment (shown in Figure 24) to measure the total chloride concentration for each sample.
6. Plot the chloride concentration profiles and compare the results (Figures 25-27).

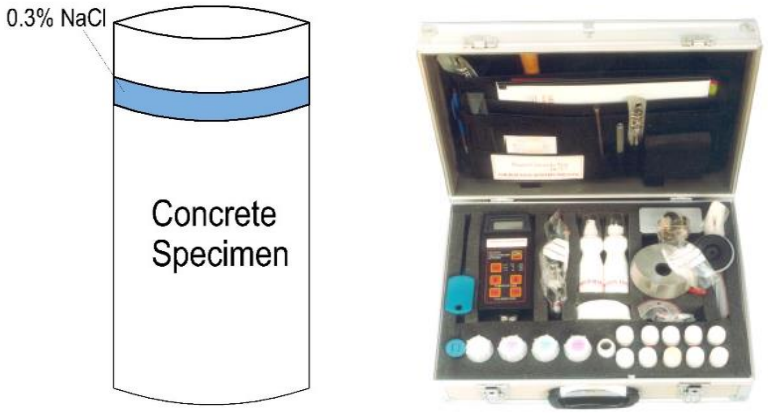

(a) (b)

Figure 23 (a) The specific sample under ponding test; (b) The RCT equipment used for measuring the chloride concentration

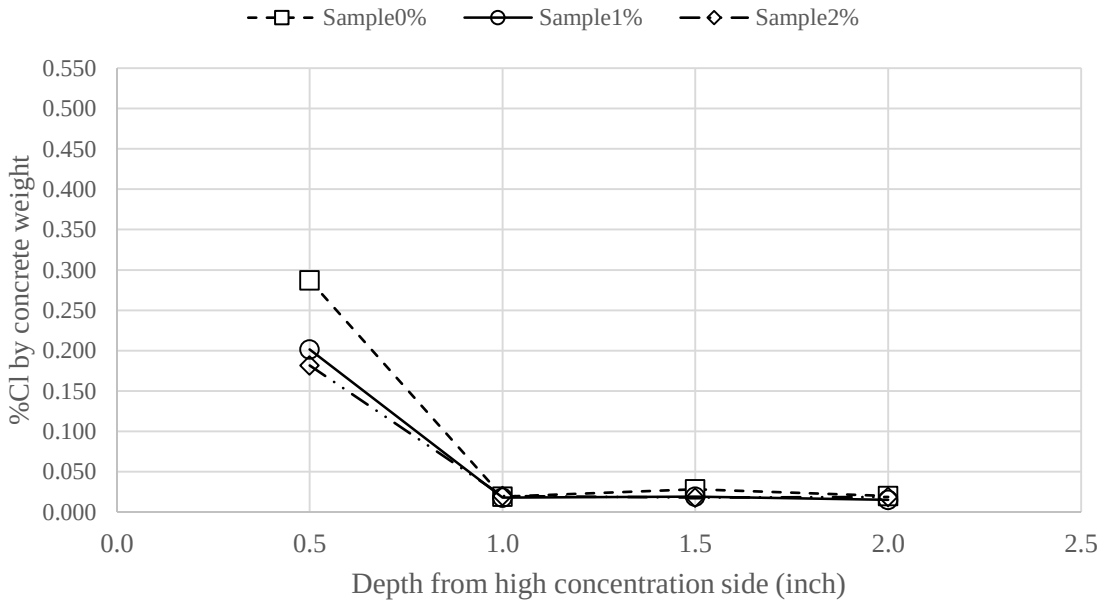

Figure 24 Comparison among the chloride concentration profiles for the samples at 24days

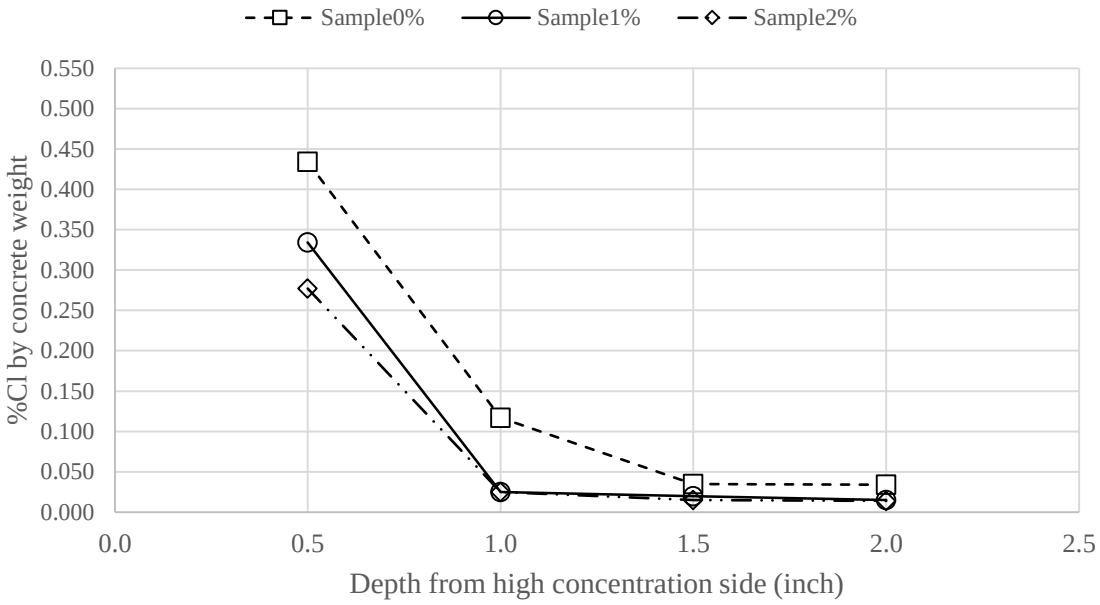

Figure 25 Comparisons among the chloride concentration profiles for samples at 36days

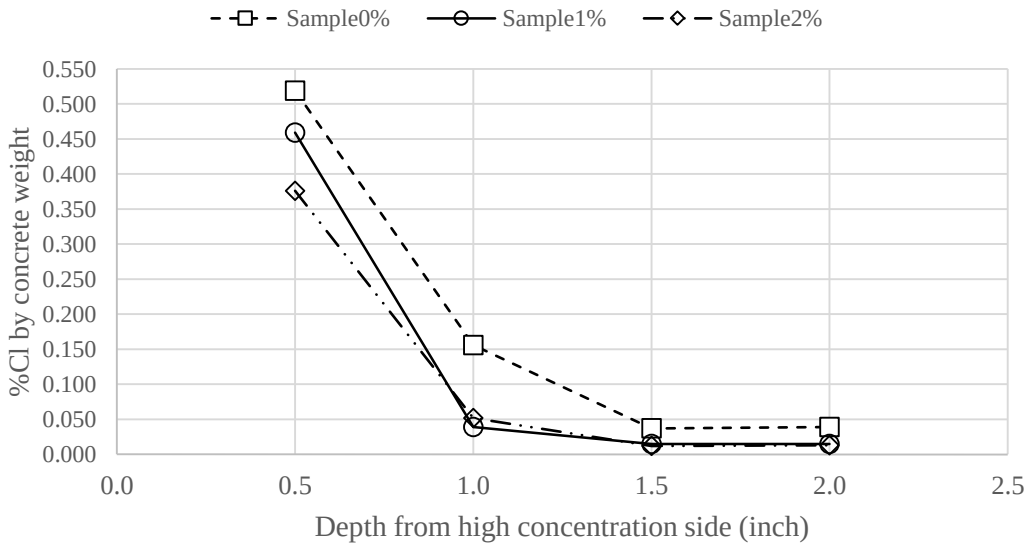

Figure 26 Comparison among the chloride concentration profiles for the samples at 48days

Figures 25 - 27 compare the concentration profiles of three samples at 24days, 36days and 48days, respectively. One can see that the square dots in all three figures have highest concentration and largest while the diamond dots have the smallest values. This because the admixture (glycerol) slows down the chloride transporting in concrete. Moreover, the amount 2% has better effect than the 1%.

4.2 Experimental study on the property of concrete with Nano Silica

Type I/II cement is used. Fine aggregate is the all-purposed normal sand and the size of coarse aggregate is 3/8''. In order to avoid the agglomeration when disperses the Fumed Silica, the adding proportion of this admixture should be small and we use 0.4% and 0.8% in this experiment. Before adding the Fumed Silica, the ultrasonic dispersion technique is needed and the program is: 2sec rotate –- 1sec rest –- 2sec rotate, and total period is 15min. The details of mix design are shown in Table11.

Label	Admixture	Water-cement	Sand-cement	Gravel-cement
1	0%	0.5	2.4	2.9
2	0.4% FS	0.5	2.4	2.9
3	0.8% FS	0.5	2.4	2.9

Table 12 The proportions of each component

4.2.1 Temperature dependent CTE

The effect of fumed silica on the temperature dependent CTE was tested under the continuous cooling process. The freezing program is shown in Figure 28 and test data is plotted in Figure 30. The Eq. 14 is used to calculate the strain.

$$\varepsilon = \frac{L_i - L_0}{L_0} \tag{14}$$

In which, L_0 is the initial length of sample, while L_i is the length at temperature i.

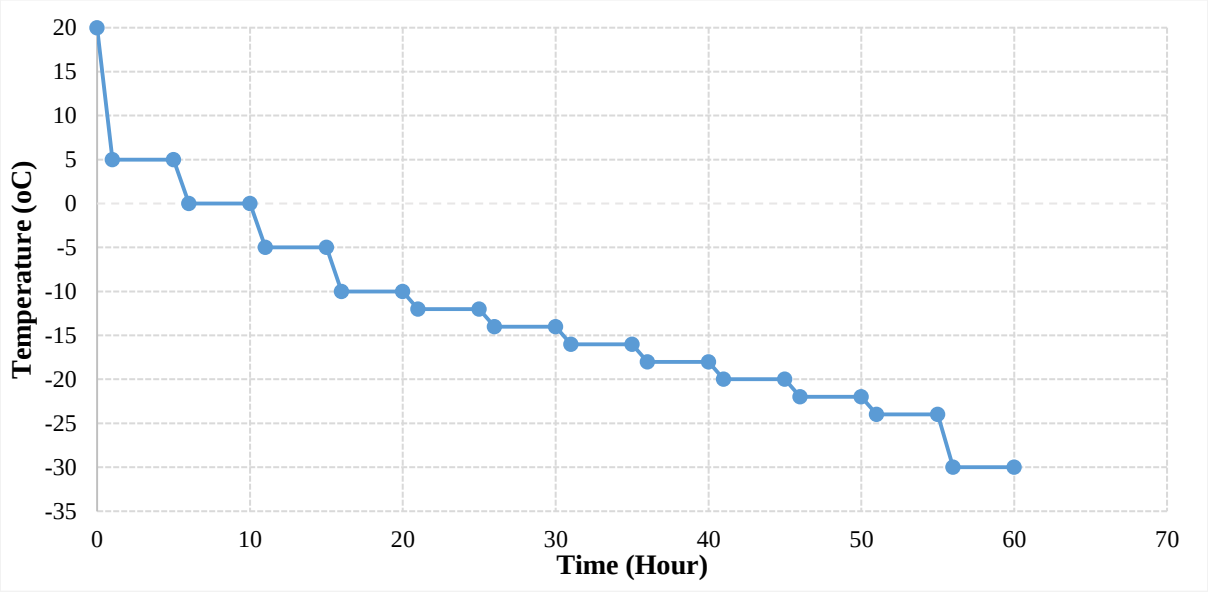

Figure 28 The freezing program

Figure 29 The method for measuring the change in length of sample under freezing process

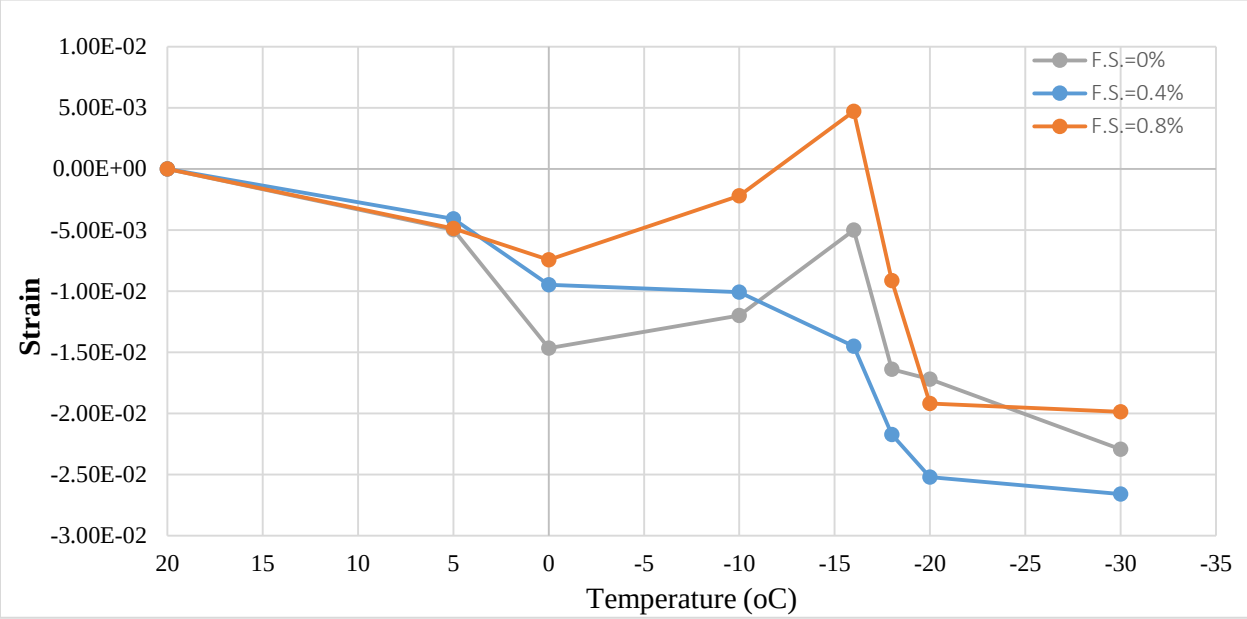

Figure 30 The strain variations of the three samples under the continuous cooling process

Figure 30 compares the strain variations of the samples with different dosages of fumed silica. From this figure, one can see that for the samples with 0% and 0.8% has the expansion at the temperature range -10 to -16oC. Additionally, the sample with 0.8% has the larger dilation part. However, the 0.4% sample contracts with temperature decreasing. In conclude, the addition of fumed silica can improve the freezing resistance and the optimal ratio should be 0.4%.

4.2.2 Total porosity

Total porosity is an indicator for the overall internal pore systems in the concrete. It is calculated by Equation 15:

$$\rho = \frac{V_{water}}{V_{sample}} \times 100 = \frac{m_{SSD} - m_D}{V_{sample}} \times 100 \quad (15)$$

In which, SSD stands for the Saturated Surface Dry moisture condition of concrete samples; D stands for the Dry condition.

The samples for measuring the total porosity were sliced from three different parts of concrete cylinder (top, middle and bottom). Each sample's depth is about 2mm and the weight is in the range of 50-100 grams. The method to reach the SSD condition has two steps: first we vacuumed the samples for 24 hours, and then submerged the sample into the water for 48 hours. For the Dry condition, we kept the samples in the oven, which provided a 105 ºC environment condition. We measured the weight of the sample each day until there was no variation between measurements.

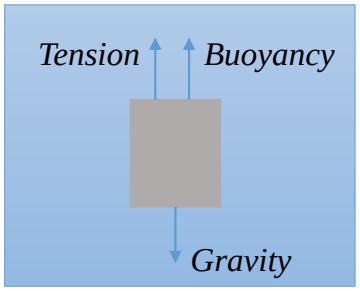

Figure 31 The method for calculating the volumes of sample

For the volumes of the irregular sample, we used the method shown in Figure 31 and Eq. 16. Figure 32 shows the test results.

$$F_{buoyancy} = G-= \rho g V_{sample} \quad (16)$$

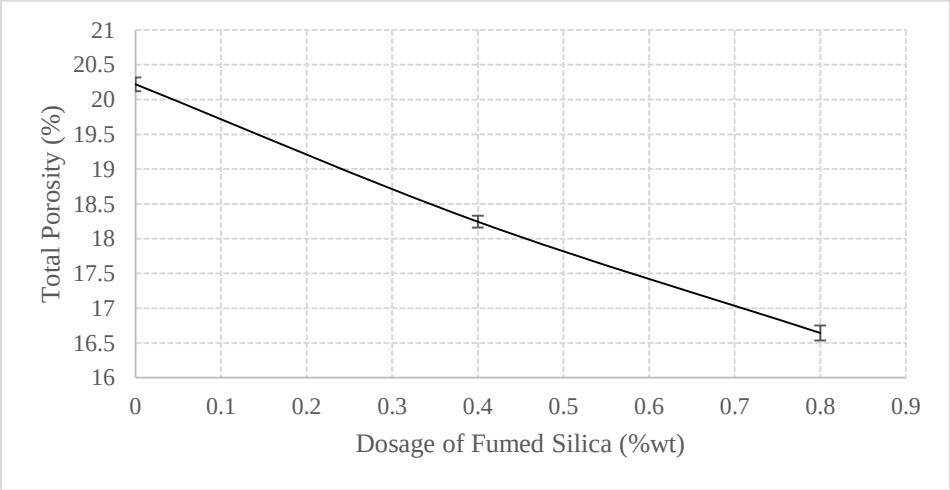

Figure 32 The relationship between the samples' total porosity and the dosages of fumed silica

From Figure 32, one can see that the total porosity of concrete samples decreases with the addition of fumed silica. The errors of measurement for each group of sample are very small as shown in the bars in Figure 32. It indicates that the concrete cylinder is uniformly mixed. In conclusion, due to the addition of fumed silica, the porosity of concrete can be decreased linearly with increasing dosage of the nanoparticles up to 0.8%.

4.2.3 Chloride penetration in concrete

The following is the testing method and the test data.

1. In order to ensure that the chloride transport is in one dimension, the lateral surface of the sample was coated with silicone.

2. According to the standard method AASHTO T259, the chloride concentration of 3.0% NaCl solution was used. We used a plastic sheet to create a side seal and dam on the top surface of cylinder for chloride solution.
3. The depth of ponding solution was 10mm and remained at the constant depth throughout the whole testing period.
4. The free chloride concentration profiles in concrete samples were obtained by measuring water-soluble chloride concentrations at different depths (0-0.5inch, 0.5-1.0inch, 1.0-1.5inch, and 1.5-2.0inch) from the surface exposed to the NaCl solution at different times (7 days, 14 days, and 28 days).

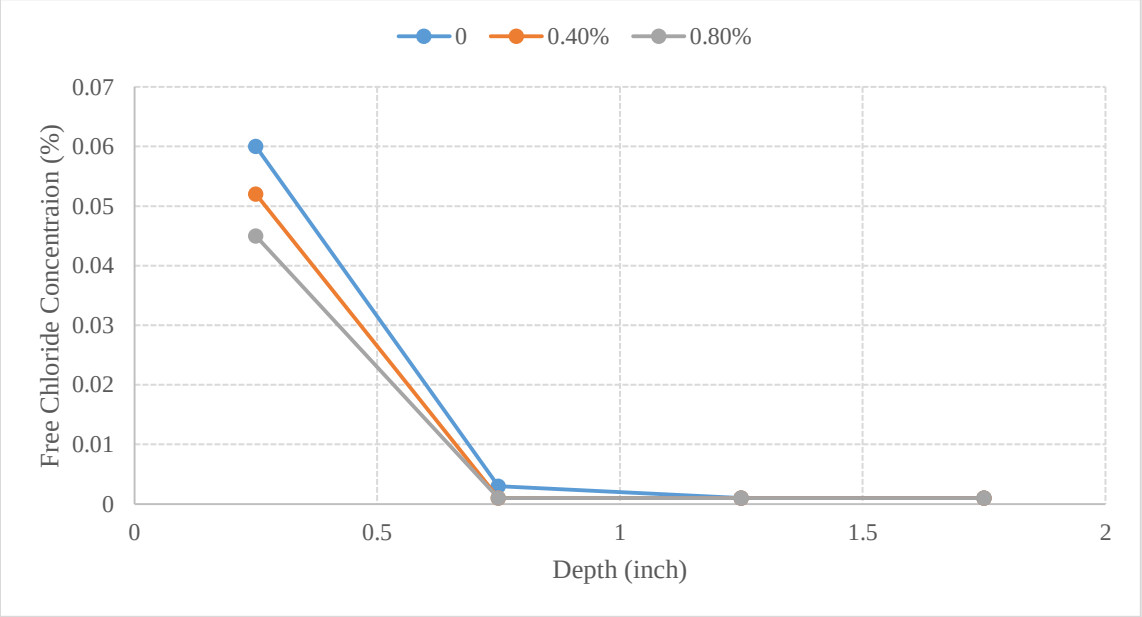

Figure 33 The chloride concentration profiles for three different dosages of fumed silica after 7 days

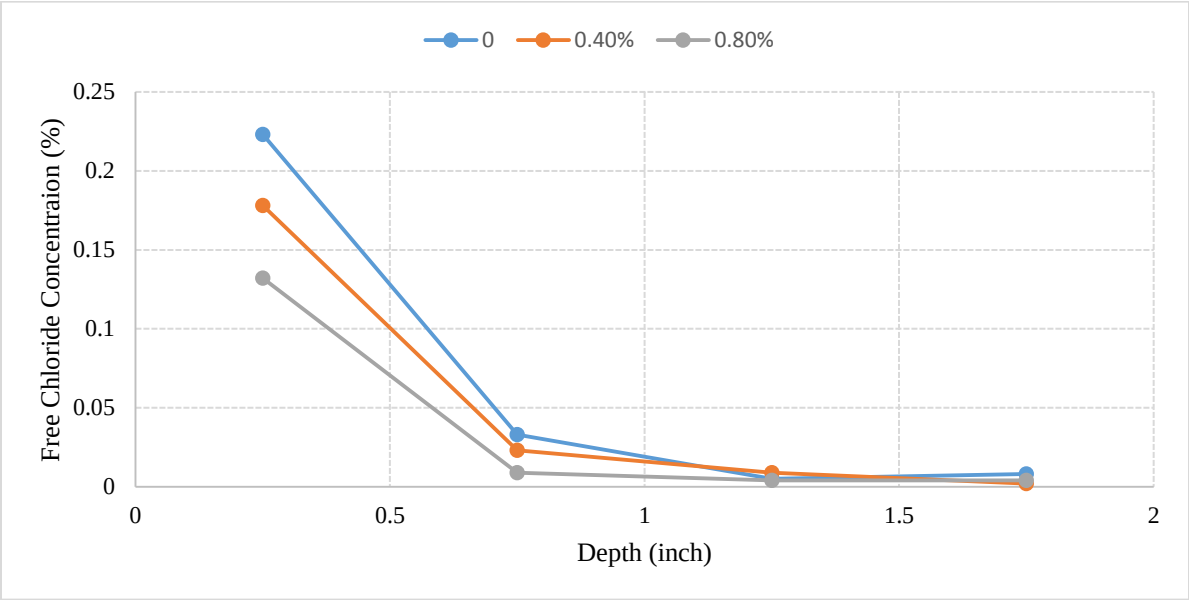

Figure 34 The chloride concentration profiles for three different dosages of fumed silica after 14days

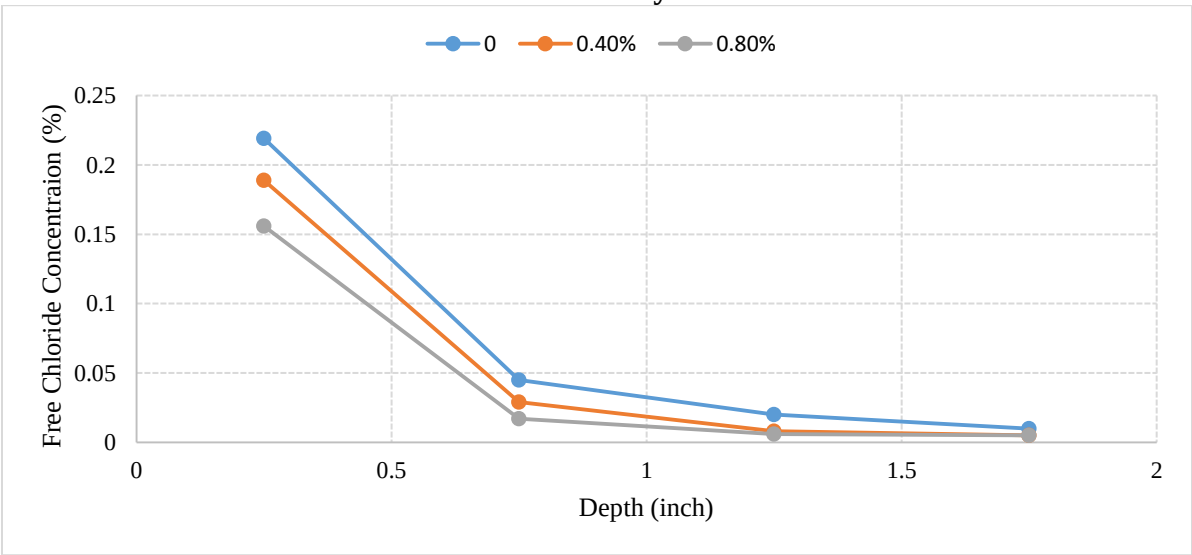

Figure 35 The chloride concentration profiles for three different dosages of fumed silica after 28 days

Figures 33-35 plot the chloride concentration profiles for the samples after 7days, 14days and 28days, respectively. From the figures, we can see that all three curves have the highest values at the left side, which is the surface subjected to the 3.0% NaCl solution. Comparing the three concentration profiles at the depth 0-0.5inch, one can see that the profile of 0% sample has the largest value and slope, while the samples with 0.8% fumed silica have the smallest values. It indicates that the concrete sample with dosage of fumed silica can slow down the chloride penetration, and the higher dosage of fumed silica can obtain the lower chloride diffusion rate.

4.2.4 Compressive strength test

After 28 days curing age, the concrete samples were capped before the compressive strength test. The test was conducted by a MTS load frame. The rate of displacement control was 0.0005 inch/sec. Figure 36 shows the results of compressive strength with different dosages of fumed silica.

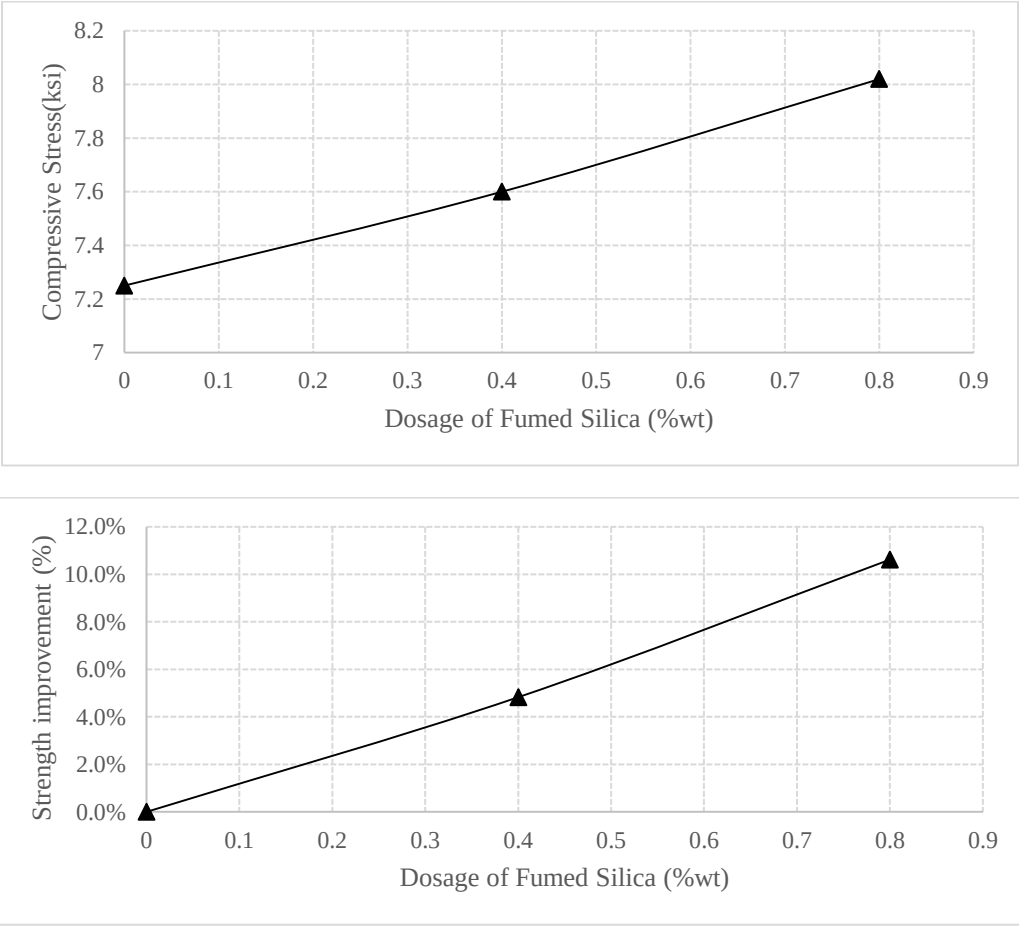

Figure 36 The relationship between the compressive strength and dosages of fumed silica

Conclusions

1. An experimental technique was established for understanding the temperature effect on moisture transfer in concrete. The technique was used for studying the moisture penetration into concrete with and without temperature gradient. The test data show that the elevated temperature without a temperature gradient does not have a significant effect on moisture transfer. Moreover, the effect of temperature gradient is significant and should be considered in the analysis of moisture transport in concrete under non-isothermal condition.

2. An analysis method was developed based on the governing equations to calculate the coupling parameter D_{HT} (coefficient of the Soret effect). The results show that D_{HT} is not a constant but increases with temperature gradient increasing. A material model was developed for D_{HT} using the test data obtained in this study.

3. For the effect of AEA on the thermal strain, it is evidenced from Figures 12, 13, and 14 that the addition of AEA can effectively decrease the variation of thermal strains during the cooling process, and thus decrease the dilation in the concrete. Similarly, from Fig. 15, 16, and 17 it is obvious that increasing w/c effectively decreases the variation of thermal strains during the cooling process. Both methods are increasing the internal porosity in the concrete: more internal space is available for the ice to deposit in the pores and thus the overall expansion is reduced.

4. The theoretical model based on the Mori-Tanaka method successfully simulated the concrete from microscale to mesoscale. Figure 21 shows the calculating results for the specific concrete sample. From the results one can see that as temperature decreasing, the Young's modulus increases at the beginning and then decreases. This agrees with the temperature dependent CTE test results.

5. Freeze-thaw performance and chloride penetration were both improved when *glycerol* was added in the concrete. The sample with *glycereol* showed a better effect than the control sample. Thus, g*lycerol* indeed has the positive effect on improving the durability of concrete.

6. From the experimental results including the compressive strength, total porosity, chloride penetration, and temperature dependent CTE, one can see that the concrete sample with *fumed silica* has better performance characteristics than the control sample. Thus, *fumed silica* can improve both mechanical and durability properties of concrete.

Recommendation for future researchers

- This task focused on the temperature effect on the moisture transfer, which is called "Soret effect". Moisture gradient affects the temperature distributions in concrete and the effect is called "Dufour effect". "Dufour effect" is just as important as "Soret effect" and it should be studied in the future.

- Only one concrete mix design was used in the study for the temperature effect on moisture transfer, a more systematic study should be conducted on concrete samples with different mix designs, such as different water-cement ratios and different aggregate volume fractions.

- The microstructure of concrete varies with addition of AEA. Systematic microscopic study needs to be performed to determine concrete's pore structure with different dosages of AEA. Similarly, a theoretical model needs to be developed to estimate the pore system of concrete with different dosages of AEA.

Products

- "The effect of temperature on moisture transfer in concrete", Wang Y., and Xi Y. (2017), submitted to *Materials*.
- "Temperature dependent CTE of concrete under low temperatures", Wang Y., and Xi Y. (2017), in preparation.
- "Mori-Tanaka model for Young's modulus of concrete under low temperatures", Wang Y., and Xi Y. (2017), in preparation.
- "Experimental study on temperature dependent CTE of concrete with Nanoscale Viscosity Modifier", Wang Y., and Xi Y. (2017), in preparation.

Task E. Effect of concrete admixtures on RILEM tube test method

Executive summary

Wind-Driven Rain (WDR) is very common in North America, North Europe and Asia. In reality, the high speed wind can produce a high pressure on surface of a concrete structure that can significantly increase the moisture penetration into the concrete structure. A non-destructive testing method, RILEM tube method, has been used to simulate the water penetration under the high pressure on a concrete surface. In this task, there were two closely related parts to study the effect of concrete admixtures on RILEM tube test method experimentally and theoretically.

For the experimental studies, the concrete samples were cast with different water-to-cement ratios and two admixtures: Air Entraining Agent (AEA) and Fumed Silica. The samples were affixed with a RILEM tube to record the absorption rate of moisture. A higher rate means there is more water penetrating into the concrete and this may increase the deterioration of concrete structure. By comparing the water absorption rates of test data, it was found that the sample with higher AEA has a relative higher moisture penetration rate under the same wind speed. The samples with higher dosages of Fumed Silica have lower water penetration rates. Thus, a proper dosage of Fumed Silica added into to the concrete can reduce the damage from the WDR.

The theoretical study, a diffusion model was developed to determine the internal moisture distributions under different boundary conditions. A new variable P (pore pressure) was introduced in the moisture transfer model for WDR, which is an internal pressure in pores related to the water pressure in liquid water transfer process or the vapor pressure in water vapor transfer process. The comparisons of theoretical prediction and experimental data showed quite good agreement.

Objectives

The damage mechanism of wind-driven rain (WDR) on concrete structures has not been studied very well. WDR can significantly increase the moisture content in concrete due to the high pressure of wind on concrete surface. A freezing temperature after a WDR can turn the moisture into ice and thus generate damage in the concrete. In this task, the resistance of concrete to WDR was evaluated by the RILEM tube method (Hens 2010). A theoretical model was developed to determine the internal moisture distribution under WDR. An experimental study was conducted to investigate the effect of concrete mix design parameters on the resistance to WDR.

Experimental approach and Results

1. The resistance of concrete with different mix design to WRD

In the experimental study, two variables for the concrete mix design were considered: water-cement ratio (*w/c*) and agent of air entraining agent (*AEA*). The size of concrete sample was 4x8 inch (diameter x height) cylinder. The Table 12 shows the details of mix design.

w=water; c=cement; s=sand; g=coarse aggregate; a=s + g; w_totl=total weight;				
Group ID	w/c	a/w_tot	s/g	AEA %vol.
1	0.35	0.78	0.82	0
2	0.35	0.78	0.82	3
3	0.35	0.78	0.82	6
4	0.4	0.78	0.82	0
5	0.4	0.78	0.82	3
6	0.4	0.78	0.82	6
7	0.45	0.78	0.82	0
8	0.45	0.78	0.82	3
9	0.45	0.78	0.82	6

Table 13 The mix design

In order to obtain the good compressive strength, we used the same combined gradation shown in Figure 7.

After 28 curing days, all samples were kept at the lab room for 45 days in order to reach the same moisture condition with the environment. Then the details of experimental procedure are shown below:

1) Cut the cylinders into 5inches to get the flat end surface;
2) Polish the end surface to ensure the side is dry and clean;
3) Paint the cylinder to provide the one-dimension diffusion;
4) Roll out a bead of the putty to approximately 1/4inches diameter and 6inches length. Attach the putty to the flat brim of the tube;
5) Firmly press the tube with the attached putty to the surface. Press in any putty that extrudes to form a tight seal.
6) Fill the tube with water to the 0 gradation mark, ensuring no air is trapped inside the body.
7) Cover the end side (attached with tube) with Silicon;
8) Put a small piece of wet cotton in the tube to prevent the effect of evaporation;
9) Check the location of water head and record the time and location per day.

RELATIONSHIP BETWEEN TUBE WATER LEVEL AND WIND SPEED

Graduation Mark (ml)	Theoretical Wind Speed (mph)
0	98.1
0.5	94.1
1.0	90.04
1.5	85.7
2.0	81.1
2.5	75.2
3.0	71.1
3.5	65.5
4.0	59.4
4.5	52.8
5	44.8

Figure 37 Relationship between tube water level and wind speed

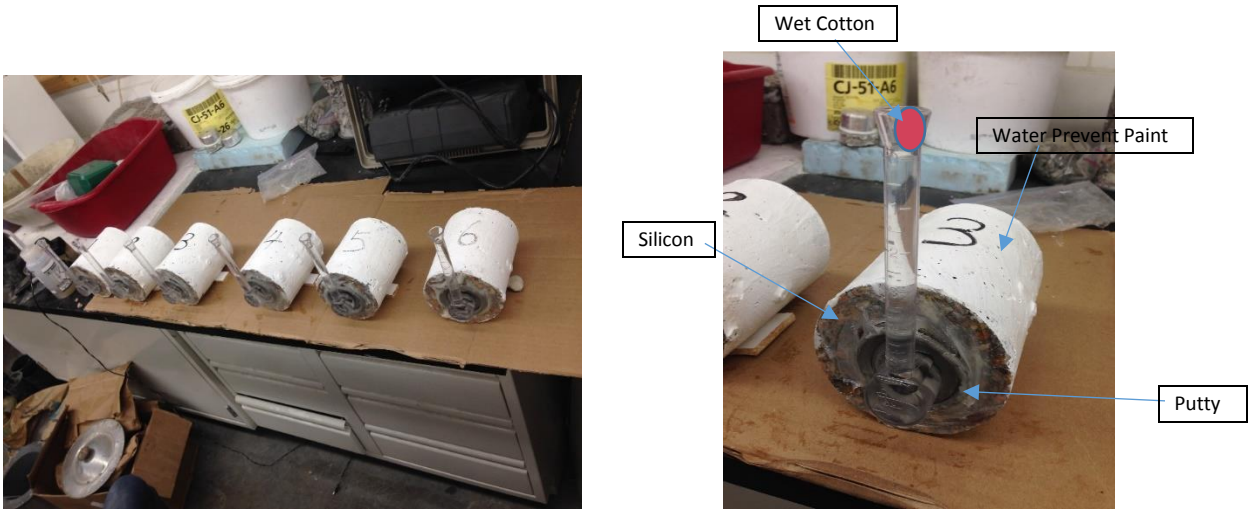

Figure 27 the testing specimen

The Table 14 shows the experimental results. During the test, when the water head dropped below 2.5 ml, there were several small bubbles inside. Therefore, we will just use the test data for 0-2 ml.

Group ID	Mix Design		Graduation Mark (ml)			
	w/c	AEA	0-0.5	0.5-1	1-1.5	1.5-2
1	0.35	0%	48 h	115 h	168 h	---
2	0.35	3%	48 h	115 h	144 h	---
3	0.35	6%	48 h	91 h	144 h	144 h
4	0.4	0%	48 h	91 h	144 h	144 h
5	0.4	3%	48 h	91 h	96 h	144 h
6	0.4	6%	19 h	67 h	96 h	120 h
7	0.45	0%	28 h		80 h	
8	0.45	3%	28 h		80 h	
9	0.45	6%	28 h			

Table 14 the experimental results (h: hour)

After 28 days, three cylinders for each group were cupped and tested the compressive strength. The compression is origins from the MTS load frame. The program is the displacement control at a rate of 0.0005 in/sec.

Group ID	Mix Design		Pu kips	Stress ksi
	w/c	AEA		
1	0.35	0%	88	7.00
2	0.35	3%	85	6.76
3	0.35	6%	78	6.21
4	0.4	0%	84	6.70
5	0.4	3%	79	6.31
6	0.4	6%	71	5.66
7	0.45	0%	70	5.58
8	0.45	3%	63	5.00
9	0.45	6%	59	4.66

Table 15 compressive strengths for each concrete sample

2. A theoretical model to estimate the moisture profiles of concrete under WDR

The moisture transfer under the isothermal condition can be expressed by the moisture capacity and pore pressure, depending on the mass conservation:

$$\frac{\partial \mathrm{w}}{\partial \mathrm{H}}\frac{\partial \mathrm{P}}{\partial \mathrm{t}} = \mathrm{K}_w \frac{\partial^2 \mathrm{P}}{\partial x^2} \qquad (17)$$

where:

∂w/∂H = moisture capacity;

$P =$ vapor pressure;

$\mathrm{K}_w =$ moisture diffusivity;

Eq. 17 can be solved for a simple 1D situation in which the specimen is an infinitely long bar with one surface is exposed to the boundary condition and all other surfaces are insulated. This simple case is similar to the concrete sample used in the RILEM tube test. After twice integration and applying the boundary condition, the Eq. 17 can be developed as:

$$\frac{\mathrm{P}-\mathrm{P_{BC}}}{\mathrm{P_{\infty}}-\mathrm{P_{BC}}}=\frac{2\sqrt{C}}{\sqrt{\pi}}\int_0^{\zeta}e^{-s^2}ds \tag{18}$$

Initial condition: $\mathrm{t}=0, \text{all } x, P=P_{\infty}$

Boundary condition: $\mathrm{t}>0, x=0, P=\mathrm{P_{BC}}, \mathrm{t}>0, x=\infty, P=\mathrm{P_{\infty}}$

in which $\mathrm{P_{\infty}}$ is the pressure at a location far away from the surface, and $\mathrm{P_{BC}}$ is the pressure on the boundary surface. *C* stands for the moisture diffusivity. ζ is the Boltzman transformation.

The size of specimen was 4 x 8inches (diameter x height) cylinder and w/c was 0.55. SHT75 Sensirion humidity and temperature sensors were installed at three different depths (1.5, 3.5 and 6.5inhces) from the surface. Figure 40 shows the internal moisture distributions at different testing day.

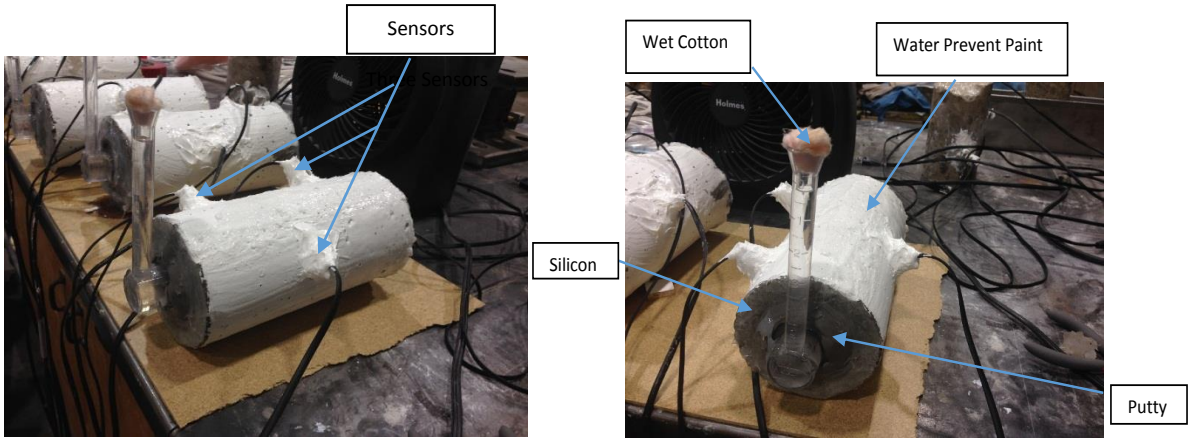

Figure 28 the testing specimen with w/c = 0.55

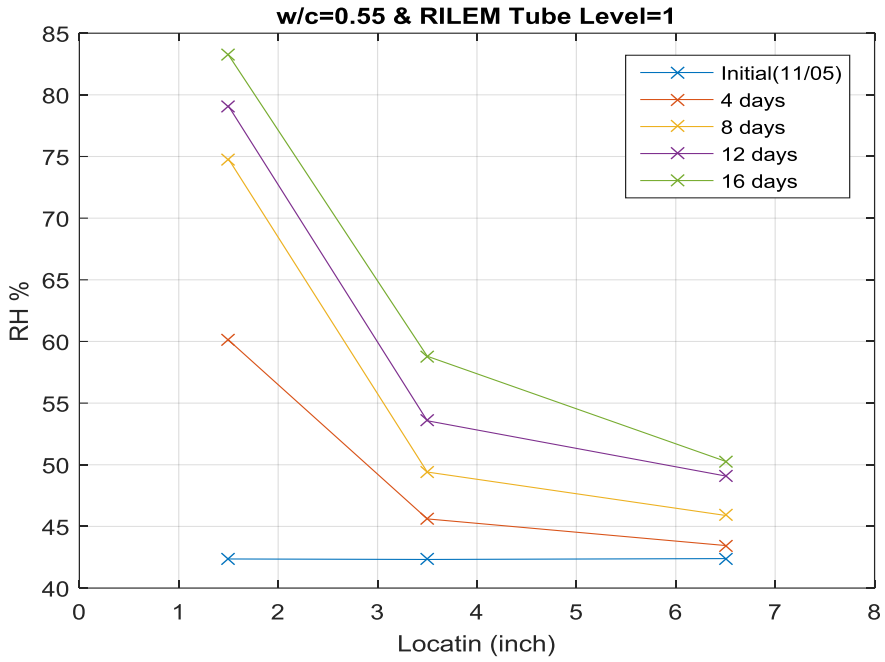

Figure 40 Moisture distributions for sample with w/c=0.5 under water level 1 (left side of sample, with location 0inch, is the surface in contact with tube)

Using the test data shown in Figure 40, the location of RH=100% at different time can be found by using curve fitting shown in Figure 41. The results for the location of RH=100% at different times are also shown in Table 16.

Location of the interface (inch)		
8 days	12 days	16 days
0.26	0.44	0.56

Table 16 the location of interface between liquid water and vapor

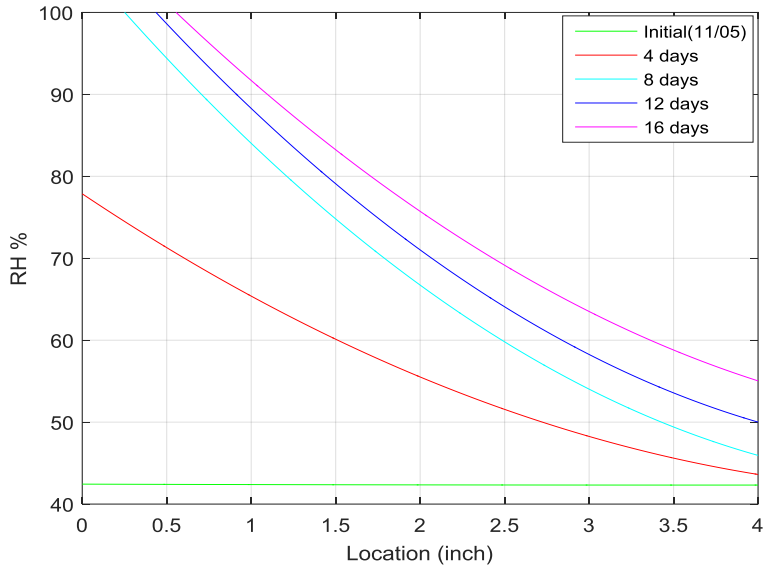

Figure 41 The locations of RH = 100% at different time by curve fitting

On the top of Figure 41, one can see that there are three curves reaching 100%, representing the locations of the interface between the two different moisture transfer mechanisms: the liquid water transfer and the water vapor transfer. On the left of the interface, the pores are saturated and the moisture transfer may be dominated by the liquid water transfer; and on the right of the interface, the RHs are lower than 100%, and thus the moisture transfer may be dominated by the water vapor transfer. With increasing time, the interface moves to the right (deeper into the concrete samples).

As we know, for liquid water transfer, the driving force is the water pressure; and for the water vapor transfer, the driving force is the vapor pressure. The two different processes can be described by similar transport equations with different transport parameters. One way is to develop two theoretical models for the two different regions. However, in this report we intended to develop a simplified theoretical model that can be used for both transport mechanisms. For the internal moisture transfer, the moisture distribution can be described by Eq. 18 with an internal pressure *P* as the driving force.

In the RILEM tube test, a specific level of water head represents a wind speed as well as a hydraulic pressure. Table 17 gives the details for the case with graduation mark at level 1:

Graduation Mark	Hydraulic Pressure (psi)	Theoretical Wind Speed (mph)
1	0.12	90.04

Table 17 Boundary condition related to RILEM tube test at water level 1

Eq. 18 was used to find the proper curve fitting of the model prediction and test data by adjusting the moisture diffusivity *C* in Eq. 18. Table 18 shows the results of curve fitting, the optimized values of moisture diffusivity for specimens with *w/c* = 0.55. One can see that the variation in the four diffusivities is not large, which means that the theoretical solution with *P* as the variable can be used to predict the pressures in concrete samples in RILEM tube test. Figure 42 shows the comparisons of the experimental data and the results of model predictions using the moisture diffusivity shown in Table 18. Figure 43 is the comparisons of the experimental data and the results of model predictions using the averaged moisture diffusivity of 0.3546 in^2/day.

Time (day)	Moisture Diffusivity (in^^{2}/day)
4	0.3378
8	0.3497
12	0.3451
16	0.3860

Table 18 Moisture diffusivity for sample with w/c=0.55 and water head level = 1

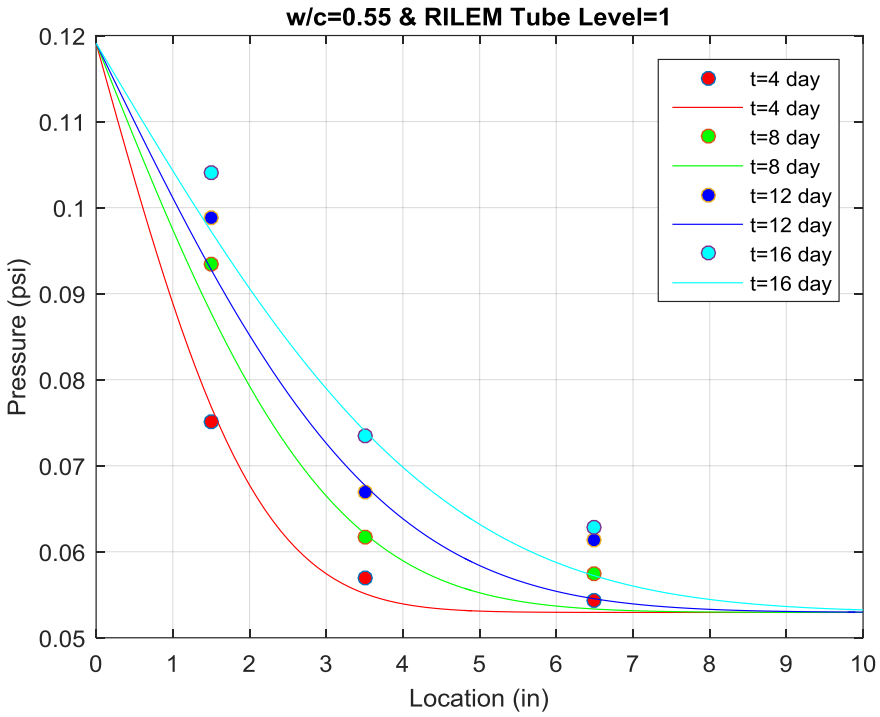

Figure 29 Comparisons of experimental data and model predictions (solid points are experimental data and solid line are model predictions)

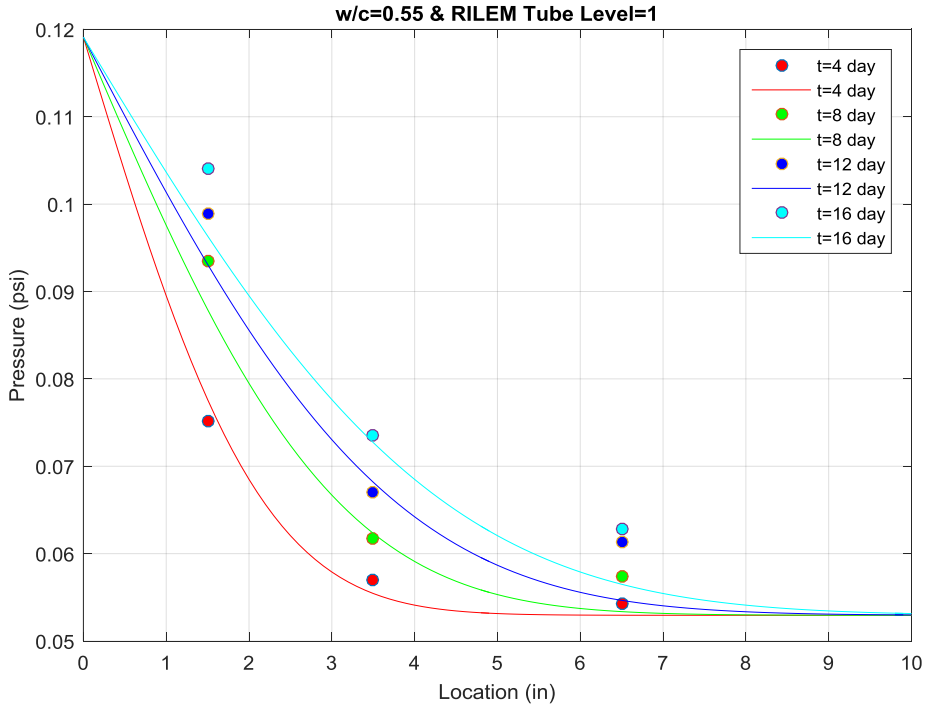

Figure 43 Use the average value of moisture diffusivity k = 0.3546 in^2/day

3. The resistance to WDR of sample with Fumed Silica

The dimension of sample was 4 x 2 inch (diameter x length), which was cut from the 4 x 8inch (diameter x length) cylinder. The experimental approach is the same with first section. Figures 44 and 45 show the sample is under testing and experimental results, respectively.

Figure 44 The sample is under the RILEM Tube Testing

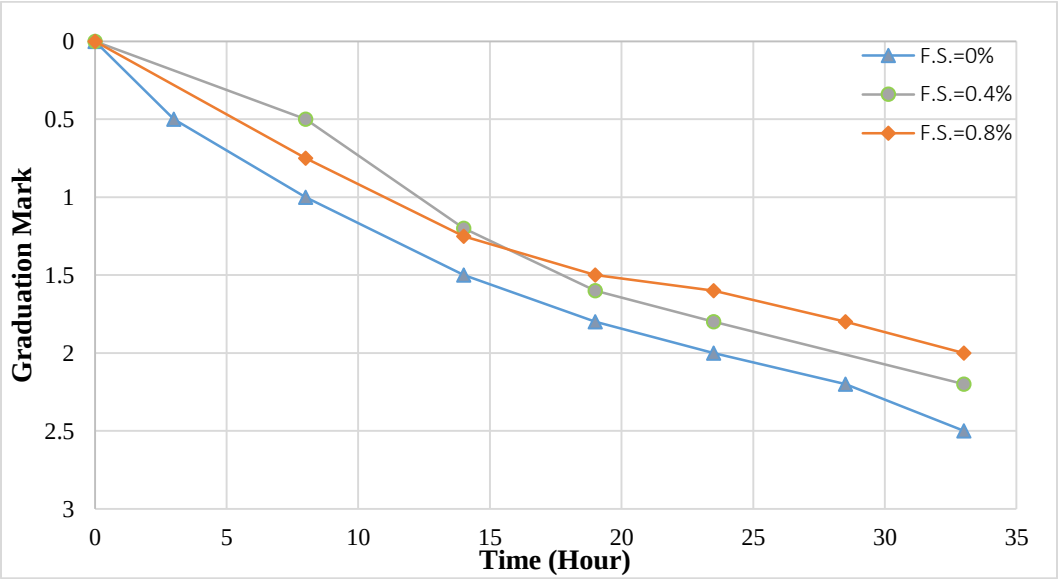

Figure 45 The relationship between the graduation mark and time spent for the three samples

Mark	0.0%	0.4%	0.8%
0	0	0	0
0.5	3	8	-
0.75	-	-	8
1	8	-	14
1.2	-	14	-
1.25	-	-	-
1.5	14	-	19
1.6	-	19	23.5
1.8	19	-	28.5
1.9	-	23.5	-
2	23.5	-	33
2.2	28.5	33	-
3	33	-	-

Table 19 Test data for RILEM Tube Test (unit: hour)

Figure 45 and Table 19 compare the time spent for adsorption test. From the experimental data, we can study the adsorption and penetration rate of water strongly depend on the dosages of fumed silica. The control group (F.S. = 0%) has the fastest adsorption rate, while the penetration of water for sample with 0.8% fumed silica is lowest. Thus, the addition of fumed silica can effectively slow the adsorption and penetration rate of water under WDR comparing to the regular concrete sample.

Conclusions

1. The water head of concrete sample with the highest w/c and largest amount of AEA drops at the fastest rate among all groups. Thus, the water transport under WDR is strongly dependent on the concrete mix design and quantity of additive. Therefore, optimization of concrete mix design for resistance to WDR is very important.
2. Adding *fumed silica* can decrease the penetration rate of water under the Wind-Driven Rain. Thus, the concrete sample can be protected from the WDR by adding a proper amount of *fumed silica*.
3. A new variable P (pore pressure) was introduced in the moisture transfer model for WDR, which is an internal pressure in pores related to the water pressure in liquid water transfer process or the vapor pressure in water vapor transfer process. The boundary condition of the pressure P is the pressure induced by the wind-driven rain defined by the RILEM tube testing method.
4. The theoretical solution of a 1D diffusion equation in an infinitely long bar can be used as a simplified theoretical model to predict the internal pore pressure P in concrete sample under the RILEM tube test.
5. The moisture diffusivity in the simplified theoretical model was inversely determined using the RILEM tube test data. And the comparisons of the theoretical predictions and the test data agreed well.

Recommendation for future researchers

- The moisture distributions of concrete samples with different water-cement ratios and dosages of *AEA* were studied. Other mix design parameters and additives need to be studied such as volume fraction of aggregate and other additives, and then the optimization of concrete mix design parameters can be achieved.

- An analytical model of 1D was developed in this study. Using the same approach, a 2D and 3D finite element method can be developed, which can provide a more realistic analysis than the present theoretical model.

Products

- "Moisture transfer under Wind-Driven Rain (WDR): experimental study and theoretical model", Wang Y., and Xi Y. (2017), in preparation.

Task C. Equivalent Circuit Models for AC Electrochemical Impedance Spectroscopy of Concrete

Prepared by: Krishnan S Raja, University of Idaho, Moscow, ID 83844-1021

Executive Summary:

Corrosion of steel reinforcement of concrete is influenced by the transport of chloride, carbonate, and sulfate ions in addition to diffusion of other redox species such as oxygen, hydroxyl, and metal cations. Permeability of ions in the concrete can be investigated by electrochemical impedance spectroscopy. In this task, the effects of addition of glycerol as viscosity modifier, addition of admixtures such as fumed silica (FS), micro silica (MS), and colloidal silica (CS), and addition of aggregates such as round rock, hydrofluoric acid treated (HF) round rock, crushed rock, pyrex, and HF-pyrex on the permeability of ions were investigated. Initial experiments were carried out at room temperature. Based on the room temperature results, select samples were investigated at 40, 50, and 65 ºC. Concrete samples with different slab thicknesses in the range of 1 – 10 mm were investigated. The test environment was 3.5wt% NaCl. Therefore, the estimated diffusivity of the samples pertained predominantly to the chloride ions. The EIS data were fitted with different equivalent circuit models. Pure cement samples (without any admixtures, aggregates, or additives) were cast as control samples, and the effect of additives was compared with the EIS data of the control samples. Based on the EIS data, the estimated diffusivity of pure cement (control) sample at room temperature was 3.2×10^{-8} cm^2/s. Addition of 1 wt% glycerol as viscosity modifier decreased the diffusivity to 2.2×10^{-8} cm^2/s. Addition of 1 wt% fumed silica decreased the diffusivity to 1.8×10^{-8} cm^2/s, almost by 43%. Both glycerol and fumed silica additions were more effective at elevated temperatures than that at room temperature since the diffusivities decreased by an order of magnitude as compared to that of the control sample.

C.1 Introduction

While considering the corrosion of rebar steels, the following facts are already well-established in the literature [1][2]

- Passivity of steel is maintained at high pH (typically greater than 11 in concrete)
- Ingress of CO_2 reduces the pH around the steel bar and the passivity is affected
- Adsorbed chloride ions on the rebar surface causes passivity breakdown
- Chloride is present in the concrete in two forms: 1) Bound chloride; and 2) Free chlorides
- Role of bound chloride in concrete on corrosion is ambiguous. Some authors report only free chlorides are responsible for corrosion.
- When the pH decreases, the bound chloride are partially released and become free chlorides
- Carbonation due to ingress of CO_2 plays a significant role in releasing the bound chloride
- Tricalcium aluminate (C3A), tetracalcium aluminum ferrite (C4AF), silica fume, and CSH affect the bound chloride content.
- The critical (free) chloride concentration for corrosion initiation is pH dependent that varies from 0.2 – 1.5% of the cement weight. Total chloride can be up to 2.5%.

- Higher binding ability of cement (higher content of C3A, C4AF, silica) can tolerate higher chloride.

On the other hand, there are some ambiguities in the literature as listed below:

- Contradicting reports on inhibiting/accelerating role of carbonate/bicarbonates on chloride induced corrosion [4][5]
- Contradicting views on the role of bound chlorides[6]
- Role of viscosity modifiers on binding the chlorides and passivity breakdown

What so ever is the exact mechanism, transport of chloride ions plays a significant role in the kinetics of corrosion of rebar steel in the concrete. Therefore, slowing down the permeability of aggressive anions would increase the life of the concrete structure. In order to understand the effect of ionic transportation in the concrete, the concrete porosity and permeability should be estimated rapidly and non-destructively. AC electrochemical impedance spectroscopy (EIS) is a non-destructive method. It is not destructive to steel rebar in concrete, and it does not disturb the concrete system, either. EIS directly measures ion mobility in concrete, which is closely associated with concrete degradation caused by the ingress of environmental aggressive species.

C.2 Objectives

The objectives of this task are to:

1. Develop an electrochemical impedance spectroscopy (EIS) based model for modified concrete microstructure;
2. Understand the influence of modifiers on the permeability of the concrete and corrosion of rebar; and
3. Determine the effect of temperature on the permeability of the modified concrete

C.3 Experimental

C.3.1 EIS Test Configuration: Electrochemical impedance spectroscopy (EIS) was carried out in different testing configurations. Initial tests were carried out on concrete samples having embedded rebar steel specimens, which is referred to as type: A. The schematic of type-A specimen is shown in Fig C-1 (a). A machined rebar steel cylinder (10 mm diameter and 10 mm long) was embedded in a concrete block (50 mm diameter 50 mm long). The rebar steel acted as
working electrode. The concrete sample was immersed in 200 ml of 3.5% NaCl solution. A 0.5 mm diameter, 600 mm long platinum wire was spiraled on a 45 mm diameter perforated

polypropylene tube and placed concentric around the concrete sample forming a counter electrode. The effective area of the Pt wire immersed in the 3.5% NaCl was about 7.5 cm^2.The glass tube provided with the concrete sample was filled with saturated KCl solution. A silver

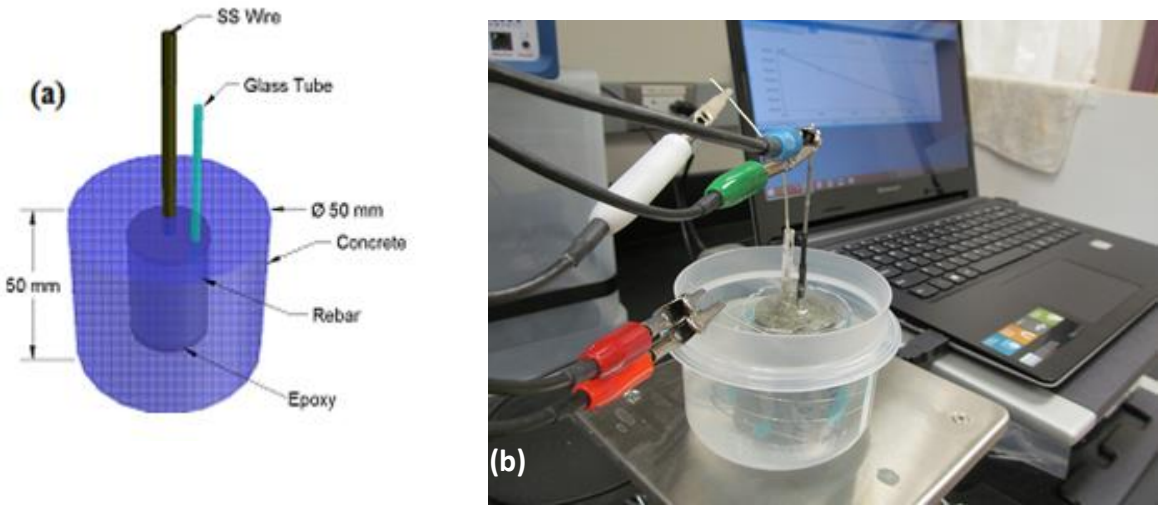

Figure C-1 (a) Schematic of the type-A consisting of concrete cast cylinder with embedded rebar steel, and provision for inserting a reference electrode. (b) Three-electrode EIS testing configuration. Pt-wire as counter electrode was spiraled around the concrete cylinder.

wire (1 mm diameter) coated with AgCl (by anodizing in the KCl solution at 5 V for 15 minutes) was used as a reference electrode. The experimental arrangement is shown in Figure C-1(b).

The second type of experimental arrangement is shown in Figure C-2. This is referred to as type-B. The major difference between type A and B is the placement of working electrode. In type-B, the working electrode is outside the concrete as shown in the schematic diagram. Concrete discs of 20.6 mm diameter and 10 mm thick were prepared with and without admixtures. The concrete disc was secured tightly at the bottom of a PVC tube. Silver epoxy was applied at the exposed surface of the concrete sample and an aluminum plate was attached to the concrete sample. The silver epoxy gave good electrical connectivity to the aluminum plate that acted as working electrode. The samples configured above were prepared and supplied by Prof. Pesic. The PVC tube was filled with 10 ml of 3.5% NaCl solution. A Pt spiral (total surface area 1.15

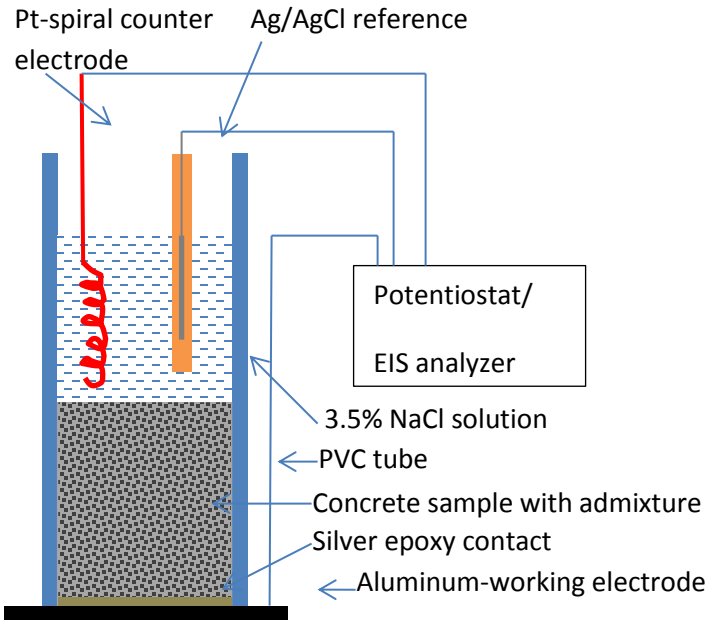

Figure C-2Schematic of 3-electrode EIS experimental set-up with concrete slab type specimen (without rebar) (type: B)

cm^2) as counter electrode and Ag/AgCl reference electrode were immersed in the 3.5% NaCl solution. EIS measurements were carried out at 0.025 V Vs the open circuit potential at every 24 h intervals.

The next experimental arrangement (type-C) is illustrated in Figure C-3. This arrangement is similar to that of type-B but with two-electrode configuration. No external reference electrode was used. The counter electrode was a Pt-spiral, similar to the one used in type-B arrangement. The working electrode was an aluminum plate.

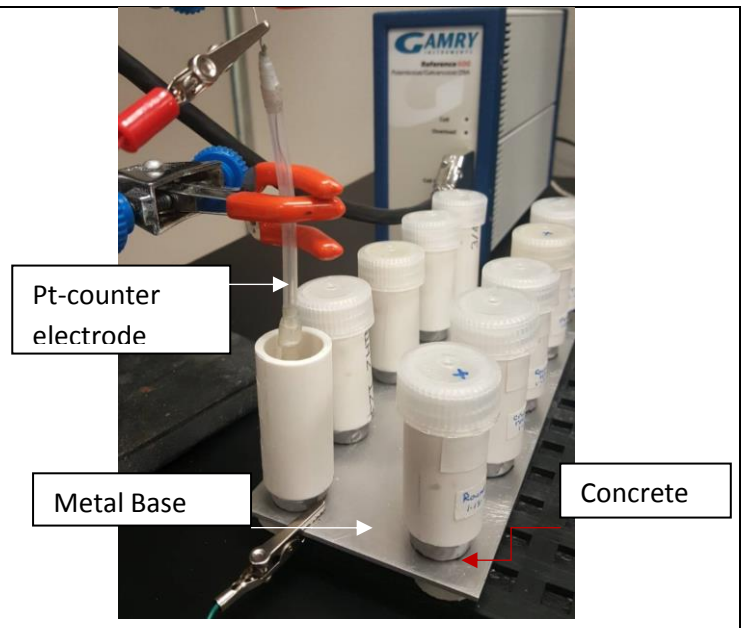

Figure C-3. Experimental setup used for 2-electrode EIS experiment. (Type: C)

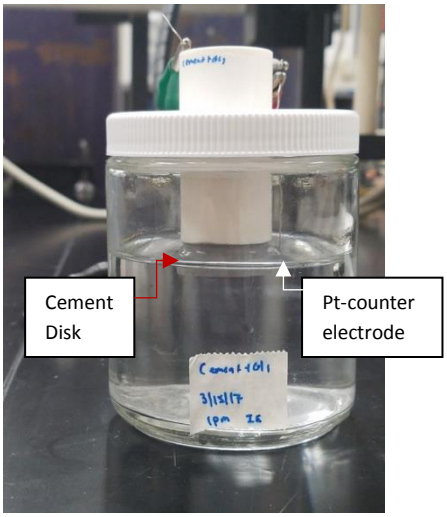

Figure C-4(a) Electrochemical cell for EIS studies under potentiostatic condition. (Type: D)

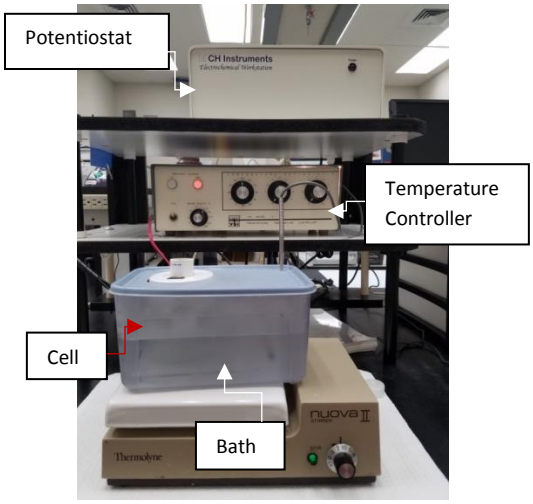

Figure C-4(b) Experiemental setup for EIS studies showing the heating arrangement

In all the above experimental arrangements, the EIS was carried out at the open circuit condition. The open circuit potential of the sample was recorded first. Electrochemical impedance spectroscopy (EIS) was carried out at +25 mV Vs. the measured open circuit potential by scanning the frequency from 0.1 MHz to 10 mHz by super imposing an *ac* potential of 10 mV. The EIS results were fitted with different equivalent circuit models, and the equivalent circuit that gives a goodness of fitting $\chi^2 = 10^{-3}$ or less was considered to be representative of the system under investigation.

The next type of EIS arrangement (type: D) is illustrated in Fig C-4 (a) and (b). This arrangement is compartmentalized and uses 2 Pt-spirals as working and counter electrodes. Each Pt electrode was placed in separate compartments and the compartments were connected through the concrete specimen disc. Concrete sample preparation was completed in four steps, *viz*. 1) casting of the concrete bars with different admixtures such as 1% glycerol (Gly1) and 1% fumed silica (FS1), 2) cutting of concrete bars into discs of desired thickness (10 mm), 3) Bonding a PVC tube on to the concrete disc as container for the electrolyte, and 4) immersion of concrete cells into 3.5 wt% salt solution. The samples tested were: 1 wt% fumed silica, 1 wt% glycerol, and control (cement only). In order to understand the effect of temperature on the permeability, the test solution was heated to the desired temperature using a temperature controlled bath. The heating arrangement is shown in Fig. C-1(b).The cell was placed in a temperature controlled water bath heated using a hot plate. Once the sample reached the appropriate test temperature, EIS measurements were carried out with a potentiostat (CH Instruments, TX, USA) under a potentiostatic condition at 2 V (DC) applied between the two Pt- electrodes and super imposing a *ac* potential of 10 mV and scanning the frequency from 100 kHz to 10 mHz. The measurements were then analyzed by equivalent circuits to model the impedance behavior of the concrete samples. During the potentiostatic bias at 2 V water splitting reaction occurs and oxygen and hydrogen gases evolve at the Pt electrodes. Cross diffusion of OH^- and H^+ ions occur through the concrete disc. The EIS results are analyzed for estimating the diffusivities of these species through the concrete disc.

C.3.2: Composition of Concrete Specimens: The details of additives, admixtures, and aggregates used in the concrete specimen preparation are given below:

1. Cement only (control)
2. Cement + Glycerol (0.5, 1.0, and 2 wt% of cement)
3. Cement + Micro Silica (0.5, 1.0, and 2 wt% of cement)
4. Cement + Fumed Silica (0.5, 1.0, and 2 wt% of cement)
5. Cement + Colloidal Silica (0.5, 1.0, and 2 wt% of cement)
6. Cement + Ln. Mountain
7. Cement + Ln. Mountain (HF treated)
8. Cement + Crushed round rock
9. Cement + Round rock
10. Cement + Round rock HF treated
11. Cement + Pyrex
12. Cement + Pyrex HF treated

The type-A configuration (embedded steel rebar) was tested using the first five compositions. The slab type specimens (keeping the working electrode outside the concrete) were prepared with all compositions.

C.4 Results and Discussion

C.4.1 Concrete samples with embedded steel rebar

Figures C-5(a) and (b) show the Nyquist plots of the concrete with 0.5% glycerol addition at different time intervals. It is noted that the imaginary impedance values decreased, in general, during the initial period (until 72 h) and started increasing after 96 h of exposure.

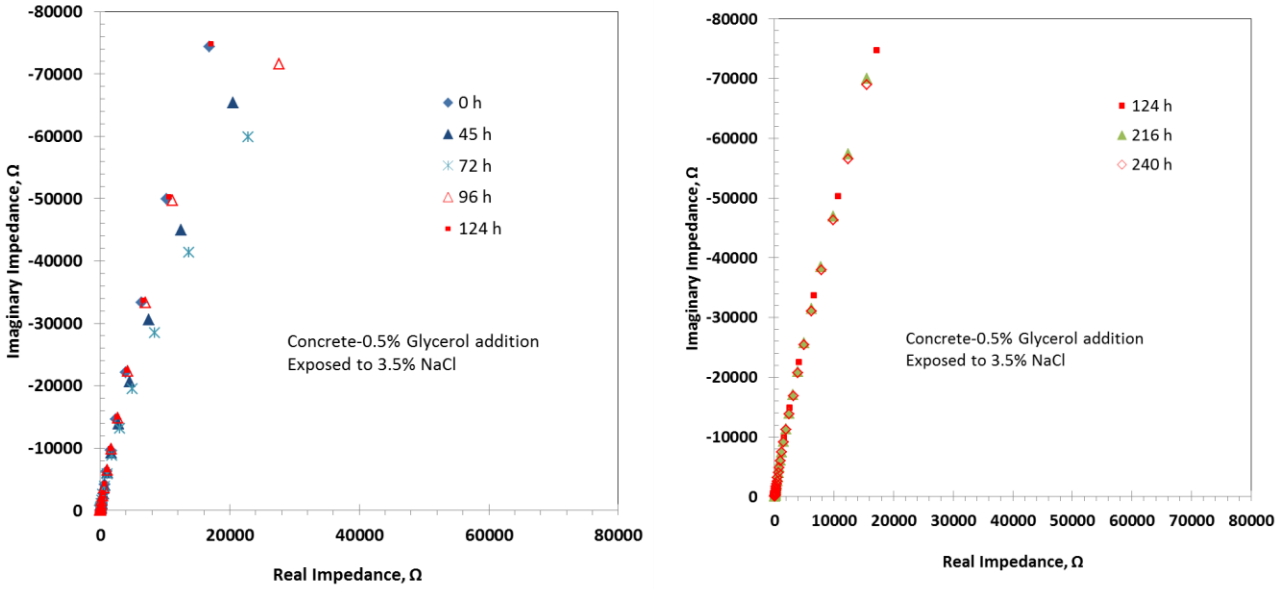

Fig. C-5 Nyquist plots of rebar steel reinforced concrete sample (0.5%glycerol) immersed in 3.5% NaCl. (a) Impedance values from 0 – 124 h; (b) 124- 240 h.

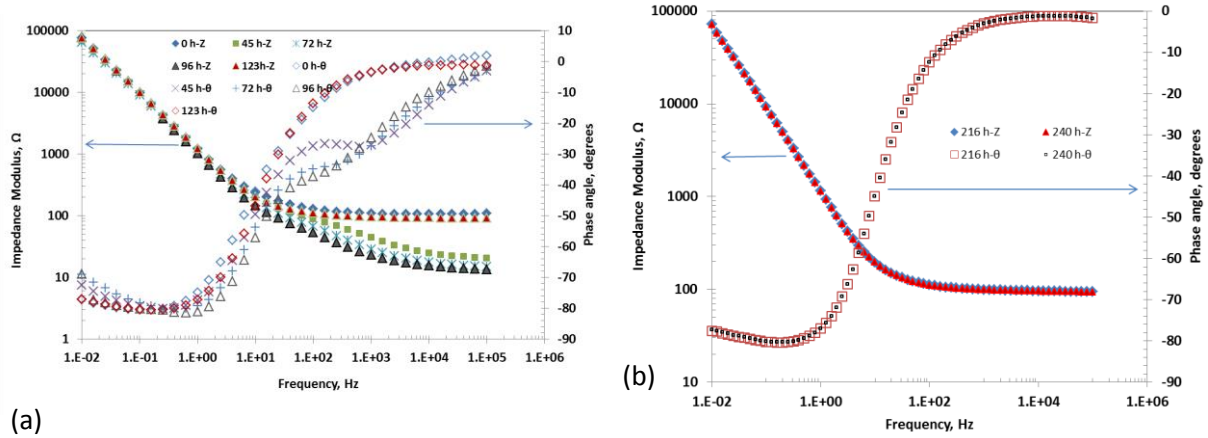

Fig. C-6 Bode plots of rebar steel reinforced concrete sample (0.5%glycerol) immersed in 3.5% NaCl. (a) Impedance values from 0 – 124 h; (b) 216 and 240 h.

Figures C-6 (a) and (b) show the Bode plots of the concrete at different time intervals. It appears that the modulus of impedance did not change significantly because of the logarithmic scale used in the plot. However, some changes in the phase angles could be noticed as the immersion continued. After 120 h of immersion, no significant changes were noticed in the phase angles and the impedance modulus values. In order to better understand the impedance behavior, the impedance values were fitted using an electrochemical equivalent circuit as shown in the Figure C-7. Table C-1 lists the fitted equivalent circuit parameters.

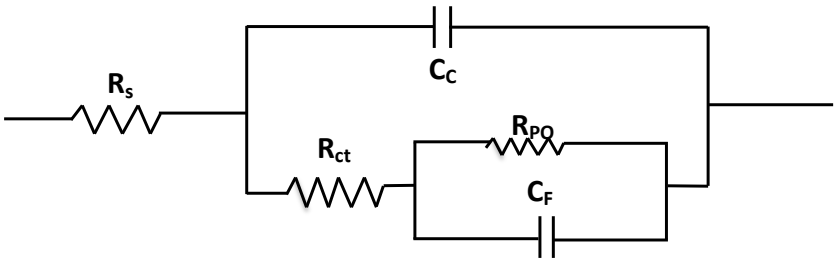

Fig. C-7 Equivalent circuit diagram of the concrete sample used for fitting the experimental values shown in Fig. C-5 and C-6 and derive the values of circuit parameters listed in the table C-1.

TABLE C-1 Model parameters for electrochemical impedance spectroscopic results of 0.5wt% glycerol addition shown in Fig C-5 and C-6 with the equivalent circuit shown in Fig. C-7.

Time interval	R_S, Ohm (Ω)	R_{PO}, kOhm ($10^3\ \Omega$)	C_F, µF	C_C, µF	R_{ct}, kOhm ($10^3\ \Omega$)
0 h	110	249	102	62	0.360
45 h	23.4	157	156	6.35	0.077
72 h	17.1	123	156	13.2	0.075
96 h	15.4	186	143	19.6	0.063
123 h	97.7	253	68	100	1.8
150 h	101	224	70	113	3.5
216 h	102	238	68	117	4.0
240 h	101	233	69	120	4.3

C.4.1.1 Effect of glycerol addition: Figures C-8 (a) and (b) show the Nyquist plots of the concrete samples without and with 0.5% glycerol addition, respectively, at different time intervals. The Nyquist plots of the concrete samples with 1.0% and 2.0% glycerol additions are given in Figure C-9 (a) and (b). Figure C-10 summarizes the EIS results in terms of moduli of impedance of the concrete samples having 0.5 – 2.0 wt% glycerol at the highest and lowest frequencies tested. Figure C-10 (a) shows the impedance modulus, which is $(Z^2_{real}+Z^2_{imaginary})^{0.5}$ at the highest tested frequency (100 kHz). This impedance could be associated with the electrolyte resistivity and the sample-electrolyte interfacial capacitance. The impedance at high frequency increased with the immersion time for all the samples as seen in Fig C-10 (a). Similarly, the low frequency impedance also increased with the addition of glycol as shown in the Fig. C-10 (b). The impedance at low frequency had several components which has been described based on the equivalent circuit model in the later section in the form of a table.

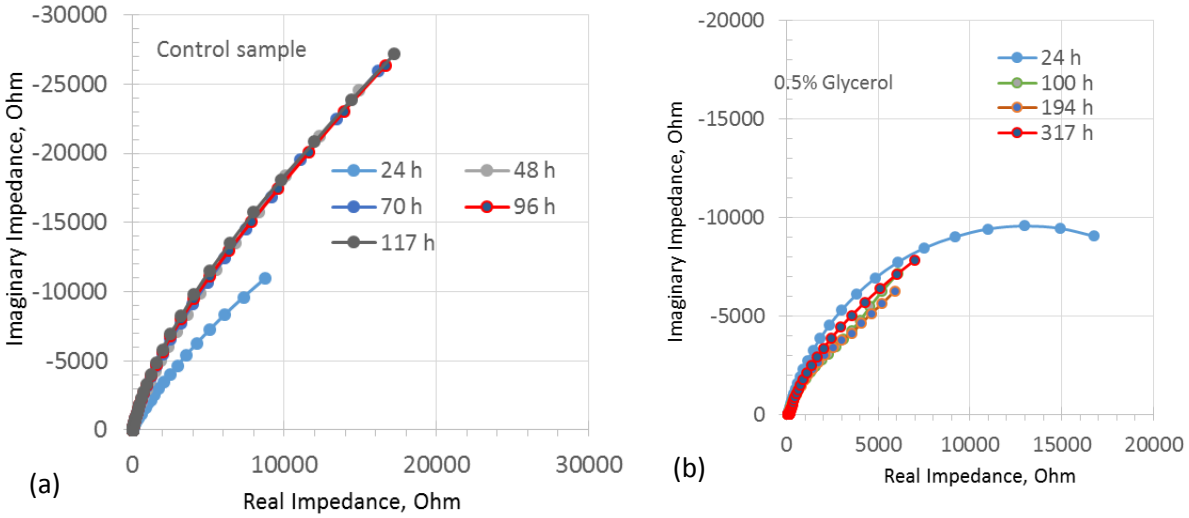

Fig. C-8 Nyquist plots of rebar steel reinforced concrete samples immersed in 3.5% NaCl: (a) control; and (b) 0.5% Glycerol addition.

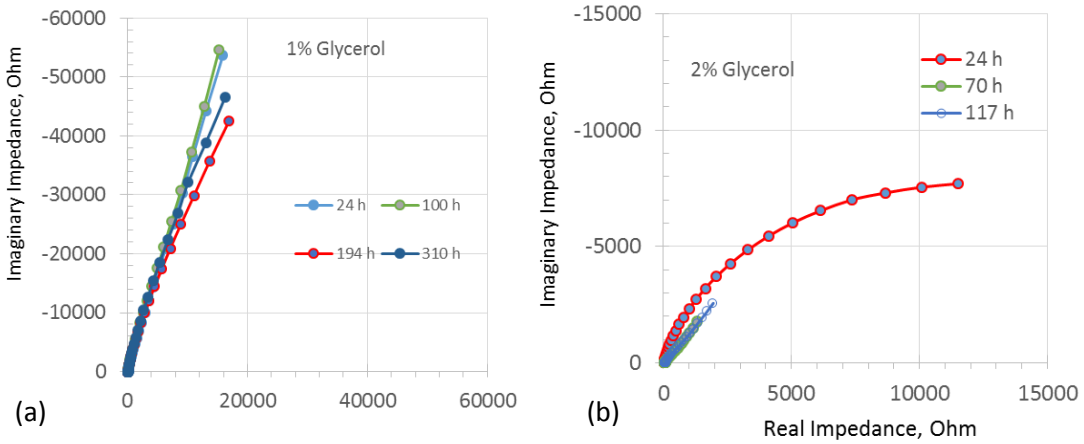

Fig. C-9 Nyquist plots of rebar steel reinforced concrete samples immersed in 3.5% NaCl: (a) 1% Glycerol; and (b) 2% Glycerol addition.

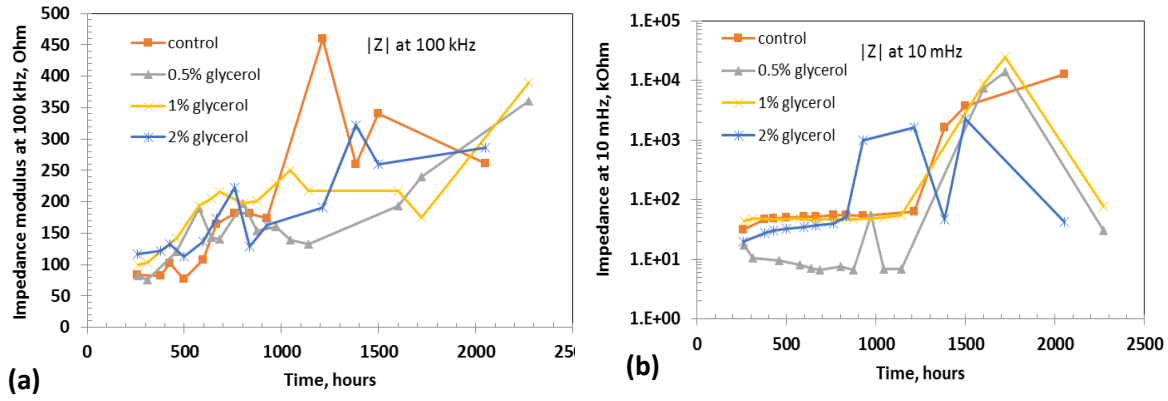

Figure C-10. Impedance modulus of the concrete samples containing glycerol at different frequencies as a function of immersion time in 3.5 % NaCl: (a) at 100 kHz, and (b) at 10 mHz.

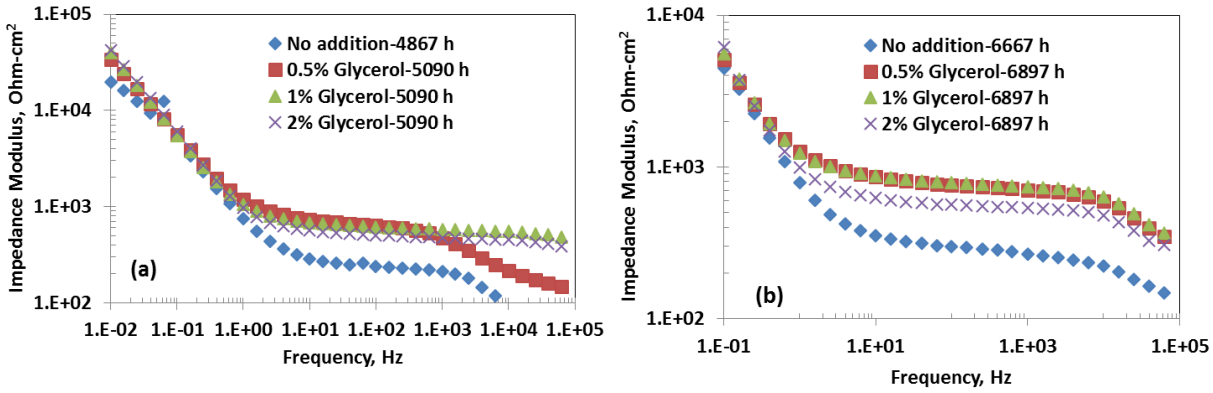

Figure C-11 Electrochemical impedance of the concrete samples with and without addition of glycerol at two different immersion times in 3.5% NaCl solution.(a) after 5090 h and (b) after 6897 h.

Figures C-11 (a) and (b) show the Bode plots of the concrete samples containing 0.5 – 2% glycerol as additive after 5090 h and 6897 h of immersion times, respectively. The impedance of the control sample (without any additives) is shown for comparison. The control sample showed relatively lower impedance at all frequencies at 5090 h of immersion in the 3.5% NaCl solution. This result indicated that the glycerol addition was effective in increasing the impedance to charge transfer. Further increase in the immersion time indicated that the impedance of the samples with glycerol additions was higher than that of the control sample only at the higher frequencies. At low frequencies (<0.1 Hz), all the samples showed almost similar impedance value. Furthermore, it is interesting to note that increasing the glycerol content did not increase the impedance values. Both the 0.5% and 1% glycerol additions showed almost similar impedance behavior and increasing the glycerol to 2%, in fact, decreased the impedance of the samples. Therefore, the optimum value of

glycerol addition could be 1%, which matches with the additional tests carried out with mixed additives such as 1% colloidal silica + 1% glycerol, and 1% micro silica + 1 % glycerol.

The electrochemical impedance data were analyzed using two different equivalent circuits as shown in Figures C-12 and C-13. The equivalent circuit of Fig C-12 is called as rebar-model that has three resistors and two capacitors. The resistors are due to resistance of the electrolyte, resistance of the bulk of the concrete, and the resistance across the porous structure of the concrete. The bulk of the concrete structure is modeled with one parallel R_{ct}-C_C elements. The porous structures present in the concrete is lumped into one R_{PO}-C_F parallel circuit embedded within the R_{ct}-C_C circuit as shown in the Fig. C-12. This type of equivalent circuit is widely reported. Most of the EIS data obtained in this study could be fitted well using this simple rebar-model equivalent circuit. Especially, the EIS data of the control sample and 1% glycerol sample followed this type of equivalent circuit. On the other hand, the EIS data of sample containing 0.5% and 2% glycerol fitted well using 2 CPE & Warburg model. The model parameters of individual circuit elements are presented in Tables C-2 through Table C-5.

From the value of W_C obtained using the model parameters (Table C-3 and C-6), the Warburg coefficient (σ_w) can be calculated using the relation:

$$\sigma_w = 1/(\sqrt{2}*W_C) \qquad \text{(C-1)}$$

The diffusion coefficient of chloride or hydroxyl ions can be estimated from the Warburg coefficient using the relation:

$$D = \left[\frac{RT}{\sqrt{2}n^2F^2A\sigma_w C_{Cl}}\right]^2 \qquad \text{(C-2)}$$

where, n = number of electrons involved, A = area of the electrode, C_{Cl} is the bulk concentration of the ions diffusing through, and other symbols have their usual meaning.

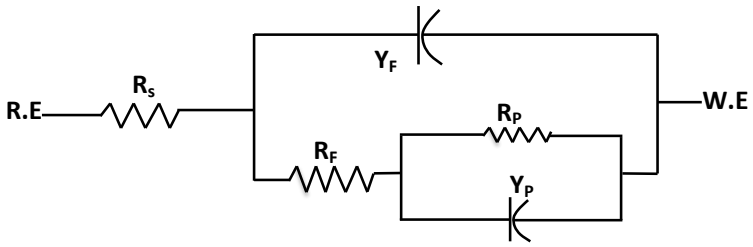

Fig. C-12 Equivalent circuit diagram of the 'rebar-model' used for fitting the experimental values and derive the values of circuit parameters for the control samples in Table C-2.

TABLE C-2 Model parameters for the electrochemical impedance spectroscopic results of the **control sample** for the equivalent circuit shown in Fig. C-12.

Time	R_S, Ohm (Ω)	R_P, kOhm (10^3 Ω)	Y_P, μF	Y_F, μF	R_F, kOhm (10^3 Ω)
0 h	411	11.5	155	19.7	1.13
24 h	37.6	16.5	550	237	1.9
48 h	40.7	44.6	247	183	5.6
70 h	46.38	46	230	176	6.7
95 h	51	47	220	175	7.2
117 h	56	49	210	175	7.5
257	82.43	49.7	234.3	189.7	8.64
427	107.4	100.5	147	132.7	10.86
498	88.4	110	144	132	12.15
663	174	117	138	128.3	13.87
760	209.4	120	120.5	122	12.51
836	214.2	118.5	123.1	122.6	12.03
920	201.2	118.5	126.3	125.7	12.23
1213	504.5	138	98.6	116.9	11.29
1382	302.5	98	101.4	121.7	9.2
1502	493.4	98.76	91.5	106.1	5.54
2050	219.7	619	133	25.2	0.254

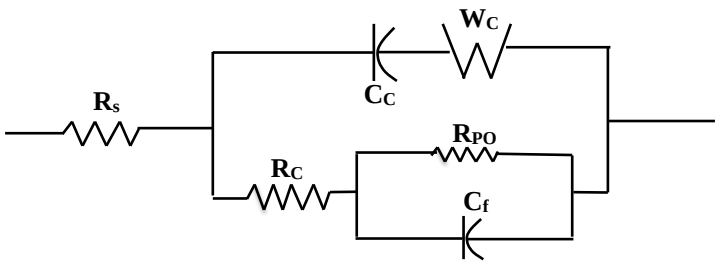

Fig. C-13 Equivalent circuit diagram of the '2 CPE-Warburg' model used for fitting the experimental values and derive the values of circuit parameters listed in the Tables C-2 and C-3 for the concrete samples with glycerol additives.

TABLE C-3 Model parameters for the electrochemical impedance spectroscopic results of the **0.5% glycerol sample** for the '2 CPE-Warburg model' equivalent circuit.

Time (h)	R_S, (Ohm)	R_{PO} (kOhm)	R_C (Ohm)	C_f ($\mu S.s^n$)	n	C_C ($\mu S.s^m$)	m	W_C ($\mu S.s^{0.5}$)
70	64.3	31	32	412	0.74	97	1	1128
100	57.4	27	35.8	373	0.82	310	0.6	807
144	69.5	18	33.6	481	0.7	154	1	882
194	80.6	18	60.5	384	0.67	308	1	1300
246	67	17.8	39.1	612	0.75	84	1	148
264	67	46	33.4	402	0.78	8.2	1	66
310	69	24	60	558	0.77	100	1	105
460	35.35	0.473	172.4	1170	0.68	224	0.247	688
573	13.26	3.8	241	1760	0.635	203	0.172	1100
635	0.43	2750	199.7	868	0.765	52	0.285	119000
684	36.82	35.2	182.9	1760	0.668	293	0.2	1070
800	1.22	0.65	297.4	1360	0.67	192	0.171	723
874	124	0.778	153.2	984.7	0.74	405	0.317	510
972	85.74	0.17	196	1400	0.67	333	0.249	869
1044	44.19	0.156	220	1570	0.655	309	0.225	1018
1140	38.34	1.823	166	3040	0.589	389	0.22	2550
1600	207	244	147.3	172	0.846	232	0.6	188
2272	36.51	44600	418.5	211	0.832	0.074	0.75	195.2

TABLE C-4 Model parameters for the electrochemical impedance spectroscopic results of the **1.0% glycerol sample** for the '2 CPE-Warburg model' equivalent circuit.

Time (h)	R_S, (Ohm)	R_P (kOhm)	R_F (Ohm)	C_P ($\mu S.s^n$)	n	C_F ($\mu S.s^m$)	m	W_P ($\mu S.s^{0.5}$)
246	98	38.4	59.3	98.6	0.96	118	0.875	36
264	102	0.015	56.16	101.4	0.97	94.12	0.91	38.2
310	106.6	38.5	60.4	91.6	0.96	109	0.872	26.6
460	148	0.446	69.5	111.5	0.963	80.8	0.9	33
635	216	100	57.3	155	0.919	66.7	0.828	35.6
684	229	0.0316	71.2	138	0.944	59	0.878	29.3
800	213	0.064	68.45	139.4	0.949	62.3	0.857	26.3
874	214	0.204	80.16	129	0.956	69.8	0.876	27.4
972	240	0.10	77.8	138.6	0.954	59.6	0.858	23.2
1044	268.5	0.10	82.46	139.4	0.952	58.1	0.867	23.49
1140	236.5	0.158	77.88	113	0.952	47	0.873	25.72
1720	168	0.001	343.8	255	0.837	1.53	0.815	66.3
2272	14.3	0.001	501	195	0.83	0.019	0.836	22

TABLE C-5 Model parameters for the electrochemical impedance spectroscopic results of the **2.0% glycerol sample** for the '2 CPE-Warburg model' equivalent circuit.

Time (h)	R_S, (Ohm)	R_{PO} (kOhm)	R_C (Ohm)	C_f ($\mu S.s^n$)	n	C_C ($\mu S.s^m$)	m	W_C ($\mu S.s^{0.5}$)
24	26.8	18.8	2400	222	0.667	289	1	6850
48	36.6	19	1670	680	0.728	853	0.94	6240
70	45.9	16	754	2840	0.7	2080	0.97	5500
95	53.4	18.2	772	2640	0.68	2050	0.99	5310
117	67.1	18.3	1100	1980	0.71	1530	1.0	3400
260	120	8.1	62.4	137.9	0.973	190	0.872	152.6
429	139.6	3.2	30.26	229	0.945	0.143	1	86
480	120.8	8.3	57.7	104	1	133	0.892	66
595	140.6	4.9	67.76	99.65	1	120	0.921	64
665	1.35	3.1	210.2	203	0.94	0.144	0.717	60.6
760	240.6	0.01	73.53	108	0.994	73.6	0.901	55.7
836	27.52	429	141	216	0.925	23	0.368	146
920	159.5	0.986	56.1	193	0.974	137	0.471	89.3
1382	0.007	0.674	409.2	175.3	0.917	0.045	0.770	35.14
2000	101.5	0.01	252.5	202	0.879	0.031	0.855	26.12

The diffusivity of the control sample decreased with the exposure time in 3.5 % NaCl solution. The observed lowest diffusivity of the control sample was in the order of 10^{-14} m^2/s. This value is two orders of magnitude lower than that reported by other researchers. For example, one reported value of diffusivity of chloride in concrete by the EIS method was 2 x 10^{-12} m^2/s [7]. The measurement conditions, and sample size could have influenced the diffusivity values. For example, Vedalakshmi et al [7] used a large sample of 0.15 m x 0.15 m x 0.15 m cube and alternate wet and dry cycles. Addition of viscosity modifiers significantly decreased the diffusivity of the

concrete samples. 1% glycerol addition showed the lowest diffusivity as compared to 0.5% and 2% glycerol additions.

C.4.1.2 Effect of silica additions

Figure C-14 summarizes the impedance moduli of the concrete samples containing micro silica as additive. The impedance at high frequency increased with the increase in micro silica addition as seen in the Fig. C-14 (a). Figure C-14 (b) illustrates the impedance at low frequency, which showed increasing and decreasing trend with the addition of 0.5 -2.0% micro silica. Figure C-9 summarizes the impedance moduli of the concrete samples containing colloidal silica as additive. The impedance at high frequency increased with the increase in the colloidal silica additions after 75 h as seen in the Fig. C-15 (a). The initial high impedance at t= 0 h could be attributed to the low ionic conductivity of the dry concrete sample before immersion in the 3.5% NaCl solution. Figure C-15 (b) illustrates the impedance at low frequency, which showed almost a plateau trend with the addition of 1.0 and 2.0% colloidal silica.

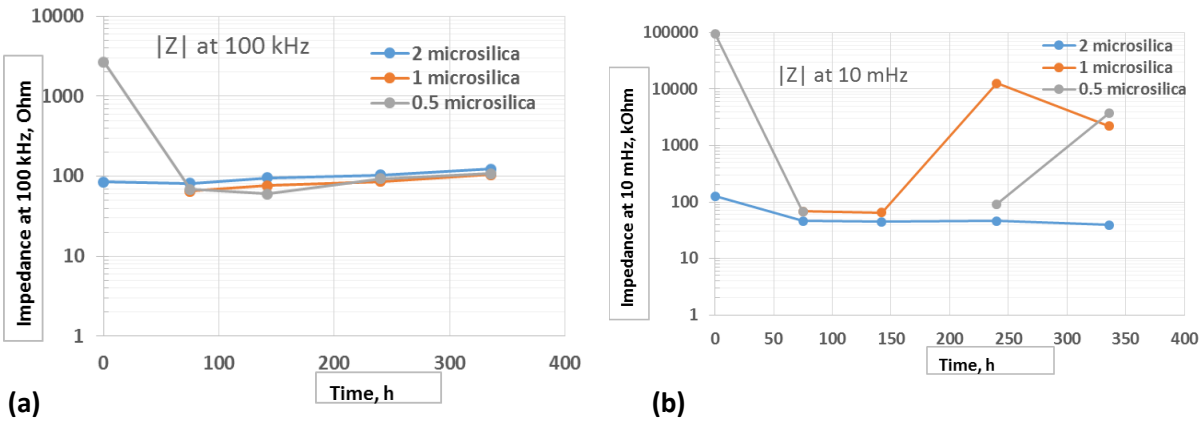

Figure C-14. Impedance modulus of the concrete samples containing micro silica at different frequencies as a function of immersion time in 3.5 % NaCl: (a) at 100 kHz, and (b) at 10 mHz.

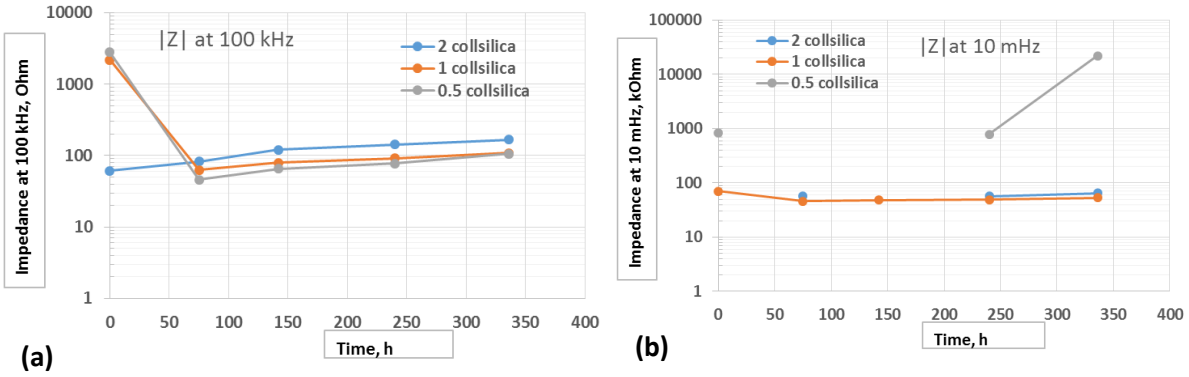

Figure C-15. Impedance modulus of the concrete samples containing colloidal silica at different frequencies as a function of immersion time in 3.5 % NaCl: (a) at 100 kHz, and (b) at 10 mHz

Figure C-16 summarizes the impedance moduli of the concrete samples containing fumed silica as additive. The impedance at high frequency marginally increased with the increase in the colloidal silica additions after 75 h as seen in the Fig. C-16 (a). Similar to the colloidal silica addition, the initial high impedance at t= 0 h could be attributed to the low ionic conductivity of the dry concrete sample before immersion in the 3.5% NaCl solution. Figure C-16 (b) illustrates the impedance at low frequency, which showed a mixed trend with the immersion time. Figures C-17 (a) and (b) show the impedance behavior of the concrete samples having 0 – 2% micro silica additions at 2885 h and 4773 h immersion times, respectively. The impedance values of the samples containing different micro silica were almost similar to those of the control sample (without any additives) until 2885 h. However, with increase in the immersion time the effect of micro silica could be noticed, especially at lower frequencies. The samples containing

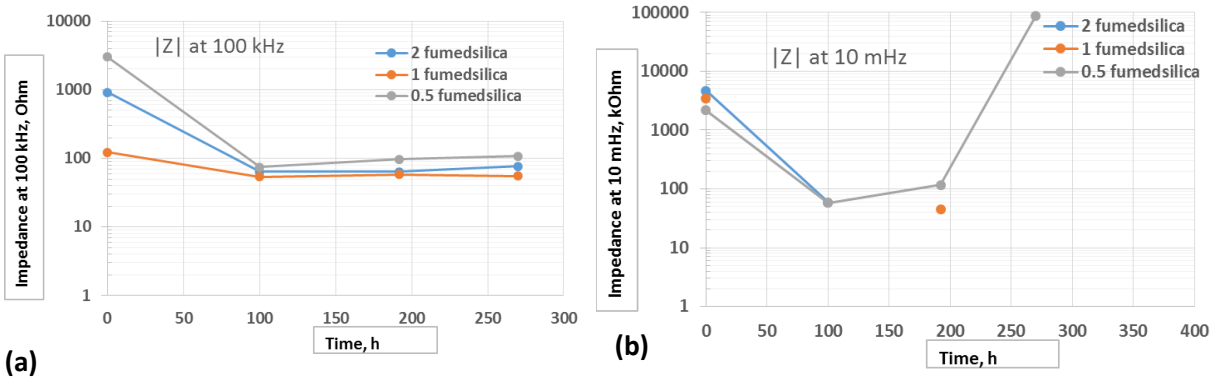

Figure C-16. Impedance modulus of the concrete samples containing fumed silica at different frequencies as a function of immersion time in 3.5 % NaCl: (a) at 100 kHz, and (b) at 10 mHz

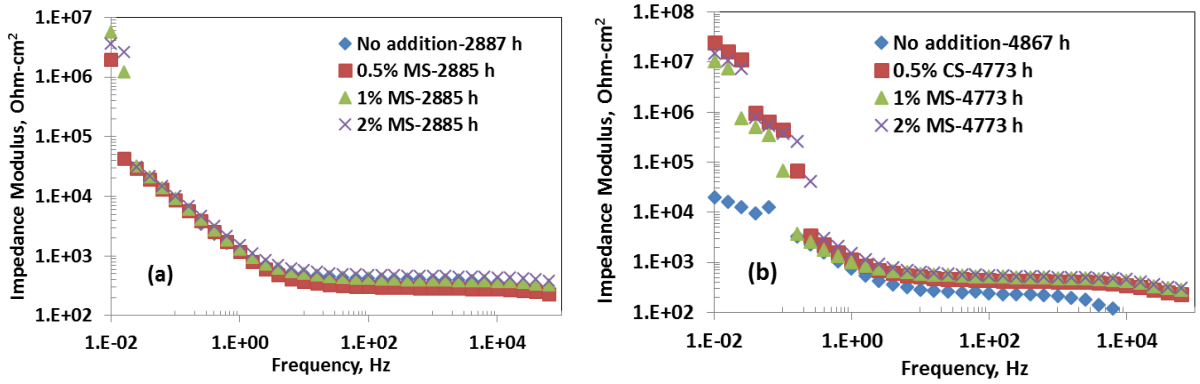

Figure C-17 Electrochemical impedance of the concrete samples with and without addition of 0.5 – 2% micro-silica at two different immersion times in 3.5% NaCl solution. (a) after 2885 h; and (b) after 4773 h.

micro silica revealed much higher impedance values than those of the control samples. Both 0.5% and 2% additions of micro silica promoted higher impedance values than the 1% addition. Figures C-18 (a) and (b) show the impedance behavior of the concrete samples having 0 – 2% colloidal silica additions at 2885 h and 4773 h immersion times, respectively. In this case also, the impedance values of the samples containing different colloidal silica were almost similar to those of the control sample (without any additives) until 2885 h. Similar to the case of micro silica, with increase in the immersion time the effect of colloidal silica addition could be noticed at 4773 h. The addition of colloidal silica revealed much higher impedance values than those of the control samples. Both 0.5% and 2% additions of micro silica promoted higher impedance values than the 1% addition.

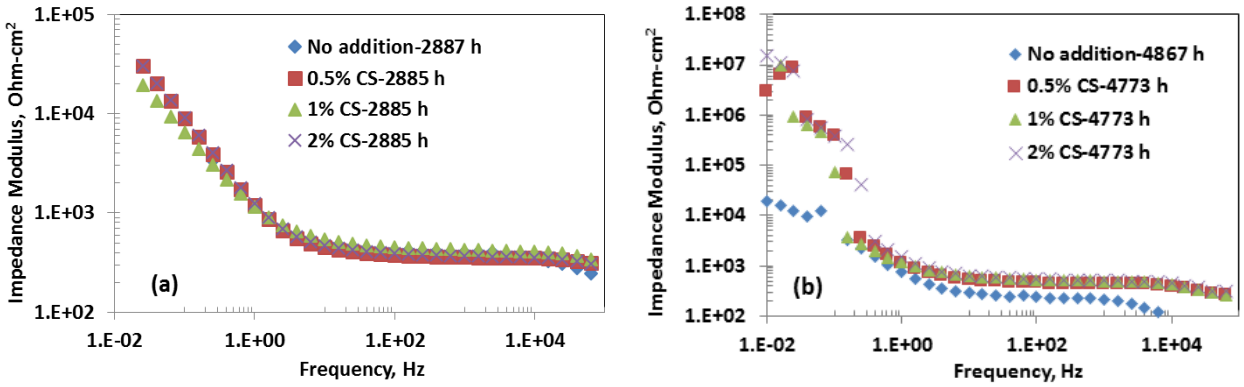

Figure C-18 Electrochemical impedance of the concrete samples with and without addition of 0.5 – 2% colloidal silica at two different immersion times in 3.5% NaCl solution. (a) after 2885 h; and (b) after 4773 h.

Addition of viscosity modifiers significantly decreased the diffusivity of the concrete samples. 1% glycerol addition showed the lowest diffusivity as compared to 0.5% and 2% glycerol additions based on the Warburg coefficients. Among the silica additions, 1% micro silica, 0.5% fumed silica, and 0.5% colloidal silica additions showed the least diffusivities an order of magnitude lower than that of the control sample (without viscosity modifiers). It should be noted that the diffusivity calculation is affected by the initial values of surface chloride concentration and actual area of the sample that participate in the diffusion process. In the absence of experimental data for the chloride concentration, a value of 24 mol/m^3 was taken as the surface chloride concentration. Any change in this value will significantly affect the diffusivity.

C.4.1.3 Effect of mixed additives (Glycerol + Silica)

Figures C-19 (a) and (b) show the impedance plots of the concrete samples having mixed additions

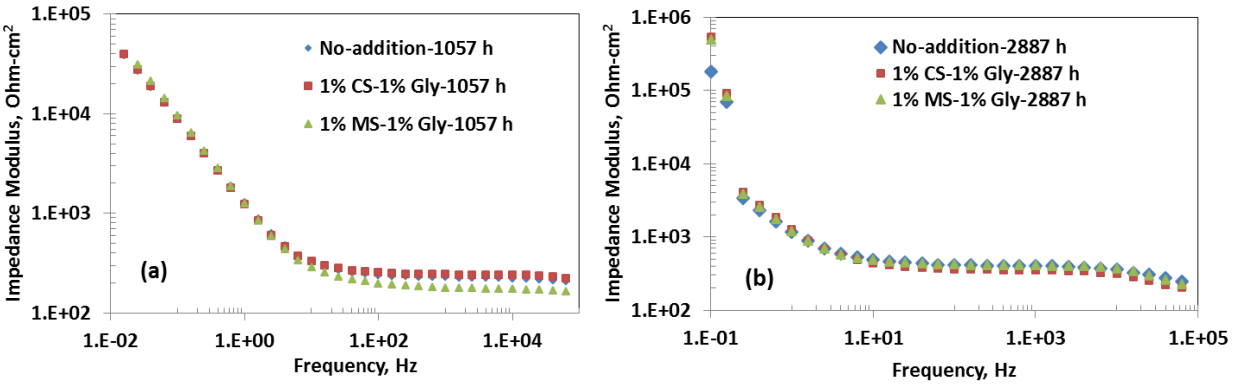

Figure C-19 Electrochemical impedance of the concrete samples with and without addition of 1% colloidal silica + 1% glycerol, and 1% micro-silica + 1% glycerol at two different immersion times in 3.5% NaCl solution. (a) after 1057 h of immersion, and (b) after 2887 h of immersion.

of 1% colloidal silica + 1% glycerol, and 1% micro silica + 1% glycerol additions at 1057 h and 2885 h immersion times, respectively. The mixed additions did not affect the impedance values significantly as compared to the control samples.

C.4.2 Electrochemical Impedance Spectroscopy of Concrete Slabs: (Working electrode outside the concrete – 3-electrode configuration)

Figure C-2 schematically illustrates the experimental arrangement. The samples configured above were prepared and supplied by Prof. Pesic. The PVC tube was filled with 10 ml of 3.5% NaCl solution. A Pt spiral (total surface area 1.15 cm^2) as counter electrode and Ag/AgCl reference electrode were immersed in the 3.5% NaCl solution. EIS measurements were carried out at 0.05 V Vs the open circuit potential at every 24 h intervals. The following samples were investigated:

a) Cement discs of 2.5, 5, and 10 mm thick
b) Concrete sample (10 mm thick) with no admixture – referred to as Control Sample
c) Concrete samples with individual additions of 1% glycerol, 1% micro-silica, and 1% fumed silica.

Figure C-20 shows the Nyquist plots of cement discs of 10 mm thick at different time intervals. The patterns show a depressed semi-circle with a possible Warburg diffusion component. Cement discs of other two thicknesses also showed similar impedance behavior. Figures C-21, C-22, and C-23 show the Nyquist plots of control concrete samples and samples with admixtures. It was observed, in general, that the impedance decreased as the number of days of exposure increased. In order to understand the effects of concrete microstructure in the presence of admixtures on the diffusion of corrosion inducing species (chloride ions in this case), the EIS data were analyzed using an electrical equivalent circuit. Initially, the equivalent circuit proposed by G. Song [8] was

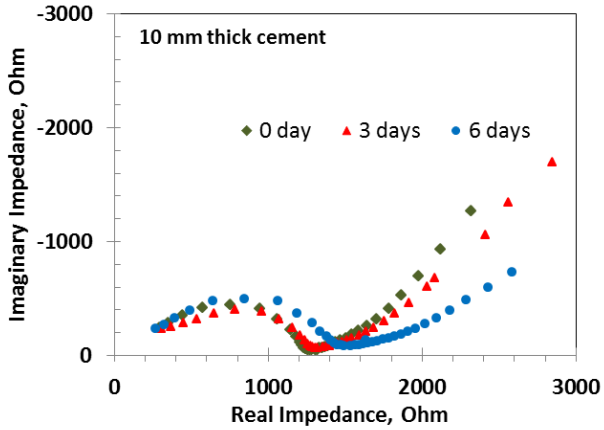

Fig C-20. Nyquist plots of 10 mm thick cement samples exposed to 3.5% NaCl solution at different time intervals.

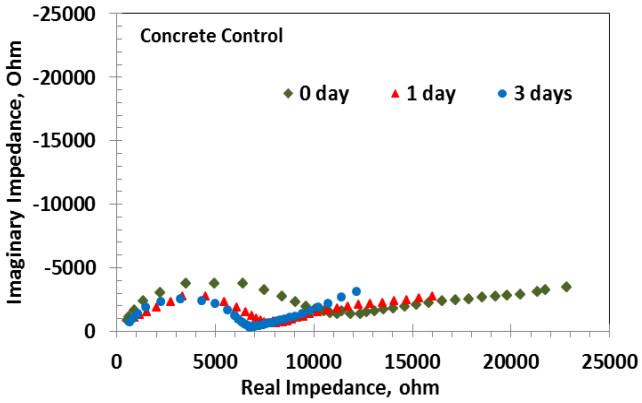

Fig. C-21. Nyquist plots of 10 mm thick concrete control samples exposed to 3.5% NaCl solution at different time intervals.

applied.

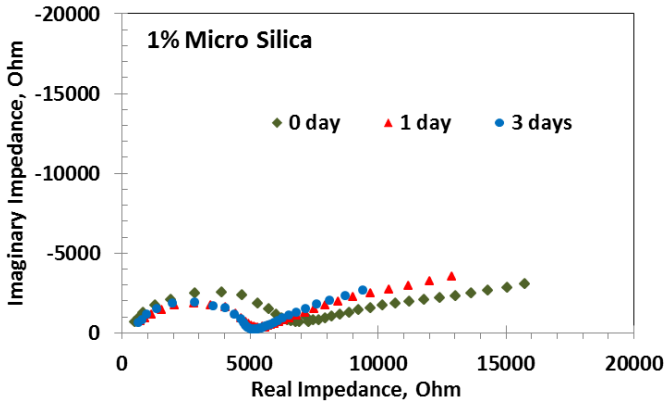

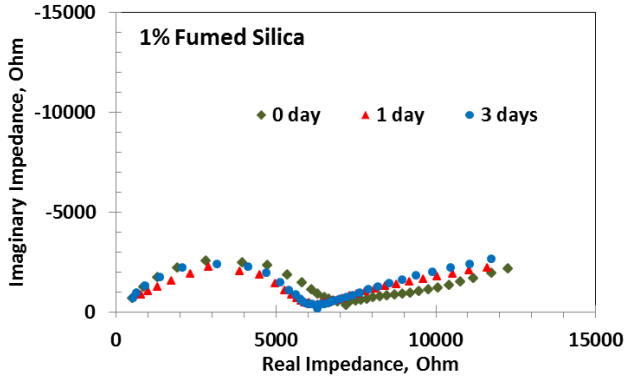

Fig. C-22 Nyquist plots of 10 mm thick concrete samples with admixtures of 1% micro-silica (left,) and 1% fumed silca (right) exposed to 3.5% NaCl solution at different time intervals.

The original equivalent circuit proposed by G. Song [8] did not consider either constant phase elements or Warburg type diffusion resistance. In such case, the Nyquist plot should have two semicircles. Apparently, the observed EIS data did not reveal two semi-circles as indicated in the

Figures C21-C23. Therefore, a modified equivalent circuit as shown in Fig. C-24. The summary of the magnitudes of the equivalent circuit components of the EIS data is presented in the Table C-6. A quick evaluation of the effect of admixtures can be obtained by considering the impedance moduli at the high and low frequencies. Figure C-25 summarizes the impedance moduli of the samples at two frequencies. It is seen that additions of glycerol and micro silica were not effective in increasing the impedance for the corrosion. Addition of fumed silica is observed to be promising at the early stage of exposure to the 3.5% NaCl solution. A better picture of the effect of admixture addition could evolve at longer exposure times.

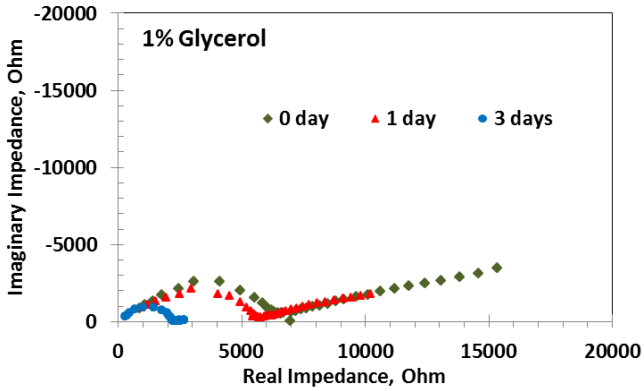

Fig. C-23 *Nyquist plots of 10 mm thick concrete samples with admixture of 1% glycerol exposed to 3.5% NaCl solution at different time intervals.*

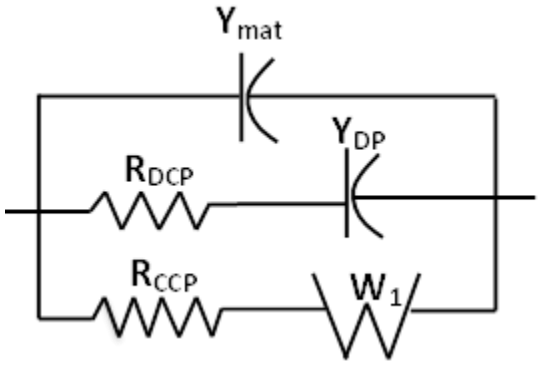

Fig. C-24 *Equivalent circuit diagram used for fitting the EIS data. Y_{mat}: Capacitance of concrete dielectric, R_{DCP} and Y_{DP} represent resistance and capacitance of discontinuous conducting microstructures of the concrete, R_{CCP}: resistance of the conducting path, and W_1: Warburg diffusion component.*

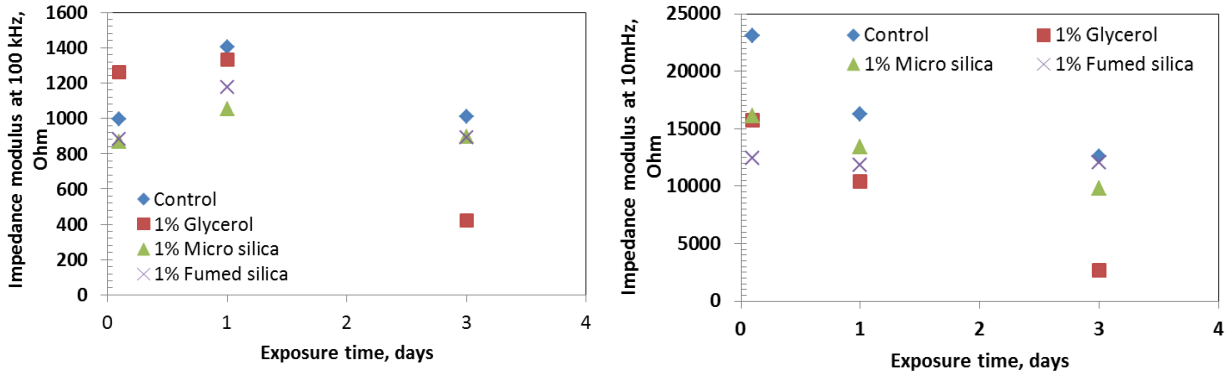

Fig. C-25 Impedance moduli of concrete samples with different admixtures of at 100 kHz (left,) and at 10 mHz (right) exposed to 3.5% NaCl solution at different time intervals.

TABLE C-6. Summary of magnitudes of equivalent circuit components based on the EIS data given in Fig. C20-C23 using the equivalent circuit shown in Fig. C-24.

Sample	Time (days)	R_{DP} (kOhm)	R_{CCP} (kOhm)	Y_{mat} ($S.s^{a1}$)	a_1	Y_{DP} ($S.s^{a2}$)	a_2	W_1 ($S.s^{0.5}$)
1% Glycerol	0.1	13.8	13.6	$86x10^{-9}$	0.678	$802x10^{-6}$	0.466	$28.7x10^{-6}$
	1	11.7	12.0	$100x10^{-9}$	0.66	$12x10^{-3}$	0.986	$65.3x10^{-6}$
	3	2.33	0.18	$23x10^{-9}$	0.848	$7.3x10^{-3}$	0.304	$364x10^{-9}$
1% Micro-silica	0.1	17.9	11.6	$54x10^{-9}$	0.74	$7.3x10^{-3}$	0.995	$39.7x10^{-6}$
	1	12.9	9.46	$104x10^{-9}$	0.676	$686x10^{-6}$	0.411	$71.7x10^{-6}$
	3	11.3	9.65	$60.5x10^{-9}$	0.729	$1.3x10^{-3}$	0.514	$158x10^{-6}$
1% Fused silica	0.1	9.5	25.7	$48.5x10^{-9}$	0.75	$779x10^{-6}$	0.384	$9.7x10^{-6}$
	1	9.64	17.57	$93.6x10^{-9}$	0.677	$736x10^{-6}$	0.356	$30.5x10^{-6}$
	3	11.1	13.9	$32x10^{-9}$	0. 78	$1.3x10^{-3}$	0.519	$42.7x10^{-6}$
Control	0.1	16.5	28.3	$27x10^{-9}$	0.785	$267x10^{-6}$	0.273	$4.8x10^{-6}$
	1	10.3	30	$97x10^{-9}$	0.66	$92.7x10^{-6}$	0.34	$41.7x10^{-3}$
	3	6.78	310	$44x10^{-9}$	0.743	$390x10^{-6}$	0.322	$785x10^{-9}$
Cement 10 mm thick	0.1	1.83	4.43	$218x10^{-9}$	0.69	$4.5x10^{-3}$	0.691	$136x10^{-6}$
	1	1.89	4.74	$313x10^{-9}$	0.65	$8.4x10^{-3}$	0.664	$155x10^{-6}$
	2	1.97	4.07	$243x10^{-9}$	0.69	$3.0x10^{-3}$	0.651	$130x10^{-6}$
	3	1.80	6.38	$802x10^{-9}$	0.59	$2.6x10^{-3}$	0.632	$126x10^{-6}$
	6	1.94	7.5	$455x10^{-9}$	0.646	$4.0x10^{-3}$	0.51	$48x10^{-6}$

C.4.3 EIS of Concrete Samples with Different Aggregates and Additives (2-electrode configuration)

The EIS data of the samples with different aggregates (2-electrode configuration, as shown in Fig. C-3) were fitted with an equivalent electric circuit as shown in Fig. C-26. This model is proposed by G. Song [8]. The model parameters are listed in Table C -7.

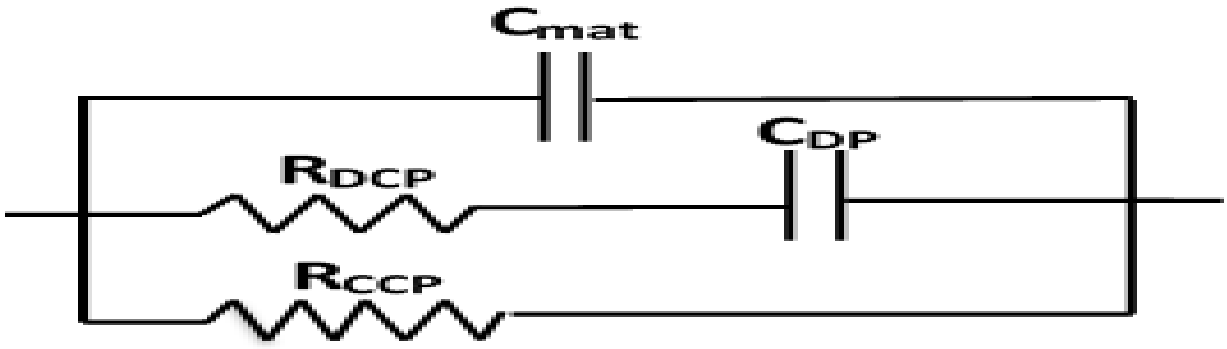

Figure C-26. Equivalent circuit model used for fitting the EIS data of the concrete slab specimens with different aggregates and admixtures. C_{mat}: Capacitance of bulk material, C_{DP}: Capacitance of discontinuous conductive path (due to discrete pores), R_{DCP}: resistance of discontinuous conductive path, and R_{CCP}: Resistance of continuous conductive path.

TABLE C-7 Summary of equivalent circuit values based on the high frequency EIS data of different aggregate additions using an equivalent circuit as shown in Fig. C-26.

Sample	**Time (days)**	**C_{mat}, (F)**	**R_{DCP}, (Ohm)**	**C_{DP}, (F)**	**R_{CCP}, (Ohm)**
Cement only	18	9.3×10^{-9}	92.71	750×10^{-15}	904
1% Micro silica	18	9.2×10^{-15}	10	13×10^{-9}	838
Pyrex	5	10.2×10^{-9}	98.8	21.9×10^{-9}	12.6×10^{3}
	12	2.3×10^{-9}	413.4	6.7×10^{-9}	273×10^{3}
Pyrex-HF	5	6.7×10^{-9}	96	21×10^{-9}	1.08×10^{3}
	12	1.2×10^{-9}	291	5.9×10^{-9}	8.57×10^{3}
Round Rock	19	1.3×10^{-9}	185	5.8×10^{-9}	2.73×10^{9}
Round Rock HF	5	13×10^{-9}	109	11×10^{-9}	205×10^{6}
	12	9.5×10^{-9}	83	1.54×10^{-12}	1.44×10^{3}
	19	3.9×10^{-9}	426	4×10^{-9}	2.03×10^{3}
Crushed round rock	19	15×10^{-159}	70	13×10^{-9}	$3.7x\ 10^{9}$
Ln. Mtn. HF	18	7.5×10^{-9}	1370	4×10^{-9}	88.3×10^{6}

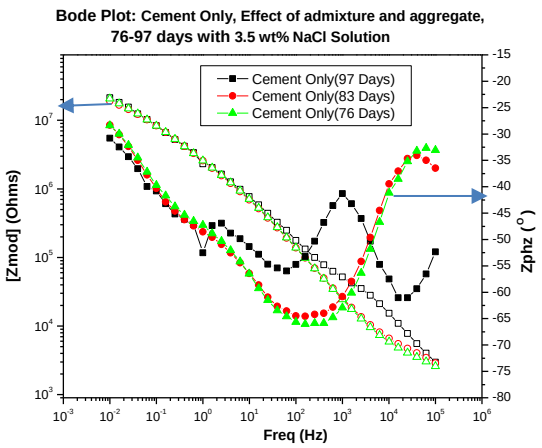

Fig. C-27(a). Bode plots of Cement Only (Control) specimen after 76, 83, and 97 days of exposure in 3.5% NaCl.

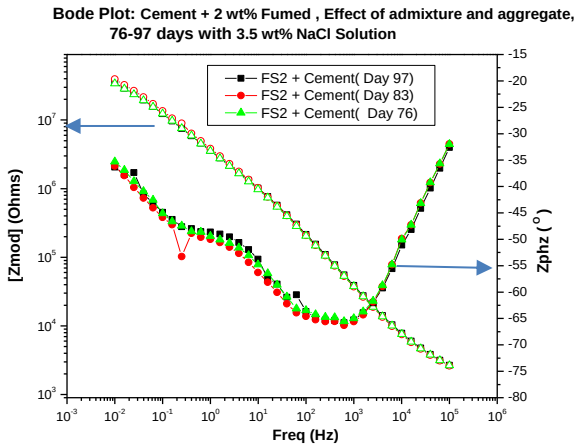

Fig. C-27(b). Bode plots of Cement with 2 wt% Fumed Silica (FS2) after 76, 83, and 97 days of exposure in 3.5% NaCl.

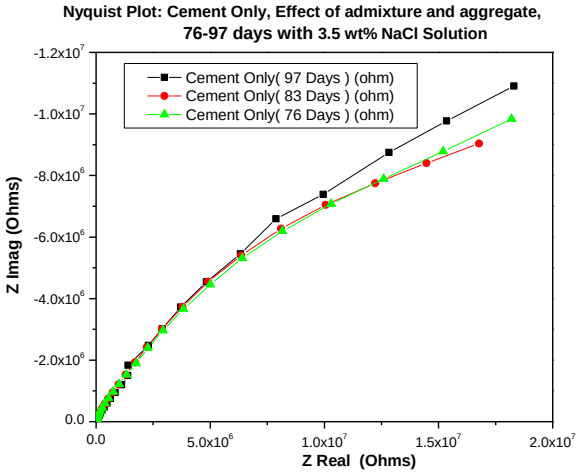

Fig. C-28(a). Nyquist plots of Cement Only (Control) specimen after 76, 83, and 97 days of exposure in 3.5% NaCl.

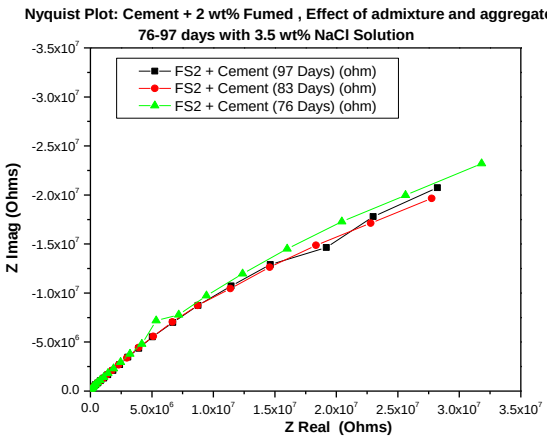

Fig. C-28(b). Nyquist plots of Cement with 2 wt% Fumed Silica(FS2) after 76, 83, and 97 days of exposure in 3.5% NaCl.

Figures C-27(a) and (b) show the Bode plots of the control (cement only) and 2% fumed silica admixture specimens respectively after exposure to the 3.5% NaCl solution for 3 different periods such as 76, 83, and 97 days. Fumed silica admixture samples showed relatively higher impedance modulus than the control sample. Figures C-28(a) and C-28 (b) show the Nyquist plots of the control and 2% fumed silica admixture specimens at different exposure times. The impedance

values decreased in general with the exposure time for the control specimen as seen in Fig. C-28(a). On the other hand, increased impedance was noted for the specimen containing 2wt% fumed silica as admixture. This observation points out the benefit of the fumed silica as admixture for concrete.

Figures C-29 (a) and (b) show the Bode plots of second batch of control sample (cement only) and 1wt% fumed silica admixture, respectively. These tests are currently in progress. Two sets of data after 7 and 15 days of immersion in 3.5% NaCl solution are given.

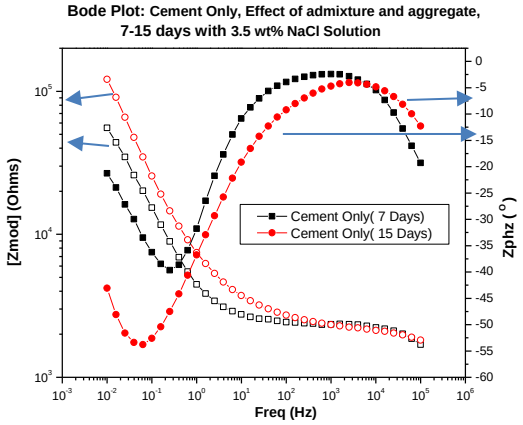

Fig. C-29(a). Bode plots of Cement Only (Control) specimen (second batch) immersed in 3.5% NaCl for 7 and 15 days.

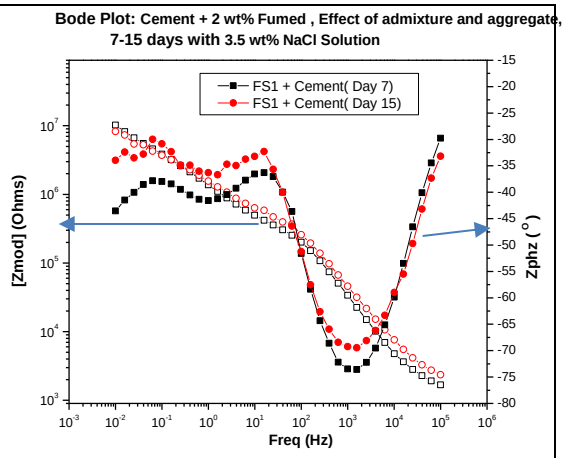

Fig. C-29(b). Bode plot with time for Cement with 1 wt% Fumed Silica (FS1) immersed in 3.5% NaCl for 7 and 15 days.

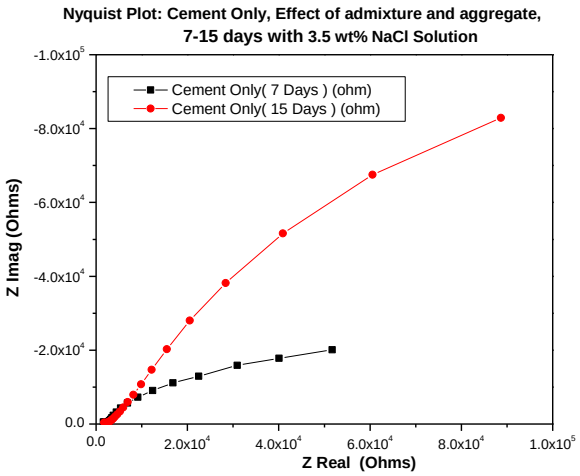

Fig. C-30(a). Nyquist plot with time for Cement Only (Control) immersed in 3.5% NaCl for 7 and 15 days.

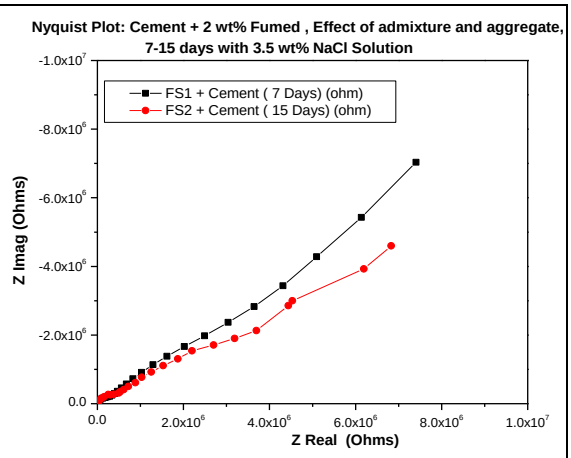

Fig. C-30(b). Nyquist plot with time for Cement with 1 wt% Fumed Silica (FS1) immersed in 3.5% NaCl for 7 and 15 days.

Figures C-30(a) and (b) are the Nyquist plots of second batch of control sample (cement only) and 1wt% fumed silica admixture, respectively. Two sets of data after 7 and 15 days of immersion in 3.5% NaCl solution are given. The Nyquist plots show a predominant Warburg type behavior at the low frequency regions.

The EIS data were fitted with equivalent circuits to model the impedance behavior of the concrete samples. A modified Song-model consisting of one-parallel RC and 1-series RC elements along with a Warburg element was used for fitting the data. From the Warburg impedance, the diffusivity was calculated and values are summarized in Table C-8 for all the specimens tested.

Table C-8 : Relative diffusivity of aggregate and admixture on concrete normalized to the diffusivity of control sample in 3.5 wt% NaCl solution

Sample	Day 62, $D/D_{control}$	Day 69, $D/D_{control}$	Day 76, $D/D_{control}$	Day 83, $D/D_{control}$	Day 97, $D/D_{control}$
Round rock	X	2.83	4.30	4.05	2.69
Round rock HF	0.02	2.86	2.17	2.53	1.67
Crushed rock	1.88	1.94	3.98	4.53	1.24
Pyrex	31.56	10.55	22.98	20.85	13.19
Pyrex HF	17.67	10.15	5.67	15.19	9.23
Cement only	1.00	1.00	1.00	1.00	1.00
Fumed silica	0.61	0.59	0.57	0.63	0.39
Micro silica	1.48	0.83	0.73	0.79	0.43
Ln Mt HF	3.42	X	2.32	2.51	1.67
Ln Mt	2.60	3.20	7.87	8.77	1.74

From the Table C-8, it can be noticed that both 2 wt% fumed silica and 2 wt% micro silica showed the lowest diffusivities among other aggregates/admixtures. The diffusivity data of control and fumed silica specimens were consistent over a period of time. The EIS results point out that both fumed silica and micro silica are diffusion controlling additives in concrete.

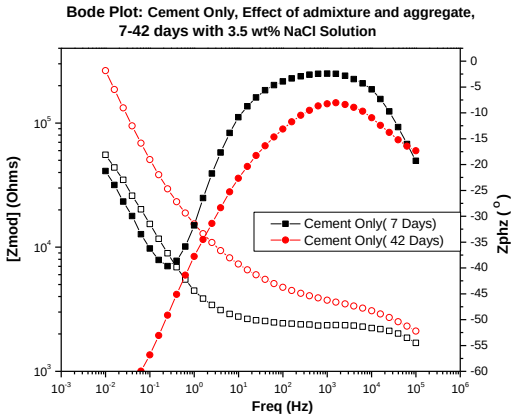

Fig. C-31(a). Bode plots of cement only (control) specimen (second batch) immersed in 3.5% NaCl for 7 and 42 days.

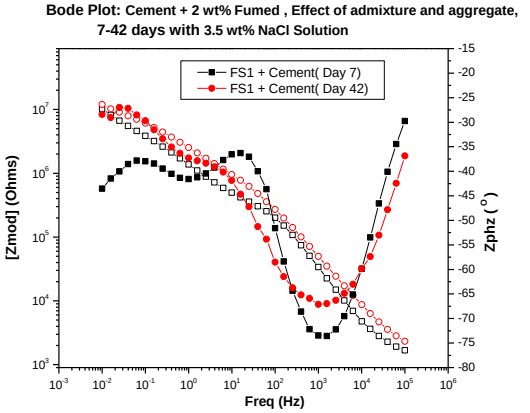

Fig. C-31(b). Bode plots of cement with 2 wt% fumed silica (FS2) after 7 and 42 days of exposure in 3.5% NaCl.

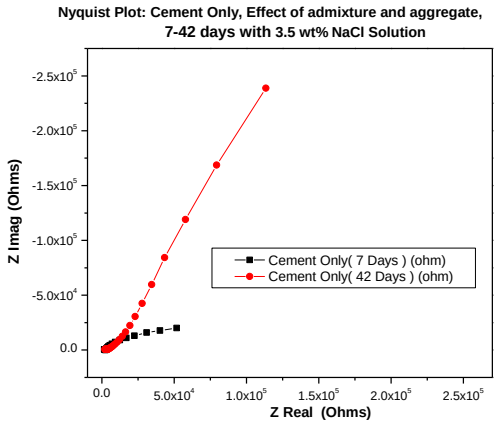

Fig. C-32(a). Nyquist plots of cement only (control) specimen (second batch) immersed in 3.5% NaCl for 7 and 42 days.

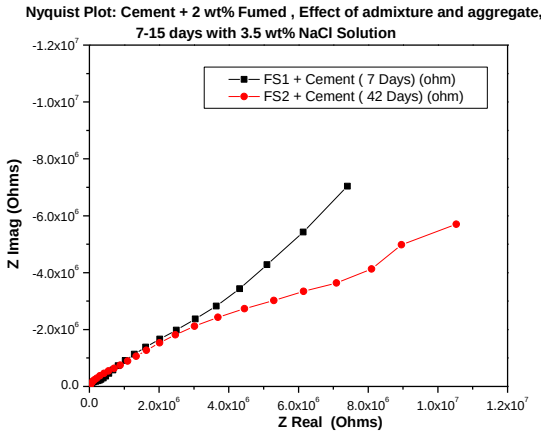

Fig. C-32(b). Nyquist plots of cement with 2 wt% fumed silica (FS2) after 7 and 42 days of exposure in 3.5% NaCl.

Figures C-31 and 32 show the Bode and Nyquist plots of the control and 2% fumed silica admixture specimens at two different exposure times. The impedance values significantly increased in general with the exposure time for the control specimen as seen in Figs. C-31 (a) and C-32(a). The impedance modulus after 7 days of exposure was 6 x 10^4 Ohm, which increased to 3 x 10^5 Ohm after 42 days of exposure at 10 mHz. On the other hand, only marginally increased impedance values (increased from 9.5 x 10^6 to 1.1 x 10^7 Ohm at 100 mHz) were noted for the specimen containing 2 wt% fumed silica as admixture with the increase in exposure time. Overall,

addition of fumed silica increased the impedance values of the concrete specimens by more than an order of magnitude.

Figures C-33(a) and (b) show the Bode plots of second batch of control sample (cement only), 1wt% glycerol admixture and 1wt% fumed silica admixture with different thickness values.

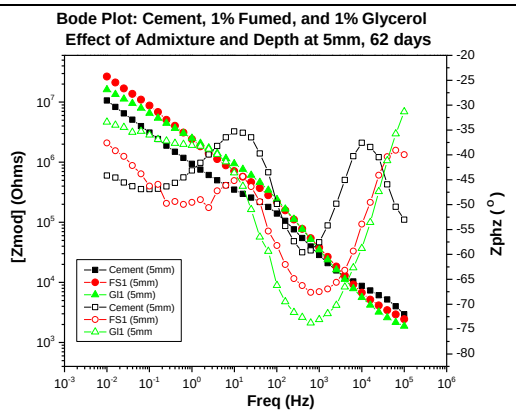

*Fig. C-33(a). Bode plots of cement only (control), 1wt% fumed silica (FS1), and 1wt% glycerol (Gl1) specimens with **5 mm** thickness immersed in 3.5% NaCl for 62 days.*

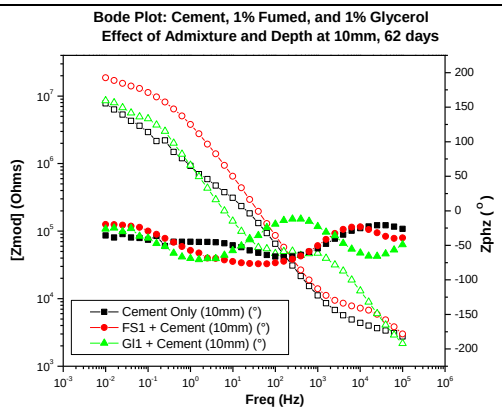

*Fig. C-33(b). Bode plots of cement only (control), 1wt% fumed silica, and 1wt% glycerol specimens with **10 mm** depths immersed in 3.5% NaCl for 62 days.*

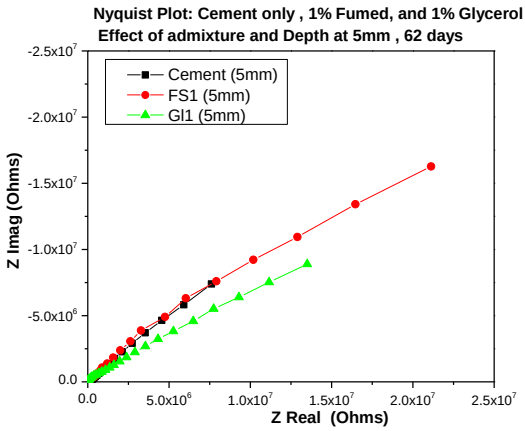

*Fig. C-34(a). Nyquist plot with time for Cement Only (Control), 1wt% Fumed silica (FS1), and 1wt% Glycerol (Gl1) with **5 mm** thickness immersed in 3.5% NaCl for 62 days.*

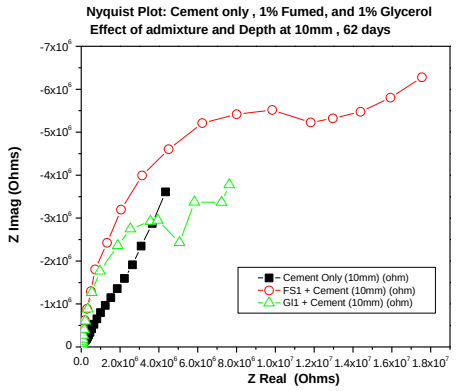

*Fig. C-34(b). Nyquist plot with time for Cement Only (Control), 1wt% Fumed silica, and 1wt% Glycerol with **10 mm** thickness immersed in 3.5% NaCl for 62 days.*

Figures C-34(a) and (b) are the Nyquist plots of second batch of control sample (cement only), 1wt% glycerol admixture and 1wt% fumed silica admixture, with two different thicknesses 5 and 10 mm, respectively. These tests are currently in progress. The Nyquist plots show a predominant Warburg type behavior at the low frequency regions.
The EIS data were fitted with equivalent circuits to model the impedance behavior of the concrete samples. A modified Song-model consisting of one-parallel RC and 1-series RC elements along with a Warburg element as described in the previous quarterly report was used for fitting the data. From the Warburg impedance, the diffusivity of chloride was calculated and values are summarized in Tables C-9 and C-10 for all the specimens tested.

Table C-9 : Relative diffusivity values normalized with control sample

Sample	Day 7, $D/D_{control}$	Day 42, $D/D_{control}$	Day 63, $D/D_{control}$
Cement only	1.00E+00	1.00E+00	1.00E+00
1%Fumed silica	3.89E-03	8.74E-02	6.45E-01
1%Glycerol	1.01E-03	1.56E-01	1.12E-01
Crushed Rock	3.70E-03	4.63E-02	7.58E+01
Round Rock	8.62E-03	9.14E-02	4.75E-02
HF Round Rock	2.58E-03	3.28E-02	2.69E-01
Ln Mt FS1	4.67E-03	6.16E-02	1.11E+02
Ln Mt Gl1_FS1	4.50E-03	7.15E-02	1.25E-02
Pyrex	7.78E-03	1.84E-01	2.09E+00
HF Pyrex	5.07E-02	6.61E-02	3.46E-01

From the Table C-9, it can be noticed that both 1 wt% Glycerol and Lane Mountain Gl1FS1 (with 1% Glycerol + 1% fumed silica addition) showed the lowest diffusivities among other aggregates/admixtures. The diffusivity data of control and fumed silica specimens were consistent over a period of time. The EIS results of 5 mm and 10 mm thick are bit non-conclusive since the 10 mm thick control specimen showed lowest diffusivity after 63 days of exposure. When the data of 5 mm thick specimens are considered, the additives glycerol and fumed silica showed diffusion controlling effects. Hypothetically, the diffusivity should not be influenced by thickness of the specimen. However, heterogeneity of microstructure of the specimen, inherent defects such as

micro-porosity and unreacted cement particles, and defects created during cutting process of the concrete slices such as micro cracks, and spalling off of the aggregates could play a significant role in affecting the diffusivity of the chloride. Overall, the tables C-9 and C-10 indicated that glycerol addition decreased the diffusivity of the chloride in concrete specimens as compared to that of cement only (control) samples.

Table C-10 : Relative diffusivity values of 5 mm and 10 mm thick samples normalized with control sample

Sample	Day 7, $D/D_{control}$	Day 42, $D/D_{control}$	Day 63, $D/D_{control}$
Cement only (5 mm)	1.00E+00	1.00E+00	1.00E+00
1%Fumed silica (5 mm)	2.29E+00	8.39E-01	5.62E-01
1%Glycerol (5 mm)	7.17E-01	5.09E-01	3.77E-01
Cement only (10 mm)	6.94E-01	2.83E+00	2.62E-01
1%Fumed silica (10 mm)	6.44E-01	1.06E+00	5.35E-01
1%Glycerol (10 mm)	7.39E-02	5.22E-01	3.38E-01

Figures C-35(a) and (b) show the Bode plots of the control (cement only) and 1% fumed silica admixture specimens respectively after exposure to the 3.5% NaCl solution for 2 different periods such as 7 and 42 days. Fumed silica admixture samples showed relatively higher impedance modulus than the control sample.

Figures C-36(a) and C-3 (b) show the Nyquist plots of the control and 2% fumed silica admixture specimens at different exposure times. The impedance values decreased in general with the exposure time for the control specimen as seen in Fig. C-36(a). On the other hand, increased impedance was noted for the specimen containing 1wt% fumed silica as admixture. This observation points out the benefit of the fumed silica as admixture for concrete.

Figures C-37(a) and (b) show the Bode plots of second batch of control sample (cement only), and 1wt% fumed silica admixture of samples 5 mm thick. Two sets of data after 7 and15 days of immersion in 3.5% NaCl solution are given.

Figures C-38(a) and (b) are the Nyquist plots of second batch of control sample (cement only), and 1wt% fumed silica admixture, respectively. Two sets of data after 7, 15, and 28 days of immersion in 3.5% NaCl solution are given. The Nyquist plots show a predominant Warburg type behavior at the low frequency regions but the impedance values are very high. The EIS data were fitted with equivalent circuits to model the impedance behavior of the concrete samples. A modified model

consisting of one-parallel RC and 1-series RC elements along with two Warburg elements was used for fitting the data. Using a relation between Fick's 2nd law and Fourier heat conduction, the diffusivity was calculated and values are summarized in Tables C-11 and C-12 for the specimens tested.

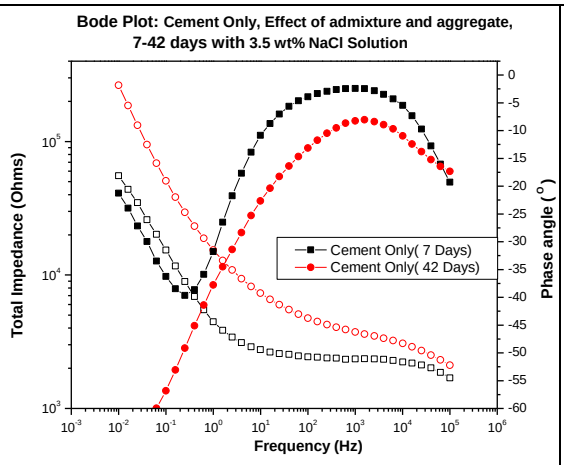

Fig. C-35(a). Bode plots of cement only (control) specimen (first batch) immersed in 3.5% NaCl for 7 and 42 days.

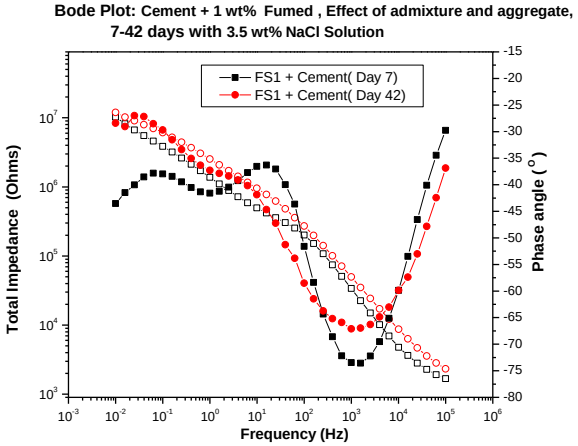

Fig. C-35(b). Bode plots of cement with 2 wt% fumed silica (FS1) after 7 and 42 days of exposure in 3.5% NaCl.

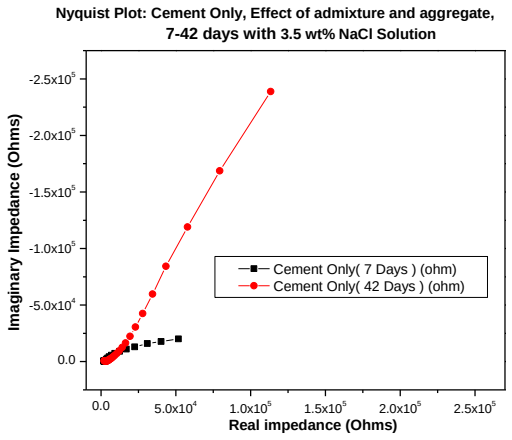

Fig. C-36(a). Nyquist plots of cement only (control) specimen (first batch) immersed in 3.5% NaCl for 7 and 42 days.

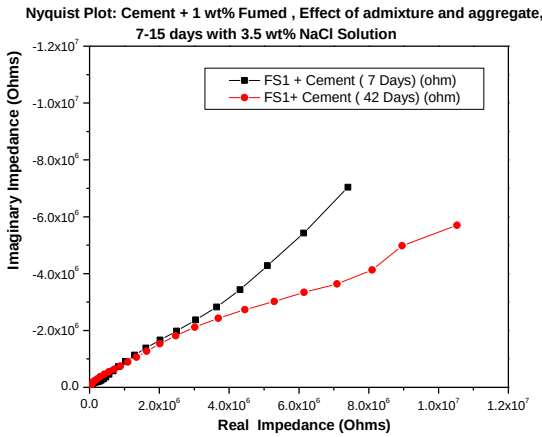

Fig. C-36(b). Nyquist plots of cement with 2 wt% fumed silica (FS1) after 7 and 42 days of exposure in 3.5% NaCl.

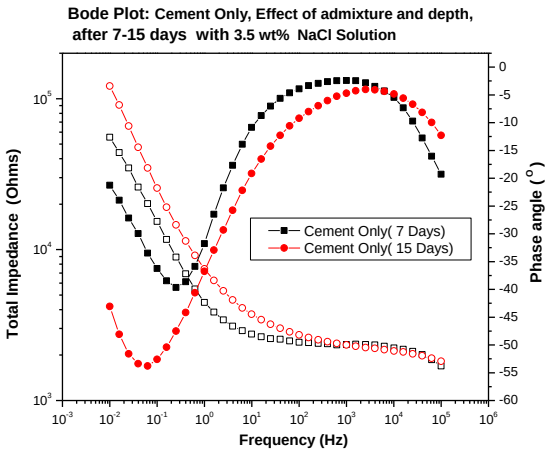

Fig. C-37(a). Bode plots of cement only (control) specimen (second batch) immersed in 3.5% NaCl for 7 and 15 days.

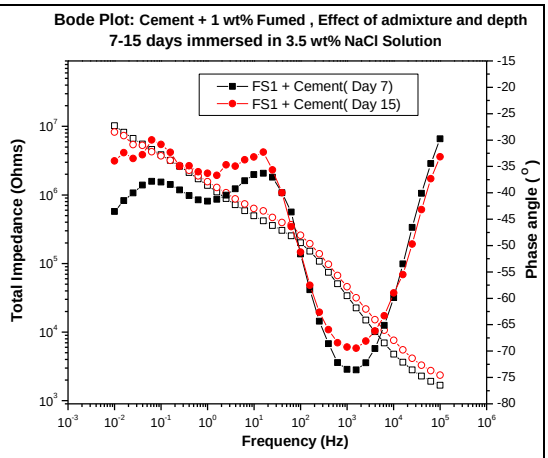

Fig. C-37(b). Bode plot with time for Cement with 1 wt% fumed silica (FS1) immersed in 3.5% NaCl for 7 and 15 days.

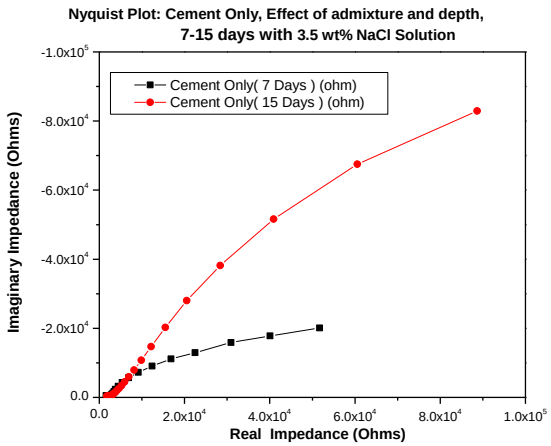

Fig. C-38(a). Nyquist plot with time for cement only (control) immersed in 3.5% NaCl for 7 and 15 days.

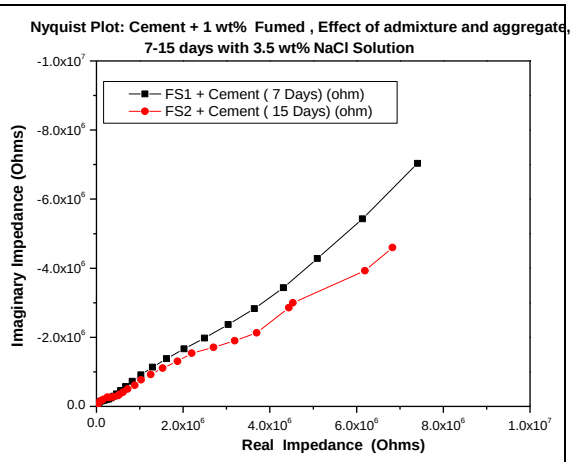

Fig. C-38(b). Nyquist plot with time for cement with 1 wt% fumed silica (FS1) immersed in 3.5% NaCl for 7 and 15 days.

Table C-11 : Diffusivity values of 10 mm thick samples based on EIS data			
Sample	Day 7, D (cm^2/s)	Day 15, D (cm^2/s)	Day 28, D (cm^2/s)
Cement only	3.88E-07	7.32E-08	1.73E-07
Fumed silica	3.29E-08	1.53E-08	8.54E-08
Glycerol	3.26E-08	1.56E-08	8.20E-08
Ln Mt Gl1_FS1	1.47E-06	1.62E-07	7.57E-07
Pyrex	3.65E-07	5.54E-08	2.76E-06

Table C-12 : Diffusivity values of 5 mm thick samples		
Sample	Day 7, D (cm^2/s)	Day 15, D (cm^2/s)
Cement only	1.45E-07	3.18E-08
1% Fumed silica	8.16E-08	3.31E-08
1% Glycerol	2.49E-08	2.04E-08

From the Table C-11, it can be noticed that both 1 wt% Glycerol and 1wt% Fumed showed the lowest diffusivities among other aggregates/admixtures. The diffusivity data of control and fumed silica specimens were consistent over a period of time. The EIS results point out that both fumed silica and glycerol are diffusion controlling additives in concrete.

C.4.4 EIS of Two Compartment Cell with Concrete Disc as Membrane

The results are based on the type: D experimental arrangement shown in Fig C-4. Figures C-39 (a-c) show the Nyquist plots and Figures C-40 (a-c) show the Bode plots of the control (cement only), 1% fumed silica admixture, and 1 wt% glycerol admixture specimens, respectively in the 3.5% NaCl solution at three different temperatures 24 (room temperature), 50 °, and 65 °C. Figure C-39 (d) show the equivalent circuit model used for fitting the EIS data. The diffusivity values were calculated from the Warburg component of the equivalent circuit. Figure C-40 (d) show the Arrhenius plot of diffusivity vs. inverse temperature for calculating the activation energy of the diffusion process. From the Nyquist and Bode plots Fumed silica admixture and glycerol samples showed relatively higher impedance modulus than the control sample. As the test temperature

increased, the impedance decreased significantly due to the expansion of the pores of the cement and increased vibration of the atoms/ions. The Nyquist plots show a predominant Warburg type behavior at the low frequency regions. A modified Song-model consisting of one-parallel RC and 1-series RC elements along with a Warburg element was used for fitting the data as shown in figure C-39(d). The diffusivity was calculated from the Warburg impedance and the values are summarized in Table C-13, for all the specimens tested. From the Table C-13, it can be noticed that both 1 wt% fumed silica and 1 wt% glycerol have the lowest diffusivity than cement without any admixture (control) at and above 40 °C. The heterogeneity of microstructure of the specimen, inherent defects such as micro-porosity and unreacted cement particles, and defects created during cutting process of the concrete slices could play a significant role in affecting the diffusivity of the ions, but overall the admixtures show improvement to the cement .

The activation energies for diffusion of the OH^- and H^+ ions in the cement discs of control, 1wt% glycerol, and 1wt% fumed silica were calculated as 172, 161, and 140 kJ/mol, respectively. These activation energies are about three times the activation energy reported for diffusion of chloride in the concrete. The higher activation energy could be attributed to the relatively stronger bonding of the H^+ and OH^- species to the Si^{4+}. Activation energies in the range of 1.5 - 2 eV have been reported for diffusion of hydroxyl/hydrogen ions in silicon [9], and ~2.5 eV (254 kJ/mol) was reported for diffusion of hydrogen in silica glass [10].

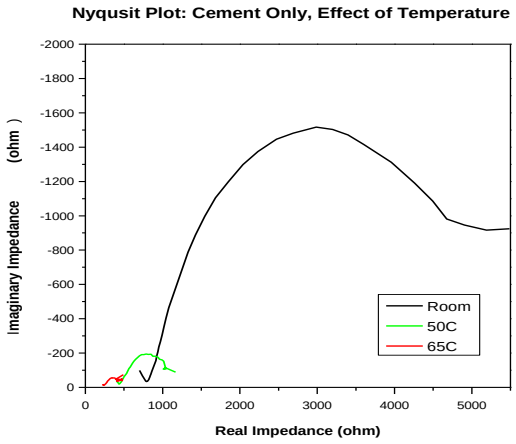

Figure C-39(a) Nyquist plots of cement (control) sample in 3.5 wt% NaCl solution at different temperatures

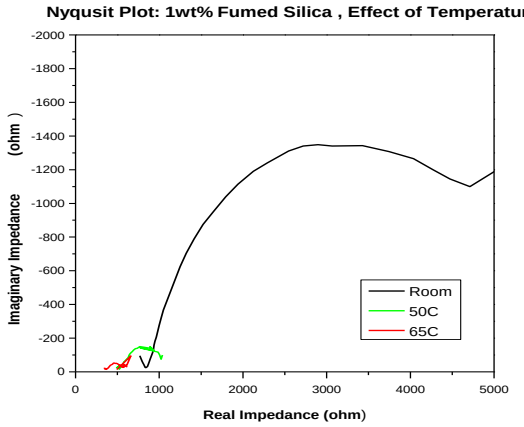

Figure C-39(b) Nyquist plots of cement with 1% fumed-silica in 3.5% NaCl solution at different temperatures

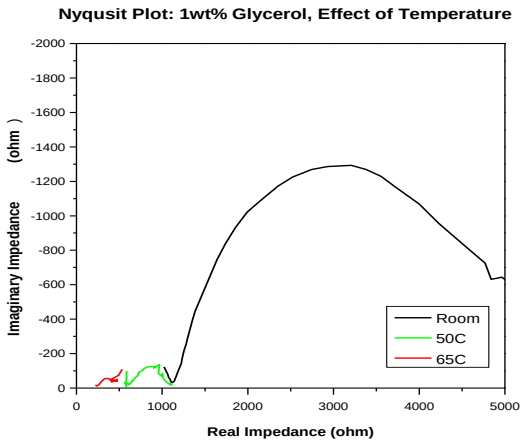

Figure C-39(c) Nyquist plots of cement with 1% glycerol in 3.5% NaCl solution at different temperatures

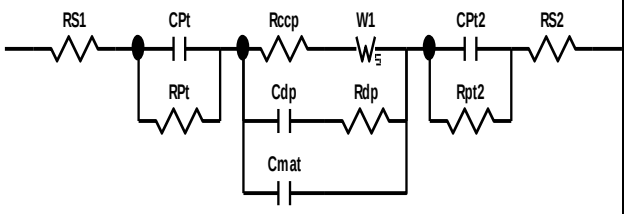

Figure C-39(d) Equivalent electric circuit used to model the EIS data

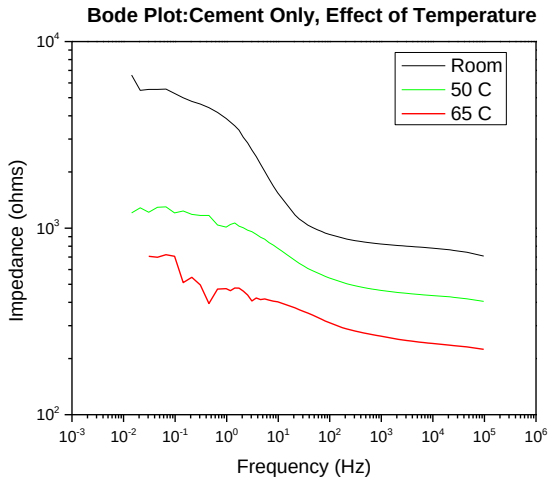

Figure C-40(a) Bode plots of cement only (control) sample in 3.5% NaCl solution at different temperatures

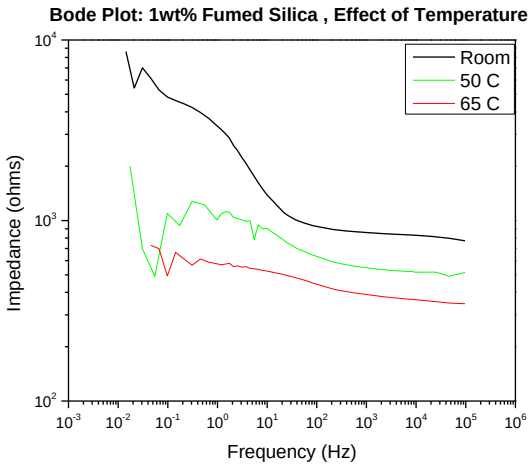

Figure C-40(b) Bode plots of cement with 1% fumed-silica in 3.5% NaCl solution at different temperatures

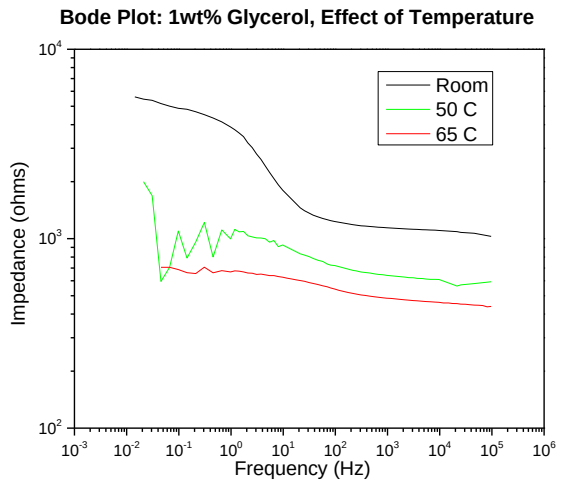

Figure C-40(c) Bode plots of cement with 1% glycerol in 3.5% NaCl solution at different temperatures

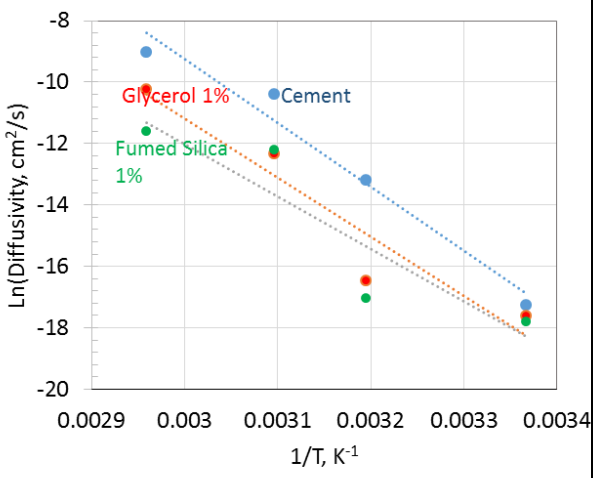

Figure C-40(d) Arrhenius plots (Ln(Diffusivity) vs. 1/T) of control, 1 wt% glycerol, and 1 wt% fumed silica samples.

Table C-13. : Summary diffusivity values of cement specimens with and without admixtures at different temperatures

Test Temperature	*Cement*	*1 wt% Glycerol*	*1 wt% Fumed silica*
°C	D, cm^2/s	D, cm^2/s	D, cm^2/s
24	3.23×10^{-8}	2.24×10^{-8}	1.86×10^{-8}
40	1.90×10^{-6}	7.21×10^{-8}	4.08×10^{-8}
50	3.07×10^{-5}	4.45×10^{-6}	5.03×10^{-6}
65	1.20×10^{-4}	3.65×10^{-5}	9.15×10^{-6}

C.5 Conclusions

The effect of additives on the permeability of modified concrete chemistry was investigated using electrochemical impedance spectroscopy (EIS). Different experimental arrangements were employed to obtain the impedance spectra. Based on the EIS results, the following conclusions are drawn:

1. *Concrete samples with embedded rebar steel as working electrode*: Addition of viscosity modifiers decreased the diffusivity of the concrete samples. 1% glycerol addition showed the highest effect of decreasing the diffusivity as compared to 0.5% and 2% glycerol additions based on the Warburg coefficients. Among the silica additions, 1% micro silica, 0.5% fumed silica, and 0.5% colloidal silica additions decreased the diffusivities by about 50% of the diffusivity estimated for the control sample (without viscosity modifiers).
2. *Concrete samples without embedded rebar steel (working electrode outside the concrete)*: Additions of 1% glycerol, and 1% fumed silica were observed to decrease the diffusivities as compared to that of control samples (without any additives). Additions of different aggregates such as round rock, crushed rock, pyrex etc. showed mixed results due to complex interfacial interactions.
3. At room temperature, addition of 1% glycerol decreased the diffusivity by 31%, and addition of 1% fumed silica decreased the diffusivity by 42% as compared to the estimated diffusivity of the control sample. At 40 °C, the additives were effective in decreasing the diffusivities by an order of magnitude as compared to the value estimated for the control sample.

C.5 References

[1] G.K. Glass, B. Reddy, N.R. Buenfeld, The participation of bound chloride in passive ®lm breakdown on steel in concrete, Corrosion Science 42 (2000) 2013-2021

[2] G.K. Glass, N.R. Buenfeld, The influence of chloride binding on the chloride induced corrosion risk in reinforced Concrete, Corrosion Science 42 (2000) 329-344

[3] M. Moreno , W. Morris , M.G. Alvarez , G.S. Duffo, Corrosion of reinforcing steel in simulated concrete pore solutions Effect of carbonation and chloride content, Corrosion Science 46 (2004) 2681–2699

[4] Yong Teck Tan, Sudesh L. Wijesinghe, Daniel J. Blackwood, The inhibitive effect of bicarbonate and carbonate ions on carbon steel in simulated concrete pore solution, Corrosion Science 88 (2014) 152–160

[5] D.H. Davies, G.T. Burstein, The effects of bicarbonate on the corrosion and passivation of iron, Corrosion 36 (1980) 416–422

[6] G.R. Meira, C. Andrade, E.O. Vilar, K.D. Nery, Analysis of chloride threshold from laboratory and field experiments in marine atmosphere zone, Construction and Building Materials 55 (2014) 289–298

[7] Vedalakshmi et al., Corrosion Science, 51 (2009) 1299–1307

[8] Cement and Concrete Research 30 (2000) 1723-1730

[9] Y.-S. Su, S. T. Pantelides, Physical Review Letters 88 (2002) 165503

[10] Z.Yongheng, G. Zhenan, Journal of Non-Crystalline Solids 352 (2006) 4030–403

NEUP Report Task C "Equivalent Circuit Models for AC Electrochemical Impedance Spectroscopy of Concrete"

Jiheon Jun and Evan Hess

Corrosion Science and Technology Group, Material Science and Technology Division
Oak Ridge National Laboratory, Oak Ridge, Tennessee 37831-6156

Executive Summary

The proposed research goals of this task are to:

4. Develop an EIS based model for modified concrete microstructure;
5. Understand the influence of modifiers on the permeability of the concrete and corrosion of rebar
6. Determine the effect of temperature on the permeability of the modified concrete

For the first goal, different circuit models to account for the concrete layer and corroding steel were discussed. Based on this, an equivalent circuit model for the corroding steel in a solution-permeated concrete was suggested. The effect of modifiers to slow down O_2 and Cl^- transport in the concrete was assessed using the real impedance of measured spectra for the second goal. *Fumed silica* was found to be the most effective modifier while *colloidal silica* was the least effect. The impact of temperature on concreate permeability was estimated using Stokes-Einstein equation for the third goal. The diffusion of O_2 and Cl^- is predicted to enhance with increasing temperature. This research permitted the measure of permeation of corrosion-related species using EIS, which revealed effective modifiers for simple (*fumed* and *micro-silica* silica) and aggregated (*fumed silica*) concretes.

Introduction

Concrete is a porous medium and susceptible to the permeation of water. The water-saturated pores of concrete could form continuous solution paths where oxygen (O_2) and chloride ion (Cl^-) can be introduced into the concrete. In the rebar-reinforced concrete structures, the ingress of O_2 and Cl^- causes the corrosion of steel-based rebar, deteriorating the integrity of concrete-based infrastructures such as roadways, bridges, and aircraft runways. The transport of O_2 and Cl^- to the rebar steel would be primarily driven by diffusion through the continuous solution path, although it can be also influenced by other factors associated with the concrete compositions and structures.

One way to mitigate the corrosion of rebar is to limit the transport of O_2 and Cl^-. In this work, four types of nanoparticle modifiers, developed at the University of Idaho, were added into simple and aggregated concretes to retard O_2 and Cl^- transport. The effectiveness of each modifier was assessed by comparing the impedance spectra measured using Electrochemical Impedance Spectroscopy (EIS). The measured spectra were analyzed based on an equivalent circuit model which accounts for the impedance response of the corroding steel in a solution-permeated concrete.

Experimental Procedure

The types of concrete mixtures tested in this work are summarized in Table 1. Simple or aggregated concrete (with addition of aggregates) was used for base matrix and 4 modifiers including three silica- and one glycol-based particles were added by 1 wt%. This gave total 10 different sample types. The hardened concrete mixtures were cut into 1 inch diameter coupons with the thickness 1, 3 or 5 mm. The configuration

of a single electrochemical cell is described in Figure 1. A steel plate was used as working electrode (WE), and a graphite rod with 5 mm diameter served as counter/reference electrode (CE and RE). Multiple concrete coupons were attached to one steel plate using conductive epoxy or carbon tape; 1 mm thick concrete coupons by conductive epoxy, but 3 and 5 mm coupons by carbon tape. A polyvinyl chloride (PVC) tube was place on each concrete coupon and sealed using insulating epoxy, which formed 8 to 10 cells in one steel plate. 25 mL 3.5 wt% NaCl solution was added as electrolyte to each cell.

The concrete-coupon cells were immersed in NaCl solution at least for 5 days before electrochemical measurements to allow solution permeation in the concrete and form conductive path(s) to the base steel plate. EIS measurement was initiated once the open circuit potential (OCP) of concrete coupon cells achieved a stable value. This usually took about 30 min. After OCP stabilization, EIS measurement was initiated using ± 10 mV amplitude against OCP with 1 MHz (in some cases, 5 MHz) for the upper limit and 0.1 Hz for the lower limit frequencies. All EIS measurements were conducted at room temperature. After the measurement, graphite rod was removed and the mouth of PVC tube was covered by a plastic paraffin film to minimize solution evaporation in the concrete coupon cells. The EIS data were named by 'day number' format which indicate the number of day after the beginning of solution immersion. For instance, day 5 indicates the EIS data was collected after 5 day-immersion of concrete coupon in NaCl solution.

Table 1. The types of base matrix and modifiers of concrete mixtures.

Base Matrix	Modifiers
• Simple concrete • Aggregated concrete (Concrete + Aggregates)	• No modifier • 1wt% Colloidal Silica (CS) • 1wt% Fume Silica (FS) • 1wt% Micro Silica (MS) • 1wt% Glycol

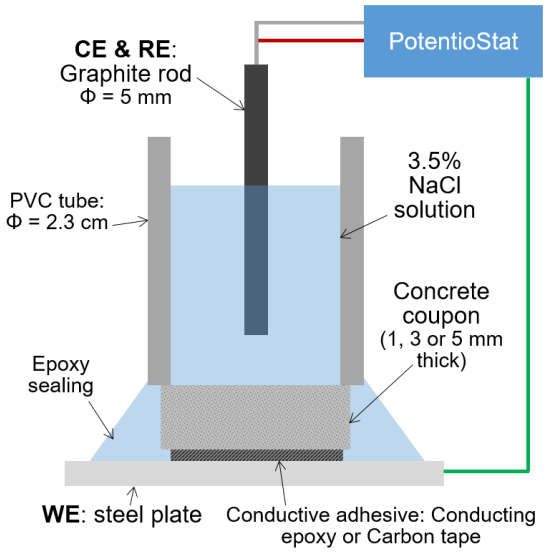

Figure 1. Schematic of experimental setup for electrochemical measurements. The potentiostat used in this work is VMP 300 from BioLogic Scientific Instrument.

Equivalent Circuit Models and Simulated Impedance Spectra for Steel in Concrete Layer

All concrete coupons were assumed to form solution paths upon sufficient permeation of aqueous solutions. A schematic of a concrete coupon cell after solution permeation is described in Figure 2. In the concrete layer, fully-wet path can form if the saturated pores of concrete are continuously connected between the bulk solution and steel plate. In partially-wet path, on the other hand, the connection of saturated pores does not reach to the steel, leaving an insulated region between the front of saturated pores and steel plate. The concept of fully- and partially-wet paths in a solution-permeated concrete layer is also discussed elsewhere [1]. In both wet paths, the interface of solution and concrete could exhibit captative behavior, indicating the equivalent circuit model for solution-permeated concrete should include a capacitor element. Underneath the concreted layer, the interface of solution and steel plate would form, where corrosion of steel can proceed.

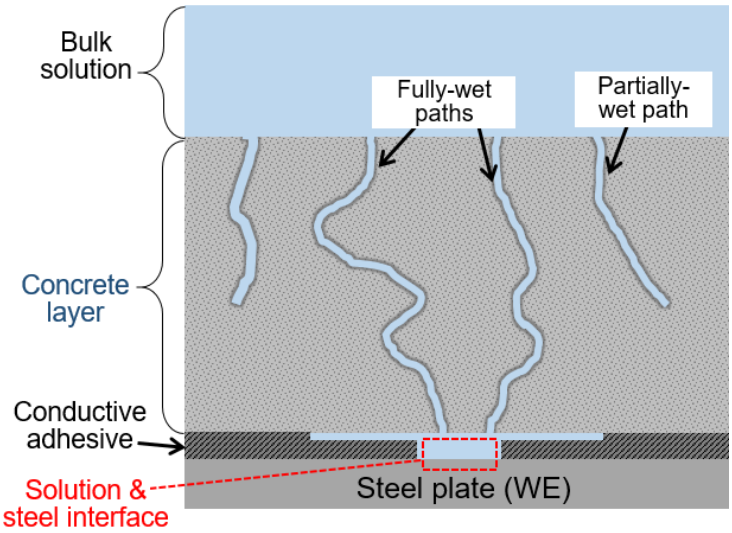

Figure 2. Schematic of solution-permeated concrete where fully- and partially-wet paths are formed. The underlying steel contacts with the solution which permeated the entire concrete layer through the fully-wet paths.

In EIS measurement, the equivalent circuit of a corroding metal is commonly described by one resistor and one capacitor in parallel connection as shown in Figure 3a. This connection is also called time constant or *RC* circuit. For a corroding metal, the resistor (*R*) of time constant corresponds to charge-transfer resistance, while the capacitor (*Q*) is used to account for double layer capacitance. In realistic conditions, however, double layer capacitance does not behave ideally. To illustrate non-ideal capacitance, constant phase element (CPE) is commonly used instead of an ideal capacitor for time constant as seen in Figure 3b. The impedance of an ideal capacitor and CPE can be calculated using Eqn. 1a and 1b [2], respectively.

$$Z_Q = \frac{1}{j \cdot \omega \cdot Q_0} \qquad \text{[Eqn. 1a]}$$

$$Z_{CPE} = \frac{1}{Q_0 (j \cdot \omega)^p} \qquad \text{[Eqn. 1b]}$$

where Q_0 is the capacitance in F (Farad), ω is the radial frequency and p is a coefficient between 0 and 1. If p = 1, CPE is equal to an ideal capacitor. p values smaller than 1 are applied for non-ideal capacitive

behaviors. Simulated impedance spectra of a parallel connection of resistor and CPE (*R*-CPE circuit) are plotted for different *p* values in Figure 4. These plots were generated using Z-view software developed by Scribner Associates Inc. [2]. For $p = 1$, a semi-circle shaped plot with its diameter equal to the resistance is obtained. In simulations using $p = 0.8$ and 0.6, the shape of plots becomes depressed semi-circle, where the peak decrease as *p* value decreases. If corrosion of steel below the concrete coupon is controlled by charge-transfer reaction, *R*-CPE circuit would be an appropriate model to use.

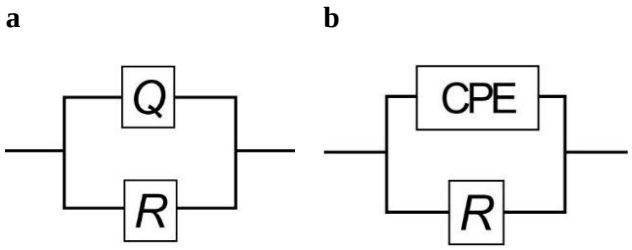

Figure 3. Parallel connections of a resistor with (a) an ideal capacitor and (b) a constant phase element.

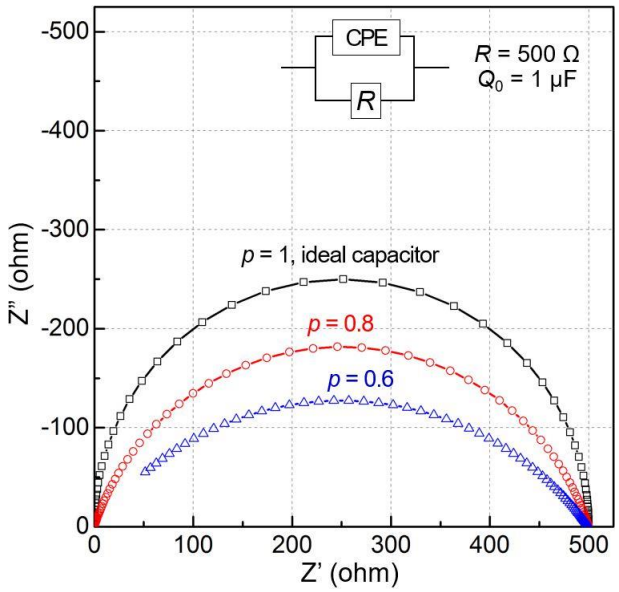

Figure 4. Simulated Nyquist plots of *R*-CPE circuit for different *p* values, the upper and lower frequency limits used for the simulation are 1 MHz and 0.1 Hz, respectively.

The transport of ions and dissolved gases is much slower in concrete than in free aqueous solution, which could cause corrosion reaction under diffusion control. To account for the diffusion effect on impedance spectra, Warburg impedance element can be used in series with charge-transfer resistance in *R*-CPE circuit as seen in Figure 5. Open-circuit Warburg impedance (W_o) in the circuit is applicable for a finite diffusion length and depleting diffusion species which are probable for corroding steels in concretes. Warburg impedance also appears in other studies to model diffusion-limited rebar corrosion in concretes [3-6]. The impedance of W_o is calculated using Eqn. 2 [2].

$$Z_{wo} = \frac{\sigma \cdot \coth[(j \cdot \tau \cdot \omega)^n]}{(j \cdot \tau \cdot \omega)^n} \qquad \text{[Eqn. 2]}$$

where σ is the Warburg coefficient in ohm, τ is the characteristic diffusion time in second, and *n* is a coefficient equal to or smaller than 0.5. If $n = 0.5$, τ is equivalent to the product of diffusion length and effective diffusion coefficient of the species involved in corrosion reaction. Simulated impedance spectra of W_o-added *R*-CPE circuit in Figure 5 are shown for different *n* and σ values in Figure 6a and 6b, respectively. Compared to *R*-CPE circuit (designated by $W_o = 0$ in Figure 6a), W_o-added circuits exhibit imaginary impedance (*Z*") increasing in low frequency regimes where the slopes of impedance spectra in W_o-added circuits depend on *n* values: as *n* decreases, the slope becomes smaller. The increase of σ, on the other hand, did not change the slope but resulted in higher impedance in low frequency regime (see Figure 6b). This sloped regime associated with diffusion can be termed 'Warburg tail' as it is resulted from W_o element.

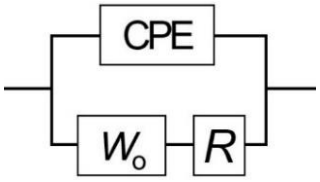

Figure 5. W_o-added *R*-CPE circuit to account for the diffusion-limited rebar corrosion.

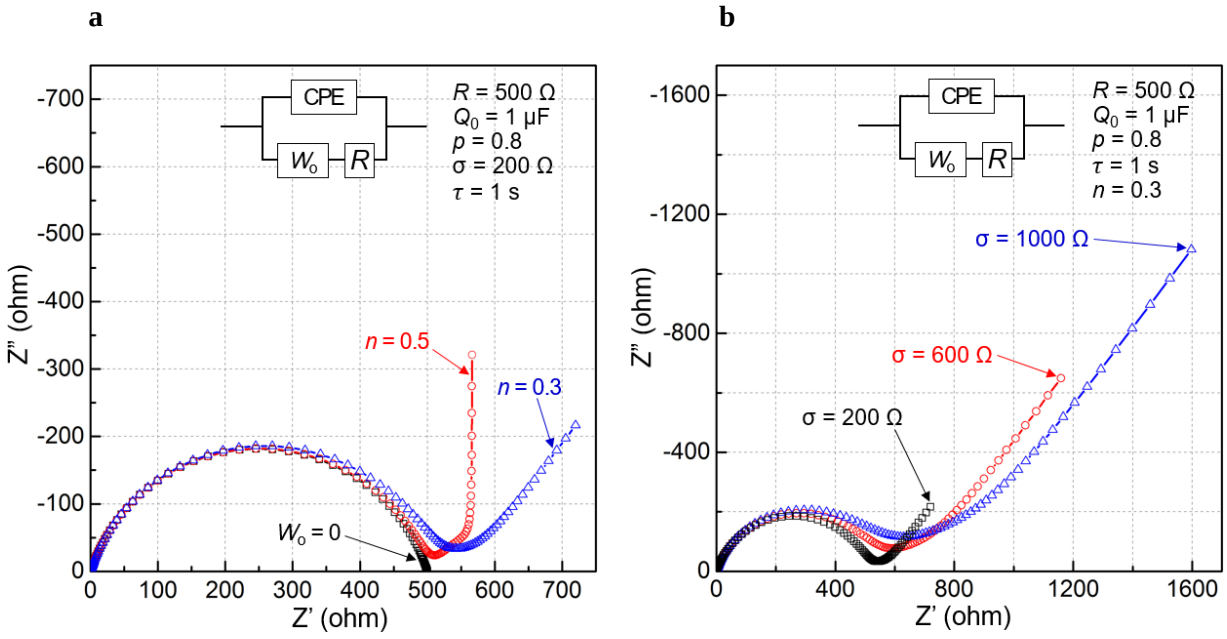

Figure 6. Simulated Nyquist plots of W_o-added *R*-CPE circuit for different (a) *n* and (b) σ values, the upper and lower frequency limits used for the simulation are 1 MHz and 0.1 Hz, respectively.

In the meantime, the impedance of solution-permeated concrete in Figure 2 depends on the resistive and capacitive elements of both fully- and partially-wet paths. If the impedance is smaller through fully-wet

path than partially-wet path in the entire frequency range, the equivalent circuit of solution-permeated concrete can be described by *R*-CPE parallel connection. In this case, *R* corresponds to the sum of the solution resistances of fully-wet paths (in parallel connection), and CPE account for non-ideal capacitive behavior at the solution-concrete interfaces. *R*-CPE parallel connection was chosen to model the equivalent circuit of concrete in some previous studies [4, 5, 7].

In case the impedance of fully- and partially-wet paths are comparable in a certain frequency range, however, a circuit composed of two resistors and one capacitor described in Figure 7 can be used. In this circuit, R_1 and R_2 correspond to the solution resistances of partially- and fully-wet paths, and CPE addresses non-ideal capacitance of the solution-concrete interfaces in partially wet paths. Assuming the two solution paths are only different in the length, the solution resistance would be higher in fully-wet paths because they would be longer. Simulated impedance spectra of R_1-R_2-CPE circuit in Figure 7 are plotted for different R_1 values and CPE with ideal (p = 1) and non-ideal (p = 0.8) capacitive behaviors in Figure 8. Increasing R_1 (the solution resistance of partially-wet paths) shifts the left intersect of semi-circle from 0 to positive values on real impedance (Z') axis and also decreases the distance between the two intersects of the semi-circle. The right intersect, however, does not change.

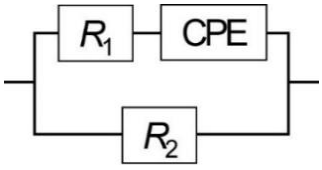

Figure 7. R_1-R_2-CPE circuit to account for the contribution of both fully- and partially-wet paths in solution-permeated concretes.

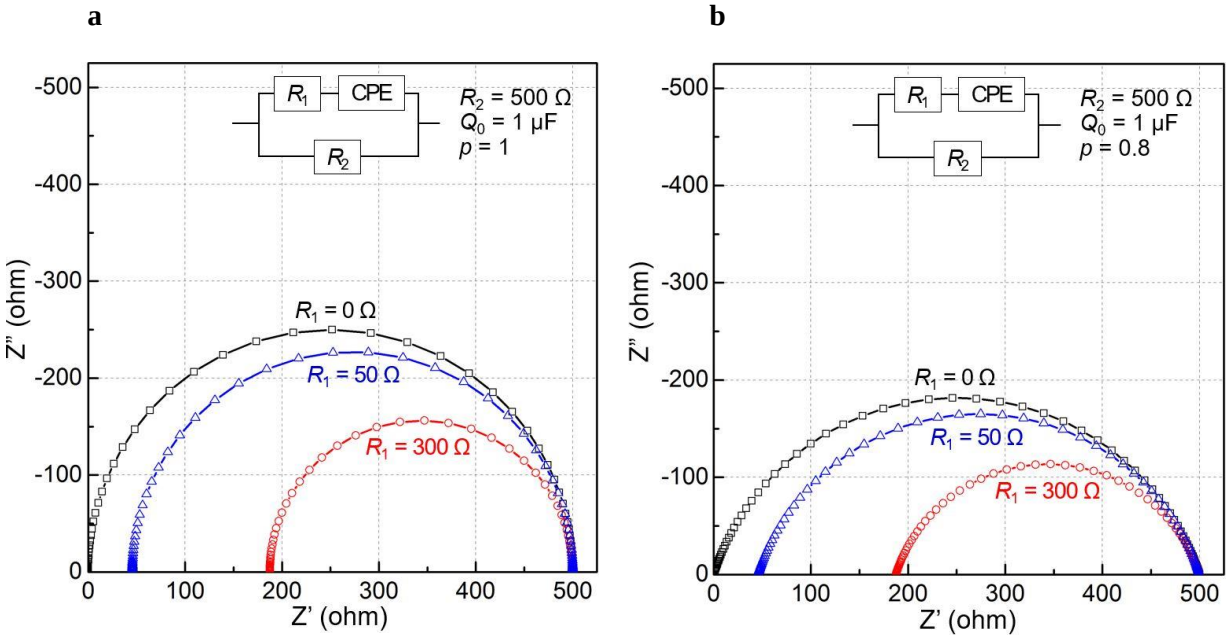

Figure 8. Simulated Nyquist plots of R_1-R_2-CPE circuit for different R_1 values in (a) p = 1 and (b) p = 0.8 conditions, the upper and lower frequency limits used for the simulation are 1 MHz and 0.1 Hz, respectively.

The circuit elements in Figures 3, 5 and 7 can be combined to describe the experimental impedance spectra of solution-permeated concrete + corrosion of steel. W_o-added *R*-CPE circuit (see Figure 5) would apply for diffusion-limited corrosion of steel while R_1-R_2-CPE circuit (see Figure 7) could account for the concrete with fully- and partially-wet paths. Simple *R*-CPE circuit (see Figure 3) can apply for the concrete dominated by fully-wet paths and steel corrosion that is not diffusion-limited. An example impedance spectra of *R*-CPE in series connection with W_o-*R*-CPE is compared with those of separate *R*-CPE and W_o-*R*-CPE in Figure 9. Here, *R*-CPE and W_o-*R*-CPE are selected to model solution-permeated concrete and corrosion of steel, respectively. The addition of R_1-CPE_1 to W_o-R_2-CPE_2 increased both real and imaginary impedances of semi-circle but did not affect Warburg tail associated with diffusion in low frequency regimes.

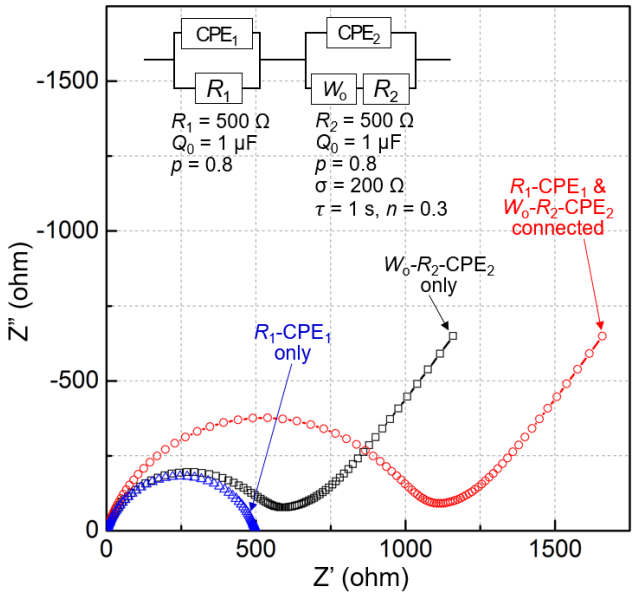

Figure 9. Simulated Nyquist plots of separate and connected *R*-CPE and *Wo*-*R*-CPE circuits, the upper and lower frequency limits used for the simulation are 1 MHz and 0.1 Hz, respectively.

Comparison of Measured Impedance Spectra and Effectiveness of Modifiers

Solution permeation in a concrete layer is time-dependent process, which implies that the formation of fully- and partially-wet paths (see Figure 2) is also time-dependent. The shape of impedance spectra, therefore, would change with time until the solution paths are stabilized. Once the formation of highly-stable solution paths is completed in concrete, the measured impedance spectra would be less dependent on time, implying that the stability of electrochemical system is reached. To assess the time for the system stability, the impedance spectra should be periodically monitored.

The impedance spectra of simple concrete with increasing immersion time are shown in Figure 10. The shape of impedance spectra is similar regardless of time, which is characterized by the combination of depressed semicircle and Warburg tail. This indicates the electrochemical system became quite stable before 10 days although the impedance values slightly increased with increasing time. The impedance spectra of aggregated concrete (concrete + aggregates) with increasing immersion time are also shown in Figure 11. The shape of impedance spectra of day 20, 25 and 30 are similar to the simple concrete spectra in Figure 10, exhibiting depressed semi-circle and Warburg tail. The impedance spectra of day 10 and 15, however, did not show semi-circle + Warburg tail explicitly. In aggregated concrete, the system stability

seems to be reached in 20-day immersion because the shape of impedance spectra (depressed semi-circle + Warburg tail) did not change noticeably afterward. For further impedance data analysis, the impedance spectra from the stable electrochemical system were chosen: these are 10-day or longer immersion data for the simple concrete and 20-day or longer immersion data for aggregated concrete.

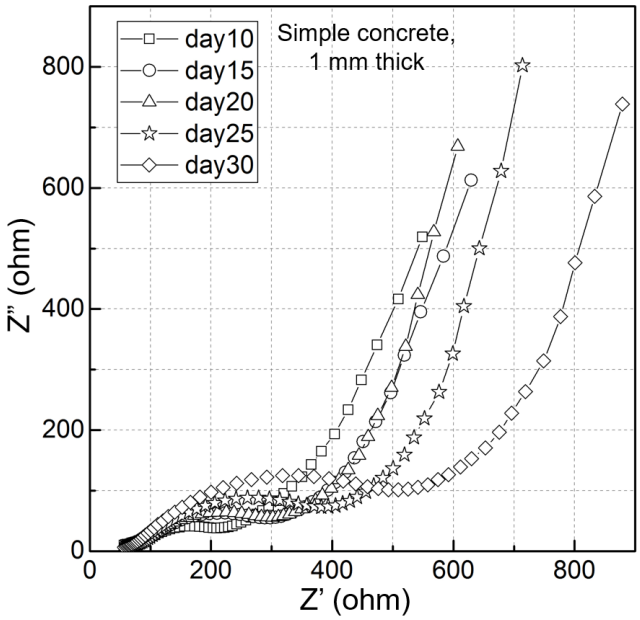

Figure 10. Nyquist plots measured for different immersion times in 1 mm thick simple concretes.

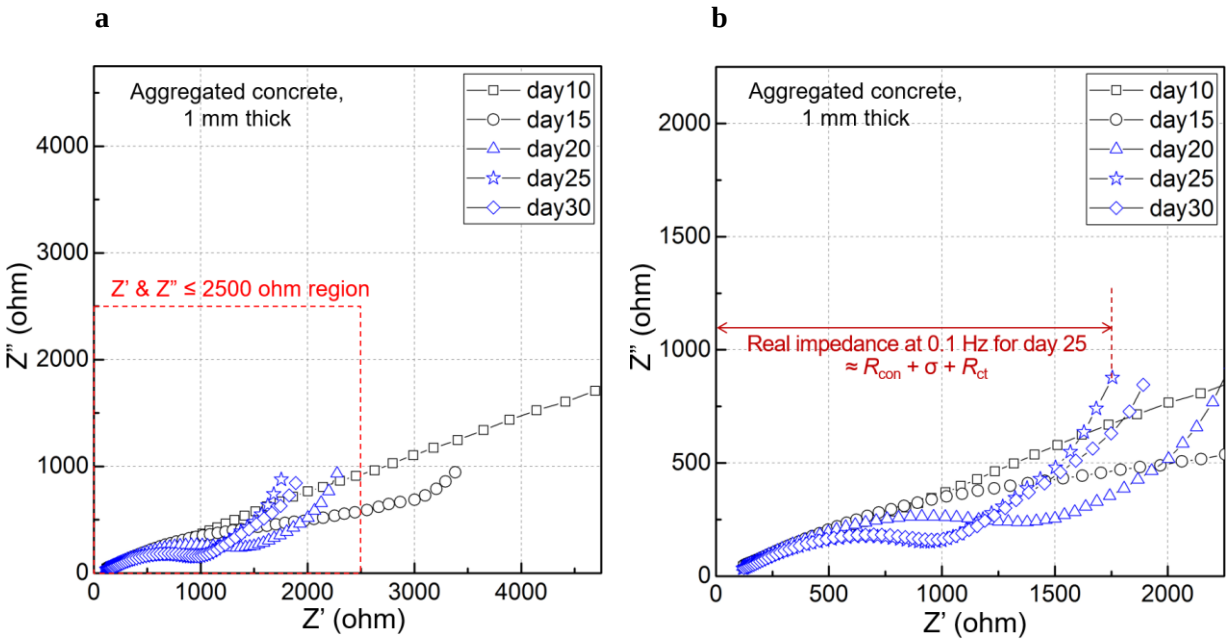

Figure 11. Nyquist plots measured for different immersion times in 1 mm thick aggregated concretes shown in (a) full and (b) lower Z’ and Z” ranges.

The measured impedance spectra characterized by depressed semi-circle + Warburg tail look similar to the simulated impedance spectra of *R*-CPE and W_o-*R*-CPE in series connection (see Figure 9), suggesting the modeled circuit could be used for impedance data fitting. Zview software, which provides automated fitting function, was used to obtain satisfying and relevant fitting between the circuit model and all measured impedance spectra from simple, aggregated and modified (modifier-added) concretes attached to steel. Unfortunately, many attempts to obtain satisfactory fitting for measured impedance spectra were not successful as they resulted in unrealistic or not-acceptable parameters for some circuit elements. For this reason, the direct comparison of resistive and diffusion-related impedances to estimate the transport properties of O_2 and Cl^- was impossible.

Instead, an alternative method to assess the transport properties was used in this work. This method assumes;

1. *R*-CPE + W_o-*R*-CPE model in Figure 9 is applicable for concrete coupon + corroding steel.
2. At the lower limit frequency (0.1 Hz), the real impedance values are close to the sum of concrete resistance (R_{con}), Warburg coefficient (σ) and charge transfer resistance (R_{ct}), which is schematically described in Figure 11b. This is because the impedance of CPE elements could be much larger than the resistors and Warburg element at the lower limit frequency, which causes the impedance to be governed by R_{con} + R_{ct} + diffusive resistances.
3. R_{ct} is not significantly different for all EIS measurement.
4. The transport of O_2 and Cl^- is slower and more difficult as the sum of R_{con} and σ increases.

Based on these assumption, the higher the real impedance at 0.1 Hz becomes, the more resistance against the transport of O_2 and Cl^- the concrete has. According to these criteria, the aggregated concretes (real impedance ~ 1850 ohm for day 30) is more efficient to slow down O_2 and Cl^- transport than the simple concrete (real impedance ~ 880 ohm for day 30) as appeared in Figure 11.

The impedance spectra of aggregated concrete with increasing thickness are presented for day 20 and 25 data in Figure 12. The real impedance values at 0.1 Hz did not depend on the thickness; 3 mm aggregated concrete gave the largest real impedance values for both day 20 and 25. In theory, R_{con} must be proportional to the concrete thickness given that the average length of fully-wet paths per unit thickness are similar in the concretes. These results could indicate that the formation of fully-wet paths is highly random and their average length may not be proportional to the concrete thickness. In 3 mm and 5 mm data, the real impedance values for day 20 and 25 were not significantly different, but in 1 mm, the impedance value for day 20 was about 500 ohm larger than day 25. Based on these results, it is reasonable to use 3 mm and 5 mm data for further comparison analyses but exclude 1 mm data for aggregated concretes because the real impedance values were more consistent in 3 mm and 5 mm thick aggregated concretes.

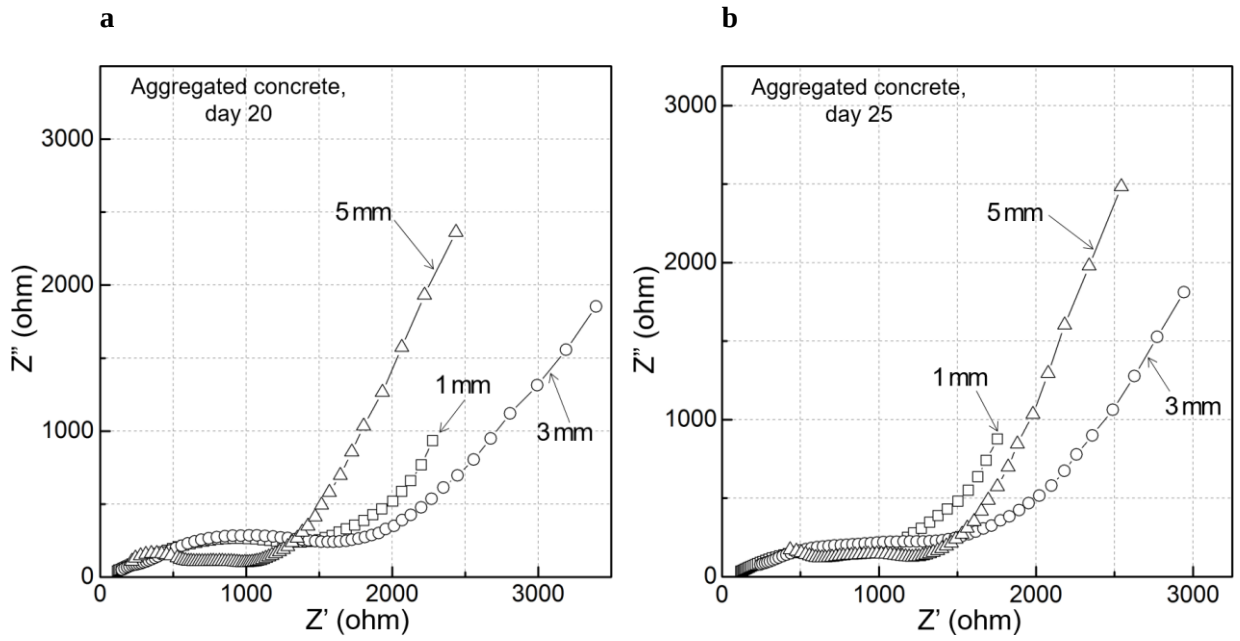

Figure 12. Nyquist plots of 1, 3 and 5 mm thick aggregated concretes for (a) day 20 and (b) day 25.

The impedance spectra of glycol-modified concretes (simple concrete + glycol) are shown for different thicknesses and immersion time in Figure 13. In this case, the real impedance values are proportional to the thickness of the modified concrete but relatively constant with increasing immersion time. Other modifiers in the simple concretes, however, did not show a positive correlation between the real impedance values and thickness, implying that the effect of thickness in modified or unmodified concrete samples are rather random and inconsistent. For this reason, it would be more appropriate to focus on the effect of different modifiers rather than the effect of thickness which is seemingly random or the effect of immersion time which was insignificant.

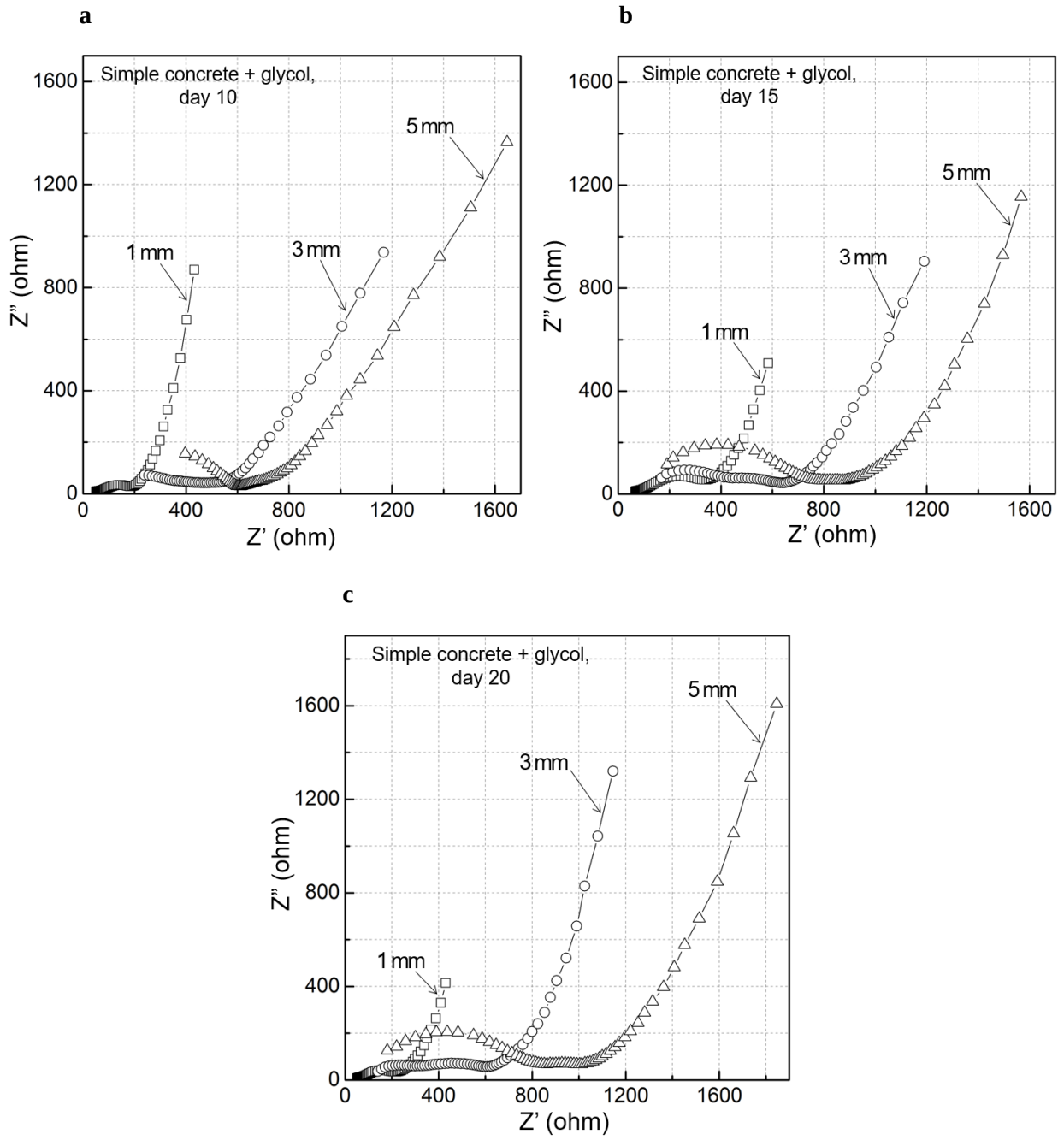

Figure 13. Nyquist plots of 1, 3 and 5 mm thick glycol-modified simple concretes for (a) day 10, (b) day 15 and (c) day 20.

To assess the effect of modifiers, the impedance spectra of 1 mm thick simple and modified concretes are compared for three immersion times in Figure 14. The real impedance values of glycol-modified concrete were not significantly different from the values of simple concrete, implying that glycol has little effect on the transport of O_2 and Cl^-. The addition of fumed silica, on the other hand, increased the real impedance values approximately three times for all immersion times, indicating fume silica was effectively slowed down O_2 and Cl^- transport. The impedance of micro silica-modified concrete were the highest and reached

to 3400 ohm after 20-day immersion. This suggests that micro silica would be the most effective modifier to retard the transport of O_2 and Cl^- in the simple concretes.

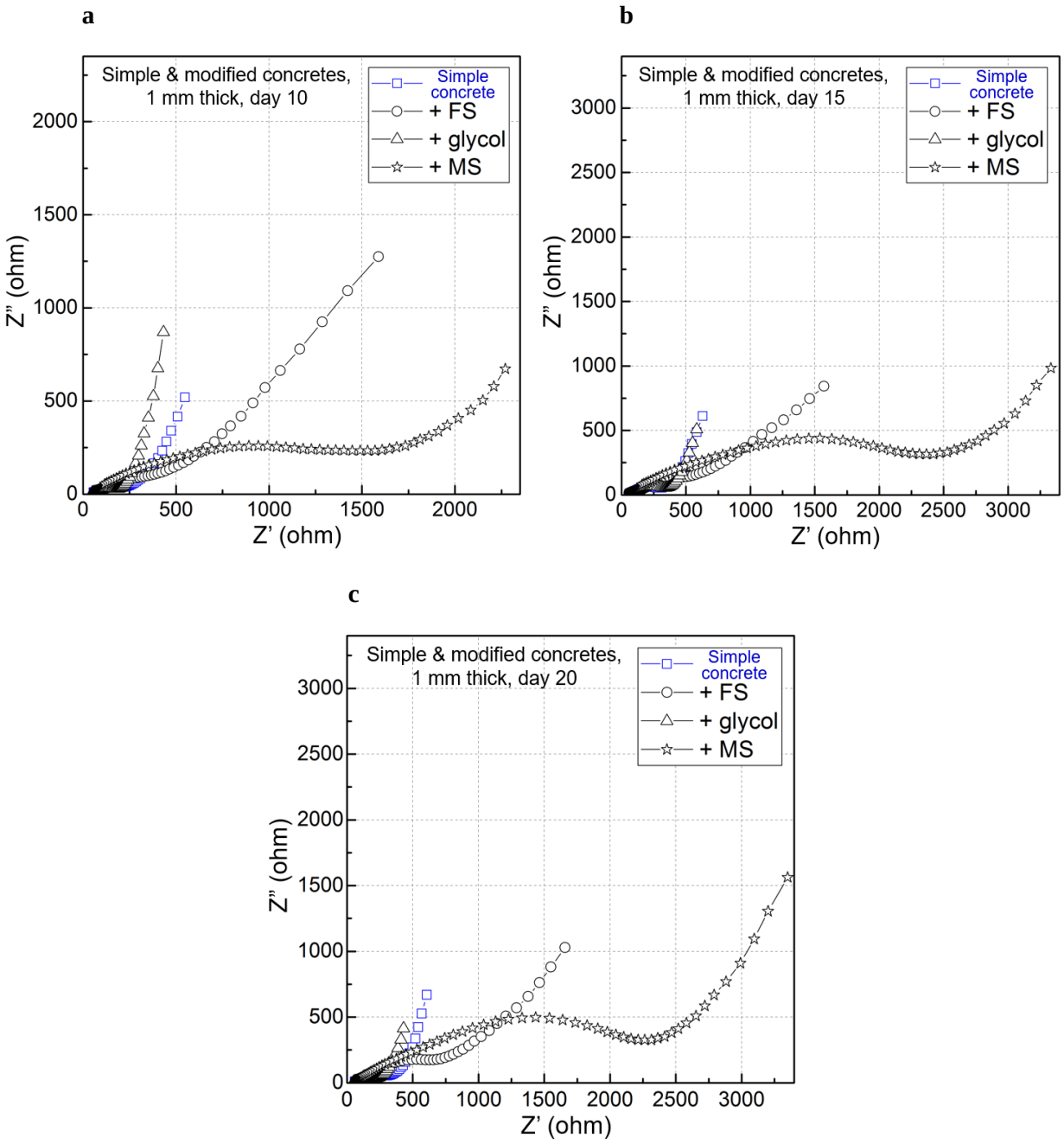

Figure 14. Nyquist plots of 1 mm thick modified and unmodified simple concretes for (a) day 10, (b) day 15 and (c) day 20.

The real impedance values of simple and modified concretes are summarized for different thicknesses and immersion times in Table 2. No data was available for 3 and 5 mm unmodified simple concretes, hence the direct comparison between the simple and modified concretes is impossible. Instead, the impedances of

modified 3 and 5 mm concretes were compared with 1 mm simple concretes. In the table, it is noticed that 83, 66 and 100% of impedance data of fumed silica-, glycol- and micro silica-modified concretes were 1.6 times or larger compared to the impedance of simple concretes. In contrast, colloidal silica-modified concretes had no impedance data that were l.6 time larger than the simple concrete. Based on the real impedance values, colloidal silica seems to have no or insignificant influence on O_2 and Cl^- transport. The addition of glycol has limited effect to retard O_2 and Cl^- while fumed and micro silica particles were effective to increase the real impedance by slowing down O_2 and Cl^-.

Table 2. Summary of the real impedance values measured for modified and unmodified simple concretes, the values in single bracket indicate that they were 1.6~2 times larger than the impedance of unmodified simple concretes. Similarly, the values in double bracket indicate that they were more than 2 times larger.

	Simple concrete real impedance (ohm)					
	Day 10		Day 15		Day 20	
1 mm	549		629		607	
3 mm	Not measured		Not measured		Not measured	
5 mm	Not measured		Not measured		Not measured	
	+ CS real impedance (ohm)			**+ FS** real impedance (ohm)		
	Day 10	Day 15	Day 20	Day 10	Day 15	Day 20
1 mm				((1588))	((1572))	((1658))
3 mm	684	479	629			
5 mm	578	723	856	872	((1306))	((1380))
1.6~2 times	0%			0%		
2 times <	0%			83%		
	+ glycol real impedance (ohm)			**+ MS** real impedance (ohm)		
	Day 10	Day 15	Day 20	Day 10	Day 15	Day 20
1 mm	432	583	430	((2271))	((3332))	((3351))
3 mm	((1167))	(1190)	(1146)			
5 mm	((1647))	((1567))	((1846))	((1235))	(1202)	(1208)
1.6~2 times	22%			66%		
2 times <	44%			33%		

The impedance spectra of 5 mm thick aggregated and modified concretes are compared for 20- and 25-day immersion times in Figure 15. The effect of each modifier appeared to be similar for both day 20 and 25 data. The real impedance values of colloidal silica-, glycol- and micro silica-modified aggregated concretes were smaller or only slightly larger than the aggregated concretes with no modifiers. In the meantime, the real impedance values of fumed silica-modified concretes were significantly higher than the blank aggregated concretes, implying it is effective to reduce the transport of O_2 and Cl^-. Fumed silica was also an effective modifier in simple concretes (see Table 2).

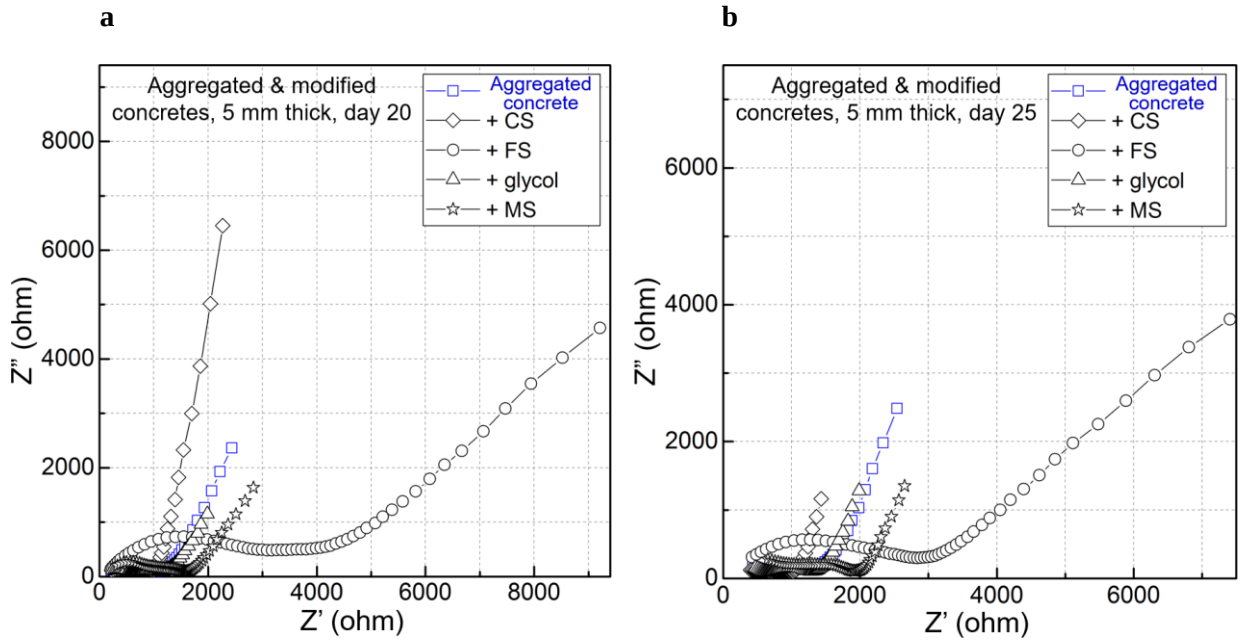

Figure 15. Nyquist plots of 5 mm thick modified and unmodified aggregated concretes for (a) day 20 and (b) day 25.

The real impedance values of aggregated and modified concretes are summarized for different thicknesses and immersion times in Table 3. The impedance values of each modified aggregated concretes were compared to unmodified aggregated concretes for the same thickness and immersion time. As noticed in the table, glycol- and micro silica-modified aggregated concretes were not effective to increase the real impedance values. In colloidal silica-modified aggregated concretes, only 17% of impedance data showed a noticeably larger (1.6~2 times) than the blank aggregated concretes. The impedance values of fumed silica-modified aggregated concretes, in contrast, were significantly higher than the blank aggregated concretes in all tested thicknesses and immersion times, indicating that fumed silica is an effective modifier to limit the transport of O_2 and Cl^-.

According to the real impedance values in Table 2 and 3, the modifiers effective to decrease O_2 and Cl^- transport can be identified for simple and aggregated concretes: fumed silica for both simple and aggregated concretes and micro-silica for the simple concretes. Colloidal silica was least efficient, and glycol was somewhat effective in the simple concretes but not in aggregated concretes.

Table 3. Summary of the real impedance values measured for modified and unmodified aggregated concretes, the values in single bracket indicate that they were 1.6~2 times larger than the impedance of unmodified aggregated concretes. Similarly, the values in double bracket indicate that they were more than 2 times larger.

	Aggregated concrete real impedance (ohm)			
	Day 20		Day 25	
1 mm	2276		1754	
3 mm	3395		2942	
5 mm	2436		2543	
	+ CS real impedance (ohm)		**+ FS** real impedance (ohm)	
	Day 20	Day 25	Day 20	Day 25
1 mm	1096	1200	((5241))	((6624))
3 mm	3785	(4931)		
5 mm	2268	1433	((9210))	((7410))
1.6~2 times	17%		0%	
2 times <	0%		100%	
	+ glycol real impedance (ohm)		**+ MS** real impedance (ohm)	
	Day 20	Day 25	Day 20	Day 25
1 mm			1562	2087
3 mm	1043	2124	679	1092
5 mm	1986	1987	2834	2653
1.6~2 times	0%		0%	
2 times <	0%		0%	

Effect of Temperature on Chloride Ion Diffusion

The effect of temperature on diffusion coefficient of aqueous species (ions and gas molecules in aqueous solutions) can be predicted using the Stokes-Einstein equation [8]:

$$D^\circ_T = D^\circ_{298} \cdot \frac{T/298}{\eta^\circ_T/\eta^\circ_{298}} \qquad \text{[Eqn. 3]}$$

where D°_T, D°_{298}, η°_T and η°_{298} denote the self-diffusion coefficient of aqueous species and dynamic viscosity of pure water at an absolute temperature T and 298 K, respectively. As the viscosity of pure water decreases with increasing temperature, the diffusion coefficient at T higher than 298 K is larger than D°_{298}. The ratio of self-diffusion coefficients in different temperatures are summarized in Table 4 using the reported dynamic viscosity of pure water [9]. The self-diffusion coefficient of aqueous species increases with increasing temperature and can be more than 2 times if the temperature is increased from 25 to 60 °C. Based in these results, the diffusion of O_2 and Cl^- in concretes is expected to accelerate in elevated temperatures.

Table 4. Dynamic viscosities of pure water and calculated multiplying factors for diffusion coefficients of aqueous species for different temperatures, the calculation of multiplying factors is based on Stokes-Einstein equation.

Temperature		Dynamic viscosity of pure water (cP) [9]	$\eta^\circ_T / \eta^\circ_{298}$	$(T/298)/(\eta^\circ_T / \eta^\circ_{298})$
°C	K			
15	288	1.139	1.28	0.76
20	293	1.002	1.13	0.87
25	298	0.890	1	1
30	303	0.789	0.9	1.13
40	313	0.653	0.73	1.43
50	323	0.547	0.61	1.76
60	333	0.466	0.52	2.13

Conclusion

The effect of modifiers to retard O_2 and Cl^- transport in simple and aggregated concretes was assessed using EIS technique and equivalent circuit model. The effect of temperature was also estimated. The results can be summarized:

1. The equivalent circuit applicable to the corroding steel in a solution-permeated concrete was suggested. This circuit consists of *R*-CPE and W_o-*R*-CPE in series connection where *R*-CPE and W_o-*R*-CPE account for the impedance responses of the concrete layer and corroding steel under diffusion control, respectively.

2. No satisfactory fitting was obtained between measured and modeled impedance spectra. The real impedance values at 0.1 Hz (the lower frequency limit) were used instead to compare the resistive and diffusion-related impedances associated with the transport of O_2 and Cl^-. The addition of fumed silica increased the real impedance of both simple and aggregated concretes indicating it is effective to slow down O_2 and Cl^-. Micro silica showed a significant effect in the simple concretes but not in aggregated concretes. Glycol had limited effect only in the simple concretes. Colloidal silica was least effective.

3. The diffusion of O_2 and Cl^- in concrete is expected to increase by increasing temperature.

Reference

1. G. Song, Cement and concrete research 30, p. 1723 (2000).

2. Zview impedance/gain phase graphing and analysis software operating manual, version 3.5, Scribner Associates Inc., Southern Pines, NC (2015).

3. M. Sanchez, J. Gregori, C. Alonso, J.J. Garcia-Jareno, H. Takenouti and F. Vicente, Electrochemica Acta 52, p. 7634 (2007).

4. R. Vedalakshmi and N. Palaniswamy, Magazine of concrete research 62(3), p. 177 (2010).

5. R. Vedalakshmi, V. Saraswathy, H. Song and N. Palaniswamy, Corrosion Science 51, p. 1299 (2009).

6. M. Shi, Z. Chen and J. Sun, Cement and concrete research 29, p. 1111 (1999).

7. N. S. Martys, "Survey of Concrete Transport Properties and their Measurement" NISTIR 5592, US Department of Commerce NIST, Gaithersburg, MD (1995).

8. A. Einstein, Annalen Der Physik 19, p. 289 (1906).

9. J. K. Venard and R. L. Street, "Elementary Fluid Mechanics" 5th ed., Wiley, New York (1975).